Monitoring Sub-Surface Storage of Carbon Dioxide

Laurence R. Cowton

A dissertation submitted for the degree of
Doctor of Philosophy
at the University of Cambridge

Fitzwilliam College
July 2017

Monitoring Sub-Surface Storage of Carbon Dioxide

Laurence R. Cowton

Since 1996, super-critical CO_2 has been injected at a rate of $\sim$0.85 Mt yr^{-1} into a pristine, saline aquifer at the Sleipner carbon capture and storage project. A suite of time-lapse, three-dimensional seismic reflection surveys have been acquired over the injection site. This suite includes a pre-injection survey acquired in 1994 and seven post-injection surveys acquired between 1999 and 2010. Nine consistently bright reflections within the reservoir, mapped on all post-injection surveys, are interpreted to be thin layers of CO_2 trapped beneath mudstone horizons. The areal extents of these CO_2 layers are observed to either increase or remain constant with time. However, volume flux of CO_2 into these layers has proven difficult to measure accurately. In addition, the complex planform of the shallowest layer, Layer 9, has proven challenging to explain using reservoir simulations. In this dissertation, the spatial distribution of CO_2 in Layer 9 is measured in three dimensions using a combination of seismic reflection amplitudes and changes in two-way travel time between time-lapse seismic reflection surveys. The CO_2 volume in this layer is shown to be growing at an increasing rate through time. To investigate CO_2 flow within Layer 9, a numerical gravity current model that accounts for topographic gradients is developed. This vertically-integrated model is computationally efficient, allowing it to be inverted to find reservoir properties that minimise differences between measured and modelled CO_2 distributions. The best-fitting reservoir permeability agrees with measured values from nearby wells. Rapid northward migration of CO_2 in Layer 9 is explained by a high permeability channel, inferred from spectral decomposition of the seismic reflection surveys. This numerical model is found to be capable of forecasting CO_2 flow by comparing models calibrated on early seismic reflection surveys to observed CO_2 distributions from later surveys. Numerical and analytical models are then used to assess the effect of the proximity of an impermeable base on the flow of a buoyant fluid, motivated by the variable thickness of the uppermost reservoir. Spatial gradients in the confinement of the reservoir are found to direct the flow of CO_2 when the current is of comparable thickness to the reservoir. Finally, CO_2 volume in the second shallowest layer, Layer 8, is measured using structural analysis and numerical modelling. CO_2 in Layer 8 is estimated to have reached the spill point of its structural trap by 2010. CO_2 flux into the upper two layers is now $\sim$40% of total CO_2 flux injected at the base of the reservoir, and is increasing with time. This estimate is supported by observations of decreasing areal growth rate of the lower layers. The uppermost layers are therefore expected to contribute significantly to the total reservoir storage capacity in the future. CO_2 flow within Layer 9 beyond 2010 is forecast to be predominantly directed towards a topographic dome located $\sim$3 km north of the injection point. This dissertation shows that advances in determining the spatial distribution and flow of CO_2 in the sub-surface can be made by a combination of careful seismic interpretation and numerical flow modelling.

Publications arising from this dissertation

Chapter 3

Cowton L. R., J. A. Neufeld, N. J .White, M. J. Bickle, J. C. White & R. A. Chadwick (2016), An inverse method for estimating thickness and volume with time of a thin CO_2-filled layer at the Sleipner field, North Sea, *Journal of Geophysical Research: Solid Earth*, Vol. 121, 5068-5085

Chapter 4

Cowton L. R., J. A. Neufeld, N. J .White, M. J. Bickle, G. A. Williams, J. C. White & R. A. Chadwick (in review), Benchmarking vertically-integrated CO_2 flow simulations at the Sleipner field, North Sea, *Earth and Planetary Science Letters*

Planned publications arising from this dissertation

Chapter 5

Cowton L. R., J. A. Neufeld, N. J .White, M. J. Bickle, J. C. White & R. A. Chadwick (in preparation), Fluid flow in a variably confined aquifer, *Journal of Fluid Mechanics*

Chapter 2 and 6

Cowton L. R., J. A. Neufeld, N. J .White, M. J. Bickle, J. C. White & R. A. Chadwick (in preparation), CO_2 migration at the Sleipner field, North Sea

Declaration

This dissertation describes my original work except where acknowledgement is made in the text. It does not exceed the page limit and is not substantially the same as any work that has been, or is being submitted to any other university for any degree, diploma or any other qualification.

Laurence R. Cowton
July 2017

"The Earth is a great laboratory and storehouse of old experiments, wherein we may discipline our thoughts, and rise to the comprehension of the laws of nature... Exact science is the creature of the human mind–a body of necessary truths built upon mere abstractions. But when physical phenomena are well defined, and their laws made out by long and patient observations, or proved adequate by experiment: they then, by an act of thought, may be made to pass into the form of mere abstractions, and so come within reach of exact mathematical analysis."

A. Sedgwick, 1842
Three Letters on the Geology of the Lake District
addressed to W. Wordsworth

Acknowledgements

I would like to thank the many people who have contributed to my work and well-being throughout this PhD. Thanks to Jerome Neufeld, Nicky White and Mike Bickle for their patience and guidance through the world of numerical modelling and geophysical observations over the past three years. Thanks also go to Andy Chadwick, Jim White and Gareth Williams for their expertise and knowledge of all aspects of the Sleipner carbon capture and storage project.

The Drum building has been a wonderful place to work during my PhD. Without the academic input and excellent company of Verónica Rodríguez Tribaldos, Marthe Klöcking, Charlie Schoonman, Matt Commin, Paddy Ball, Ross Parnell-Turner, Jacky Austermann, Conor O'Malley, Kathy Gunn and Fergus McNab, the past four years would have been much harder. Fred Richards and Jonathan Wilson have been very forgiving office mates. Thomasina Ball, Zhong Zheng and Finn Box have taught me many things about fluid dynamics.

The Earth Sciences department has provided a whole host of new climbing partners. Excellent times on cliff edges have been had with Mark Hoggard, Tim Greenfield, Jenny Jenkins, Simon Stephenson, Alex Dickinson, Jenny Roberts, Rob Green and Andy Howell. Thanks also go to Will Miller, Neil Paul, Claire Nichols and Vincent Lister for being fantastic house mates over the past four years.

I would also like to thank Ian Frame, Dave Lyness and Chris Richardson for keeping the computers running and Sarah Humbert for her wisdom and incredible skill at finding hard to reach papers. I thank the Sleipner License Partners (Statoil, Total E&P Norge and ExxonMobil) for access to the seismic reflection data sets, and Schlumberger for providing seismic interpretation software. I am indebted to the Worshipful Company of Leathersellers and Fitzwilliam College who have provided a generous scholarship for the past three years.

I would also like to thank my parents, Jeff and Gill, for their love and support throughout this time. It is undoubtedly due to their love of the outdoor world that I have followed the path I am on now. My brothers have been a big inspiration to me throughout my life, always spurring me on to bigger and better things. Finally, I would like to thank Katherine Monks for being with me all the way.

Contents

List of Figures

List of Tables

Chapter 1

Introduction

1.1 Carbon Capture and Storage

Carbon Capture and Storage (CCS) describes the process of separating carbon dioxide (CO_2) from industrial and energy-related gas emissions and storing it within sub-surface reservoirs. CCS is one of a number of proposed methods to reduce anthropogenic CO_2 emissions that also include energy efficiency improvements and switching to renewable energy sources. However, many CO_2 emission reduction strategies cannot meet the 450 ppm concentration target by 2100 without CCS (IPCC, 2014). CCS can also be used to reduce the emissions from industrial processes such as steel or concrete manufacturing, for which alternatives are not easily available.

For CCS to be an effective means of reducing greenhouse gas emissions, CO_2 must be stored securely in isolation from the atmosphere on time scales of thousands of years. The largest available reservoir for captured CO_2 is within sedimentary rocks, either in depleted hydrocar-

bon reservoirs or in pristine saline aquifers. It is estimated that there is at least 2000 Gt CO_2 capacity globally in such reservoirs (IPCC, 2005). The potential storage capacity for the UK alone is estimated to be 78 Gt (APGTF, 2014). For comparison, a large coal-fired power station produces approximately 8 Mt CO_2 yr^{-1} (Benson & Cole, 2008).

CO_2 is injected into the sub-surface in a super-critical phase, enhancing the storage efficiency of the rock. Once injected into the sub-surface, the CO_2 flows buoyantly through the pore space of rocks, displacing any ambient fluid as it rises through the reservoir. To be securely stored in the sub-surface, CO_2 must be trapped by one of four mechanisms. The simplest of these mechanisms is structural trapping, in which CO_2 ponds beneath an impermeable geological trap. Alternatively, CO_2 can dissolve in the ambient brine, producing dense plumes of CO_2-saturated brine. CO_2 flowing through pore spaces can also become trapped by capillary forces as discrete bubbles. Finally, CO_2 can react with minerals present in the geological formation to form carbonate rocks. In the short term, the CO_2 is likely to rise buoyantly through the reservoir, eventually becoming structurally trapped. In the long term, it is expected that CO_2 will either dissolve or form new minerals, significantly reducing the possibility of it returning to the atmosphere.

Careful monitoring of injected CO_2 is important to demonstrate storage security and to improve our understanding of the behaviour of CO_2 in porous reservoirs. Large-scale field trials of CO_2 storage are yielding high quality, geophysical datasets that improve our ability to assess the long-term stability of sequestered CO_2. Geophysical monitoring techniques that have been trialled at the field scale include time-lapse seismic reflection surveying, electromagnetic resistivity measurements, passive micro-seismicity monitoring, micro-gravimetry and interferometric synthetic aperture radar (InSAR). The monitoring system deployed at each site will be determined by factors such as reservoir geology, injection depth and location, as well as available financial resources.

Statoil's Sleipner project in the North Sea is the longest running industrial CCS project globally (Chadwick & Noy, 2010). CO_2 extracted from natural gas produced from the nearby

Sleipner Vest field has been injected into a pristine saline aquifer 1000 m below sea level at a rate of approximately 0.85 Mt yr^{-1} since 1996 (Korbøl & Kaddour, 1995; Baklid *et al.*, 1996). The Sleipner project is an important site for studying CO_2 migration for three significant reasons. First, CO_2 is being injected into a pristine, saline reservoir. The pristine nature of the aquifer means that changes in the sub-surface that can be detected by geophysical monitoring are attributable to CO_2 injection alone. Secondly, the shallow depth of burial optimizes the resolution of monitoring techniques. Thirdly, the project's marine setting enables high quality time-lapse seismic reflection surveys to be acquired at regular intervals. In terms of vertical and horizontal resolution, seismic reflection surveying is the most successful monitoring technique currently available but it is also the most expensive to acquire and process. One pre-injection and seven post-injection time-lapse seismic reflection surveys have been made available for this study.

Time-lapse seismic reflection surveys acquired at the Sleipner project have enabled the migration of CO_2 flow within the reservoir to be studied in considerable detail. In these surveys, it is well-documented that super-critical CO_2 is progressively filling a series of nine sandstone layers within the reservoir (e.g. Arts *et al.*, 2004; Bickle *et al.*, 2007; Boait *et al.*, 2012). However, until recently, constraints on the volume of CO_2 stored within these layers, and therefore the migration rates of CO_2 into these layers, were limited. Knowledge of the volume of CO_2 within these layers would provide key information about the proportion of CO_2 injected at the base of the reservoir that reaches the caprock. The rate at which CO_2 migration from the injection point to the caprock occurs indicates whether the intermediate layers are contributing significantly to the total CO_2 storage capacity in the reservoir.

Numerical simulations of the flow of CO_2 through potential storage reservoirs are an important part of hazard assessment and site selection for future CCS projects. The time-lapse data available from the Sleipner project makes it an ideal place to test and develop reservoir simulators that can accurately predict the flow of CO_2 through the sub-surface. The irregular planforms of the CO_2 layers within the reservoir have proved challenging to explain using history-matching flow models. Understanding the dominant processes controlling the

flow of CO_2 in reservoirs such as these will help to refine these simulators and increase computational efficiency.

1.2 Aims and Approaches

This dissertation is concerned with understanding the dynamics of the flow of CO_2 through a pristine geological reservoir. A combination of geophysical observations and fluid dynamical models are used to explore the flow of CO_2 through the reservoir at the Sleipner site. This study aims to further current understanding of two important questions posed by availability of seismic reflection surveys at the Sleipner CCS project. First, can the flux of CO_2 into the observed layers be accurately constrained through time? Secondly, what are the dominant controls on the lateral flow of CO_2 through the reservoir at Sleipner?

To address these questions, the thickness of the shallowest layer of CO_2 within the aquifer, Layer 9, is constrained using detailed observations of amplitude and changes in travel time of seismic reflections between surveys. A numerical model is then used to investigate the flow of CO_2 within this layer. Permeability of the reservoir is constrained by inverting the flow model to find the best match to the estimate of layer thickness from the seismic reflections. The effect of the proximity of an impermeable base to the reservoir on the flow of a buoyant fluid is investigated using analytical and numerical models. Finally, the volume of CO_2 in Layer 8 is constrained using a variety of geophysical, geometrical and numerical models.

1.3 Dissertation Structure

Chapter 2: The Sleipner Project. The CO_2 injection history and available information on the Sleipner carbon capture and storage project are discussed. Estimates of the change in areal extent for each CO_2 layer with time are updated from Boait *et al.* (2012) to include the 2010 seismic reflection survey.

Chapter 3: Measuring the Thickness of a CO_2 Layer. An inverse method for measuring the thickness of thin fluid layers using time-lapse seismic reflections surveys is developed and applied. This method utilises small changes in travel time and amplitude of the caprock reflection, to measure the thickness of CO_2 ponded beneath this boundary. Synthetic tests are used to calculate uncertainties in the measured thickness using this method. The thickness of the shallowest CO_2 layer, Layer 9, is mapped for each seismic reflection survey, and the CO_2 volume in Layer 9 is estimated. The measured thickness of the layer is compared to estimates from the 2010 broadband survey. Seismic chimneys are described as evidence of vertical flow conduits through the reservoir.

Chapter 4: Modelling CO_2 Flow in Layer 9. A gravity current model is developed to simulate the flow of CO_2 in Layer 9. A numerical model for a gravity current on a slope is first developed in two, and then three, dimensions. The model is benchmarked against analytical results from Huppert & Woods (1995) and Vella & Huppert (2006). Estimates of the topography of the Layer 9 caprock-reservoir contact, the estimated input flux and input location from Chapter 3, and reservoir and fluid properties taken from the literature are then used to model flow within Layer 9. Reservoir properties are inverted for by matching flow model results to the calculated thickness. Spectral decomposition is used to infer the existence of a high permeability channel running through Layer 9. The ability of this model to forecast the flow of CO_2 in this layer, and the future flow of CO_2 into Layer 9 is discussed.

Chapter 5: Gravity Currents in Aquifers with Diverging Boundaries. When additional CO_2 migrates into Layer 9, the effect of the confined nature of the aquifer will become more apparent on its flow through the aquifer. Motivated by the problem of estimating the future flow of CO_2 in Layer 9, the flow of fluids in variably confined aquifers is discussed in two dimensions. Analytical solutions are compared with numerical models for an aquifer with uniformly diverging boundaries. The influence of the lower boundary on the flow of a buoyant fluid is discussed.

Chapter 6: CO_2 in Layer 8. A variety of techniques are applied to obtain estimates of the volume of CO_2 in Layer 8, including structural analysis hemi-ellipsoid trap filling.

An inverse numerical flow model is developed to recover the volume of CO_2 in a layer by minimising the difference between modelled and observed areal extents. This model is first tested on Layer 9 before being applied to Layer 8. The future migration of CO_2 in Layer 8 is discussed.

Chapter 7: Conclusions and Further Work.

Chapter 2

The Sleipner Project

2.1 Introduction

Since 1996, dense-phase CO_2 has been injected into the sub-surface at the Sleipner field, located in the Norwegian North Sea (Figure 2.1). The CO_2 is extracted from natural gas produced from the Sleipner Vest field, which contains up to 9.5% CO_2 by volume (Korbøl & Kaddour, 1995; Baklid *et al.*, 1996). This CO_2 is extracted at the platform and re-injected 2.5 km to the north-east into a pristine saline reservoir, known as the Utsira Formation (Furre & Eiken, 2014). Migration of CO_2 through the reservoir has been monitored using time-lapse (i.e. four-dimensional) seismic reflection surveying. The changing pattern of reflectivity within the reservoir can be used to track the flow of CO_2 away from the injection point. In this chapter, I discuss the acquisition and processing of the seismic reflection data, the geometry and geology of the reservoir, and how the spatial distribution of the CO_2 has evolved through time.

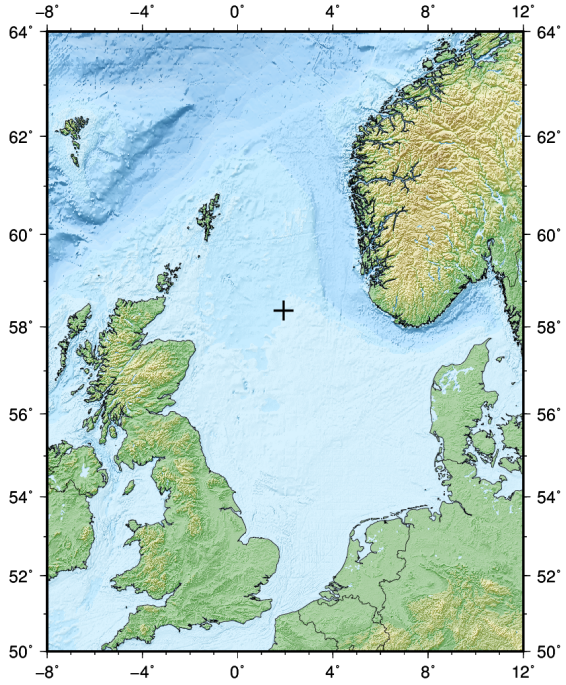

Figure 2.1: Location of Sleipner Carbon Capture and Storage Project in the Norwegian North Sea (Boait *et al.*, 2012).

2.2 Reservoir Properties and Conditions

Injection of CO_2 into the Utsira Formation occurs at a depth of 1012 m below sea level by means of a deviated well at a rate of $\sim$ 0.85 Mt yr^{-1} (Figure 2.2; Chadwick & Noy, 2015). In the vicinity of the Sleipner field, the Utsira Formation is up to 300 m thick and it is overlain by approximately 250 m of shale from the Nordland Group. The Utsira Formation is a highly porous and unconsolidated sandstone deposited in the Upper Miocene to Lower Pliocene times. It is thought to mostly consist of low relief mounds, deposited as submarine fans in a shallow marine environment with a source area in the west (Gregersen *et al.*, 1997; Arts *et al.*, 2008; Halland *et al.*, 2011). The porosity of the sand in the main part of the reservoir has been measured as 37±3 %, and the permeability as 2 D, although regional measurements from the Utsira Formation suggest a range between 1–8 D (Zweigel *et al.*, 2004). Wireline logs indicate that it is sub-divided at approximately 30 m intervals by $\sim$ 1 m thick mudstone layers (Figure 2.3). A thicker mudstone layer is also observed on these logs towards the top of the reservoir, known as the 5 m Shale. This mudstone layer separates

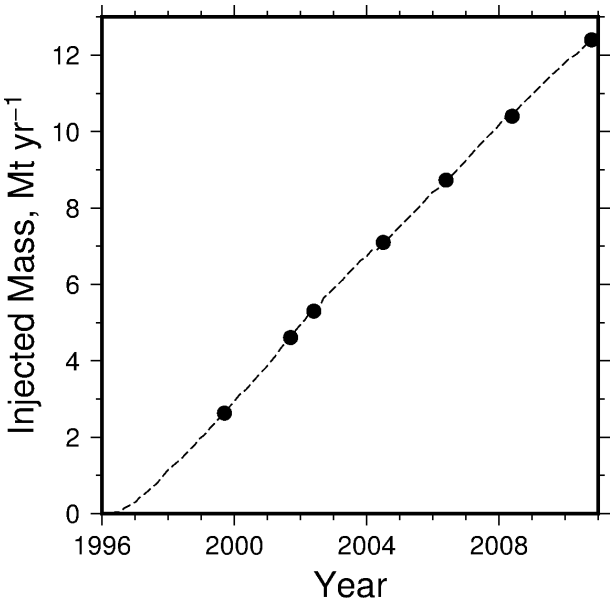

Figure 2.2: Injected mass of CO_2 at the Sleipner Carbon Capture and Storage project. Dashed line = Injected mass. Circles = Acquisition of seismic reflection survey. Adapted from Chadwick & Noy (2015).

the main part of the Utsira Formation from a smaller sandstone unit above, known as the Sand Wedge. The base of the Utsira Formation is affected by mud diapirism and polygonal faulting within the underlying Hordaland Formation (Zweigel *et al.*, 2004). Faulting is not observed within the Utsira Formation above the injection region.

In the absence of down well gauges, the temperature and pressure at the base of the well are estimated to be 35.5° C and 10.5 MPa, based on measurements from a water production well in the Vovle field, 10 km north of the injection well at Sleipner (Alnes *et al.*, 2011; Williams & Chadwick, 2017). The injected CO_2 is heated during compression from well-head conditions down to the injection point where it is thought to be approximately 48.1±0.1° C, assuming hydrostatic pressure at the well-head (Nooner *et al.*, 2007; Alnes *et al.*, 2011). As the CO_2 migrates away from the injection point, it will cool rapidly towards the ambient temperature of the reservoir. The thermal gradient within the reservoir is estimated to be 31.7° C km^{-1}, with the average reservoir temperature thought to be 30 ± 0.5° C (Alnes *et al.*, 2011; Williams & Chadwick, 2017). Williams & Chadwick (2017) also modelled the temperature evolution of the CO_2 plume as it rises through the reservoir using PFLOTRAN (Lichtner *et al.*, 2015). Assuming that the plume is radially symmetrical, these authors

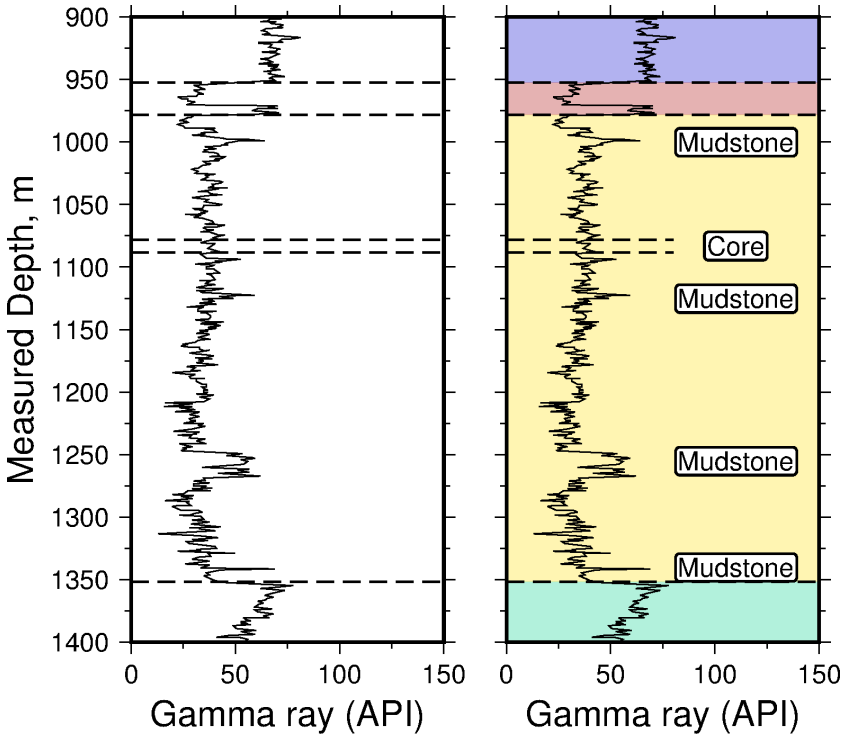

Figure 2.3: Gamma ray log from well 15/98-A23. Well situated close to the CO_2 injection site. Spikes in gamma ray signal within the Utsira Formation interpreted as thin mudstone layers. Sand Wedge separated from main reservoir by larger spike. Core from which permeability and porosity measurements have been made is from between 1080-1088 m drilled depth, 905-910 m below sea level. Blue = Nordland Shale, red = Sand Wedge and 5 m Shale, yellow = Utsira Formation, green = Hordaland Group. Figure adapted from Williams & Chadwick (2017).

found that a central core of CO_2 rose through the aquifer directly above the injection point with a thermal anomaly of approximately 7° C hotter than ambient temperature. However, in these simulations the CO_2 returned to ambient temperatures only short distances away from this central region. At the pressures and temperatures within the reservoir, CO_2 is near its critical point, and so small changes in temperature and pressure will have a significant effect on its density. CO_2 density is therefore expected to be approximately 690±30 kg m^{-3} towards to top of the plume. The viscosity of CO_2 towards the top of the plume is estimated to be $5 \pm 1 \times 10^{-5}$ Pa s (Williams & Chadwick, 2017). These estimates are in line with estimates made using measured micro-gravity anomalies above the plume (Alnes *et al.*, 2011).

2.3 Time-lapse Seismic Reflection Surveys

Seismic reflection imaging is the primary method for monitoring offshore CO_2 storage reservoirs due to the excellent spatial resolution that can be achieved relative to other monitoring methods (e.g. electro-magnetic resistivity, passive micro-seismicity, etc.; Benson & Cole, 2008; Verdon *et al.*, 2010; Martens *et al.*, 2012). At the Sleipner Project, time-lapse seismic reflection surveys have been acquired in 1994, 1999, 2001, 2002, 2004, 2006, 2008 and 2010 (Figure 2.2 and 2.4). The pristine nature of the aquifer (i.e. there is no residual oil or gas in the reservoir) means that any changes in reflectivity can be directly attributed to the presence of CO_2. The marine setting for this project also reduces the financial cost of carrying out regular time-lapse surveying and improves the quality of the data relative to land-based seismic surveys. The 1994 survey was shot prior to the injection of CO_2 and acts as a baseline against which changes in the sub-surface can be gauged.

2.3.1 Seismic Acquisition

The ideal time-lapse seismic reflection survey would be acquired with exactly the same equipment and the same shot and receiver positions. The same set-up would then be used to process the data to maximise comparability of the different surveys. However, due to different contractors acquiring the seismic reflection data for the different surveys, using the same acquisition parameters was not possible. A summary of the acquisition parameters used in each time-lapse survey is given in Table 2.1.

When imaging the sub-surface it is important to record as broad a range of frequencies as possible. Higher frequencies sharpen the peak of the reflecting wavelet, while low frequencies reduce the energy of the side-lobes of the wavelet, making precise interpretation easier (Soubaras & Dowle, 2010). The frequency content of the recorded signal is partly controlled by the depth at which the receivers are towed. The depth of the receivers determines the location of the 'notch' (i.e. low power region) in the frequency spectrum. The notch occurs due to destructive interference between the seismic wave returning from the sub-surface and

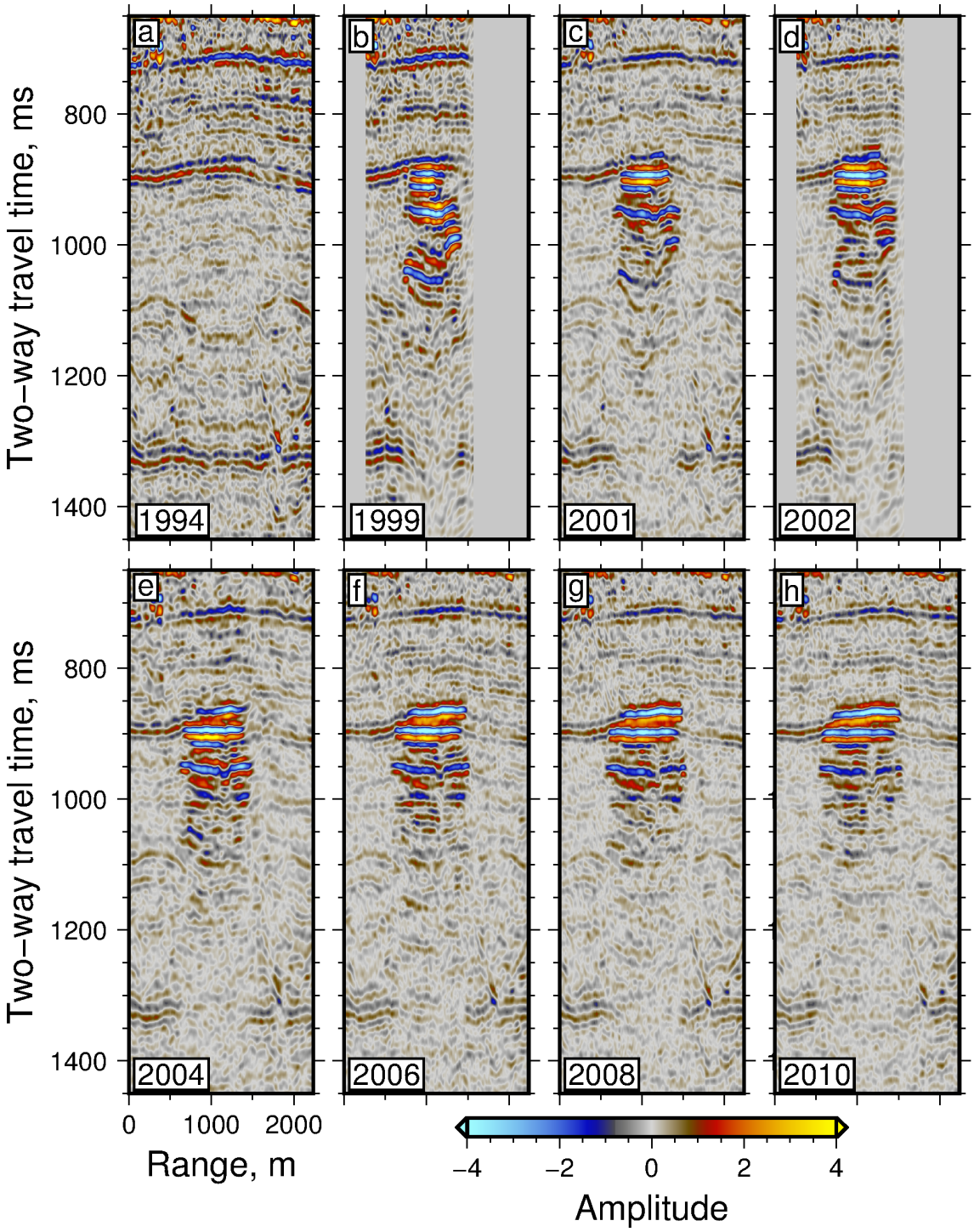

Figure 2.4: Seismic line (cross-line 1125) from all time-lapse surveys. Surveys from 1999 and 2002 are smaller in their extent. See Figure 2.5 for location.

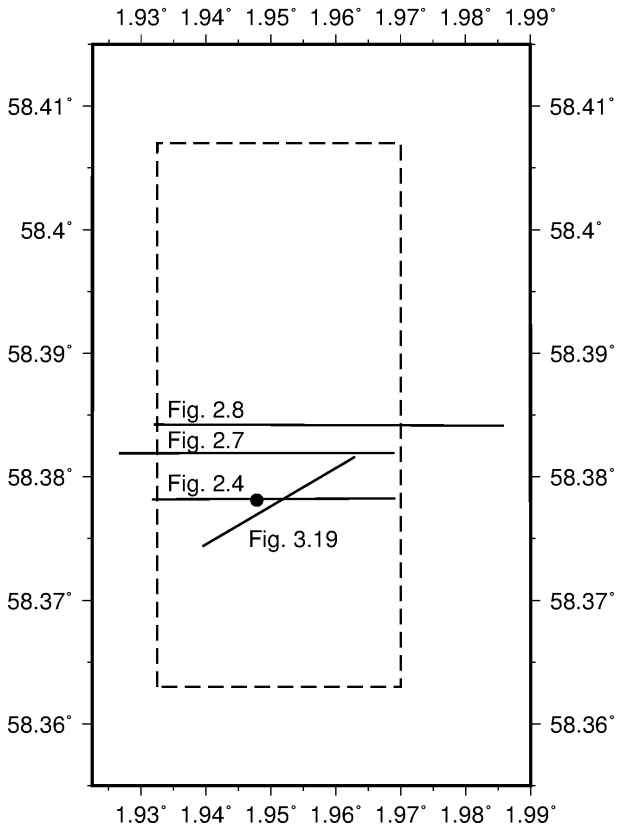

Figure 2.5: Location of seismic lines from Figures 2.4, 2.7 and 2.8. Black circle = CO_2 injection point. Dashed box = extent of Figure 2.9.

Table 2.1: Key parameter values for the acquisition of seismic reflection surveys. Data taken from Boait *et al.* (2012) and Furre & Eiken (2014).

Survey	1994	1999	2001	2002	2004	2006	2008	2010
Shooting direction	N-S	N-S	N-S	N-S	E-W	N-S	N-S	N-S
Number of sources	2	2	2	2	1	2	2	2
Source volume, in^3	3400	3542	3397	3147	4280	3660	3660	4135
Source depth, m	6	6	6	6	6	6	6	5
Shotpoint interval, m	18.75	12.5	12.5	18.75	18.75	18.75	18.75	12.5
Number of streamers	5	4	6	6	10	8	9	12
Streamer separation, m	100	100	100	100	37.5	100	50	75
Receiver depth, m	8	8	8	8	8	8	8	15
Record length, ms	5500	4500	4500	6000	6000	6000	6000	4608

its reverse polarity reflection from the sea surface. This sea surface reflection is known as the receiver 'ghost'. The notch frequency, f_n, is determined by

$$f_n = \frac{v_w k}{2d_r}, \tag{2.1}$$

where v_w is the velocity of seismic waves through water, d_r is the depth of the receiver, and k is an integer value. From (2.1), it is clear that decreasing the tow depth will mean that the first notch frequency ($k = 1$) will be higher, increasing the bandwidth of the seismic data. However, a shallower tow depth attenuates lower frequencies and makes the data more susceptible to sea surface noise (Kragh *et al.*, 2010). The pre-injection survey, along with many of the subsequent surveys, were shot with the primary objective of imaging the Sleipner East natural gas reservoir at a depth of $\sim$ 2300 m (Eiken *et al.*, 2000; Furre & Eiken, 2014). Thus the frequency content of this survey is not optimal for imaging the target depth of the CO_2-filled reservoir (i.e. $\sim$ 800 m). A shallower tow depth would have permitted higher frequencies, and therefore better vertical resolution in the CO_2 reservoir, but to keep parameters the same as for the baseline survey, identical tow depths were used from 1994–2008. The vertical resolution of the time-lapse survey has therefore been limited to improve comparability with the pre-injection survey.

In 2010, a broadband seismic survey was acquired using a dual-sensor streamer (PGS Geostreamer) configuration that combines a particle velocity detector with hydrophones, so that directionality can be assigned to the wave field (Tenghamn *et al.*, 2007; Furre & Eiken, 2014). Knowing the direction of the wave enables the ghost reflection from the sea surface to be accurately measured, and then removed. However, this streamer technology cannot correct for the source ghost. The survey acquired in 2010 used a much deeper tow depth to reduce the sea surface noise and, since the receiver ghost can be removed, it is richer in high frequencies and has considerably better vertical resolution than previous surveys (Figure 2.6; Furre & Eiken, 2014). The effects of improved frequency content are obvious when this broadband survey is compared with its filtered equivalent (Figure 2.7).

Table 2.1 shows that the other acquisition parameters used throughout these surveys are

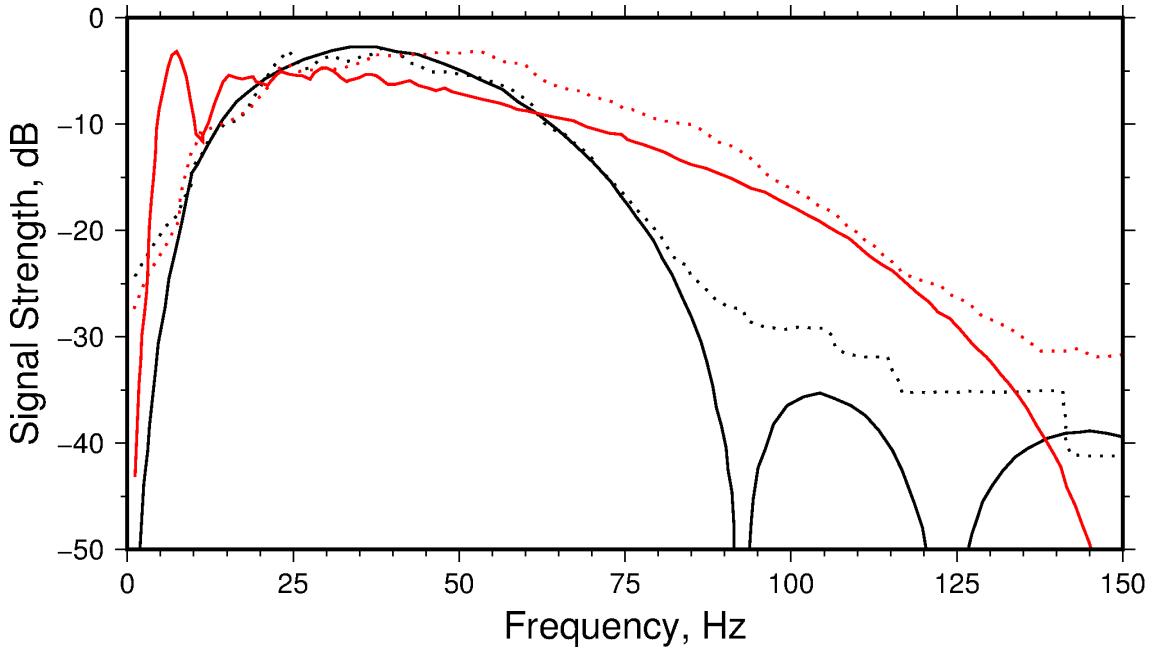

Figure 2.6: Observed and modelled frequency spectra from 2010 survey Black = time lapse processing, red = broadband processing. Dotted = observed frequency spectra, solid = modelled frequency spectra. Frequency content is reduced to match baseline survey for time-lapse processing. Source notch at higher frequency for broadband processing due to shallower source depth. Source depth for time-lapse processing was shifted from 5 to 6 m by wavelet transformation. Signal strength vertically shifted to a maximum of 3 dB for comparison. Figure adapted from Furre & Eiken (2014).

consistent. Importantly, for all surveys except the 2004 survey, a comparable airgun array and volume were used, meaning that the strength of the source will be similar between the surveys. The air guns were also all towed at the same depth so that the notch frequencies associated with the source are the same for all surveys. However, the 2004 survey was acquired at 90° to other surveys meaning that parameters such as shot and receiver locations could not be repeated. The 2002 survey did not cover the whole of the CO_2 plume.

Figure 2.7: Time-lapse seismic reflection surveys (overleaf). **(a)–(c)** Single cross-line from 1994 (i.e. pre-injection), 2010, and 2010 (broadband) surveys. Red/blue reflections = positive/negative amplitudes. **(d)–(f)** Interpreted images. HF (green) = Hordaland Formation; UF (yellow) = Utsira Formation; NG (blue) = Nordland Group; SW and 5S (red) = Sand Wedge unit and 5 m thick mudstone horizon; encircled numbers = 9 mappable layers; GP = pockets of natural gas; IP = projected CO_2 injection point; M = peg-leg multiple event; IR = incoherent reflections; P = pushdown of base Utsira Formation; NSR = unseparated reflection at Layer 9, SR = separated reflections at Layer 9. See Figure 2.5 for location.

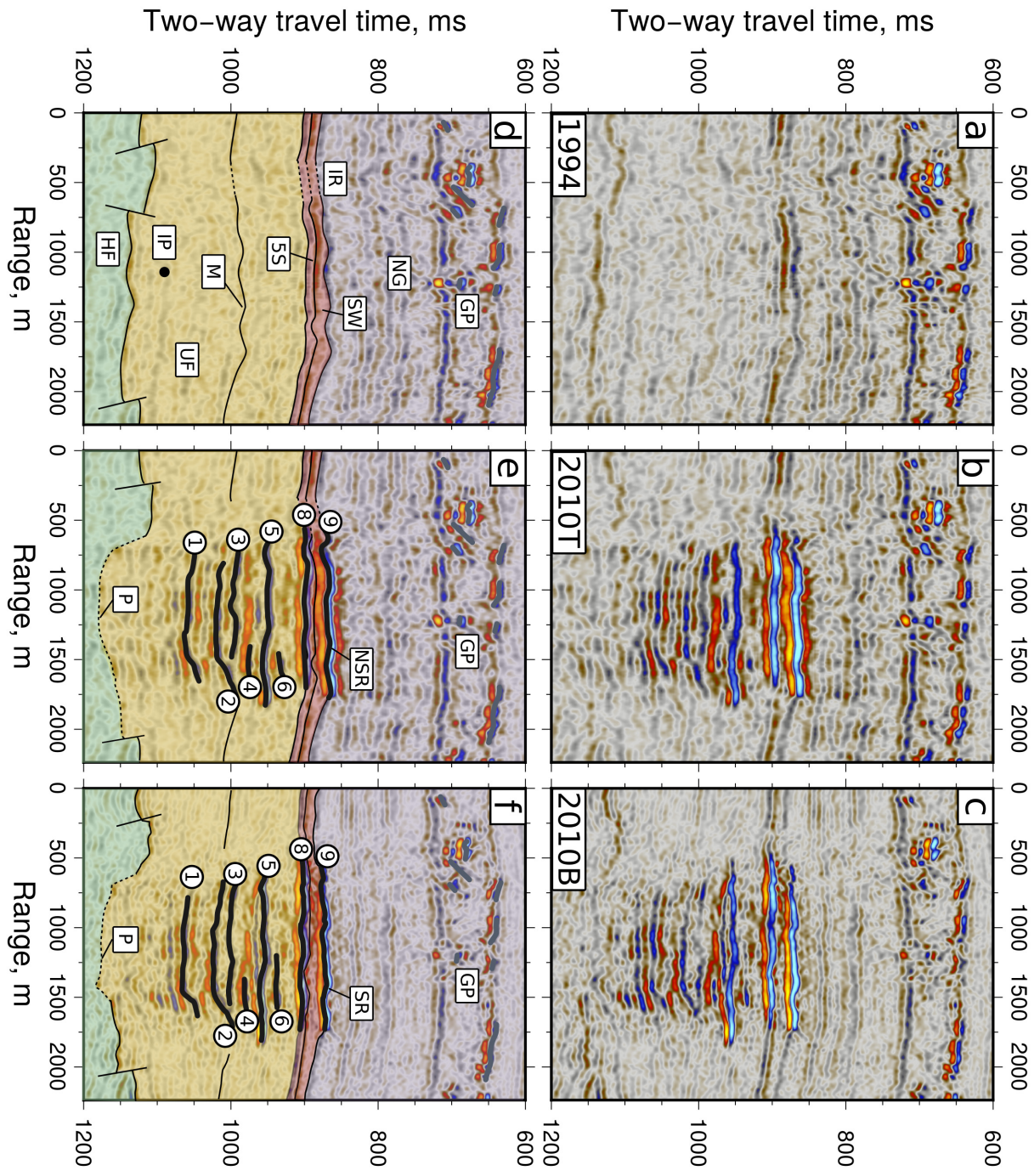
Two−way travel time, ms
Two−way travel time, ms
Range, m
Range, m
Range, m
1994
2010T
2010B
a
b
c
d
e
f
IR
5S
NG
SW
GP
HF
IP
M
UF
P
NSR
SR
1
2
3
4
5
6
8
9
600
800
1000
1200
0
500
1000
1500
2000

2.3.2 Seismic Processing

Due to the nature of time-lapse surveying, the survey has been processed in several batches. Each batch was processed by different contractors, in which the same processing sequence was performed on a subset of the time-lapse survey. In this work, four of these batches were used: the 2002 processing set, which covers 1994, 1999 and 2002; the 2006 processing set, covering 1994, 2001, 2004, and 2006; the 2008 processing set, covering 1994 and 2008; and the 2010 processing set, covering 1994 and 2010. Each time-lapse survey was processed with reference to, and by benchmarking against, the 1994 baseline survey. This approach facilitates comparison between pre- and post-injection surveys. To account for the changes in source depth for the 2010 survey, the source depth was shifted from 5 to 6 m by wavelet transformation (Furre & Eiken, 2014). For all time-lapse surveys, data is binned horizontally into 12.5 m by 12.5 m blocks.

The 2008 and 2010 processing sequences were designed to be similar to the 2006 processing sequence, to boost comparability between the processing sets. These processing sequences include τ-p deconvolution, which transfers the signal into the time-slowness domain in which noise and multiples can be filtered out, and 3D pre-stack time-migration. Pushdown below the plume was used to aid picking stacking velocities within the plume, made difficult by multiples and velocity variations below the resolution of velocity analysis. The 2002 processing set also used τ-p deconvolution, but used dip move-out (DMO) instead of 3D pre-stack time-migration (Furre & Eiken, 2014). DMO is similar to normal move-out (NMO), but is applied when dipping horizons are present.

In these surveys, amplitudes have been corrected for spherical divergence of wavefronts as they propagate through the sub-surface. Amplitudes have also been corrected for fold of cover (i.e. low-fold and high-fold seismic arrivals have the same amplitude). Finally, amplitudes have not been scaled or normalized. In general, each post-injection survey was processed in conjunction with the pre-injection survey to ensure that pre- and post- injection surveys are comparable.

The 2010 survey was also processed separately to the time-lapse survey, meaning that comparability with the pre-injection survey was forsaken in favour of boosting vertical resolution. The processing sequence for this survey involved three methods for removing multiples and true amplitude pre-stack time-migration. The data for this survey were binned into 6.25 m by 25 m bins. For further information on the processing of these seismic reflection surveys see Boait (2012) and Furre & Eiken (2014).

During the processing of these surveys, deconvolution techniques were used to ensure that the reflected waves have zero phase (i.e. maximum amplitude of the wave coincides with the locus of impedance contrast in two-way travel time). Ricker wavelets provide a good approximation of these zero-phase wavelets (Arts *et al.*, 2004; Boait *et al.*, 2012).

To objectively assess differences between the time-lapse surveys, Furre & Eiken (2014) calculated a normalised root mean square (NRMS) difference of a 6 km^2 area directly above the Utsira Formation between each post-injection survey and the 1994 survey (Kragh & Christie, 2002). These values generally lie between 52 and 62%, suggesting that this suite of time-lapse surveys are appropriately comparable (Cantillo, 2012). An outlier in these NRMS measurements is the 2004 survey, with a value of 77%. This anomalously high value is attributed to the seismic reflection survey being acquired perpendicularly to the other surveys in the suite.

2.4 Interpretation of Pre-injection Survey

Seismic reflection surveys measure the reflectivity of the sub-surface as a function of two-way travel time (TWTT). TWTT is the time a wave takes to travel from source to receiver, via a sub-surface reflection. To convert from TWTT to true depth, the velocity structure of the sub-surface must be known. Seismic reflection surveys can provide detailed estimates of the geometry of the reservoir, including the topography of the caprock and the base. The geometry of the reservoir is likely to play an important role in the lateral migration of CO_2

beneath low-permeability horizons. In this section, I discuss the information that can be extracted from the baseline survey about the reservoir and overburden.

2.4.1 Overburden and Reservoir Caprock Topography

Geological units in the overburden of the CO_2 reservoir at Sleipner are approximately horizontally bedded (Figure 2.8). The nature of these beds can be determined from the seismic reflections, which are primarily horizontal from the seabed ($\sim$ 100 ms TWT) down to a bright reflection within the Nordland Formation ($\sim$ 700 ms TWT, Figure 2.8). This simple 'layer-cake' structure means that the only acoustic velocity required to calculate the topography of the reservoir caprock is the average velocity of seismic waves through the Nordland Formation, which is $v_N = 2150 \pm 46 \text{ms}^{-1}$ (Chadwick *et al.*, 2016). These uncertainties have been measured from the spatial variation in stacking velocities calculated during the processing of the seismic data. However, measured values of v_N from nearby wells show much less variation, in the range 2133-2159 ms^{-1}, suggesting that this estimate is adequate.

The topography of the reflection from the caprock of the reservoir can be converted from TWTT, t_c, to depth, d, in metres below sea level using

$$d = \frac{t_c}{2} v_N - c, \tag{2.2}$$

where $c = 115$ m is a constant that shifts the relative depth estimate to true depth based on core logs (A. Chadwick, pers. comm., 2017). A major assumption in the use of (2.2) is that the acoustic velocity of the overburden is spatially consistent. Pre-existing pockets of natural gas in the Nordland Formation mean that this assumption does not hold across the entire region (bright reflections around $\sim$700 ms TWT, Figure 2.8). Figure 2.9 shows the distribution of natural gas pockets through the Nordland Formation in a depth range of 600-850 ms. These pockets of natural gas saturated rock will have a lower acoustic velocity than that of the surrounding brine-saturated rock. The effect of this slower velocity material is to 'push down' the reflections below these gas pockets, artificially increasing the depth to the caprock reflection. These gas pockets also disrupt the coherency of the reflections

below them, meaning that the peak of the reflected wave cannot be accurately picked (Figure 2.7a,d). In these regions, the topography is interpolated using a continuous curvature spline in tension to estimate the missing data (Smith & Wessel, 1990). The caprock reflection shows no evidence of faulting in the region near the injection site.

The topography of the caprock-reservoir reflection is dominated by two anticlinal domes, connected by a prominent north-striking ridge (Figure 2.10a). The southern dome sits directly above the injection point for CO_2 at the base of the reservoir. The topographic gradients for this boundary are shallow.

2.4.2 The Utsira Formation

The prominent positive reflection immediately below the reservoir-caprock reflection ($\sim$ 900 ms, Figure 2.8) is interpreted to be a 6.5 m thick mudstone layer observed on wireline logs in nearby wells, known as the '5 m Shale' (Figure 2.3; Chadwick *et al.*, 2004a). This mudstone layer separates the uppermost section of the reservoir from the main reservoir, and is thought to represent the lowermost unit of the Nordland Shale in the west. In the vicinity of the CO_2 injection point, this mudstone layer is separated from the rest of the Nordland Shale by a sand unit known as the Sand Wedge. The Sand Wedge is observed to become thinner towards the west until it pinches out approximately 5 km from the injection point (Zweigel *et al.*, 2004). The gamma-ray signal in the Sand Wedge is lower than for the main reservoir, suggesting that the sand in this part of the reservoir has a lower mud content (Williams & Chadwick, 2017). Prior to injection of CO_2, the Sand Wedge was expected to be hydrologically separate from the main reservoir due to the 5 m Shale (Zweigel *et al.*, 2004).

Figure 2.8: Cross-line 1179 from the 2008 processing vintage of the 1994 survey. Top Utsira Formation reflection at $\sim$830 ms, base Utsira Formation at $\sim$1100 ms. All reflections above Utsira Formation are approximately flat. Mud diapirism that has affected base Utsira Formation reflection has not disrupted Intra-Hordaland reflection ($\sim$1300 ms). Positive amplitude reflections shown in red, negative amplitude reflections in blue. See Figure 2.5 for location.

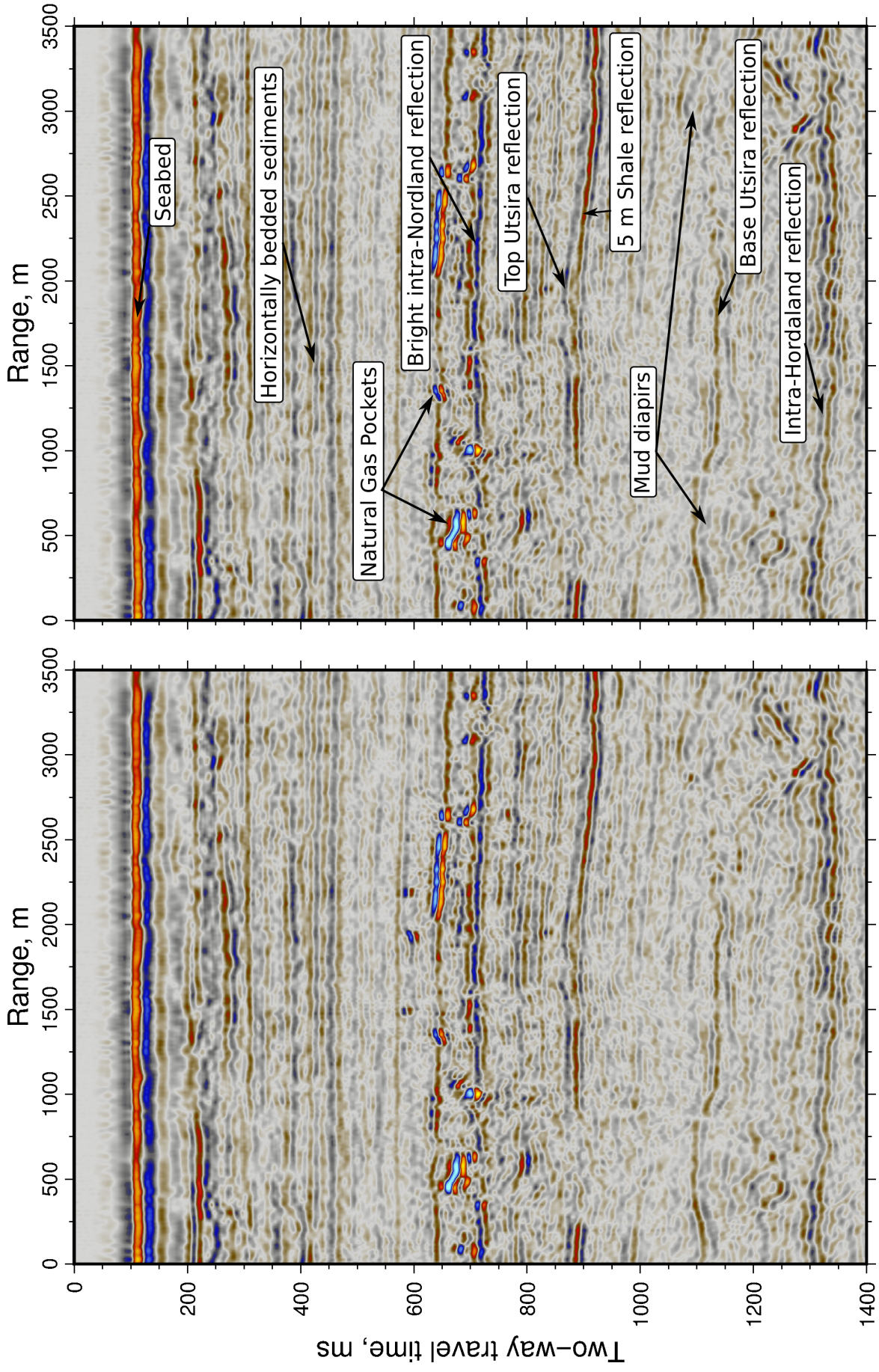
Seabed
Horizontally bedded sediments
Natural Gas Pockets
Bright intra-Nordland reflection
Top Utsira reflection
5 m Shale reflection
Mud diapirs
Base Utsira reflection
Intra-Hordaland reflection
Range, m
0
500
1000
1500
2000
2500
3000
3500
Two–way travel time, ms
0
200
400
600
800
1000
1200
1400

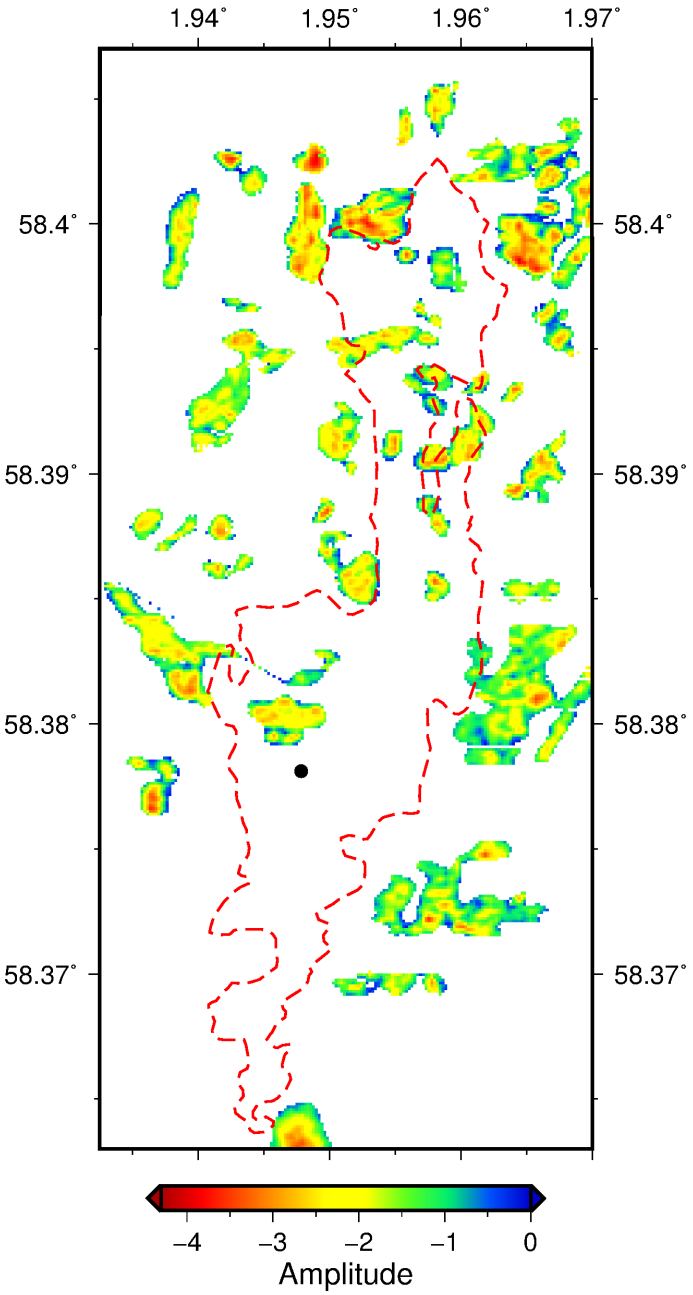

Figure 2.9: Map of major gas pockets in the overburden above the Utsira Formation. Red dashed line shows outline of uppermost CO_2 layer (Layer 9) in 2010. Black circle shows location of injection point at base of reservoir.

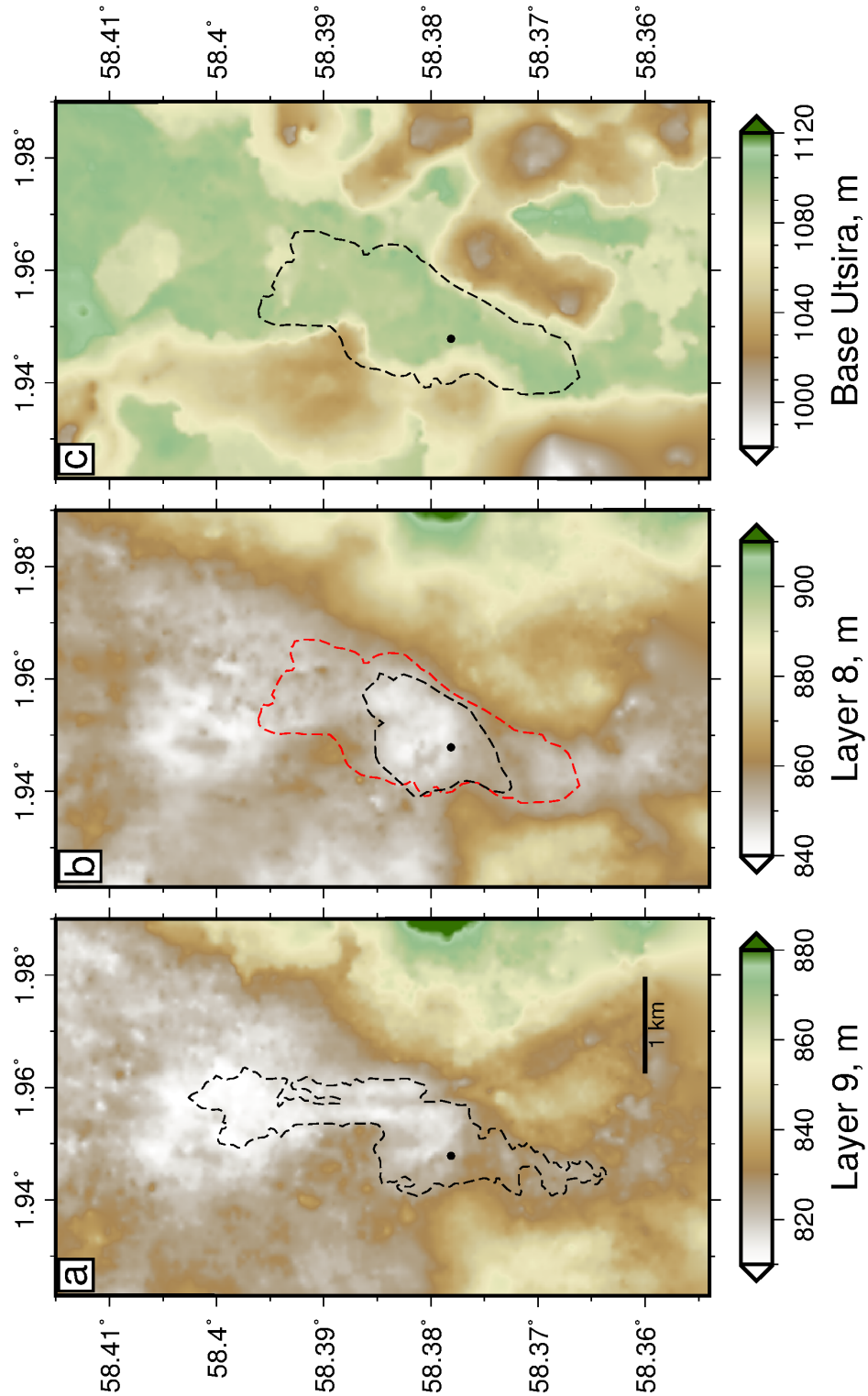

Figure 2.10: Depth to Layer 9 caprock, Layer 8 caprock and base Utsira Formation in metres below sea level. Depth calculated using layer cake model. **(a)** Topography of Layer 9 caprock calculated using uniform overburden velocity of 2150 m s^{-1} and corrected to match well depth. Black dashed line: outline of Layer 9 in 2010. **(b)** Topography of Layer 8 caprock calculated using velocity of 2050 m s^{-1} for Sand Wedge. Black dashed line: outline of Layer 8 in 2010. Red dashed line: outline of Layer 5 in 2010. **(c)** Topography of base Utsira Formation calculated using velocity of 2050 m s^{-1} for Utsira Formation. Black dashed line: outline of Layer 5 in 2010. Black circle shows location of injection point at base of reservoir.

The topography of the reflection from the base of the 5 m Shale can be calculated by assuming a constant velocity between the caprock reflection and the 5 m Shale reflection of 2050±30 m s^{-1} (Figure 2.10b). The topography of this mudstone layer is similar to that of the caprock, dominated by two anticlinal domes. However, the prominent north-striking ridge seen on the caprock reflection is not apparent in this lower reflection.

Within the reservoir, spikes in the gamma-ray signal on wireline logs from all nearby wells indicate that thin mudstone layers sub-divide the reservoir that occur approximately every 30 m (Figure 2.3). The mudstone layers are too thin to be observable on the seismic reflection surveys and do not appear to be correlatable between exploration wells spaced kilometres apart (Zweigel *et al.*, 2004). The lateral continuity of these layers is therefore unknown. Faulting is not observed within the reservoir.

The base of the reservoir exhibits significant domed topography and polygonal reverse faulting (Figure 2.7 and 2.10). These domes are on the order of kilometres in diameter and ∼100 m in height. These features are attributed to mud diapirism within the Hordaland Formation (i.e. the underburden) that is thought to have initiated shortly after the deposition of the lower part of the Utsira Formation (Arts *et al.*, 2000). The effect of these diapirs on the lateral continuity of the mudstone layers within the Utsira Formation is unknown, but, given the significant change in the thickness of the Utsira Formation in the vicinity of these edifices, some disruption of the internal structure seems likely. There is also significant correlation between the topography of the caprock and the locations of these domes at the base of the reservoir, suggesting that the mud diapirism also caused subsidence or preferential compaction of the Utsira Formation in these regions. A bright reflective horizon within the Hordaland Formation (1300 ms, Figure 2.8) is approximately flat across the entire region, indicating that these mud diapirs only affect the uppermost section of the Hordaland Formation.

2.5 Interpretation of Post-injection Surveys

The first post-injection seismic reflection survey was acquired in 1999, three years after injection of CO_2 had commenced. Following this survey, seismic reflection surveys were acquired approximately every two years to monitor the migration of CO_2 through the reservoir. Because the amplitude and polarity of reflections depend on the velocity and density contrasts between two adjacent media, it is useful to estimate the velocity of seismic waves through CO_2 saturated rocks prior to interpreting the observed reflections within the reservoir.

2.5.1 Acoustic Velocity of CO_2 Saturated Sandstone

The acoustic velocity of CO_2-saturated sandstone at the top of the CO_2 reservoir has been estimated in many different studies and is still debated (e.g. Arts *et al.*, 2004; Carcione *et al.*, 2006; Ghaderi & Landro, 2009). These studies, discussed below, have estimated the acoustic velocity either using observations from the seismic reflection surveys, or rock physics modelling.

Four estimates of the seismic velocity of CO_2-saturated sandstone have been made using seismic observations: Chadwick *et al.* (2004a) obtained a value of 1420 m s^{-1} based on the observed pushdown of reflective horizons beneath seismic chimneys; Williams & Chadwick (2012) calculated a velocity of 1478 m s^{-1} based on reflectivity of the upper boundary of the shallowest CO_2 layer by exploiting higher resolution two-dimensional seismic profiles acquired in 2006; Furre *et al.* (2015) suggest that a velocity of 1400 m s^{-1} yields the optimal agreement between their thickness measurements and other studies; and finally Chadwick *et al.* (2016) measured a velocity of 1431 ± 62 m s^{-1} by correlating synthetic models with very small time shifts of reflections from the upper and lower boundaries of the shallowest layer on the 2010 broadband survey.

The acoustic velocity of seismic waves through CO_2-saturated sandstone can also be estimated using rock physics models. When modelling the velocity of seismic waves through

CO_2-saturated rocks, an important consideration is whether CO_2 saturation within the reservoir rock is 'uniform' or 'patchy' (Chadwick *et al.*, 2004a; Boait *et al.*, 2012). These terms describe the extent to which the CO_2 is mixed with the ambient brine in the reservoir, relative to the frequency of the seismic signal. The critical length scale, L_c, for mixing of fluids in the reservoir imaged with a seismic signal of frequency, f, is given by

$$L_c = \sqrt{\frac{kK_{fl}}{f\eta}} \tag{2.3}$$

where k is the permeability of the medium, and K_{fl} and η are the bulk modulus and viscosity of the most viscous fluid, respectively (Mavko & Mukerji, 1998). For a mixture of CO_2 and brine in the Utsira Formation, where $k = 2\times10^{-12}$ m^2, $K_{fl} = 2.3\times10^9$ Pa, $\eta = 7\times10^{-4}$ Pa s, this length scale has been estimated to be $\sim$0.5 m for a seismic wave with $f = 30$ Hz (Boait *et al.*, 2012). This length scale defines the distance that seismic wave induced pore-pressure gradients can equilibrate during one seismic period.

If fluids are mixed at scales less than L_c (i.e. saturation is uniform), the increased pore pressure can diffuse away within a seismic period. However, if saturation is heterogeneous over length scales larger than L_c (i.e. saturation is patchy), then seismic wave induced flow, driven by spatial gradients in pore-pressure, can cause attenuation and velocity dispersion of the seismic wave (Toms *et al.*, 2007). Patchy saturation might be caused by viscous fingering, spatial variation in wetability, or variable mud content within the rock (Mavko & Mukerji, 1998).

For uniform CO_2 distributions, and sufficiently low seismic frequencies (i.e. $\lesssim$ 100 Hz), the Gassmann model using the Reuss average for the effective fluid bulk modulus can be used to describe the velocity of seismic waves through CO_2-saturated rocks (Figure 2.11; Sengupta & Mavko, 2003). However, if saturation is patchy, the Voigt model provides an upper bound on the acoustic velocity, suggesting that it will vary approximately linearly between end-members (Figure 2.11; Rubino *et al.*, 2011; Williams & Chadwick, 2012). A more useful estimate of the seismic velocity for patchy CO_2 saturation is given by the Brie model, which

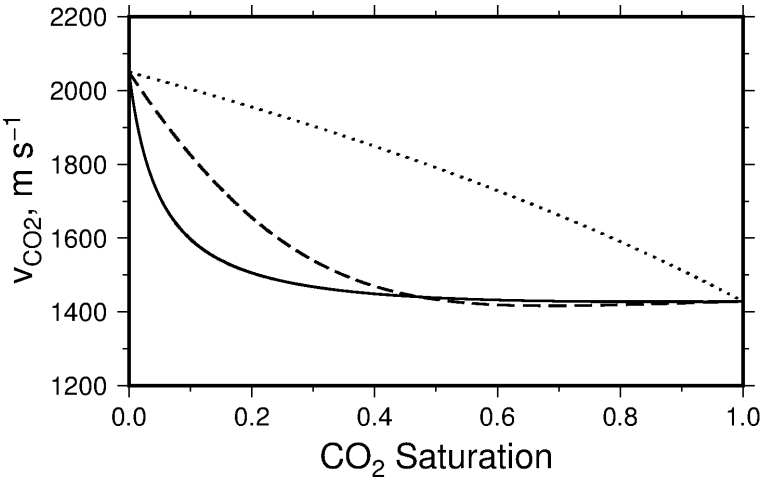

Figure 2.11: Velocity of seismic waves through CO_2 saturated sandstone at the Utsira Formation calculated using the Gassmann model. Solid line = Effective fluid bulk modulus, K_{fl}, calculated using Reuss average. Dashed line = K_{fl} calculated using Brie average. Dotted line = K_{fl} calculated using Voigt average. See Appendix A for more details.

is an empirical model that suggests that there are only significant differences between patchy and uniform models for CO_2 saturations lower than 40 % (Figure 2.11; Carcione *et al.*, 2006; Mavko *et al.*, 2009). The differences between the model are due to the different approaches taken to averaging of the fluid properties within the pore space. A detailed description of these models is provided in Appendix A.

Evidence for the existence of patchy saturation is provided by measurements of push-down on the base of the Utsira Formation. Attempts to match the total push-down on the base of the reservoir due to the presence of CO_2 suggest that CO_2 is distributed in highly saturated, thin layers between regions with more diffuse, and possibly patchy, saturation (Chadwick *et al.*, 2005; Boait *et al.*, 2012). The existence of high saturation layers is supported by laboratory centrifuge experiments on core material from the Utsira Formation, which suggest that CO_2-saturation within each thin layer is likely to be high with a very thin capillary fringe along its base (Figure 2.12; Chadwick *et al.*, 2005). Rubino *et al.* (2011) found that the effect of patchy saturation on acoustic velocity increased when saturation was low. These authors also concluded that wave-induced flow effects can be neglected when considering the thin, highly CO_2-saturated layers within the reservoir. Because this work mostly concentrates on the regions thought to contain uniform CO_2 saturation, a Gassmann model with a

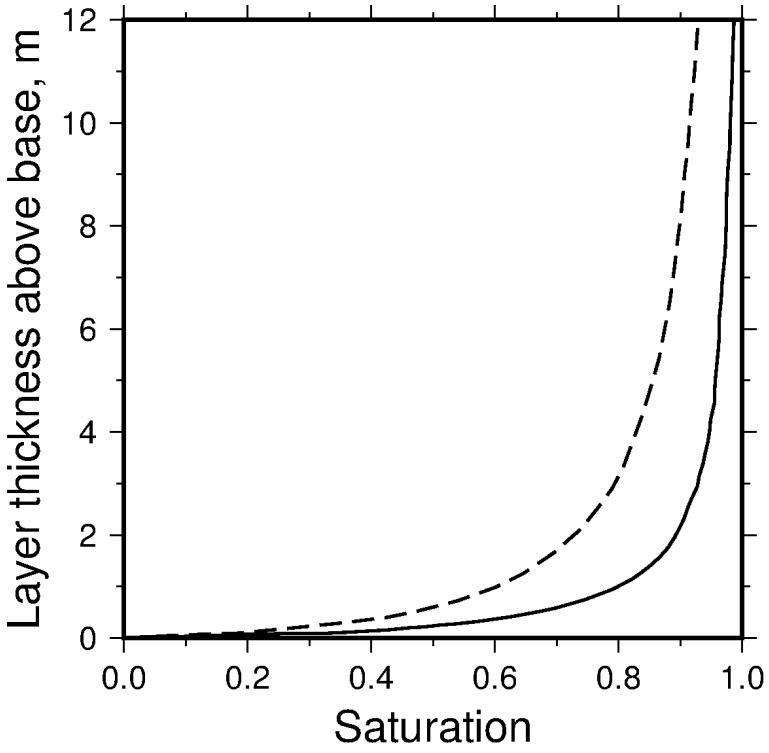

Figure 2.12: Estimated CO_2 saturation against thickness of CO_2 layer. Saturation is estimated to be high apart from thin capillary fringe at the base of the layer. Solid line = saturation at thickness above base. Dashed line = mean saturation of layer. Figure adapted from Chadwick *et al.* (2005).

Reuss-averaged effective fluid bulk modulus is used to calculate the seismic velocity for CO_2 saturated sandstone in this analysis. However, it is important to stress that this estimate is a lower bound, and that changes in the distribution of CO_2 can cause the velocity of seismic waves through CO_2 saturated media to increase. The patchy saturation model acts as an upper bound for this velocity.

Variations in pore fluid pressure triggered by CO_2 injection could also affect the acoustic velocity of CO_2 itself. Pore fluid pressure variations have been inferred from temporal changes in amplitude signals at the Snøvit CO_2 injection site (Eiken *et al.*, 2011). However, no such changes have been observed within the Sleipner field, which is consistent with the high permeabilities and porosities of the Utsira formation (Chadwick *et al.*, 2005).

Estimates of the acoustic velocity of a sandstone layer that is uniformly saturated with CO_2

calculated using these models lie between 1400 and 1500 m s^{-1} (Arts *et al.*, 2004; Chadwick *et al.*, 2005; Ghaderi & Landro, 2009; Williams & Chadwick, 2012). There are two significant outliers of 1600 m s^{-1} and 1150 m s^{-1} (Eiken *et al.*, 2000; Carcione *et al.*, 2006). Here, the Gassmann model for uniformly saturated CO_2 is used to obtain a value of 1428 $\pm$ 95 m s^{-1} for a CO_2 saturation of 80 %. The quoted uncertainty reflects the range of estimates found in the literature for different input parameters (Appendix A). This value embraces almost all of the estimates that are based on seismic observations as well as those estimated from rock physics modelling.

2.5.2 Interpretation of Seismic Reflections within the Reservoir

Injected CO_2 is visible on the seismic reflection surveys due to the significant impedance contrast between CO_2-saturated and brine-saturated reservoir rocks. For seismic waves crossing a boundary at normal incidence, the reflectivity, R, is a function of the change in impedance across a boundary,

$$R = \frac{I_2 - I_1}{I_2 + I_1} = \frac{\rho_2 v_2 - \rho_1 v_1}{\rho_2 v_2 + \rho_1 v_1} \tag{2.4}$$

where I_i is the impedance of the upper ($i = 1$) or lower ($i = 2$) medium, ρ_i is the density of the medium and v_i is the velocity of seismic waves through the medium. Due to the impedance contrast at the upper boundary of a CO_2-saturated layer, reflections from this boundary are of negative polarity (blue on the seismic reflection images). Reflections from the base of a highly-saturated CO_2 layer are of the opposite polarity (red on the seismic reflection images). The greater the impedance contrast between the layers, the more reflective that boundary is, and the higher amplitude (i.e. brighter) the reflection will be.

Careful interpretation of the seven post-injection seismic reflection surveys has revealed the presence of nine consistently bright pairs of negative and positive polarity reflections within the reservoir (Figure 2.7). These pairs of reflections are interpreted to be from the top and bottom of thin layers of uniformly CO_2-saturated sandstone (Bickle *et al.*, 2007; Boait *et al.*, 2012). The CO_2 is thought to be trapped beneath the thin, low-permeability mudstone layers observed on the geophysical logs. These layers of high CO_2 saturation are labelled

from 1–9 (Figure 2.7). No CO_2 is observed to have migrated through the reservoir caprock.

The migration of the CO_2 through the reservoir can therefore be tracked by measuring the extent of the amplitude anomaly associated with each of the nine layers (Figures 2.13, 2.14 and 2.15). Reflection amplitudes are extracted from the seismic reflection surveys using Schlumberger's seismic interpretation software Petrel to track the spatial extent of the peak amplitude of the reflected wavelets. These amplitude maps provide insight into the vertical and horizontal migration of CO_2 within the reservoir.

The first post-injection survey, acquired in 1999, reveals that CO_2 had migrated to the top of the reservoir within three years of injection starting. Given the small spatial extent of all of the layers at this time, the path taken by the CO_2 between the injection point and the shallowest layer must be approximately vertical. The nature of this pathway is not known for certain; it has been suggested that vertical migration can occur either around the edges of the mudstone layers within the reservoir or through fractures within these mudstone layers (Chadwick & Noy, 2010). Prominent seismic chimneys within the reservoir have also been interpreted as evidence of vertical migration pathways. The low amplitudes associated with these features are potentially indicative of a vertical column of CO_2 with no horizontal boundaries to reflect seismic waves. Significant pushdown is also observed around the most prominent of these chimneys, indicative of a large accumulation of CO_2 (Chadwick *et al.*, 2004a). Seismic chimneys observed elsewhere have been associated with gas migration through sedimentary formations (Heggland, 1998; Loseth *et al.*, 2003).

The planforms of these CO_2 layers are irregularly shaped. Previous authors have noted that the layers can be approximated as ellipses (Boait *et al.*, 2012). It has been suggested that this elliptical shape might be caused by an inferred anisotropic permeability of the reservoir sands, but core material provides no evidence for this anisotropy (Chadwick & Noy, 2010). However, there is significant correlation between the planforms of some of these layers and the general reservoir geometry. Figure 2.10 shows the topography of the caprock for Layer 9, caprock for Layer 8 and the base of the Utsira Formation with the planforms of Layer 9, 8

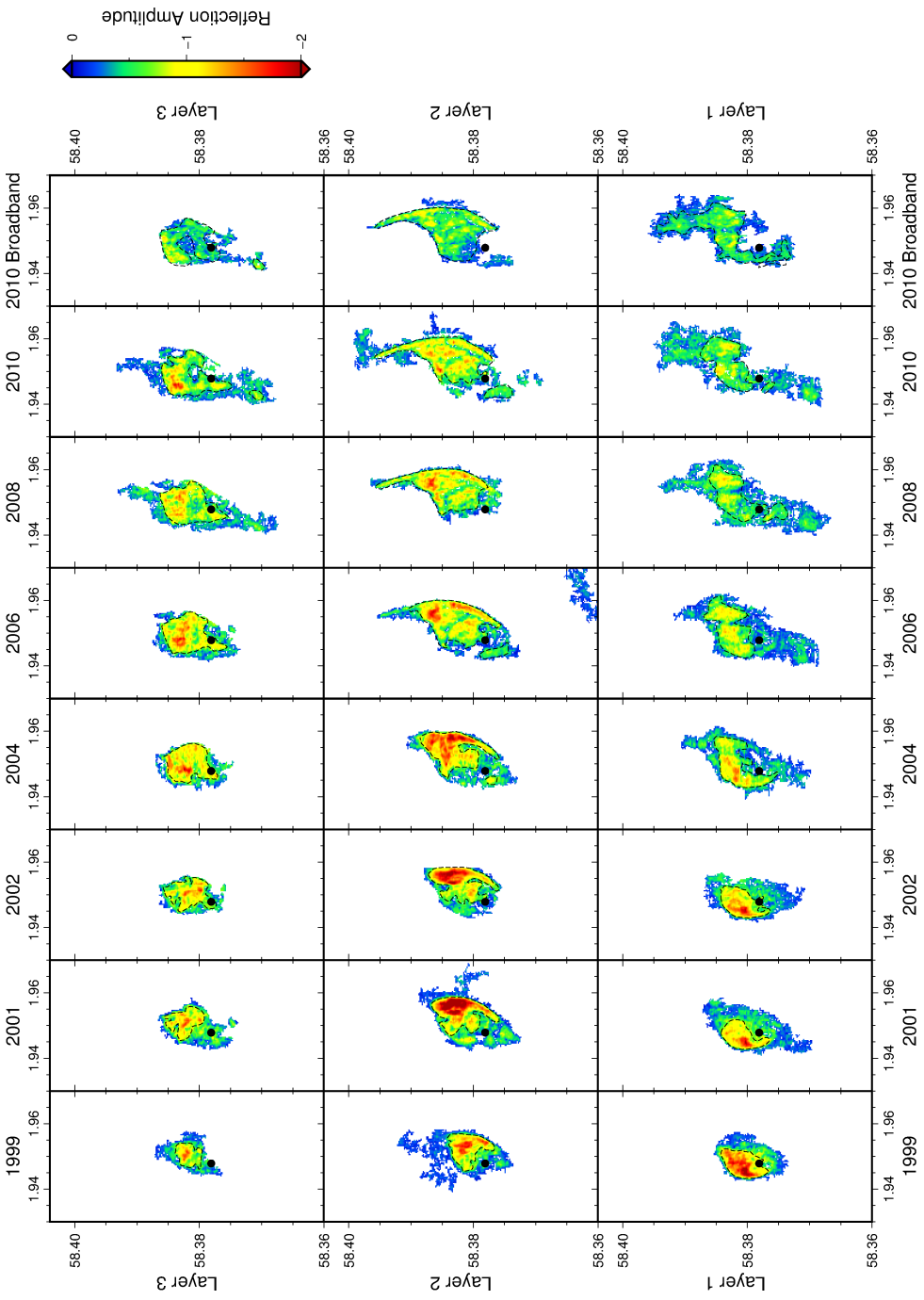

Figure 2.13: Reflection amplitude for Layers 1, 2 and 3 for all seismic reflection surveys. Top row = Reflection amplitude for Layer 3 for seismic reflection surveys acquired in 1999, 2001, 2002, 2004, 2006, 2008, 2010 time lapse processing and 2010 broadband processing. Middle row = Likewise for Layer 2. Bottom row = Likewise for Layer 1. Black line shows manually picked edge of layer. Reflection amplitude for 2010 broadband survey scaled to be consistent with other surveys. Black circle shows location of injection point at base of reservoir.

Figure 2.14: Reflection amplitude for Layers 4, 5 and 6 for all seismic reflection surveys. Top row = Reflection amplitude for Layer 6 for seismic reflection surveys acquired in 1999, 2001, 2002, 2004, 2006, 2008, 2010 time lapse processing and 2010 broadband processing. Middle row = Likewise for Layer 5. Bottom row = Likewise for Layer 4. Black line shows manually picked edge of layer. Reflection amplitude for 2010 broadband survey scaled to be consistent with other surveys. Black circle shows location of injection point at base of reservoir.

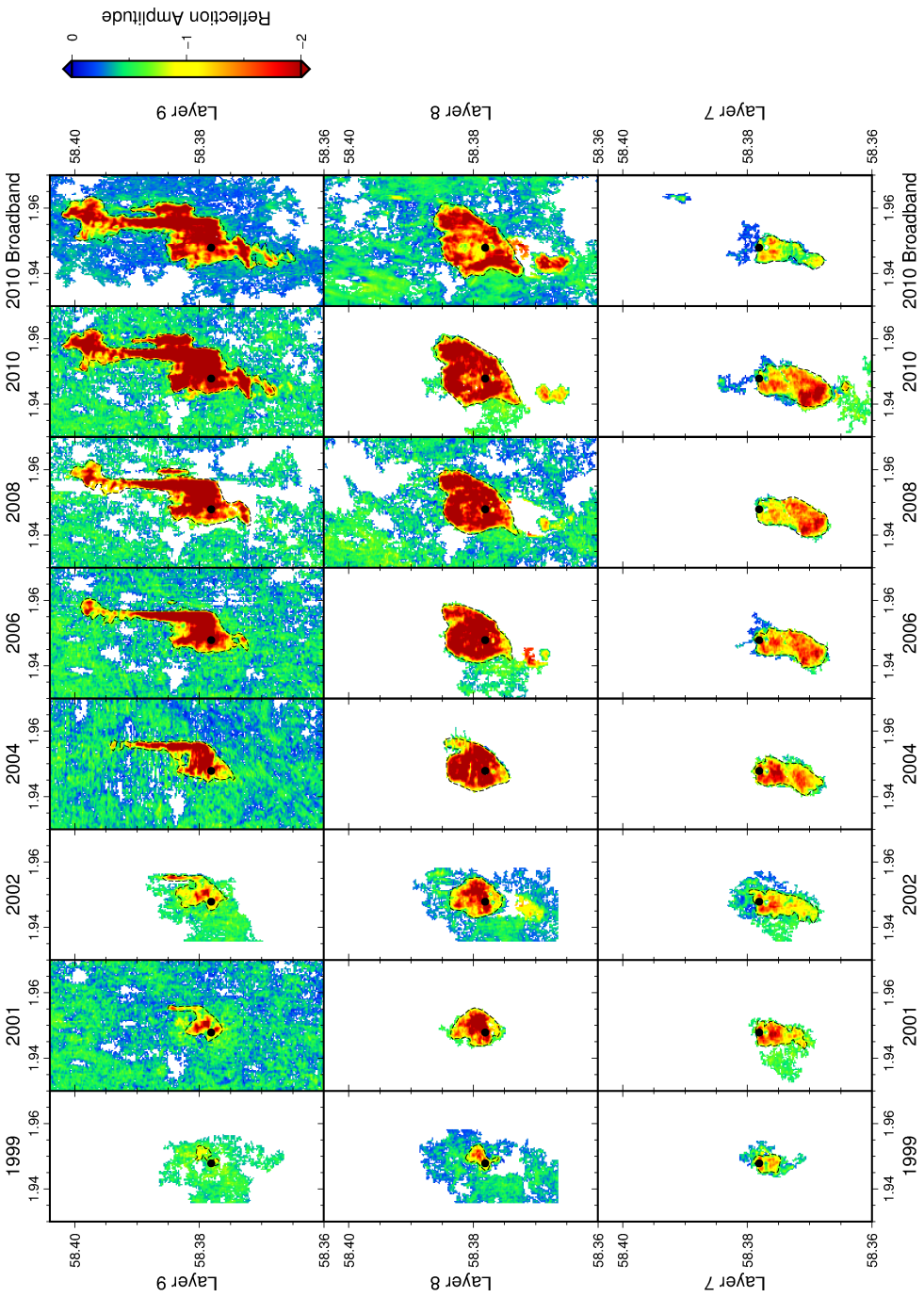

Figure 2.15: Reflection amplitude for Layers 7, 8 and 9 for all seismic reflection surveys. Top row = Reflection amplitude for Layer 9 for seismic reflection surveys acquired in 1999, 2001, 2002, 2004, 2006, 2008, 2010 time lapse processing and 2010 broadband processing. Middle row = Likewise for Layer 8. Bottom row = Likewise for Layer 7. Black line shows manually picked edge of layer. Reflection amplitude for 2010 broadband survey scaled to be consistent with other surveys. Black circle shows location of injection point at base of reservoir.

and 5 overlain. Figure 2.10a suggests that a dominant control on the shape of the CO_2 layer is the topography of the caprock, with the north-running finger of CO_2 extending along a north-striking ridge between two anticlinal domes. Figure 2.10b shows similarly good correlation between the planform of Layer 8 (black dashed line) and the topography of the 5 m Shale that acts as the caprock for this layer. The CO_2 in Layer 8 appears to simply be trapped beneath the anticlinal dome present in this caprock.

Despite the intra-reservoir mudstone layer that acts as the caprock for Layer 5 not being visible on the seismic reflection images, the planform of Layer 5 also shows good correlation with the topography of the 5 m Shale (Figure 2.10b, red dashed line). It seems plausible therefore that the caprock geometry for Layer 5 is similar to that of the 5 m Shale, with a relatively significant topographic gradient controlling the straight eastern side of the plume. An alternative control on the shape of Layer 5 is the overall reservoir thickness. Figure 2.10c shows that the CO_2 in Layer 5 also correlates well with the topography of the base of the Utsira Formation. The Utsira Formation is approximately 250 m thick in the injection region, but due to mud diapirism of the underlying Hordaland Formation and preferential compaction of the Utsira Formation above these diapirs, the reservoir is only 150 m thick in the regions affected by this deformation. The reduction in the thickness of the total reservoir might act as a baffle to flow in the direction of thinning, preferentially promoting flow towards the north and south.

2.5.3 Layer Growth

The areal extent of each of the layers can be used to infer the vertical distribution of the CO_2 within the reservoir. To find the areal extents of each CO_2 layer, all reflections that could be associated with CO_2 were extracted from the seismic data. The areal extents were then measured in two ways. First, the extent of each horizon for each survey was picked manually by eye three times, to give an upper, middle and lower estimate of the area of CO_2 (Figure 2.16). Secondly, the area was calculated by counting the number of grid squares above a threshold amplitude to give an upper, middle and lower estimate of the

area (Figure 2.16). These two methods are generally in good agreement for all layers. For Layers 8 and 9, the caprock is visible on the seismic reflection surveys. Uncertainties in the upper bound for the automatically extracted areas are therefore high due to the set threshold erroneously including more reflective sections of the caprock. The extent of each layer was also picked on the broadband seismic reflection survey acquired in 2010 (Figure 2.16). The area of a small layer of CO_2 to the south of Layer 8 but trapped by the same caprock has been measured as a separate entity to Layer 8. The area of this significantly smaller patch of CO_2 is shown as a second set of points on top-middle panel of Figure 2.16.

The limit of detectability for the thickness of CO_2 at the edge of the observed plume using amplitude measurements is estimated to be $\sim$0.75 m towards the top of the reservoir on the time-lapse survey. Deeper within the reservoir, attenuation and pushdown mean that this resolution is reduced. The areal extent of the layers measured on this survey are, in general, greater for the broadband survey than the time-lapse processed survey. This difference arises due to the broadband survey having better vertical resolution due to its broader frequency content. Detectability of a thin layer is increased to $\sim$0.5 m on this survey due to the higher peak frequency of the signal.

Boait *et al.* (2012) also measured the areal extents of each of these layers using the same seismic reflection surveys up to 2008. These authors suggested that the pattern of growth of the areal extents of these layers could be categorised into three stages. In the first stage, the horizons grow and the amplitudes brighten. In the second stage, the amplitude of the layer starts to dim in the centre, although amplitudes towards the edges may brighten. In the final stage, the layers stop growing and may start to shrink. Boait *et al.* (2012) also observed shrinking in layers 1, 2, 3 and 4, while the areal extent of layer 7 plateaued after 2004. In their analysis, reflectivity dimming was also observed on all layers.

The observations presented by Boait *et al.* (2012) are generally in agreement with those presented here for the upper layers. The rate of growth of the areal extent of the lower layers has continued to decrease, while for Layers 5, 6, 8 and 9 this rate has increased.

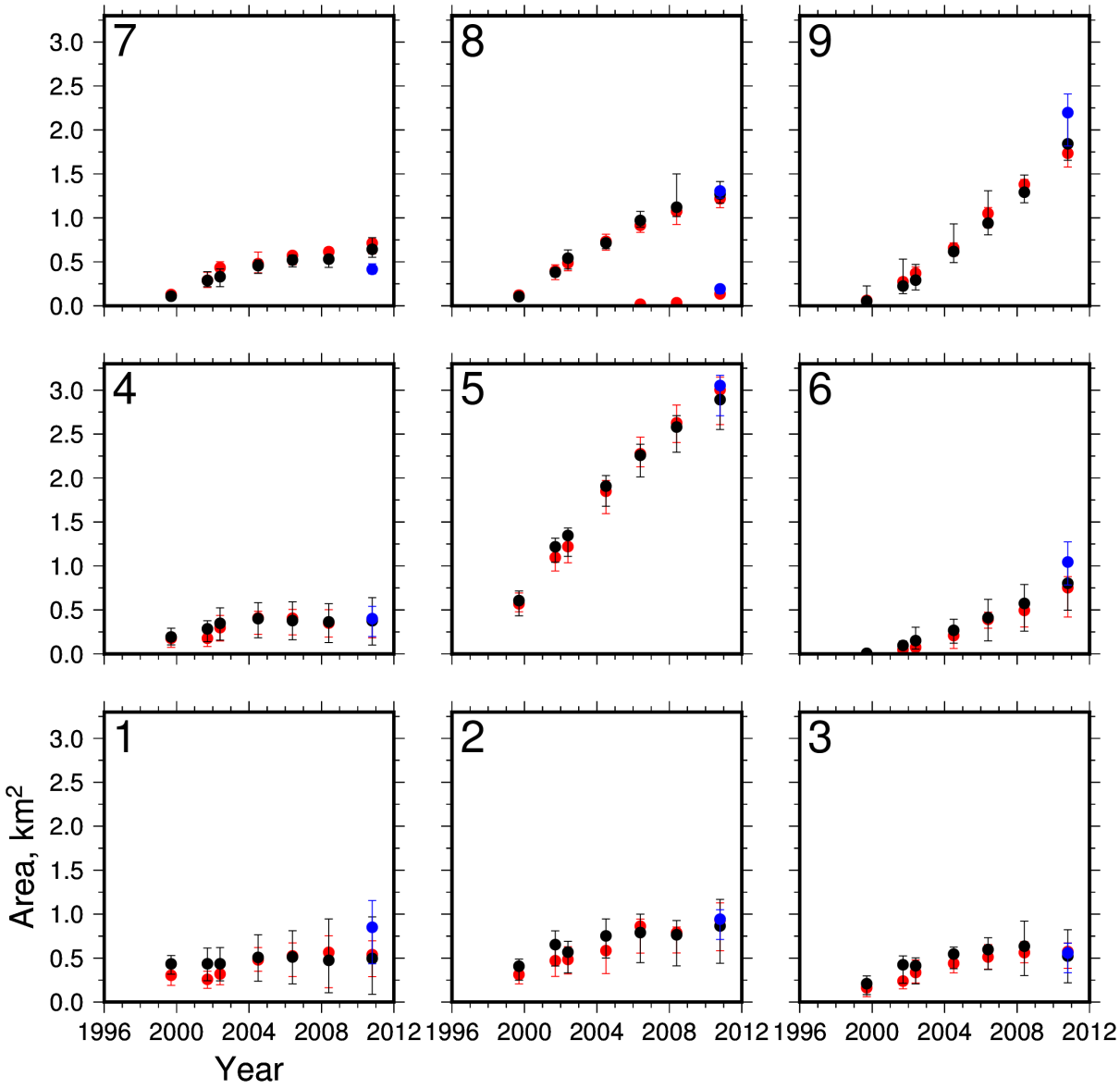

Figure 2.16: Area measurements for all layers, years and seismic surveys. Red circles = manually picked layer areas based on the edge of amplitude anomalies, with upper and lower bounds. Black circles = areas based on total grid squares above a threshold amplitude for the extracted horizon, with upper and lower bounds. High upper bounds exist for Layers 8 and 9 due to high reflectivity in parts of the caprock for that layer. Blue circles = layer areas for 2010 broadband processing picked manually. Layer 8 has a second set of points that relate to a small CO_2 accumulation distinct from the main body of Layer 8 but trapped by the same caprock.

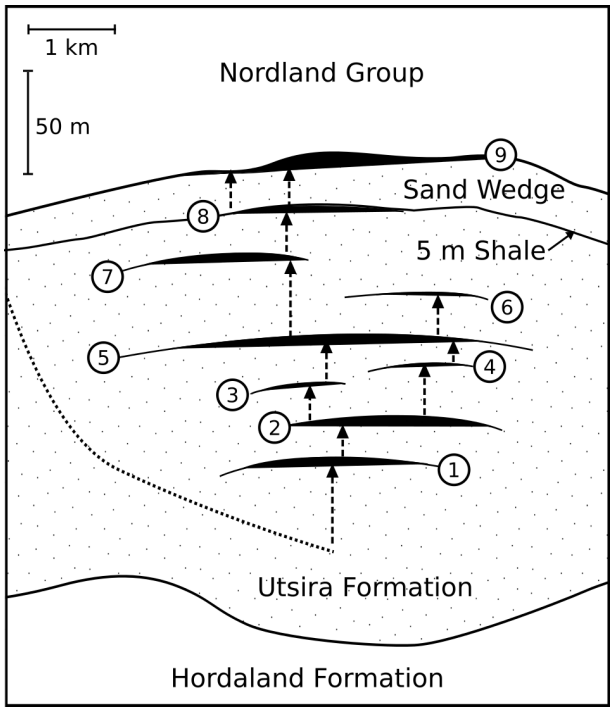

Figure 2.17: Cartoon showing present-day configuration of injected CO_2 within reservoir. Unit with dotted pattern = Utsira Sandstone Formation; numbered black layers = nine CO_2-filled sandstone horizons separated by thin mudstones; dotted line = injection well; vertical arrows = notional inter-layer flow of CO_2. Note vertical exaggeration.

However, in this analysis, no layers are observed to shrink. This difference is probably due to the more conservative approach taken in this analysis to estimating uncertainties in these measurements towards the base of the aquifer. At this depth within the reservoir, significant dimming of the reflections means there are large uncertainties associated with identifying layers of CO_2. The most likely causes of this dimming are a combination of attenuation and scattering of the seismic waves due to the overlying CO_2, artefacts such as multiples from within the plume itself, and pushdown of the reflections causing neighbouring reflections to appear incoherent. The effect of attenuation is evident on Layer 5, where a low amplitude region occurs directly below the major CO_2 accumulations in Layers 8 and 9 (Figure 2.14 and 2.15).

2.6 Summary

Eight seismic reflection surveys have been acquired over the CO_2 plume at the Sleipner carbon capture and storage site. The seven post-injection surveys have been processed to be comparable to the baseline survey, acquired prior to CO_2 injection in 1994, and to be broadly comparable between each other. A broadband survey acquired in 2010 using a dual sensor streamer has provided a higher resolution image of the plume.

Nine consistently bright reflections, visible on all post injections surveys, have been interpreted as thin layers of CO_2 trapped beneath $\sim$1 m thick mudstone layers within the Utsira Formation (Figure 2.17). The uppermost CO_2 accumulation, Layer 9, is trapped beneath the Nordland Formation, which acts as the reservoir caprock. The topography of the caprock can be extracted for Layers 8 and 9 from the baseline seismic reflection survey. The correlation between the topography and the extent of the CO_2 accumulation suggests that buoyancy driven flow is a significant control on the migration of CO_2 within these layers.

The lateral extent of all nine CO_2 layers have been mapped on the seven post-injection surveys and the broadband processing of the 2010 survey. In contrast to results presented by Boait *et al.* (2012), layer shrinkage is not observed. However, the large uncertainties involved in picking reflections at this depth within the reservoir, primarily caused by attenuation and scattering of the seismic energy by the overlying CO_2, means that the extents of these lower layers are difficult to extract. The poor resolution at the base of the plume provides a good example of the limitations of using seismic reflection surveying to monitor the migration of CO_2 within the reservoir.

While the areas of these layers are relatively easy to extract from the seismic surveys, relating these measurements to the volume of CO_2 stored in each layer is not straightforward due to the limiting vertical resolution (Widess, 1973). Volumetric measurements are important for understanding migration rates through the reservoir, the storage capacity of the reservoir, and estimating the dissolution rate of CO_2 into the ambient brine. Knowledge of the

distribution of CO_2 in each layer in three dimensions is necessary to benchmark reservoir simulations against more accurate observations.

Chapter 3

Measuring the Thickness of a CO_2-filled Layer

3.1 Introduction

The subdued topography of the structural traps within the Utsira Formation has given rise to thin CO_2-filled layers with extensive planforms. On most of the time-lapse seismic reflection surveys, the bulk of these layers are thinner than the one quarter wavelength limit of vertical resolution for seismic reflection images (Widess, 1973). Consequently, it is challenging to directly measure layer thickness from the seismic reflection images, leading to poorly constrained volumetric estimates as a function of time.

Attempts to measure the thickness of the thin CO_2 layers have mostly concentrated on Layer 9. There are two major reasons for this approach. First, Layer 9 is the shallowest layer of CO_2 within the reservoir and so reflections from this layer are not affected by attenuation or pushdown caused by CO_2 above the layer. Secondly, the topography of the caprock can be measured on the pre-injection survey, providing extra information that is required by

some methods to estimate thickness.

In the first part of this chapter, I model the reflections of seismic waves from a thin layer of CO_2. This model is then used to measure the thickness of resolvable regions of Layer 9 using the broadband seismic reflection survey acquired in 2010. Due to the broader range of frequencies in this survey, the vertical resolution is improved when compared to the time-lapse survey acquired over the same region. This survey offers insight into the maximum thickness of CO_2 in Layer 9, but cannot measure the thickness of the majority of the plume.

In the second part of this chapter, I extend the classic thin bed analysis of Widess (1973) and Kallweit & Wood (1982) by developing an inverse approach that exploits a set of observations from a suite of time-lapse seismic surveys to find the thickness of a thin layer. These observations consist of a combination of amplitude and travel-time anomaly measurements from a reflective horizon with respect to the baseline, pre-injection survey. The goal is to constrain the thickness of a layer that cannot be directly measured as a result of interference effects since it is thinner than the nominal vertical resolution. First, the reflectivity model is used to explore the relationship between layer thickness, reflection amplitude and travel-time anomaly caused by interference of waves reflected from the boundaries of a thin layer. Secondly, this model is used to develop and test an inverse model that uses amplitude and travel-time anomaly measurements to calculate layer thickness. Formal uncertainties are quantified and propagated using synthetic tests. Finally, I apply the inverse model to amplitude and travel-time anomaly observations taken from time-lapse surveys of the Sleipner field acquired between 1994 and 2010.

These results have been used to estimate the volume of CO_2 within Layer 9 as a function of time. In this way, a quantitative understanding of the spatial distribution of CO_2 together with its rate of migration through a saline storage reservoir can be obtained.

3.2 Previous Work

Many different approaches have been used to estimate thickness of the CO_2-saturated sandstone in Layer 9. Structural analysis was used to estimate the thickness of Layer 9 by Chadwick & Noy (2010). This technique estimates the CO_2-water contact around the edge of the layer and interpolates a flat base between these points. The difference between this interpolated base of the CO_2 layer and the caprock topography is then used as an estimate of the thickness of the layer. While this technique is potentially appropriate for layers trapped in simple topographic domes, the complex topography of the Layer 9 caprock means that the predicted thickness of the plume is close to zero for much of the plume.

Observed amplitudes of reflections have been used to estimate thickness changes of Layer 9 (Chadwick *et al.*, 2005; Kiær, 2015). Using amplitude information to measure layer thickness requires either the reflectivity of the layer to be known with good accuracy or calibration of the model against a layer of known thickness. Uncertainties in the velocity of seismic waves through CO_2 saturated sandstones and density of CO_2 mean that the impedance contrast between the reservoir caprock and the CO_2 filled layer cannot be calculated with certainty (Section 2.2 & 2.5.1). These uncertainties then propagate into measurements of layer thickness.

Williams & Chadwick (2012) used spectral decomposition to estimate the thickness of Layer 9. Spectral decomposition is a technique that analyses the tuning of reflected wavelets at different frequencies. By finding the frequency range at which interference between reflections from the top and base of the CO_2 layer is constructive (i.e. amplitudes are increased), the thickness of the layer can be estimated. However, these authors found that it is difficult to resolve thicknesses of less than $\sim$4 m using this technique.

Furre *et al.* (2015) used push-down observations at the top of Layer 8 to estimate the thickness of the CO_2-saturated sandstone in Layer 9 required to produce this effect. This approach is complicated by the need to correct for pull-up of the reflection from Layer 8 caused by

interference effects. Estimating this pull-up requires accurate knowledge of the thickness of Layer 8. This pull-up could therefore not be properly accounted for in their study, introducing uncertainty into this estimate.

The method presented here simultaneously inverts measurements of both amplitude and differences in travel-time for a given reflective horizon between different time-lapse surveys. This approach builds upon previous attempts to constrain layer thickness using amplitude and travel time measurements (Kiær, 2015; Furre *et al.*, 2015).

3.3 Reflection Model

Consider a zero-phase Ricker wavelet, $\psi(t)$, the normalized amplitude of which is given by

$$\psi(t) = \left[1 - 2\left\{\pi f_p(t - t_1)\right\}^2\right] \exp\left[-\left\{\pi f_p(t - t_1)\right\}^2\right], \tag{3.1}$$

where t is time, t_1 is the position of the peak of the wavelet in time, and f_p is the peak frequency of the wavelet (Ryan, 1994). The shape of this wavelet depends only on its peak frequency. The amplitude and polarity of the reflected wavelet principally depend upon the acoustic impedance contrast at the boundary. If the wavelet is reflected from a layer with upper and lower boundaries in close proximity, the amplitude, arrival time and shape of the reflected wavelet are strongly dependent upon layer thickness. A synthetic reflection experiment along a wedge-shaped, low-impedance layer illustrates how interference between the reflected wavelets from the lower and upper boundaries occurs when the layer is thin compared with the wavelet (Figure 3.1).

If a thin layer of low impedance is embedded within a medium with an otherwise uniformly high impedance, reflections from the upper and lower boundaries have opposite polarity (Figure 3.1). The resultant wavelet, $\chi(t)$, produced by interference, is given by

$$\chi(t) = A_1\left[\psi(t) + A_r\psi(t - \delta)\right], \tag{3.2}$$

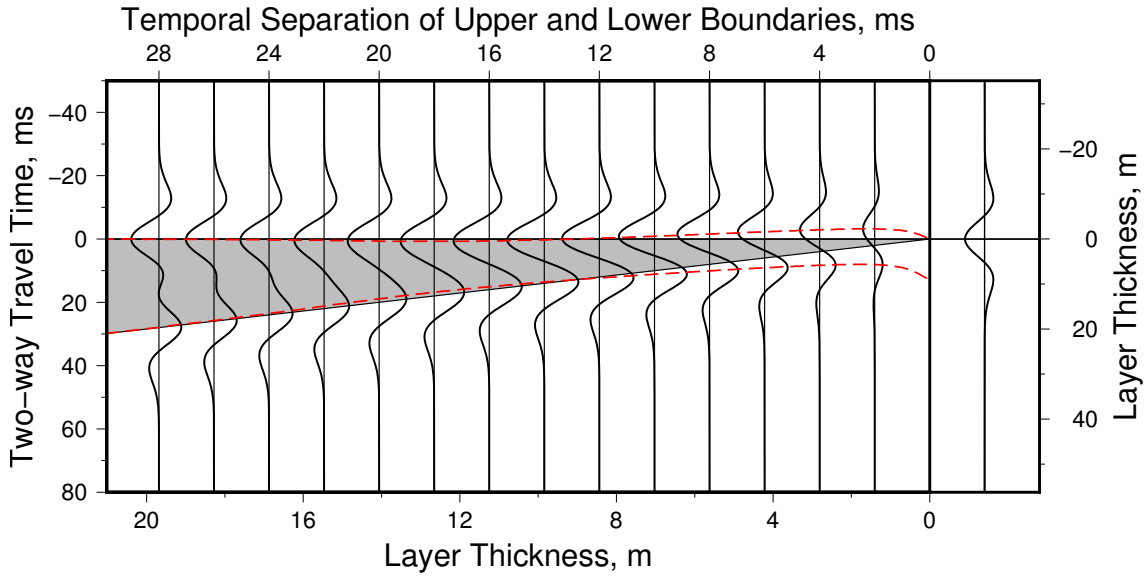

Figure 3.1: Seismic reflection modelling of wedge-shaped structure. Grey wedge = idealized CO_2 layer, for which lower boundary has impedance contrast that is 0.8 times that of upper boundary with opposite sign. Vertical wiggle to right of emboldened zero line = seismic trace calculated by convolving impedance contrast at single boundary with zero-phase Ricker wavelet; set of 14 vertical wiggles to left of zero line = seismic traces calculated for different wedge thicknesses; pair of red dashed lines = locus of peak-to-trough separation of each wavelet generated by interference. Note that velocity used to calculate thicknesses is 1428 m s^{-1}.

where δ is the separation of the upper and lower boundaries of the layer in two-way travel time (TWTT), A_1 and A_2 are the amplitudes of reflections from the upper and lower boundaries, and $A_r = A_2/A_1$ (Figure 3.2a). The reflection from the top and base of the layer might have different impedance contrasts due to differing lithological boundaries or changes in CO_2 saturation through the layer. To aid comparison with other published estimates of layer thickness, δ is also converted into layer thickness, given by $(\delta v)/2$, where $v = 1428 \pm 95$ m s^{-1} is the acoustic velocity of seismic waves that travel through a uniformly saturated, CO_2-filled layer at the top of the Utsira Formation (Section 2.5.1; Appendix A).

3.4 Reflection Separation

For thin layers, the effects of interference complicate straightforward correlation of the peak and trough of the resultant wavelet, $\chi(t)$, and boundaries of the layer (Figure 3.1). A

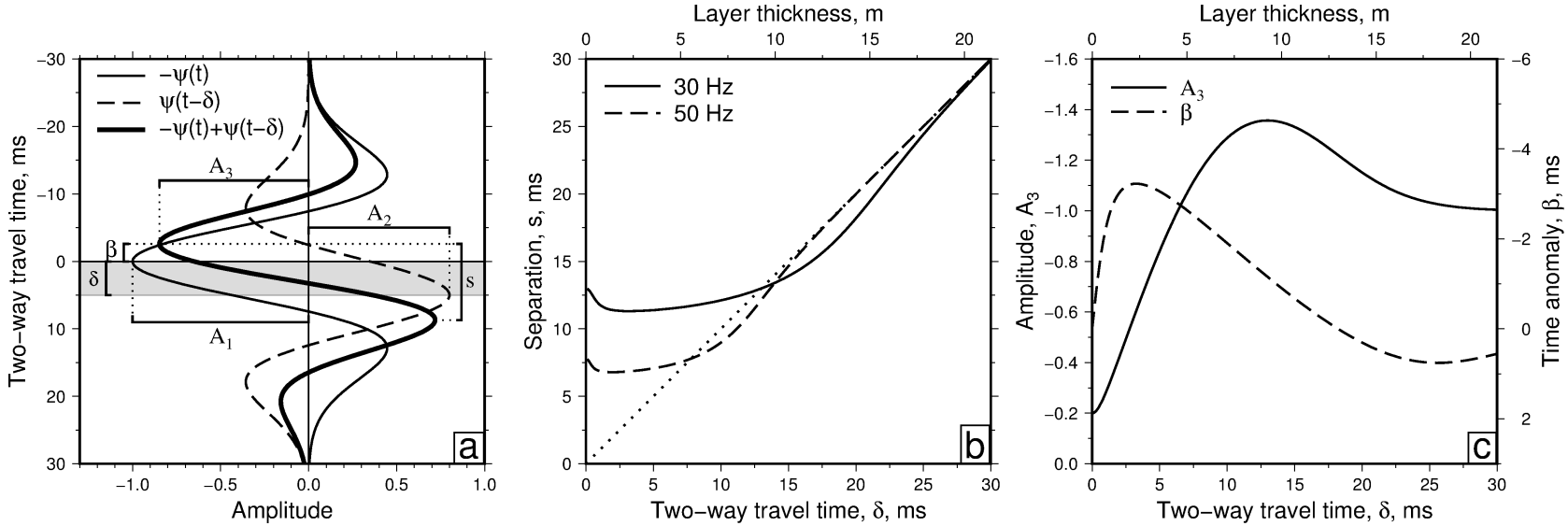

Figure 3.2: Separation, amplitude and time anomaly as a function of layer thickness for a thin bed. **(a)** Amplitude as function of two-way travel time. Thin wiggle = wave with amplitude A_1 reflected from top of thin bed; dashed wiggle = wave with amplitude A_2 reflected from base of thin bed ($A_2 = -0.8A_1$); bold wiggle = resultant wave with amplitude A_3 recorded at surface; δ-wide grey band = time delay across thin bed; β = travel-time anomaly between reflected wave from top of thin bed and resultant wave; s = separation between peak and trough of bold wiggle. **(b)** Separation, s, as function of time delay, δ, for two different frequencies. Solid line = 30 Hz; dashed line = 50 Hz; dotted line = 1:1 relationship. **(c)** Solid line = A_3 plotted as a function of δ; dashed line = β plotted as a function of δ. Note that velocity used to calculate thicknesses is 1428 m s^{-1}.

common approximation for the minimum resolvable layer thickness that can be found by measuring the separation of reflections from the top and bottom of a layer is one quarter of the wavelength of the incident wavelet. For a 30 Hz wavelet, this approximation suggests that the thickness of a CO_2 layer thinner than $\sim$ 11.9 m cannot be resolved using the separation of reflections. For a 50 Hz wavelet, this minimum resolvable thickness is $\sim$ 7.1 m. However, these estimates are approximations that depend on the level of noise in the data and the full frequency content of the recorded signal. Yilmaz (2001) suggests that for reflections with bright easily picked amplitudes, such as these ones, this approximation is too stringent. Kallweit & Wood (1982) suggest that the absolute limit for the minimum resolvable thickness is the point of maximum constructive interference between reflections from the top and base, known as the tuning thickness. These authors give an expression for the tuning thickness, $b = \frac{1}{2}v_c(2.6f_p)^{-1}$, which in this situation yields 9.1 m for a 30 Hz wavelet, and 5.5 m for a 50 Hz wavelet.

Figure 3.2b shows the relationship between reflection separation and layer thickness for 30 Hz and 50 Hz Ricker wavelets. It can be seen that this relationship is further complicated by a small increase in the reflection separation for layers thinner than 1 m. This increase means that measurements of regions towards the edges of the plume can be interpreted as being much thicker layers if care is not taken to manually remove these zones.

Analysis of the reflections from the 2010 broadband survey suggests that while reflections can be measured down to 5.5 m, doing so means that significant regions towards the edge of the plume are also measured as being overly thick. These erroneous measurements reduce confidence in the measured thickness of the rest of the plume. To combat this problem, a higher confidence limit of 6.5 m is suggested for this dataset (Figure 3.3). This higher limit still requires some regions towards the edge of the plume to be manually removed, but means that the thickness of the central regions can be measured with confidence. The uncertainty associated with these measurements is therefore almost entirely due to uncertainty in the estimated velocity of seismic waves through CO_2 saturated sandstone, rather than uncertainties in the reflection separation (Figure 3.4).

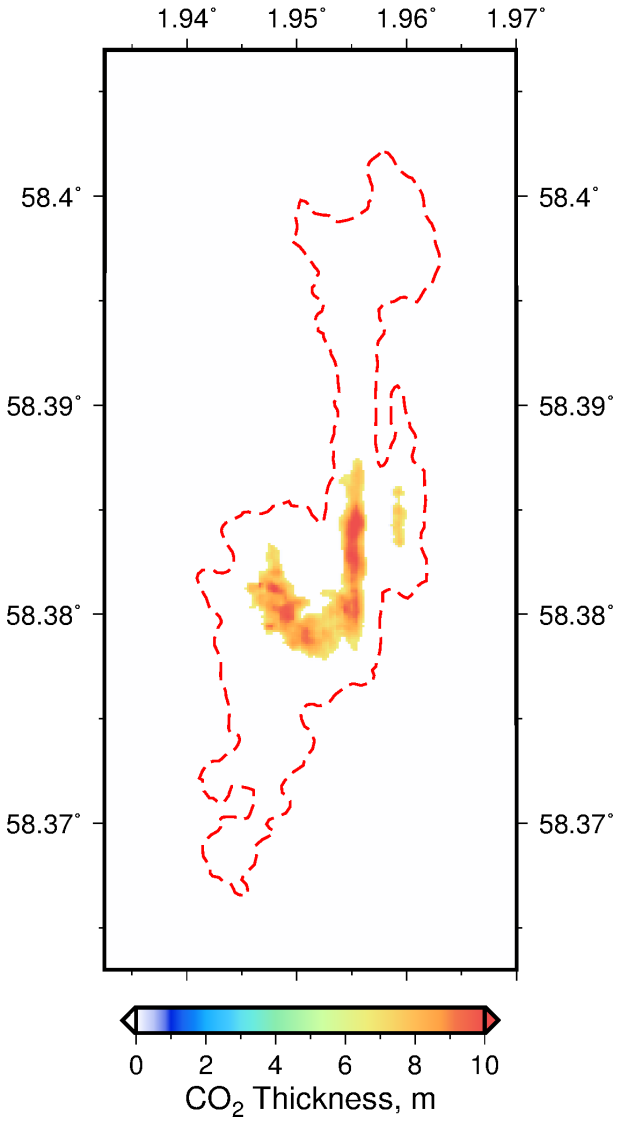

Figure 3.3: Thickness of Layer 9. Thickness determined from separation of reflections on the 2010 broadband survey. Red dashed line shows edge of plume picked from amplitude measurements.

Figure 3.3 shows that only a small portion of the plume is greater than 6.5 m thick in 2010. This portion is confined to the central region of the CO_2 plume and the north striking ridge. The vast majority of the plume is thinner than 6.5 m, meaning that another method is required to investigate the thickness of the plume outside of this region and for the other seismic reflection surveys.

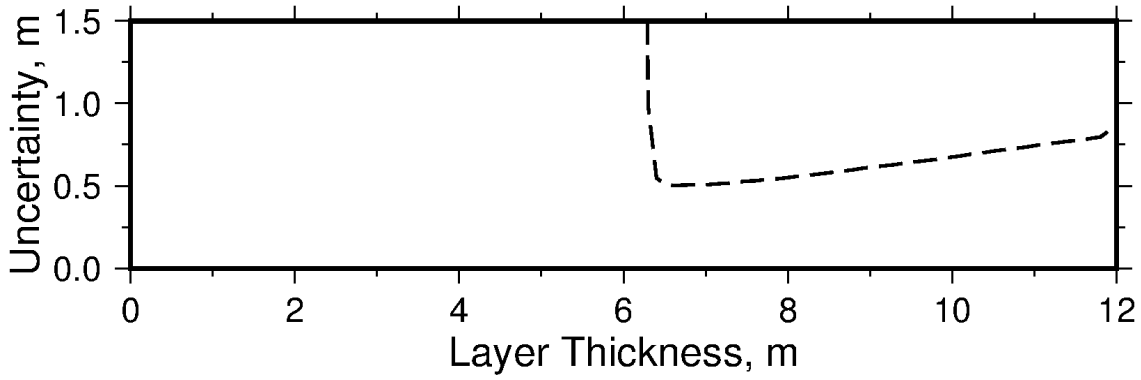

Figure 3.4: Uncertainty of thickness measurement using separation of reflections method. Uncertainty estimate includes uncertainty in velocity of seismic waves through CO_2 saturated medium. Thickness cannot be measured using this method below ~6.5 m.

3.5 Time-lapse Layer Thickness

Due to the reduced frequency bandwidth in the time-lapse seismic reflection survey, interference of wavelets reflected from the top and base of Layer 9 prevents the direct calculation of layer thickness using reflection separation. However, this interference causes tuning of the reflection amplitude and affects the TWTT of the top reflection relative to where the top of the layer is located. The best studied of these two effects is tuning of the reflection from the upper boundary (Figure 3.2c; Widess, 1973; Kallweit & Wood, 1982). For thick layers, where there is no interference between the reflections from the top and base, the amplitude of the upper reflection is constant. As the thickness of the layer decreases, the amplitude of the upper reflection increases. For layers that are thinner than the tuning thickness, the amplitude of the upper reflection decreases rapidly toward the value expected for a reflection from a single boundary without the presence of the low impedance layer. The thickness of a thin layer can therefore be estimated by measuring the amplitude of the reflected wavelet and using the relationship given in Figure 3.2c.

However, there are two important drawbacks. First, it is difficult to calibrate the relationship between amplitude and layer thickness without knowledge of the amplitude of a layer of known thickness. In the absence of this information, the values of A_1 and A_r must be calculated using uncertain estimates of density and seismic wave velocity. Secondly, amplitude does not monotonically increase with layer thickness, which introduces a fundamental

ambiguity in the vicinity of the tuning thickness since two different values of layer thickness are consistent with a given value of amplitude (Kallweit & Wood, 1982).

Interference of reflected wavelets from the top and base of a thin layer also causes small shifts in the travel-time of a wavelet reflected from the upper boundary (i.e. upper red dashed line shown in Figure 3.1; Furre *et al.*, 2015). The maximum theoretical time anomaly for a Ricker wavelet with a peak frequency, $f_p = 30$ Hz, is ~ 3 ms (Figure 3.2c). This maximum value increases as frequency decreases, and is particularly sensitive to very thin layers. While the time anomaly is small, it is measurable by comparing the TWTT of the caprock on pre- and post-injection surveys, although the ability to accurately measure it is susceptible to ambient and systematic noise. This measurement also suffers from the same form of ambiguity as reflection amplitude since two different values of layer thickness are consistent with a given time anomaly.

By combining amplitude and travel-time anomaly measurements, an amplitude-thickness relationship can be calibrated without requiring a layer of known thickness. In this way, both forms of ambiguity can be reduced. In Figure 3.5a–c, the travel-time anomaly, β, is plotted as a function of normalized amplitude for different values of other parameters. In each case, layer thickness varies along a unique curve, the precise shape of which depends upon f_p, the peak frequency of the reflected wavelet, A_1, the amplitude of the reflection from the upper boundary, and A_r, the ratio of the amplitudes of reflections from the upper and lower boundaries. Distance along a given curve is a function of the temporal separation between reflections from the upper and lower boundaries of the layer. The value of this separation is converted into thickness using $v_{CO_2} = 1428$ m s^{-1}.

It is clear that a combination of amplitude and travel-time anomaly measurements greatly reduces, but does not entirely resolve, the problem of ambiguity. In practice, both measurements are subject to degrees of uncertainty which will be dependent upon the quality of the seismic reflection survey. Furthermore, positive and negative trade-offs arise when f_p, A_1 and A_r are varied. In order to explore these issues, it is useful to carry out tests by inverting

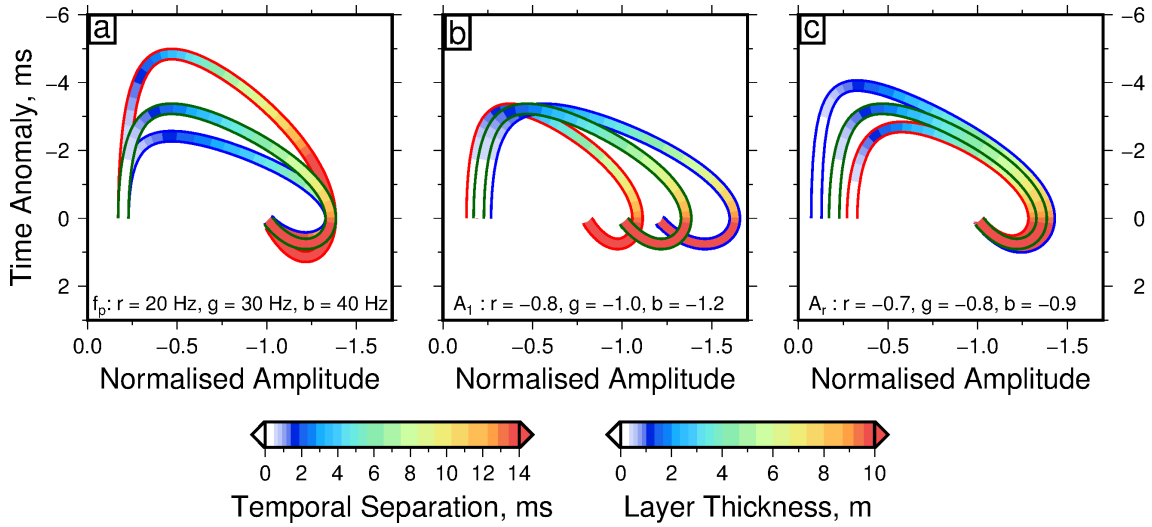

Figure 3.5: Relationships between amplitude, travel-time anomaly and layer thickness. **(a)** Change in time plotted as function of amplitude for different frequencies, f_p, where $A_1 = -1$ and $A_r = -0.8$. Red outline = 20 Hz; green outline = 30 Hz; and blue outline = 40 Hz. **(b)** Same for different values of A_1 where f_p = 30 Hz and $A_r = -0.80$. Red outline = -0.8; green outline = -1; and blue outline = -1.2. **(c)** Same for different values of A_r, where $A_1 = -1$ and f_p = 30 Hz. Red outline = -0.7; green outline = -0.8; and blue outline = -0.9. Colour scales refer to separation of upper and lower boundaries in ms and to layer thickness in m, using a velocity of 1428 m s^{-1}.

a synthetic dataset generated by forward modelling.

Figure 3.6a shows a disk of CO_2-filled reservoir rock with arbitrary dimensions, for which thickness varies linearly as a function of radius. First, the synthetic seismic image of this disk is calculated where f_p = 30 Hz, $A_1 = -2.5$ and $A_r = -0.8$ (Figure 3.6b-c). Secondly, travel-time anomalies, β, and amplitudes, A_3, across the disk are calculated by assuming that ambient noise is normally distributed with standard deviations of ± 1 ms and ± 0.1, respectively (Figure 3.6d and e). Levels of ambient noise were chosen to match those encountered in time-lapse seismic surveys from the Sleipner field. Finally, β is plotted as a function of A_3 which reveals the expected trend (Figure 3.6f).

3.5.1 Inverse Model

The challenge is to use this distribution of synthetic measurements and their associated uncertainties to estimate the radial variation of thickness across the original disk. Since there

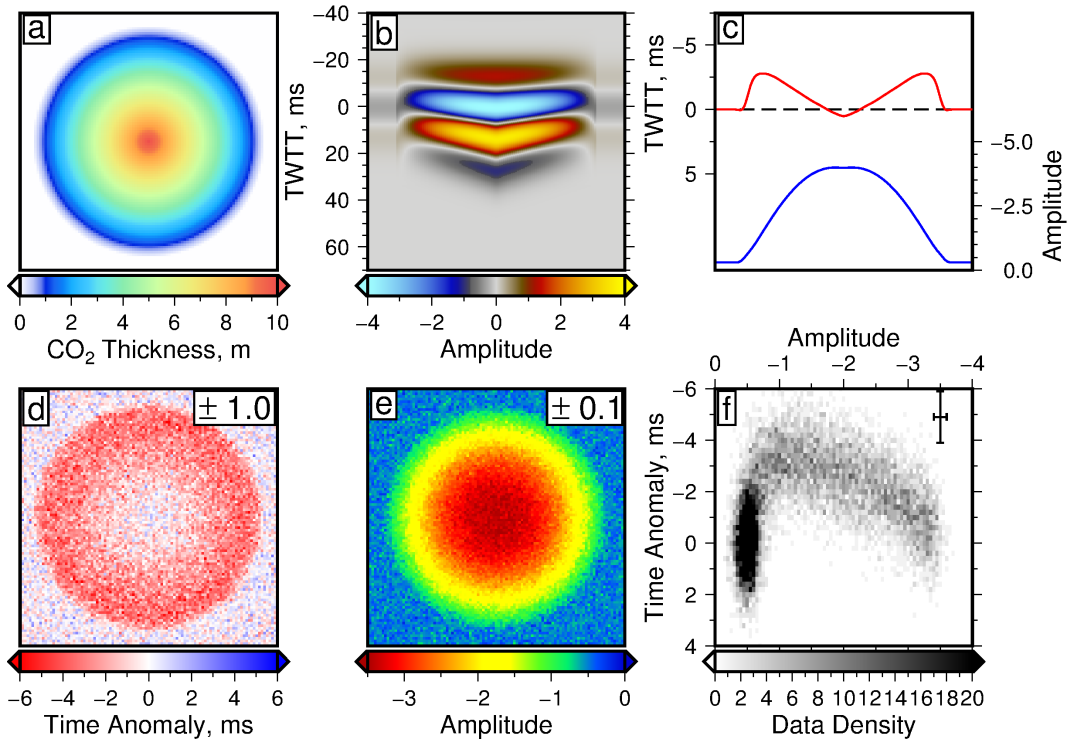

Figure 3.6: Forward model. **(a)** Circular patch of CO_2-filled layer (10 m thick at centre). **(b)** Synthetic vertical seismic image through centre of patch. **(c)** Details of seismic image showing travel-time anomaly (red) and reflection amplitude (blue). **(d)** Travel-time anomaly for region of patch with added random noise chosen from normal distribution with standard deviation of ± 1 ms. **(e)** Reflection amplitude for region of patch with added random noise chosen from normal distribution with standard deviation of ± 0.1. **(f)** Density plot of travel-time anomaly as function of amplitude (error bars indicative of uncertainties).

are only three independent parameters, (i.e. f_p, A_1, A_r), a pragmatic method for solving this inverse problem is by parameter sweep. Travel-time anomaly and amplitude measurements are scaled by their respective uncertainties and a misfit function, M, is defined as a measure of the difference between the observed variation of β with A_3 and a calculated model. Here, M is given by

$$M = \sqrt{\frac{1}{N}\sum_{i=1}^{N}\left[\left(\frac{A^o_{3,i} - A^c_{3,i}}{\sigma_{A_{3,i}}}\right)^2 + \left(\frac{\beta^o_i - \beta^c_i}{\sigma_{\beta_i}}\right)^2\right]}, \tag{3.3}$$

where i refers to each individual data point, N is the number of data points, A^o_3 and β^o are the observed amplitude and travel-time anomaly measurements, A^c_3 and β^c are their calculated values, and σ_{A_3} and σ_β are uncorrelated uncertainties. The variation of M as a function of f_p, A_1 and A_r is shown in three orthogonal slices (Figure 3.7). These slices demonstrate that A_1 and A_r trade off positively against each other. Noise in the travel-time

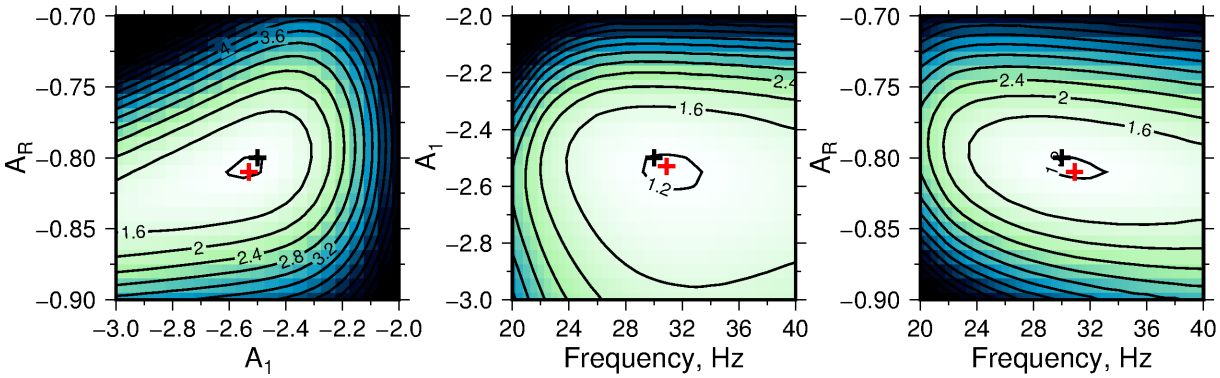

Figure 3.7: Misfit plots for A_r, A_1 and f_p for synthetic dataset with $\sigma_\beta = 1$ ms and $\sigma_{A_3} = 0.1$. Orthogonal slices through misfit function used to identify optimal values of A_r, A_1 and f_p. Red cross = loci of global minimum found by grid search, where $A_r = -0.81$, $A_1 = -2.53$ and $f_p = 30.9$. Black cross = loci of forward model parameters, where $A_r = -0.8$, $A_1 = -2.5$ and $f_p = 30$.

anomaly means that the misfit minimum constraining frequency is relatively shallow.

Once the global minimum of the misfit function has been identified by parameter sweep, the way in which layer thickness varies as a function of β and A_3 can be determined (Figure 3.8a). Note that the maximum value of layer thickness can be fixed in order to improve the fit when ambient noise levels are high. In this synthetic test, a maximum value of 10 m was found by iteratively fitting the observations until a calculated distribution was identified that honours the distribution of observations without the risk of over-estimating thickness values. Limiting the maximum measurable thickness in this way means that in some regions thickness could be under-estimated. A significant advantage is that it sidesteps any remaining ambiguity in the vicinity of the tuning thickness when ambient noise levels are high.

The best-fitting model is used to translate individual measurements of both amplitude, A_3, and travel-time anomaly, β, into layer thicknesses. In the complete absence of ambient noise, this translation is accurate and recovery of layer thicknesses is perfect, even for thicknesses that exceed the tuning thickness. If realistic levels of ambient noise are included, the original parameters are recovered to a high accuracy (i.e. < 5 % of the original values, Figure 3.9). The difference between the original and recovered disks is small (Figure 3.6a and 3.8b).

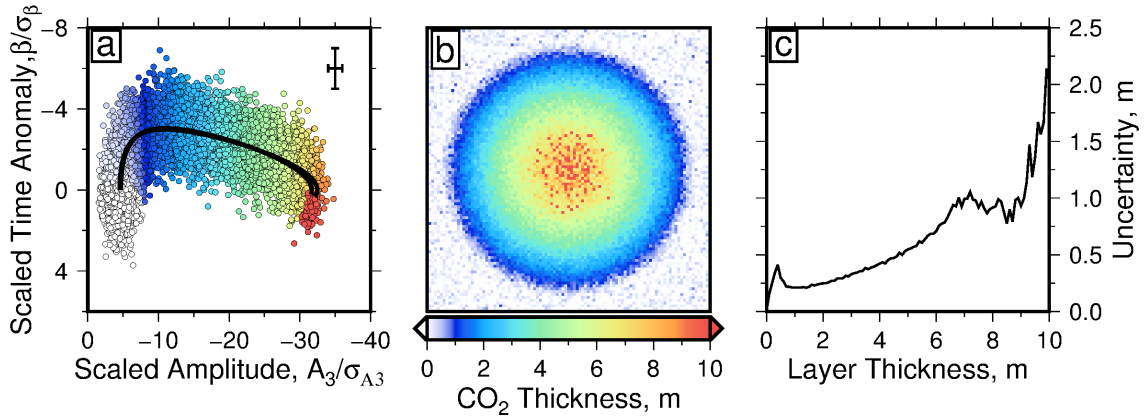

Figure 3.8: Inverse model. (a) Travel-time anomaly as function of amplitude scaled by their respective uncertainties (error bars indicative of uncertainties). Colour scale indicates measured layer thickness. Black line = relationship used to generate forward model; red line = best-fit relationship determined by grid search of misfit function. **(b)** Thickness of CO_2-filled layer for region of patch determined using inverse model. **(c)** Measurement uncertainty against measured layer thickness (one standard deviation).

These synthetic tests are used to calculate the uncertainty associated with the measurement of a particular thickness. Estimating the measurement uncertainty of a particular thickness is achieved by comparing the 'true' starting model thickness and recovered model thickness. A histogram is constructed showing the absolute difference between all grid squares measured at a particular thickness and the true thickness of these grid squares. The uncertainty for a measurement of that thickness is then chosen as the distance from 0 m absolute difference that encompasses 67 % of the data points in the histogram. Including uncertainties in the velocity of seismic waves through CO_2 saturated sandstone, these results suggest that calculated thicknesses have an uncertainty of less than $\pm$ 0.6 m between 1 m and 6 m (Figure 3.8c). Above 6 m, this uncertainty increases as values of A_3 and β become less sensitive to layer thickness.

To test how well the inversion recovers the starting parameters for different levels of ambient noise a grid search over noise levels in travel-time anomaly, σ_β, and amplitude, σ_{A_3}, is performed (Figure 3.9). For each combination of σ_β and σ_{A_3}, the synthetic data is inverted to recover the starting parameters. To improve computational efficiency, this inversion is performed using Powell's minimisation scheme (Powell, 1964; Press, 2007). This scheme was chosen because it can efficiently find the minimum of a misfit function without the need to

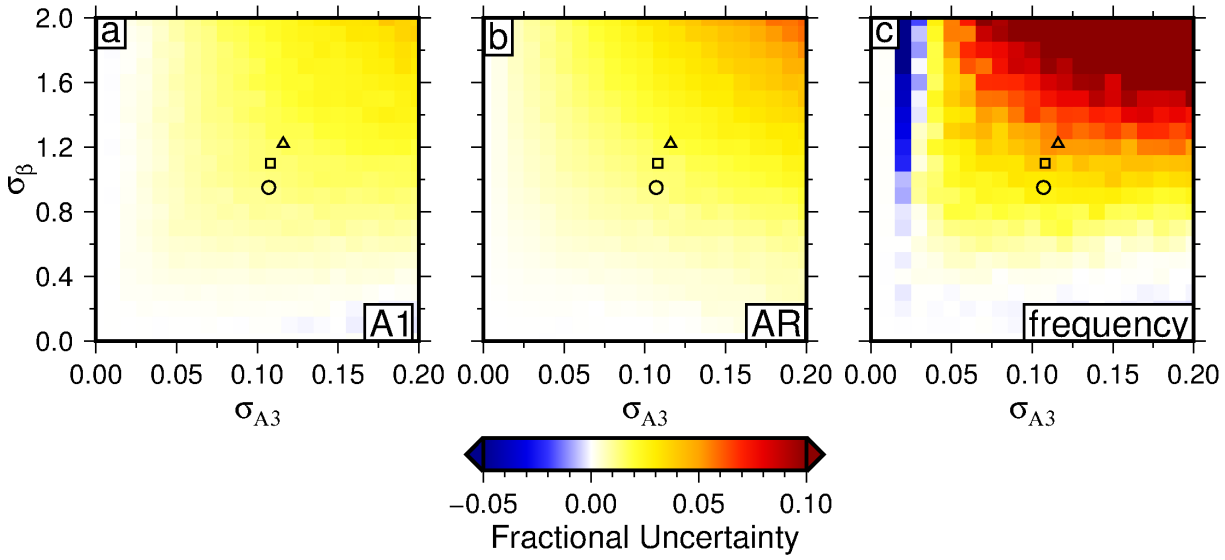

Figure 3.9: Fractional uncertainty of parameter recovery as a function of noise in travel-time anomaly and amplitude. Recovery uncertainty for **(a)** A_1, **(b)** A_R and **(c)** frequency. Circle = estimated noise level from 2010; square = 2008; triangle = 2006.

calculate gradients of the functions.

Each inversion was performed four times, and the mean recovered parameter for each level of ambient noise was calculated. The offset from these starting parameters is reported as a fractional uncertainty on the starting parameters. For an idealised time-lapse seismic reflection survey with no noise, the starting parameters are recovered perfectly. As noise levels increase for both amplitude and travel-time anomaly, some uncertainty is present in the recovery of the starting parameters. For levels of noise similar to those found in the Sleipner time-lapse seismic reflection surveys, parameters are recovered to within 5 % of their initial values. It can be seen that frequency is more sensitive to noise than either A_1 or A_R. However, the uncertainty in the recovery of these parameters is much smaller than that from calculating the reflectivity using estimated values of density and velocity of seismic waves in CO_2-saturated sandstone.

In these synthetic examples, the uncertainty in recovering the parameters is observed to be systematic. However, due to small differences between the synthetic and real examples (e.g. in data distribution), these uncertainties are not used to 'correct' the recovered parame-

ters found when inverting real amplitude and travel-time anomalies. The error in recovering parameters is taken into account in the uncertainty in measured thickness.

3.5.2 Application

This inverse modelling strategy is applied to the time-lapse seismic surveys acquired over the CO_2 plume at the Sleipner field. These seismic reflection surveys are an ideal data set to test this method, as the data has been processed to be comparable between the pre- and post-injection surveys, both in terms of the TWTT and amplitudes. This comparability has been achieved by processing the baseline survey in conjunction with each post-injection survey by following the same processing sequence (Section 2.3.2).

The first step in this analysis involves determining the travel-time anomaly and amplitude measurements. To measure the time anomaly produced by the presence of CO_2 ponding beneath the caprock, the caprock reflection (i.e. the boundary between the Nordland Group and the Utsira Formation) is picked on all post-injection surveys and the relevant version of the processed pre-injection survey (Figure 3.10). These picked horizons are smoothed using a median filter that suppresses ambient noise while preserving sharp gradients at the edges of the CO_2 plume (Hall, 2007). Mapping of both pre- and post-injection surveys for all years shows that, where CO_2 is present, travel time to the caprock-reservoir contact can be accurately identified and its relative change measured by differencing the TWTT to this horizon for each survey (Figure 3.11h-n). A systematic shallowing of the reflective boundary occurs where CO_2 is present in all surveys. In the region surrounding the CO_2 plume, there should be no difference between surveys aside from minor variations in seismic acquisition and processing strategies. However, small differences do occur, which suggests that random noise is present. Analysis of this surrounding region shows that this noise follows an approximately normal distribution with a standard deviation of ~ 0.95 ms (Figure 3.12). The mean value of this noise is approximately zero (0.04 ms in 2010) suggesting that systematic noise is negligible in these measurements. Sections that have been identified as being affected by overlying gas pockets in the overburden have been cropped out due to uncertainty in the

picking of the reflections in these regions (Figure 3.11).

The amplitude of these reflections is also extracted from the seismic reflection data (Figure 3.11a-g). In the region surrounding the CO_2 plume, the range of amplitude values is normally distributed with a standard deviation of 0.09 (Figure 3.12). This variation probably arises from a combination of small changes in lithology, measurement uncertainty and minor differences in acquisition and processing strategies.

Crucially, uncertainties in travel-time anomaly and amplitude measurements do not co-vary (Figure 3.13). The R^2 value for the best fit line for this data is 1×10^{-5}, indicating that there is no spatial correlation between uncertainty in amplitude and uncertainty in travel-time anomaly measurements. Travel-time anomaly is plotted as a function of amplitude, revealing the anticipated trend for all years (Figure 3.14a-g).

In the second step of this method, travel-time anomaly and amplitude measurements are fitted using a parameter sweep in f_p-A_1-A_r space (Figure 3.15). A global minimum is found at $f_p = 29.4$ Hz, $A_1 = -2.54$ and $A_r = -0.84$. The value of f_p is consistent with an estimated frequency content of 30 Hz for the 2010 seismic survey (Furre & Eiken, 2014). Calculated values of δ are converted into thicknesses using the estimated acoustic velocity of CO_2-saturated sandstone, $v_{CO_2} = 1428$ m s^{-1}.

Finally, limiting the maximum measurable thickness to 10 m yields satisfactory results for 2010 and 2008. For 2006 the maximum thickness was limited to 8 m. Due to the modest planform areas and layer thicknesses, this inverse approach worked less well for the 1999, 2001, 2002 and 2004 surveys. For these surveys the fitted parameters for the 2006 survey were used. These parameters were chosen because the 2001 and 2004 surveys were processed in conjunction with the 2006 survey, and so the frequency content and amplitudes of these surveys are likely to be more comparable. While the 2002 and 1999 surveys were not processed in conjunction with the 2006 survey, the distribution of travel-time anomaly and

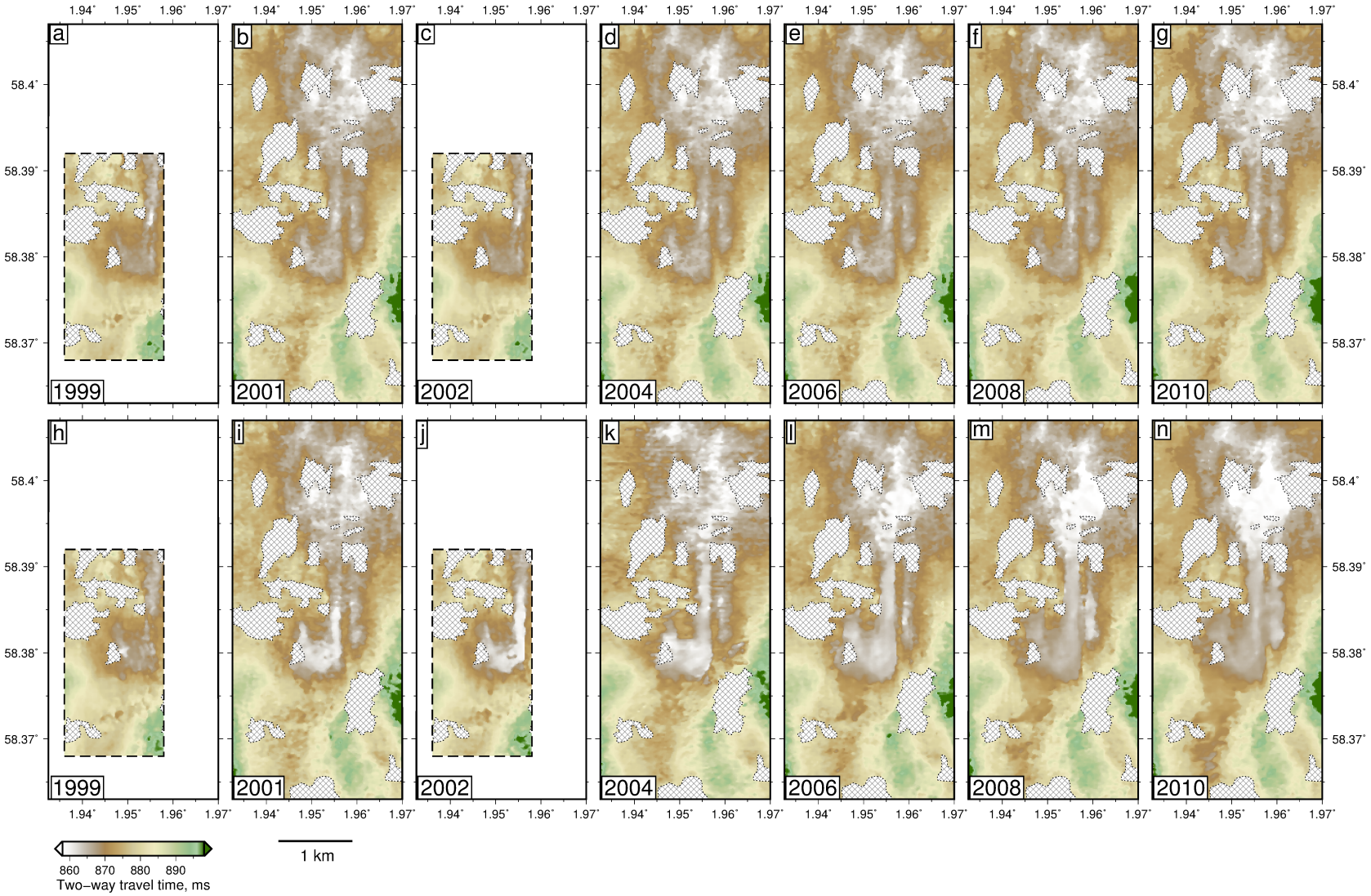

Figure 3.10: Comparative analysis of two-way travel time for Layer 9 caprock reflection. **(a-g)** TWTT to caprock reflection on baseline survey processed to be comparable with each year of survey. **(h-n)** TWTT to caprock reflection on post-injection surveys. 1999 and 2002 surveys cover a smaller extent. Hatched polygons = regions where reflections are incoherent due to natural gas pockets in the overburden.

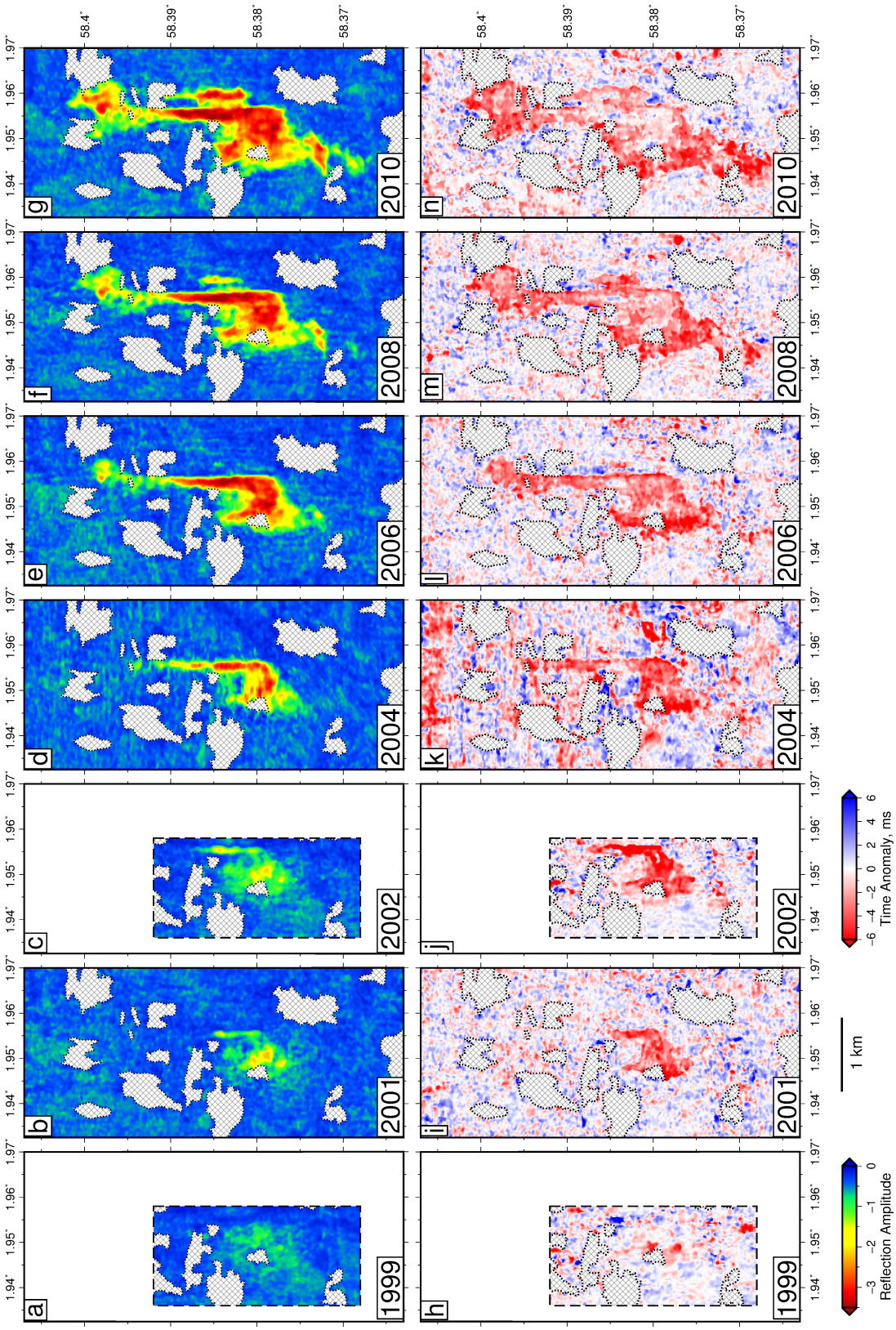

Figure 3.11: Comparative analysis of reflection amplitude and time anomaly for Layer 9 caprock. (a-g) Amplitude anomalies for all surveys. **(h-n)** Travel-time anomalies for all surveys. Hatched polygons = regions where reflections are incoherent due to natural gas pockets in the overburden. 1999 and 2002 surveys cover a smaller extent.

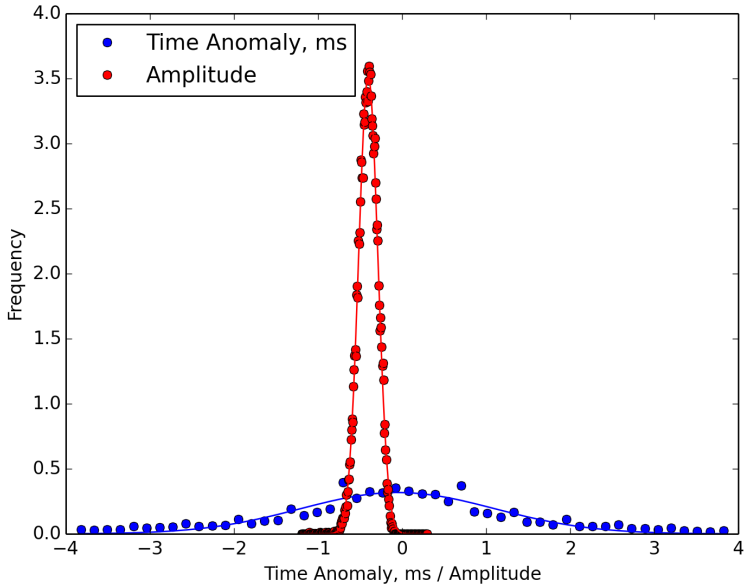

Figure 3.12: Histograms showing scatter in amplitude and time anomaly measurements around CO_2 plume.

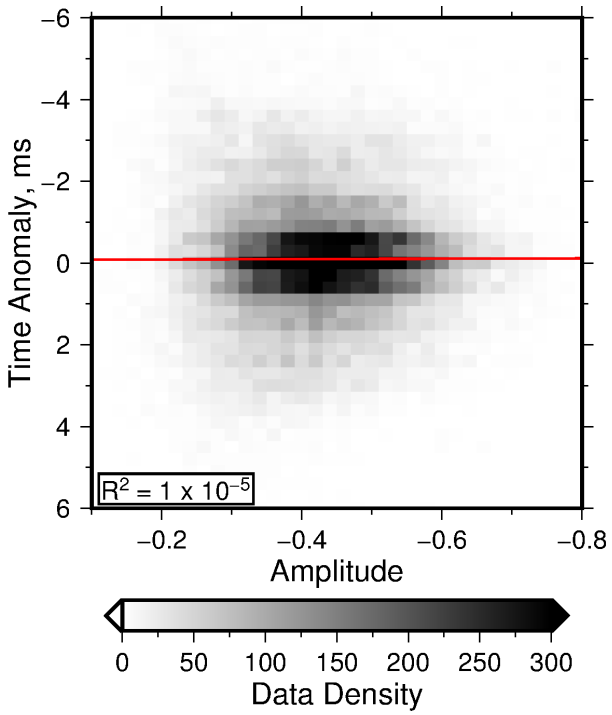

Figure 3.13: Correlation between travel-time anomaly and amplitude uncertainty. Red line shows best fit. $R^2 = 1 \times 10^{-5}$.

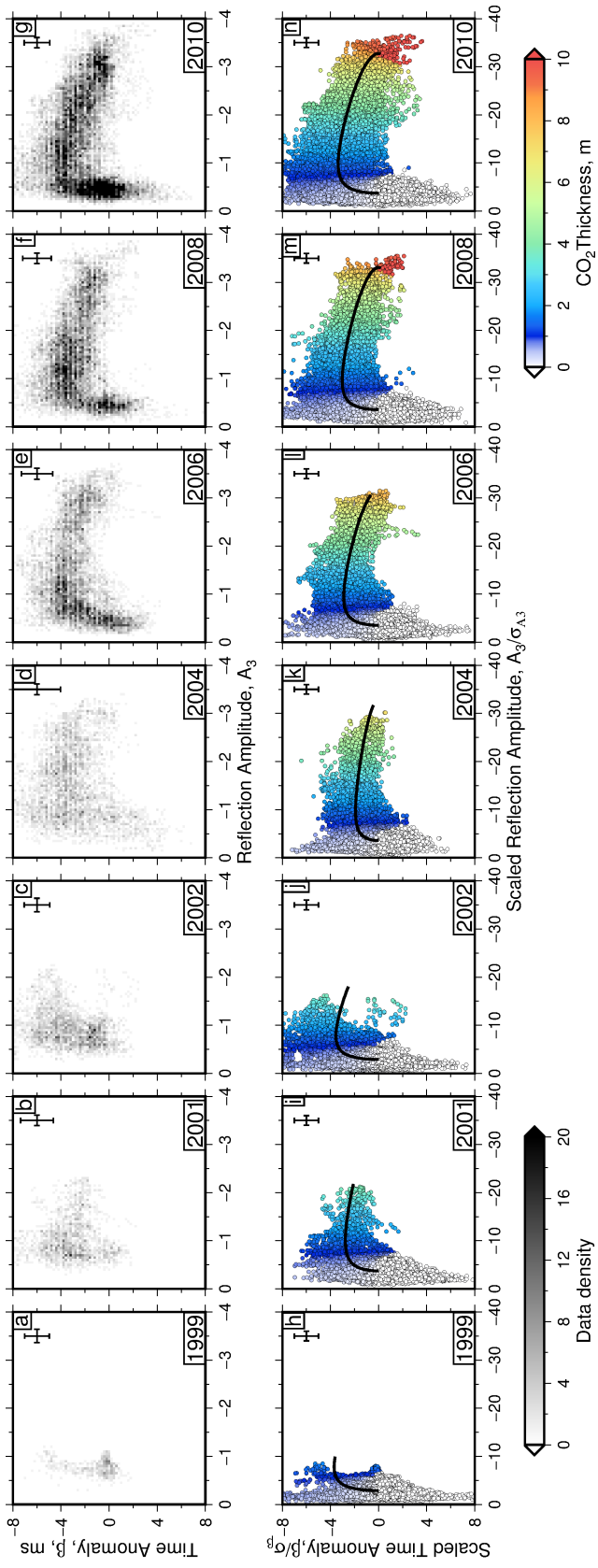

Figure 3.14: Comparative analysis of reflection amplitude and time anomaly for Layer 9. (a-g) Density plot for all years of surveys. **(h-n)** Scaled amplitude vs. travel-time anomaly. Solid line = best-fitting model. Colours show layer thickness.

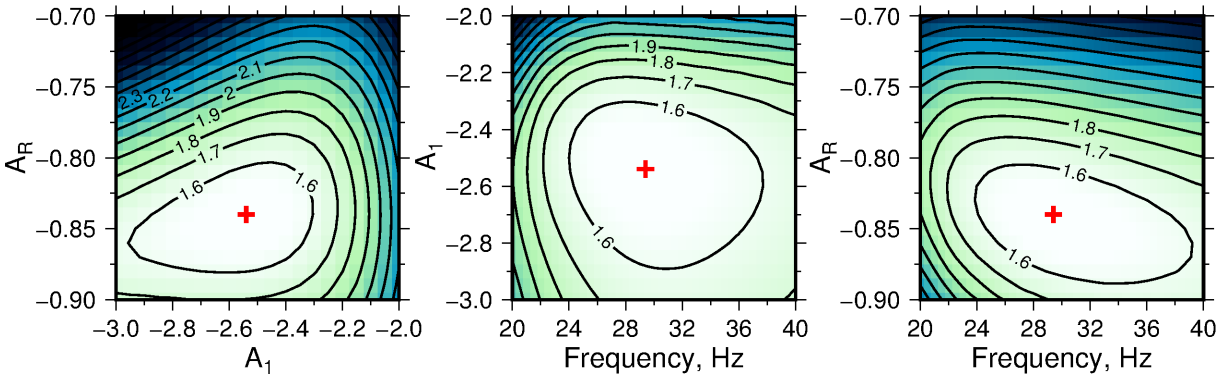

Figure 3.15: Misfit plots for A_r, A_1 and f_p for 2010. Orthogonal slices through misfit function used to identify optimal values of A_r, A_1 and f_p. Red cross = loci of global minimum found by grid search, where $A_r = -0.84$, $A_1 = -2.54$ and $f_p = 29.4$.

amplitude measurements suggests that the data is appropriately comparable. This approximation does not significantly affect the principal conclusions presented here.

For these surveys, it is apparent that limiting the maximum thickness has removed any potential ambiguity if the thickness were to be determined solely using amplitude measurements. However, it is important to emphasize that, without using travel-time anomaly measurements in conjunction with amplitude measurements, an absence of ambiguity in amplitude values could not be discerned. Use of travel time anomalies also permits accurate fitting of f_p, A_1 and A_r, improves resolution at the edge of the plume, and enables uncertainties to be gauged.

This limitation of 10 m for 2010 is consistent with the maximum thickness found by direct measurement of the separation of reflections from the upper and lower boundaries of the CO_2-filled layer imaged on the 2010 broadband survey (Figure 3.3; Furre & Eiken, 2014).

3.5.3 Results

The resultant distribution of thickness estimates shown in Figure 3.14h-n is then used to generate a planform map of CO_2-filled layer thickness (Figure 3.16). Calculated planform distributions show that the CO_2-filled layer thickens and grows rapidly along a north-south axis. The spatial distribution of thicker patches of CO_2 is consistent between surveys and

spatially coheres with the shape of the caprock-reservoir contact. The CO_2-filled layer evidently thins towards the edge of the plume. This edge of the CO_2 plume is relatively accurately resolved since changes in travel-time are very sensitive to thicknesses of less than $\sim$2 m. In contrast, using amplitude measurements alone is less sensitive to tapering edges of thin layers. Discontinuous regions of plume thickness are generally rare and mostly occur in later surveys when layer thicknesses exceed 6 m. Synthetic tests show that they are caused by greater degrees of uncertainty in the vicinity of the tuning thickness, where thickness is more sensitive to minor changes in A_3, β and noise in the data.

These inverse modelling results can be tested against the 2010 (broadband) seismic survey (Figure 3.17). Mapping of the broadband survey shows that clear separation of reflections is mostly confined to the central portion of the CO_2-filled layer on the broadband survey (Figure 3.17a). When the inverse modelling results and direct mapping are compared in this central portion, it is evident that inverse modelling yields slightly lower than expected thickness estimates (Figure 3.17c-d). However, in this region, the uncertainty associated with using the inverse method to measure layer thickness increases towards $\sim$1 m. Away from this central portion, estimates of thickness using reflection separation become either not possible to make or highly uncertain, making comparison between these methods difficult. Uncertainties for both of these methods are shown in Figure 3.17e. Note that the uncertainties shown in this figure do not account for uncertainty in the velocity of CO_2-saturated sandstone since this uncertainty affects both of these methods equally. It is evident from this comparison that even broadband surveys are still limited in their ability to constrain the thickness of this CO_2 layer. Methods such as the one developed in this chapter will continue to be useful for constraining thickness even with improved seismic reflection technology.

The results presented here compare favourably with previous attempts to constrain the thickness of Layer 9 at the Sleipner field. Other studies that exploit amplitude measurements have yielded broadly similar results, but the methods used have not permitted the uncertainties associated with these measurements to be quantified (Kiær, 2015; Chadwick *et al.*, 2005). These results also imply that thickness maps generated using the observed pushdown

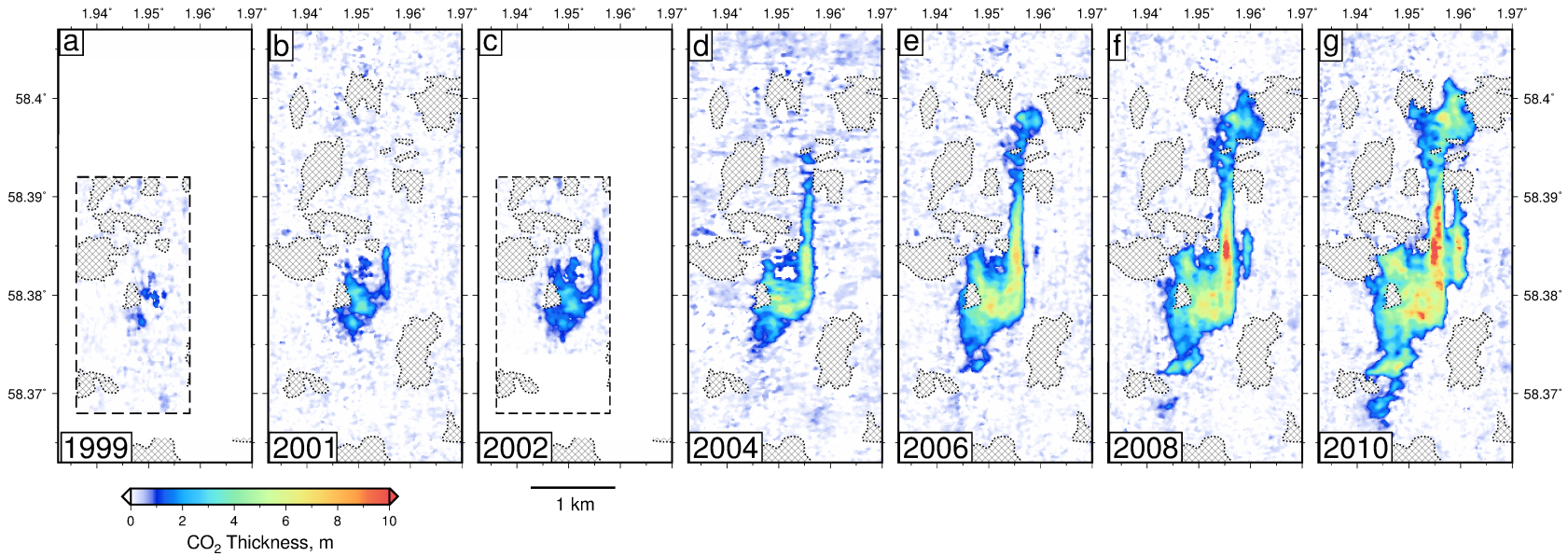

Figure 3.16: CO_2 distribution within Layer 9. Isopach maps showing CO_2 distribution within Layer 9 as a function of calendar year from 1999 to 2010. Hatched polygons = regions where reflections are incoherent due to natural gas pockets in the overburden; blue patches outside main CO_2 distribution caused by ambient noise. Note that 1999 and 2002 surveys have smaller extent.

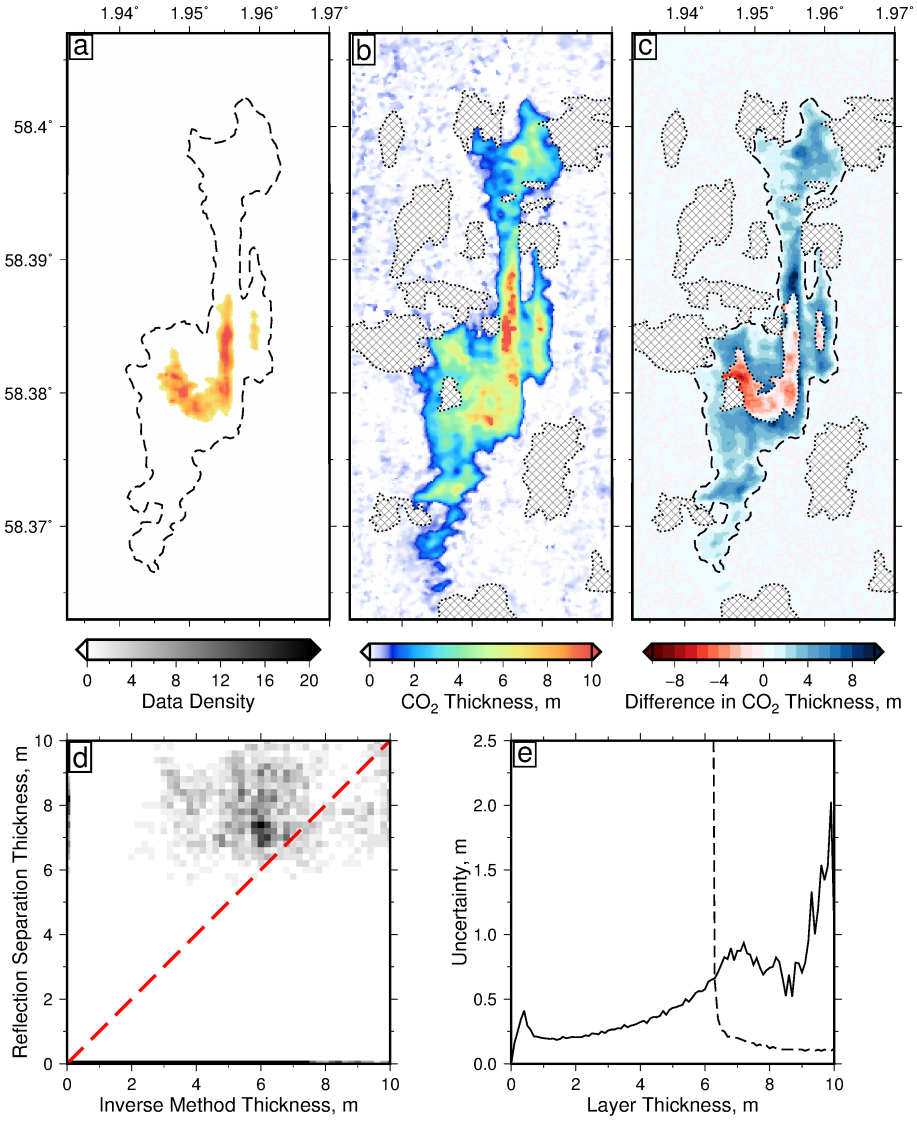

Figure 3.17: Comparison between inverse modelling and results of broadband survey. **(a)** Isopach map of CO_2 distribution within Layer 9 obtained using separation of reflective horizons on 2010 (broadband) survey. Dashed line = observed edge of amplitude anomaly. **(b)** Isopach map CO_2 thickness map for Layer 9 obtained using inverse modelling. **(c)** Difference in measured thickness between (a) and (b). Dotted line = region within which visible reflection separation occurs. **(d)** Density plot showing comparison of thickness estimates based upon inverse modelling and broadband measurements. **(e)** Uncertainties in broadband measurements (dashed line) and inverse model (solid line). Uncertainties do not include uncertainty in seismic wave velocity as this affects both measurement methods.

of Layer 8 are excessively thick (Furre *et al.*, 2015). This discrepancy could be accounted for by including diffuse and patchy saturation of CO_2 between Layers 8 and 9, which would tend to increase pushdown without requiring a thickness change of the more highly saturated layer.

3.6 Fluid Dynamical Implications

3.6.1 Volumetric Estimates

The inverse modelling results are used to calculate the volume of CO_2 trapped within Layer 9 of the Utsira Formation as a function of time (Figure 3.18). In this calculation I assume that the sandstone of Layer 9 has a porosity of 0.37 and a uniform CO_2 saturation of 0.8 (Arts *et al.*, 2004; Chadwick *et al.*, 2004a; Bickle *et al.*, 2007). Uncertainty estimates are gauged by running synthetic models that replicate ambient noise levels within the different seismic surveys and do not account for uncertainty in either porosity or saturation.

The volume of CO_2 into Layer 9 increases with time and can be fitted using a function of the form

$$V = C(t - t_0)^n, \tag{3.4}$$

where V is the volume of CO_2 given in m^3, t is time given in years, $C = 9500 \pm 5700$ m^3 yr^{-n}, $t_0 = 1998.1 \pm 0.5$ yr and $n = 2.1 \pm 0.2$. These results are approximately consistent with a linearly increasing flux, $Q = (20000 \pm 12000)t^{1.1}$ m^3 yr^{-1}. Using this relationship, the volume of CO_2 trapped inside Layer 9 by 2012 (the year of the next time-lapse seismic reflection survey) is predicted to be approximately 2.4×10^6 m^3. Equation (3.4) implies that super-critical CO_2 took $\sim 1.4 \pm 0.5$ years to reach the top layer, following initiation of injection. Assuming a density of 690 kg m^{-3}, the volume of CO_2 residing in Layer 9 in 2010 equates to about 12 % of the total injected mass of CO_2 (Williams & Chadwick, 2012). Between 2008 and 2010, an amount equivalent to ~23 % of the injected CO_2 entered Layer 9, suggesting that a significant volume of CO_2 from the lower layers is migrating to the top of the reservoir.

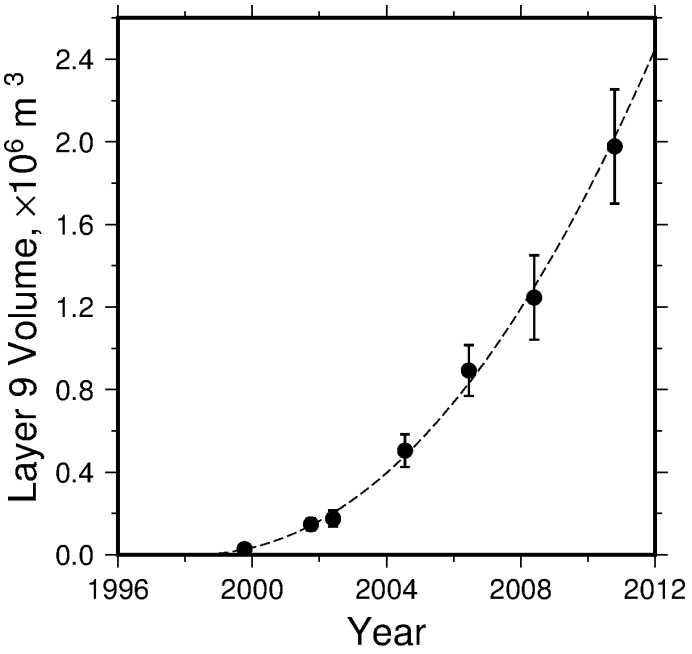

Figure 3.18: Volume estimates. Calculated volume of CO_2 based upon inverse modelling as function of calendar year for porosity of 0.37 and saturation of 0.8. Circles with error bars = estimates and their uncertainties; dashed line = best-fitting relationship using $V = C\left(\frac{(t-t_0)}{year}\right)^n$ where $C = 9500 \pm 5700$ m^3, $t_0 = 1998.1 \pm 0.5$ yr and $n = 2.1 \pm 0.2$.

CO_2 injection at the base of the Utsira Formation has been approximately constant since initiation of the Sleipner Project in 1996 (Figure 2.2; Chadwick & Noy, 2015). Measurement of the areal extent of CO_2 trapped within each of the lower CO_2-filled layers suggest that some of these layers may have ceased growing (Figure 2.16; Boait *et al.*, 2012). This observation suggests that the flux of CO_2 out of some layers is equal to that entering from below. New leakage pathways through the Utsira Formation may be generated as a given layer expands, causing the leakage flux from a given layer to increase with time. These putative pathways could account for the proposed balance between input and leakage flux for lower layers. An important corollary is that the flux into upper layers should increase with time. Since there is no seismic evidence that CO_2 is migrating out of Layer 9, it is anticipated that the flux of CO_2 into this layer will continue to grow. These general inferences are consistent with modelling of CO_2 migration in layered strata (Neufeld & Huppert, 2009).

3.6.2 Topographic Controls and Migration Pathways

The topography of the caprock, together with thickness of the CO_2-filled layer, permit the response of the flow of CO_2 to topographic relief to be analysed. Figure 3.19a shows a cross-section from the storage reservoir, which illustrates how Layer 9 has progressively filled. Uncertainty in converting travel time to depth means the shape of the structural trap is not precisely known. Differencing the reflection from this horizon picked on the baseline and post-injection surveys suggests that random noise with a standard deviation of $\sim$1 ms is present in these measurements, which translates into an uncertainty of $\sim$1 m. Uncertainty in the stacking velocity used during seismic processing indicates that this value could be higher. Here, topographic relief has been smoothed using a median filter and interpolated using a continuous spline in tension (Smith & Wessel, 1990).

The bulk of the CO_2 is flowing buoyantly up slope and filling the dome-shaped trap. This observation suggests that topographic relief plays a significant role in controlling the shape of the top of the CO_2 plume. For the 1999 survey, the planform of CO_2 distribution suggests that a patch of CO_2 exists away from the main part of the dome-shaped trap. This isolated patch can be accounted for if CO_2 migrates vertically from a lower layer at this location. This migration may have been facilitated by the presence of a prominent vertical chimney, SC1, observed on seismic reflection profiles (Figure 3.19b-c). This chimney was discussed as a possible pathway for CO_2 migration through the whole reservoir in Section 2.5.2. A smaller chimney, SC2, is visible further up-dip which may also have affected CO_2 flow to a lesser extent by generating an anomalously thick zone of CO_2. Low amplitude features such as these ones are commonly interpreted to be near-vertical gas migration pathways (Chadwick *et al.*, 2004a).

3.7 Summary

In this chapter, I present an inverse method for estimating the three-dimensional distribution of CO_2 within seismically imaged storage reservoirs as a function of time using a combination

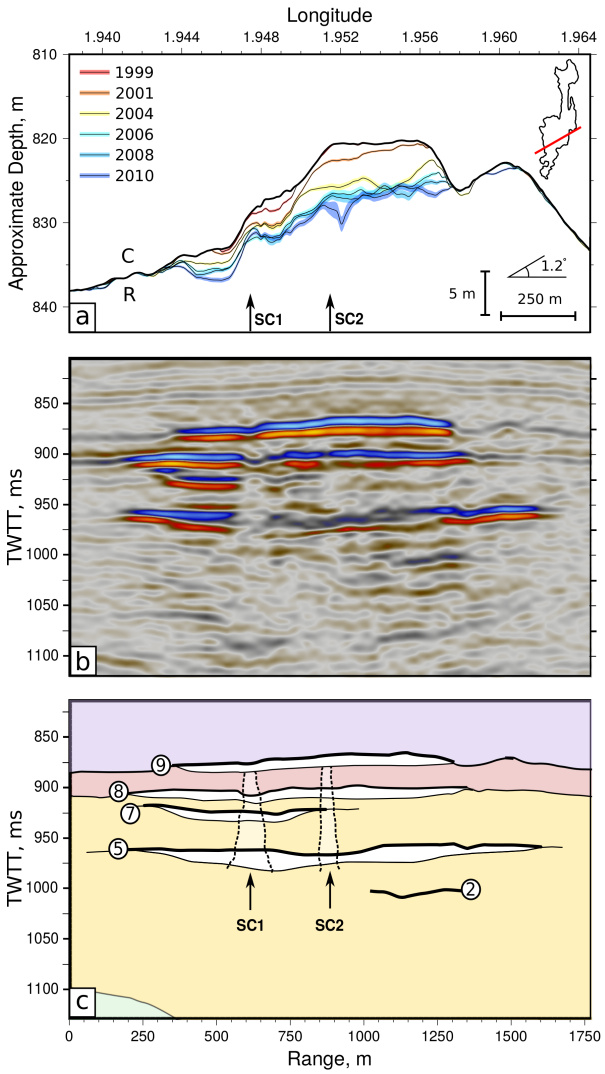

Figure 3.19: Vertically exaggerated cross-section through Layer 9. **(a)** Coloured lines = depth to base of Layer 9 through time where colour and thickness indicate year of seismic survey acquisition and 1σ uncertainty, respectively (overburden velocity of 2150 m s^{-1} was assumed ; Zweigel *et al.*, 2004); black line = top of reservoir; vertical arrows = loci of possible seismic chimneys; C = caprock; R = reservoir; inset shows location of cross-section. Note that the 2002 survey is omitted for clarity. **(b)** Coincident seismic profile from 2010 (broadband survey). Red/blue = positive/negative amplitudes. **(c)** Interpretation of (b) (see Figure 2.7 for colour scheme). Numbered black lines capping white patches = selected CO_2-filled layers; vertical arrows = loci of possible seismic chimneys.

of travel-time anomaly and reflection amplitude measurements. An important advantage of a combined approach is that *a priori* knowledge about the impedance of the thin layer in question is not required. The validity and robustness of this method was carefully tested using forward and inverse modelling of synthetic datasets. In the absence of ambient noise, layer thickness can be resolved without ambiguity. For typically observed levels of ambient noise, it has been shown that the technique can resolve layer thicknesses in the range of 1–6 m with a vertical resolution of $\pm$ 0.6 m.

This method was applied to the CO_2 storage reservoir at the Sleipner project. The planform of thickness variation for Layer 9 at the top of the reservoir was calculated. This planform was checked by comparing the 2010 time-lapse and broadband surveys. In regions where a direct seismic measurement of layer thickness can be made, there is satisfactory agreement between both approaches within the bounds of uncertainty.

These results can be used to calculate the volume of CO_2 within Layer 9 as a function of time. Volume increases with time at a growing rate, which indicates that CO_2 is migrating out of the lower part of the reservoir at an increasing rate. Migration is probably facilitated by initiation of new pathways through intermediate shale layers or by changes in the flow capabilities of existing pathways. By comparing patterns of layer growth with appropriate cross-sections from the 2010 broadband survey, it seems likely that sub-vertical chimney structures play a significant role in the upward migration of dense-phase CO_2.

These thickness and volume estimates provide a new benchmark against which analytical and numerical fluid dynamical models can be tested. In the next chapter, I develop and test a reservoir simulator using the thickness maps presented here as a benchmark. Using this simulator, I infer the reservoir properties of the aquifer Layer 9 and discuss the ability of reservoir simulators such as these to predict the future flow of CO_2 within the reservoir.

Chapter 4

Modelling CO_2 Flow in Layer 9

4.1 Introduction

Numerical flow simulations are an important part of site selection and hazard assessment for future carbon storage reservoirs. It is therefore crucial that observations from existing carbon storage sites are used to test and improve these numerical simulations. Modelling of CO_2 flow within these reservoirs is challenging due to the long time and length scales involved in carbon capture and storage projects. Potential storage reservoirs may also have complex geometries and geological heterogeneities that affect parameters such as permeability. When simulating CO_2 flow it is important to understand which parameters are essential to model, and on what length scales geological heterogeneities become significant. In this chapter, I develop and implement a simple reservoir simulator and geological reservoir model that enables a good match to be found to the observed CO_2 distribution in Layer 9 at the Sleipner field.

The seven post-injection seismic reflection surveys acquired over the CO_2 reservoir have provided unique insight into the movement of CO_2 through porous media on a field scale. The spatial and temporal pattern of CO_2 thickness in Layer 9 has been carefully mapped on each time-lapse survey (see Chapter 3). These seven snapshots of the CO_2 distribution in this layer provide an important testing ground for reservoir simulators. By matching the results of numerical models to the observed CO_2 distribution in Layer 9 in three-dimensions, the physical processes that control CO_2 flow can be examined.

Previous attempts to model CO_2 flow in Layer 9 have used commercial flow simulation packages (e.g. GEM and ECLIPSE), or free numerical modelling software (e.g. TOUGH2). These packages typically solve Darcy's law for flow in porous media on a three-dimensional grid. They are capable of simulating the flow of CO_2 through complex geological reservoir models. However, when modelling CO_2 flow in a CCS context, these simulations are required to be run over large length scales (of order km) and time scales (of order tens of years). Due to the computational expense of running these commercial models on such large scales, spatial resolution is often compromised to reduce running time.

A previous lack of accurate estimates of the thickness of CO_2 in Layer 9 has meant that modelling attempts have focussed primarily on matching the seismically observed areal planform. The modelled thickness of the CO_2 layer, and the information about flow dynamics that can be gleaned from it, is therefore often neglected. Despite the number of attempts and variety of software packages used, an accurate match to the spatial and temporal distribution of CO_2 in Layer 9 has not yet been produced using a conventional, three-dimensional reservoir simulator.

Here, I develop a simplified numerical reservoir simulator based on a vertically-integrated, sharp-interface model for gravity currents. The vertically-integrated nature of this simulator reduces the number of dimensions that the governing equations need to be solved over from three to two. Using this new simulator, the underlying physics of CO_2 flow through the reservoir at the Sleipner field, and the properties of this reservoir, are investigated.

In this chapter, I first describe the assumptions associated with the model, and discuss analytical solutions to the governing equations in two and three dimensions. A flow reservoir simulator is then developed using a finite difference approach. This numerical simulator is benchmarked against analytical solutions to check the stability and accuracy of the model. Once the accuracy of the simulator has been verified, it is used to model the flow of CO_2 in Layer 9 using values for the reservoir and fluid properties taken from literature. While the shape of the plume is generally recognisable in this simulation, this combination of reservoir and fluid properties does not permit the rapid migration of CO_2 along the north striking ridge. The flow model is then inverted to find the simplest set of reservoir properties present in Layer 9 that minimises the difference between the observed and modelled CO_2 distribution. Good agreement between the observed and modelled CO_2 distribution is attained when using a reservoir model with a high permeability channel, the existence of which is supported by seismic analysis. Finally, the future flow of CO_2 through Layer 9 is forecast.

4.2 Previous Work

Matching the unusual spatial distribution of CO_2 in Layer 9, and in particular the rapid migration rate of CO_2 along the north-striking ridge, has proved a difficult challenge for reservoir simulators. Previous simulations of CO_2 flow in Layer 9 can be divided into two major categories: invasion percolation and Darcy flow simulators. Invasion percolation models are applicable when capillary forces dominate over dynamic pressure (Cavanagh, 2013). These models assume a steady-state equilibrium between capillary forces and buoyancy, and therefore lack any inherent time-dependence (Oldenburg *et al.*, 2016). The model compares all neighbouring and available pore throats and selects the throat that offers the least resistance to displacing ambient fluid with invading CO_2. In this model, time is determined by the volume of CO_2 in the reservoir. Invasion percolation models have been used to simulate the flow of CO_2 in Layer 9 by Cavanagh (2013). The rapid migration of CO_2 along the north-striking ridge is predicted by this model, but otherwise it provides a poor match to the

observed planform. The lack of intrinsic time dependence in this model is also a significant shortcoming to this approach.

Modelling software such as GEM, ECLIPSE or TOUGH2 solve for Darcy's law over a three dimensional domain. In this case, flow is driven by pressure gradients associated with the injection of CO_2 into the reservoir and buoyancy. Resistance to flow is provided by frictional forces from solid grains, the magnitude of which is determined by the estimated permeability of the rock. Darcy flow simulators are generally computationally expensive due to the large number of parameters. As such, grid sizes tend to be large (of order $\sim$ 50 $\times$ 50 m) to reduce computation time, which has the effect of under-resolving key inputs such as caprock topography (Oldenburg *et al.*, 2016).

Chadwick & Noy (2010) modelled the flow of CO_2 in Layer 9 using TOUGH2 Darcy flow simulator assuming an isotropic permeability of 3 D (1 D $\approx 1 \times 10^{-12}$ m^2), but found that the CO_2 did not migrate away from the injection point quickly enough (Pruess, 1991). The resultant planform of the CO_2 layer was effectively radial. The match between the seismically observed planform and the modelling result was improved by invoking an anisotropic permeability such that the N-S permeability was 10 D and E-W permeability was 3 D. However, this adaptation still did not match the full migration rate along the north-striking topographic ridge. Chadwick & Noy (2010) also tested an idealised caprock topography to see if the mismatch in migration rate along the ridge could be accounted for by uncertainty in the reservoir geometry, but found that while the fit was improved, the inferred reservoir geometry was highly unlikely.

Similar modelling results were attained by Zhu *et al.* (2015) using GEM and TOUGH2, in which an anisotropic permeability of 10/2 D was invoked to improve the match between observed and calculated planforms. These authors also noted that some discrepancy between observed and modelled planforms could be due to topographic uncertainties, although this could also be attributed to under-resolved caprock topography due to large grid sizes in the model.

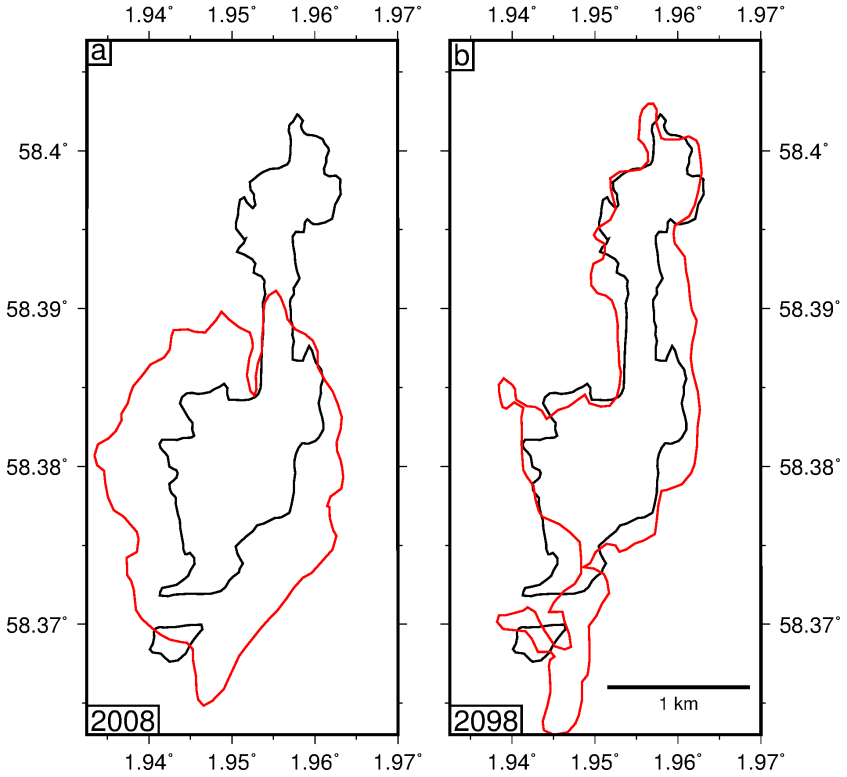

Figure 4.1: History matching flow model for 2008 adapted from Cavanagh & Nazarian (2014). **(a)** Red line = outline of flow simulation produced using black oil simulator with upscaled Corey relative permeability for 2008. Black line = observed outline of plume in 2008. **(b)** Red line = outline of flow simulation after injection is stopped in 2008 and the model is run to 2098 to allow CO_2 to approach equilibrium. Black line same as above.

Cavanagh (2013) used a black oil simulator adapted for CO_2 flow to model CO_2 flow in Layer 9, the advantage of which is that the dissolution of CO_2 in the brine can also be modelled. The relative permeability models tested in this study provide a poor fit to the observed planforms in the correct time frame. However, the author noticed that if injection of CO_2 was halted at a particular time step and the model was left running for $\sim$ 100 years, the planform of the CO_2 layer eventually matched the observed planform (Figure 4.1). Leaving the model to run for a significant period of time with no further injection permits the over-pressure associated with injection to dissipate, and the CO_2 to spread under buoyancy alone. This interesting long-term behaviour suggests that flow in Layer 9 is perhaps driven primarily by buoyancy, not injection pressure.

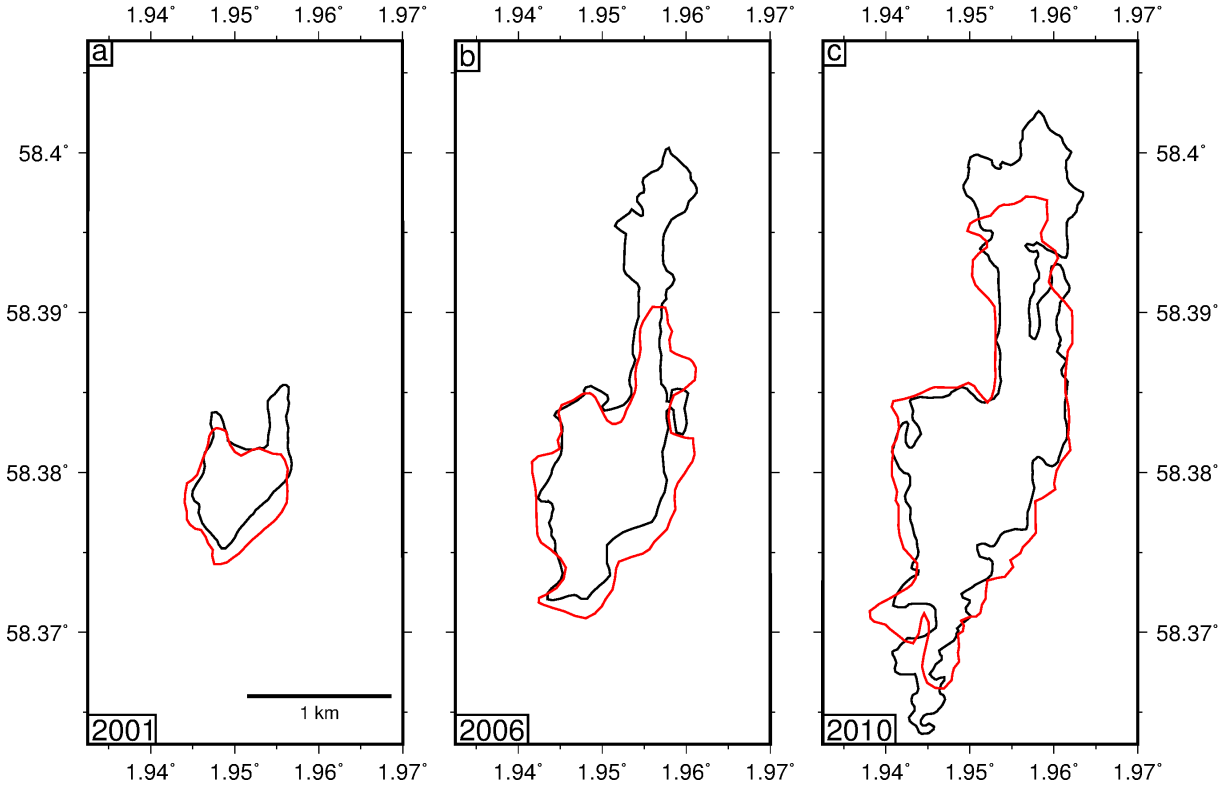

Figure 4.2: History matching flow model using high permeability channel adapted from Williams & Chadwick (2017). Red line = outline of flow simulations shown for **(a)** 2001, **(b)** 2006 and **(c)** 2008. Flow simulations produced using ECLIPSE 100. Black polygon shows CO_2-water contact observed on seismic data.

A recent model by Williams & Chadwick (2017) suggests that a high permeability channel may be present in the section of the reservoir in which the Layer 9 plume spreads (Figure 4.2; Zweigel *et al.*, 2004). Williams & Chadwick (2017) used an ECLIPSE 100 simulator with a channel permeability of 8 D, and a bulk reservoir permeability of 3 D. This simulation produced a better match to the observed planform for most of the plume, but still did not match the full rate of migration along the ridge. The existence of channels in the Utsira Formation is also suggested by Gregersen (1998).

Darcy's law is the basis for a significant number of analytical models describing the flow of CO_2 through porous media. Bear (1972) derived one of the first sharp-interface, vertical-equilibrium gravity current models that accounted for slope of the aquifer and proximity of the upper and lower bounding low-permeability horizons. Subsequently, analytical solutions have been derived for gravity currents in a variety of simple geometries. For example,

Huppert & Woods (1995) analytically, numerically and experimentally studied unconfined two-dimensional gravity currents on slopes, as well as exchange flows between aquifers where the flow spans the space between the upper and lower impermeable boundaries (i.e. confined flow). They found that the flow of an injected fluid on a slope would initially be dominated by gravitational slumping of the current, before advection of the fluid up-slope begins to dominate. Lyle *et al.* (2005) used a similar approach to find analytical solutions to the problem of a radial unconfined gravity current on a horizontal boundary, while the radial confined solution was provided by Nordbotten & Celia (2006).

Analytical solutions have also been found for the problem of a three-dimensional, unconfined gravity current on a slope (Vella & Huppert, 2006). These authors suggest that, for parameters representative of the Utsira Formation, the effect of caprock topography on CO_2 flow in Layer 9 would be felt between 0.03 and 14.2 years after flow initiated, depending on reservoir and fluid properties such as permeability and viscosity. This suggested time scale indicates that advection due to gradients in the caprock is likely to be a major driving force for the migration of CO_2 over the time period observed by the time-lapse seismic reflection surveys. Pegler *et al.* (2013) re-evaluated this estimate and suggested that this transition time scale was likely to be considerably longer (of order 100 years), and that the flow would therefore be dominated by gravitational slumping and pressure due to injection. However, topographic gradients present in the Layer 9 caprock were significantly underestimated in this analysis, resulting in a significant overestimate of the transition time between gravitational slumping and advection along caprock topography. The effect of capillary forces on gravity currents has also been discussed analytically and experimentally but the impact on fluid flow was found to be relatively minor (Golding *et al.*, 2011).

In the past few years, there has been a drive to increase efficiency of computation for modelling CO_2 storage over long time and length scales, leading to the increased development of vertical-equilibrium reservoir simulators (Liu *et al.*, 2010; Nilsen *et al.*, 2016a). This breed of reservoir simulator exploits the large body of work on vertical-equilibrium models, and applies it to geologically realistic settings for which analytical solutions cannot be

found. Since these simulators use a vertically-integrated formulation, the flow of CO_2 may be solved on a two-dimensional grid, increasing computational efficiency significantly. For example, Bandilla *et al.* (2014) report running times of 12 minutes on a single core for their vertical-equilibrium model when simulating CO_2 flow in Layer 9, compared to several hours on 100 cores for a TOUGH2 simulation using the same input parameters. Comparative studies between vertical equilibrium models and more conventional three-dimensional Darcy flow simulators have shown that these simulators achieve very similar results (Nilsen *et al.*, 2011; Bandilla *et al.*, 2014). However, the problem of matching the observed spreading rates has not been resolved simply due to a new formulation of the governing equations. Nevertheless, the speed of computation has opened up new possibilities to investigate uncertainties in the input parameters for these models by inversion.

Nilsen *et al.* (2017) used the adjoint method to invert for the caprock topography, permeability, CO_2 density, porosity and injection rates to produce an excellent match to estimated plume thickness measurements from 2001, 2004, 2006 and 2010 (Chadwick & Noy, 2010; Furre & Eiken, 2014). This work shows that uncertainties in input parameters are likely to be responsible for the failure of previous simulations to match the observed spreading rate. In this study, each input parameter was given equal weight in the misfit function, producing a non-unique set of parameters that enable a good match to the spreading plume. While inversions such as this can clearly produce an accurate match to the data, no constraint is placed on whether the recovered model is geologically reasonable. The results therefore provide only a partially satisfactory explanation of the spreading planform of the plume. Uncertainties in the measured thicknesses, and the fact that different methods were used to estimate the thickness in 2010 and the other years, are also not accounted for clearly in this study.

The reservoir simulator developed in this chapter follows a similar approach to the vertical-equilibrium models described above. A combination of detailed seismic analysis and reservoir simulation is then used to find a geologically informed reservoir model that can produce a good match between measured and modelled CO_2 spreading.

4.3 Modelling Strategy

The flow simulator described here models the flow of CO_2 through a saturated porous media as a buoyancy-driven gravity current. A key feature of these currents is that they have much greater lateral extent than thickness. This aspect ratio is also observed in the CO_2 layers at Sleipner, where the layers are on the order of one hundred times greater in their lateral extent than thickness. Many studies have also shown experimentally that the flow of a density-driven invading fluid through porous media is accurately described by gravity currents (e.g. Huppert & Woods, 1995; Lyle *et al.*, 2005; Golding *et al.*, 2011). The governing equation for gravity currents is vertically integrated meaning changes in reservoir properties in the vertical direction are neglected. However, detailed information concerning the variation of reservoir properties on the metre scale in the vertical direction is not available at Sleipner in the region occupied by Layer 9 so this assumption does not limit the conclusions presented here.

An important consideration in modelling CO_2 flow through porous media is whether the reservoir is confined or unconfined. An aquifer is considered to be unconfined if the flow of the ambient water may be neglected, often when the thickness of the aquifer is much greater than the thickness of the intruding fluid. Pegler *et al.* (2014) found that in a horizontally confined aquifer, confinement may be neglected provided that

$$h \ll \frac{\mu_c}{\mu_a} H_a, \tag{4.1}$$

where h is the thickness of the CO_2-saturated layer, H_a is the thickness of the aquifer, μ_a is the viscosity of the ambient water and μ_c is the viscosity of the CO_2.

The thickness of the uppermost part of the Utsira Formation that contains Layer 9, known as the Sand Wedge, is shown in Figure 4.3. The Sand Wedge is bounded on its top surface by the caprock for the Utsira Formation and on its base by a 5 m thick shale layer. The aquifer is estimated to be around 20 m thick, increasing to 30 m where the CO_2 is thickest (Williams & Chadwick, 2017). Using a viscosity ratio of $\mu_c/\mu_a \simeq 0.1$ suggests that where the

plume is thinner than 2-3 m the CO_2 layer behaves as an unconfined current, encompassing most of the plume at early times and the nose of the current at all times. However, this formulation is for a two-dimensional aquifer (i.e. x, z) and does not account for topographic gradients in the caprock. These important caveats mean that it is likely that the current can be much thicker and still be considered to be effectively unconfined. Another consideration is that Layer 9 is separated from the injection point at the base of the reservoir by eight thin shale baffles which are thought to be up to 5 m in thickness. The presence of these baffles means that Layer 9 can be considered to be isolated from the increased pressure caused by CO_2 injection that may affect some of the lower layers. Here, I therefore make the simplifying assumption that the current is unconfined at all times. A vertically integrated reservoir simulator that can account for changes in confinement of the reservoir is an area for further research.

The dominant driving forces considered in this model are therefore buoyancy-driven spreading of CO_2 away from regions where the CO_2 is thickest and advection due to gradients in the caprock topography. While this model assumes an unconfined aquifer, the confined aquifer case is important in many other CCS sites. Thus, Chapter 5 is devoted to providing the building blocks for incorporating the forces associated with confinement into this numerical model.

In this simplified model, capillary forces are also neglected and I consider only the sharp-interface gravity current problem. While this assumption is an obvious simplification of the governing physics, estimates of the vertical CO_2 saturation profile within these thin layers from centrifuge experiments on core material from the Utsira Formation suggest that the capillary transition zone at the base of the CO_2 layer is approximately 1 m thick (Figure 2.12; Chadwick *et al.*, 2004a). Comparisons between models that account for capillarity and sharp interface models suggest that capillary forces can be neglected when using vertically integrated simulations (Bandilla *et al.*, 2014). Analytical and experimental results also suggest that the rate of migration of the plume is not significantly affected by capillary forces during the injection phase, and so their effects are neglected here (Golding *et al.*, 2011). The

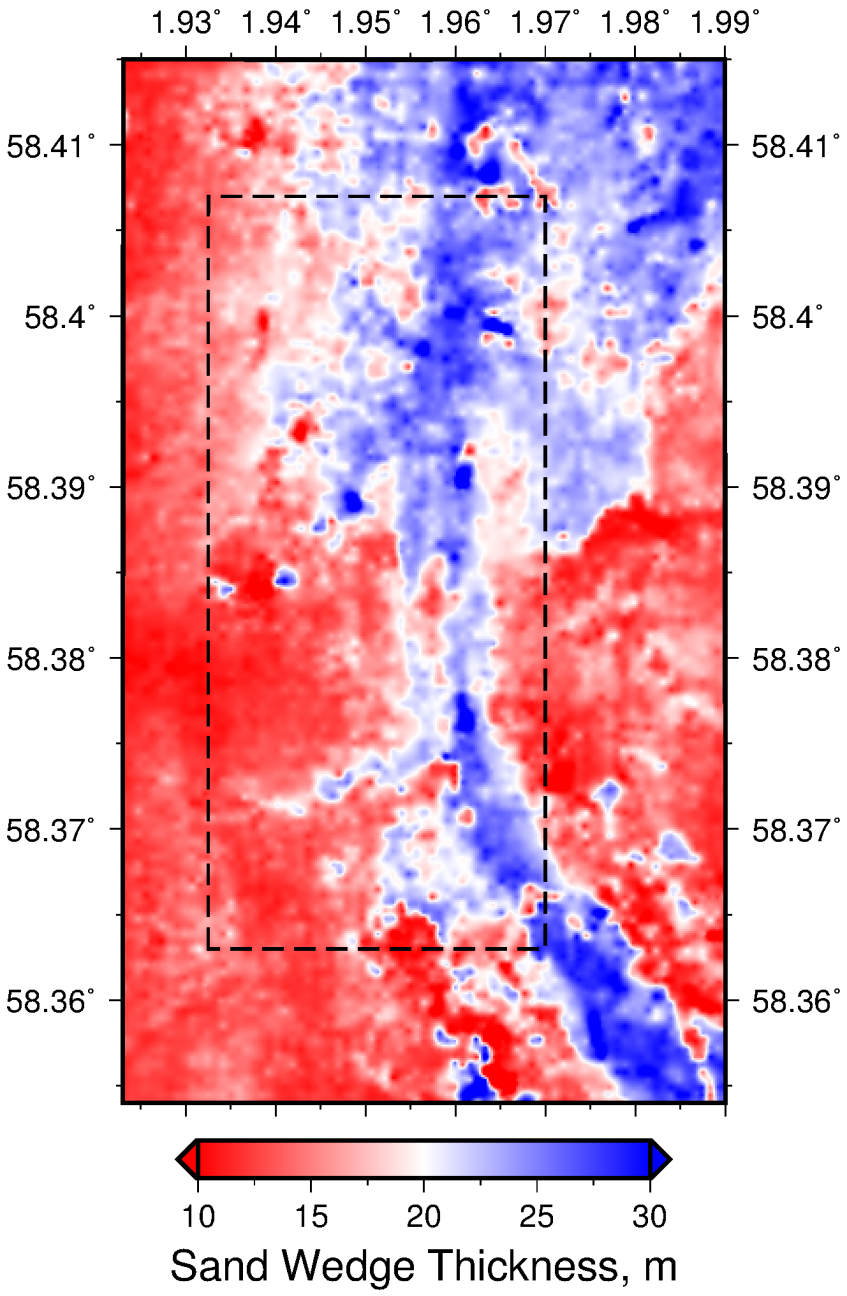

Figure 4.3: Thickness of the Sand Wedge. Sand Wedge is the uppermost part of the reservoir and the region within which Layer 9 is found. Dashed box shows extent of region used in reservoir simulations.

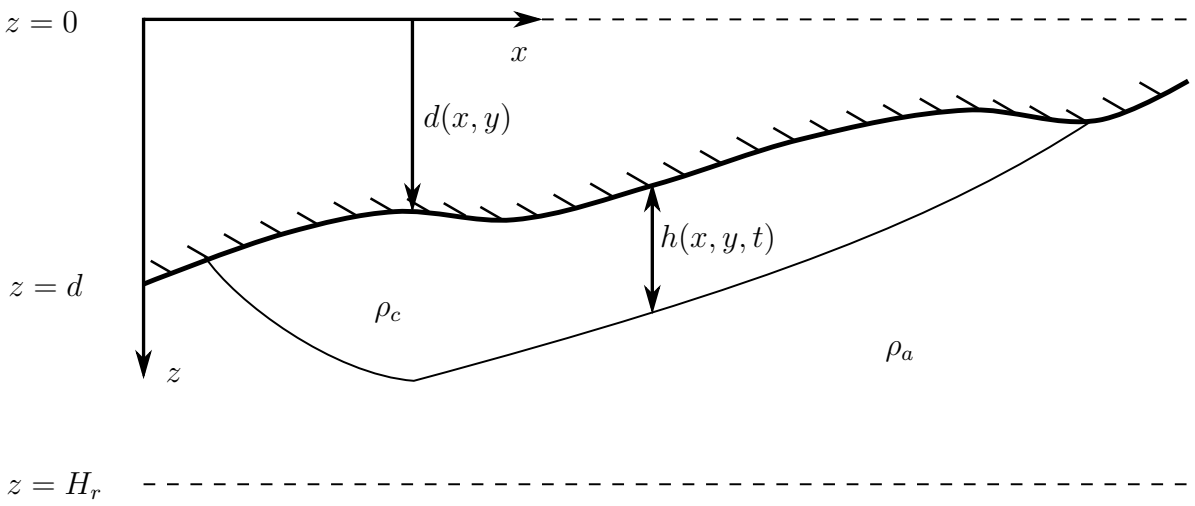

Figure 4.4: Three dimensional gravity current on a slope. Bold line = caprock, thin line = base of gravity current

following model therefore describes the flow of a single phase gravity current on a slope in an unconfined aquifer.

4.3.1 A Gravity Current on a Slope

Fluid flow in porous media is governed by Darcy's law which balances the driving forces (pressure gradients and buoyancy) with viscous drag at the pore scale,

$$\phi\tilde{u} = \mathbf{u} = -\frac{k}{\mu}\left(\nabla p + \rho g\hat{z}\right), \tag{4.2}$$

where ϕ is the porosity, $\tilde{u}$ is the interstitial fluid velocity, $\mathbf{u} = (u, v, w)$ is the Darcy velocity or fluid flux, k is the permeability, μ the viscosity, $\nabla p = \left(\frac{\partial p}{\partial x}, \frac{\partial p}{\partial y}, \frac{\partial p}{\partial z}\right)$ the pressure gradient, ρ is the density of the injected fluid, g is gravitational acceleration and $\hat{z}$ is a unit vector in the vertical direction (Figure 4.4).

The CO_2 is assumed to be incompressible, hence mass conservation requires that

$$\nabla \cdot \mathbf{u} = \frac{\partial u}{\partial x} + \frac{\partial v}{\partial y} + \frac{\partial w}{\partial z} = 0. \tag{4.3}$$

A key assumption in the formulation of gravity currents is that the lateral extent of the flow

is much greater than the vertical extent, and hence the vertical velocity, $w \ll u, v$.

For a gravity current flowing beneath an impermeable boundary with topography $d(x, y)$, as shown in Figure 4.4, the hydrostatic pressure can be written as

$$P = P_{H_r} - \rho_a g\{H_r - (d + h)\} - \rho_c g\{(d + h) - z\} \qquad d < z < d + h, \tag{4.4a}$$

$$P = P_{H_r} - \rho_a g(H_r - z) \qquad d + h < z < H_r, \tag{4.4b}$$

where P_{H_r} is the pressure at a reference horizon below the gravity current at depth $z = H_r$ that does not vary in space or time, ρ_c is the density of the injected buoyant fluid, ρ_a is the density of the ambient water, and $h(x, y)$ is the thickness of the gravity current. In contrast to the models proposed by Huppert & Woods (1995) and Vella & Huppert (2006) that were in a slope-parallel reference frame, this model is based on a horizontal reference frame in which it is simpler to compute complex geometries (e.g. the caprock topography for Layer 9).

By combining (4.2) and (4.4a) and assuming that P_{H_r} is a constant through space and time, the horizontal velocity, $\mathbf{u_H} = (u, v)$, is given by

$$\mathbf{u_H} = -\frac{k}{\mu}\nabla_H P = -\frac{kg\Delta\rho}{\mu}\nabla_H(d + h), \tag{4.5}$$

where ∇_H is the horizontal gradient and $\Delta\rho = \rho_a - \rho_c$, is the density difference between the fluids.

Since horizontal flow within the current is uniform with depth, it is straightforward to integrate the conservation of mass equation (4.3) over the depth of the current to give the evolution equation

$$\phi\frac{\partial h}{\partial t} - \nabla_H \cdot \left[\frac{k\Delta\rho g}{\mu} h\nabla_H(h + d)\right] = 0, \tag{4.6}$$

which describes the flow of the CO_2 current over variable topography with small gradients with time.

4.3.2 Gravity Currents in One Dimension

In this section, I examine the equations for a simple two-dimensional gravity current on a slope and discuss analytical expressions for the flow of the resultant current at early and late times. A buoyant gravity current flowing on an impermeable boundary with topography, $d(x)$, can be described in one dimension by

$$\phi\frac{\partial h}{\partial t} - \frac{\partial}{\partial x}\left(u_b\frac{\partial d}{\partial x}h\right) = \frac{\partial}{\partial x}\left(u_b h\frac{\partial h}{\partial x}\right), \tag{4.7}$$

where the buoyancy velocity, u_b, is given by

$$u_b = \frac{\Delta\rho g k}{\mu}. \tag{4.8}$$

Conservation of mass for a current heading in the positive x-direction is therefore

$$V(t) = \phi\int_0^{x_N} h\ dx \tag{4.9}$$

where x_N is the position of the nose of the gravity current, and $V(t)$ is the injected volume per unit width (m^2). The model has two further requirements: the thickness of the current at the nose must be zero; and the flux of fluid through the nose of the current must be also be zero. Thus,

$$h(x_N) = 0, \tag{4.10a}$$

$$-u_b h\frac{\partial(h+d)}{\partial x}\Big|_{x_N} = 0. \tag{4.10b}$$

To gain insight into the time-dependent behaviour of these currents and to benchmark the numerical scheme, a simple analytical relationship between the length and thickness of the current with time can be found using scaling analysis in the case of a simple linear topography, $d = d_0 - \alpha x$, and constant injection rate, $V(t) = qt$, where q is the two-dimensional injection rate, ($m^2 s^{-1}$). In this case, (4.7) is written as

$$\phi\frac{\partial h}{\partial t} + u_b\alpha\frac{\partial h}{\partial x} = \frac{\partial}{\partial x}\left(u_b h\frac{\partial h}{\partial x}\right). \tag{4.11}$$

This equation suggests that the flow of a gravity current on a slope will be controlled by buoyancy-driven slumping or by advection up topographic gradients. Scaling analysis of (4.11) suggests characteristic thickness, length and time scales given by

$$h_c = \frac{q}{u_b \alpha}, \tag{4.12a}$$

$$x_c = \frac{q}{u_b \alpha^2}, \tag{4.12b}$$

$$t_c = \frac{\phi q}{u_b^2 \alpha^3}. \tag{4.12c}$$

These scalings mark the transition between gravitational slumping due to buoyancy and along-slope advection-dominated regimes. Defining $T = t/t_c$, $X = x/x_c$ and $H = h/h_c$, (4.11) may be rewritten as

$$\frac{\partial H}{\partial T} + \frac{\partial H}{\partial X} = \frac{\partial}{\partial X}\left(H \frac{\partial H}{\partial X}\right), \tag{4.13}$$

with the mass conservation expressed as

$$T = \int_0^{X_N} H \; dX \tag{4.14}$$

and subject to the boundary conditions

$$H(X_N) = 0, \tag{4.15a}$$

$$H\left(\frac{\partial H}{\partial X}\Big|_{X_N} - 1\right) = 0. \tag{4.15b}$$

At early times, $T \ll 1$, for which the extent of the current is small, $X \ll 1$, diffusion dominates over advection, $H_X \ll (HH_X)_X$, and hence the current spreads in a classical self-similar manner in which $X \sim T^{2/3}$ and $H \sim T^{1/3}$ (Huppert & Woods, 1995).

To describe the early time flow regime in full a similarity solution can be found with similarity variable, η, and thickness, H, given by

$$\eta = \frac{X}{T^{2/3}}, \tag{4.16a}$$

$$H = T^{1/3} f(\eta). \tag{4.16b}$$

Equation (4.13) is therefore transformed into an ordinary differential equation in terms of $\eta = [0, \eta_N]$,

$$\frac{1}{3}f - \frac{2}{3}\eta f' - (ff')' = 0, \tag{4.17}$$

subject to the boundary conditions

$$1 = \int_0^{\eta_N} f \; d\eta, \tag{4.18a}$$

$$f(\eta_N) = 0, \tag{4.18b}$$

$$ff'|_{\eta_N} = 0. \tag{4.18c}$$

where $f' = \frac{\partial f}{\partial \eta}$. Numerically solving (4.17)-(4.18) gives $\eta_N = 1.48$ and hence

$$X_N = 1.48T^{2/3}, \tag{4.19a}$$

$$H = 1.3T^{1/3}. \tag{4.19b}$$

These relationships describing the evolution of the extent and thickness of the current with time are identical to those of Huppert & Woods (1995) for a gravity current on a horizontal boundary. This result suggests that the effect of topographic gradients is not important at early times.

At later times, $T \gg 1$, when advection becomes dominant, (4.13) can be approximated as

$$\frac{\partial H}{\partial T} = -\frac{\partial H}{\partial X}, \tag{4.20}$$

and the boundary conditions become

$$T = \int_0^{X_N} H dX, \tag{4.21a}$$

$$H(X_N) = 1. \tag{4.21b}$$

Defining the similarity variable, η, as thickness of the current as

$$\eta = \frac{X}{T}, \tag{4.22a}$$

$$H = f(\eta), \tag{4.22b}$$

a similarity solution can be found. By using an equivalent method to that shown above, it can be shown that $\eta = 1$ and $f(\eta) = 1$. The following relationships describe the flow of CO_2 in this regime

$$X_N = T, \tag{4.23}$$

$$H = 1. \tag{4.24}$$

These relationships show that, at late times, the thickness of the current is constant and proportional to the inverse of the slope. The nose of the current will advance at a constant rate proportional to the slope of the boundary. Again, this result is analogous to the slope-parallel solution given by Huppert & Woods (1995).

4.3.3 Gravity Currents in Two Dimensions

In this section, I consider the governing equations for a two-dimensional gravity current on a slope and describe analytic expressions for the flow of the resultant current at early and late times. For a two-dimensional gravity current, (4.6) may be written as

$$\phi \frac{\partial h}{\partial t} - \nabla_H \cdot \{u_b (\nabla_H d) h\} = \nabla_H \cdot (u_b h \nabla_H h), \tag{4.25}$$

where ∇_H is the horizontal gradient operator. For a constant injection flux, the conservation of mass can be expressed as

$$qt = \phi \int_{-y_N}^{y_N} \int_{-x_N}^{x_N} h \; dx \; dy, \tag{4.26}$$

where q is the injection flux, with units $m^3 s^{-1}$. Figure 4.5 shows the orientation of the coordinate system with respect to the slope direction.

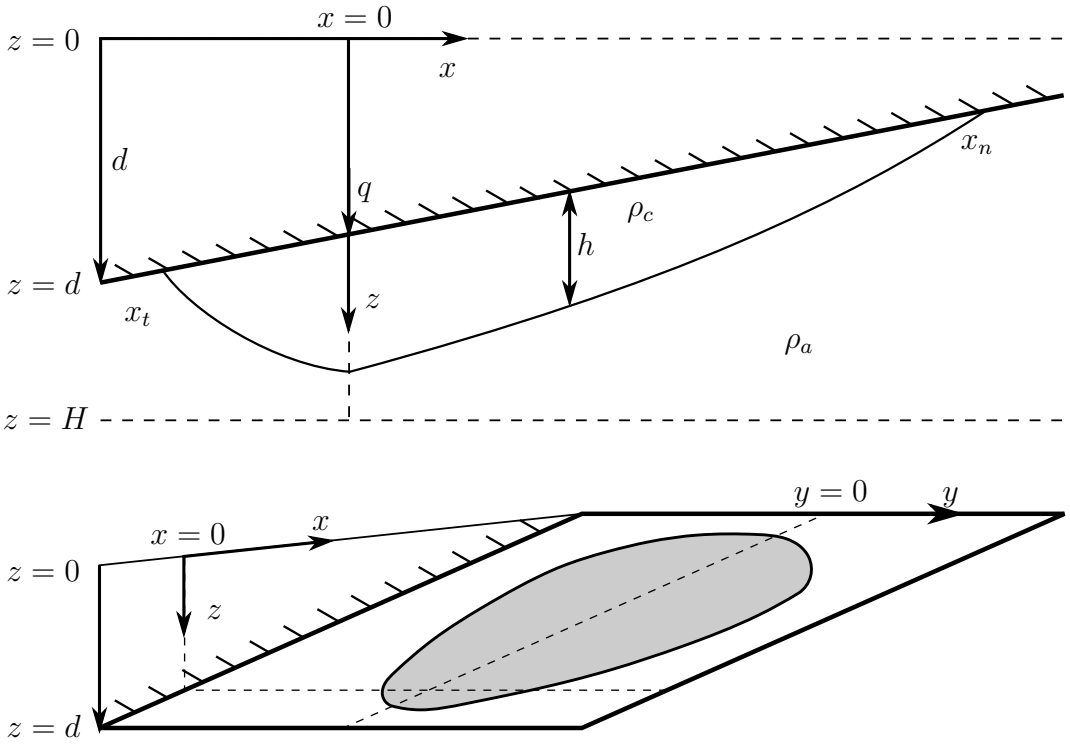

Figure 4.5: Gravity current in three dimensions on a slope. Gradient given by $\partial d/\partial x = -\alpha$

.

The problem of gravity currents on a slope in three dimensions was studied in detail by Vella & Huppert (2006), once again in a reference frame with the x-direction parallel to the maximum gradient of the slope and the y-direction across the slope. Here we follow their analysis but in a horizontal reference frame, with α equal to the maximum gradient of the slope (Figure 4.5), defined by $d(x, y) = d_0 - \alpha x$. Equation (4.25) can be expressed as

$$\phi \frac{\partial h}{\partial t} + u_b \alpha \frac{\partial h}{\partial x} = \nabla_H \cdot (u_b h \nabla_H h) \,. \tag{4.27}$$

In this reference frame, (4.27) is made dimensionless by setting $T = t/t_c$, $X = x/x_c$, $Y = y/y_c$

and $H = h/h_c$ where

$$h_c = \left(\frac{q}{u_b}\right)^{1/2}, \tag{4.28a}$$

$$x_c = y_c = \left(\frac{q}{u_b}\right)^{1/2} \frac{1}{\alpha}, \tag{4.28b}$$

$$t_c = \left(\frac{q}{u_b^3}\right)^{1/2} \frac{\phi}{\alpha^2}. \tag{4.28c}$$

Using these scalings, (4.27) may be written as

$$\frac{\partial H}{\partial T} + \frac{\partial H}{\partial X} = \nabla \cdot (H \nabla H), \tag{4.29}$$

which reproduces (2.8) from Vella & Huppert (2006), despite being initially posed in a different frame of reference. Scaling the conservation of mass equation (4.26) yields

$$T = \int_{-Y_N}^{Y_N} \int_{-X_N}^{X_N} H \; dX \; dY. \tag{4.30}$$

At early times, $T \ll 1$, the extent of the current is small, $X, Y \ll 1$, so the advective up slope term can be neglected. In this limit, (4.29) and (4.30) lead to the relationships $Y_N \sim X_N \sim T^{1/2}$ and $H \sim 1$, reproducing the radial, self-similar gravity current modelled by Lyle *et al.* (2005). A solution of the self-similar problem provides the pre-factors for the constant flux case, giving

$$X_N = 1.15 T^{1/2}, \tag{4.31a}$$

$$H = (1.15)^2 = 1.32, \tag{4.31b}$$

In the late time regime, $T \gg 1$, advection up slope dominates over buoyancy driven slumping. Scaling this term with the change in thickness with time gives $X_N \sim T$ and $H \sim 1/Y$. The flow regime away from the injection point at long time scales can then be investigated by setting $X \sim T$ and relating the diffusive spreading in the y-direction with the advective flow up-slope, leading to the relationship $Y \sim T^{1/3}$. Vella & Huppert (2006) found a similarity

solution for this behaviour, leading to the relationship

$$Y_N = \frac{9X}{2}^{1/3} \sim \frac{9T}{2}^{1/3}. \tag{4.32}$$

The maximum extent in the cross slope direction was found to occur up slope of the injection point (Vella & Huppert, 2006).

4.3.4 Benchmarking Numerical Schemes

While analytical models are useful for understanding the different flow regimes gravity currents may experience in simple cases, a numerical model is required when more complex situations are explored. The numerical model implemented for the two-dimensional gravity current case is a Crank-Nicholson finite difference scheme centred in time and space. A predictor corrector scheme is used to evaluate the non-linear diffusive buoyancy (Press, 2007).

This model incorporates an adaptive time step that is designed to increase stability when required and decrease the total calculation time. The time step can either increase or decrease based on the accuracy of comparing two half time steps to one full time step. The numerical model also incorporates an adaptive grid spacing for the benchmarking case. This spacing is initiated at a very small value, increasing the accuracy of the model at early times when the current is small. When the extent of the gravity current is 90% the length of the grid, the grid spacing is doubled and the gravity current is mapped back onto the first half of the grid. These additions to the basic numerical model reduce the computational time required to propagate the current to late times without losing accuracy at early times. This approach enables all relevant time and length scales to be investigated in appropriate detail.

To further improve the numerical model in regions susceptible to numerical instability, such as sharp changes in topographic gradient, a three-point differencing scheme is implemented, known as the Il'in scheme (Il'in, 1969; Clauser & Kiesner, 1987). This scheme calculates the amount of 'upwinding' required to keep the model stable at high Peclet numbers, where the

Peclet number is the ratio of advection over diffusion. At high positive or negative Peclet numbers the advective term becomes strongly upwind or downwind, while for low Peclet numbers the scheme reverts to the usual space-centred Crank-Nicholson scheme (Appendix B).

For a two-dimensional gravity current flowing in the positive x-direction, where injection occurs at the edge of the numerical grid, the expected relationships are given by (4.19a) and (4.19b) for early times and (4.24) and (4.23) at late times. Figure 4.6 shows the numerical simulation of this scenario. At early times, the current does not feel the effects of topographic gradients and spreads diffusively away from the injection point (Figure 4.6a). At late times the effect of topographic gradients becomes dominant, and advection up the slope occurs at a rate proportional to the slope and time (Figure 4.6b). Figures 4.6c-d show the dimensionless extent of the nose of the current and the thickness with time. The numerical model clearly asymptotically approaches the analytical solution at both early and late times. From these simulations, it can be seen that the natural time scale, t_c, indicates the transition time between these two regimes, while the natural thickness scale h_c gives the maximum current thickness.

To calculate the propagation of the current in three dimensions, an alternating direction implicit (ADI) scheme was added to the model described above (Peaceman & Rachford, 1955; Press, 2007). This method advances the numerical simulation by a half time step in the x-direction, and then by a half time step in the y-direction, thus advancing the simulation by a whole time step after one iteration. Additional details of this scheme and the relevant discretisation are given in Appendix B.

Figure 4.7 shows two snapshots of the flow, one during the early diffusive spreading regime, one in the advective spreading up slope regime. Figure 4.8 shows the development of the nose of the current in the up-slope direction (red) and cross-slope direction (green). At early times, it can be seen that the current follows the analytical solution found by Lyle *et al.* (2005) in both up- and cross-slope directions (Figure 4.8). At late times, the up-slope flow

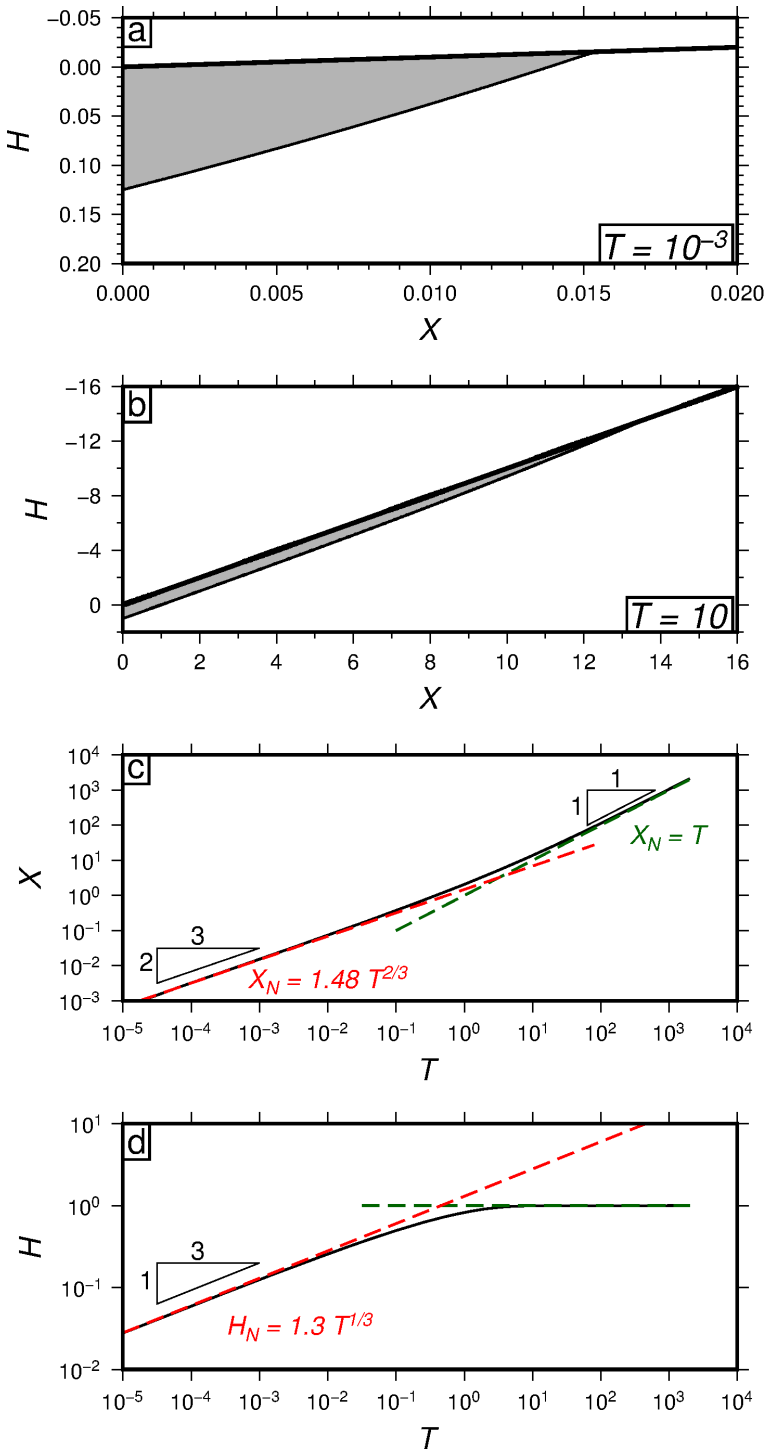

Figure 4.6: 2D gravity current on a slope of gradient $\alpha = 0.1$**. (a)** Early time ($T = 10^{-3}$) shape of gravity current. **(b)** Late time ($T = 10$) behaviour of gravity current. **(c)** Dimensionless extent of nose vs time of gravity current. **(d)** Dimensionless thickness vs time of nose of gravity current. Early and late time regimes from analytical solutions shown in red and green, respectively. Numerical solutions show good agreement.

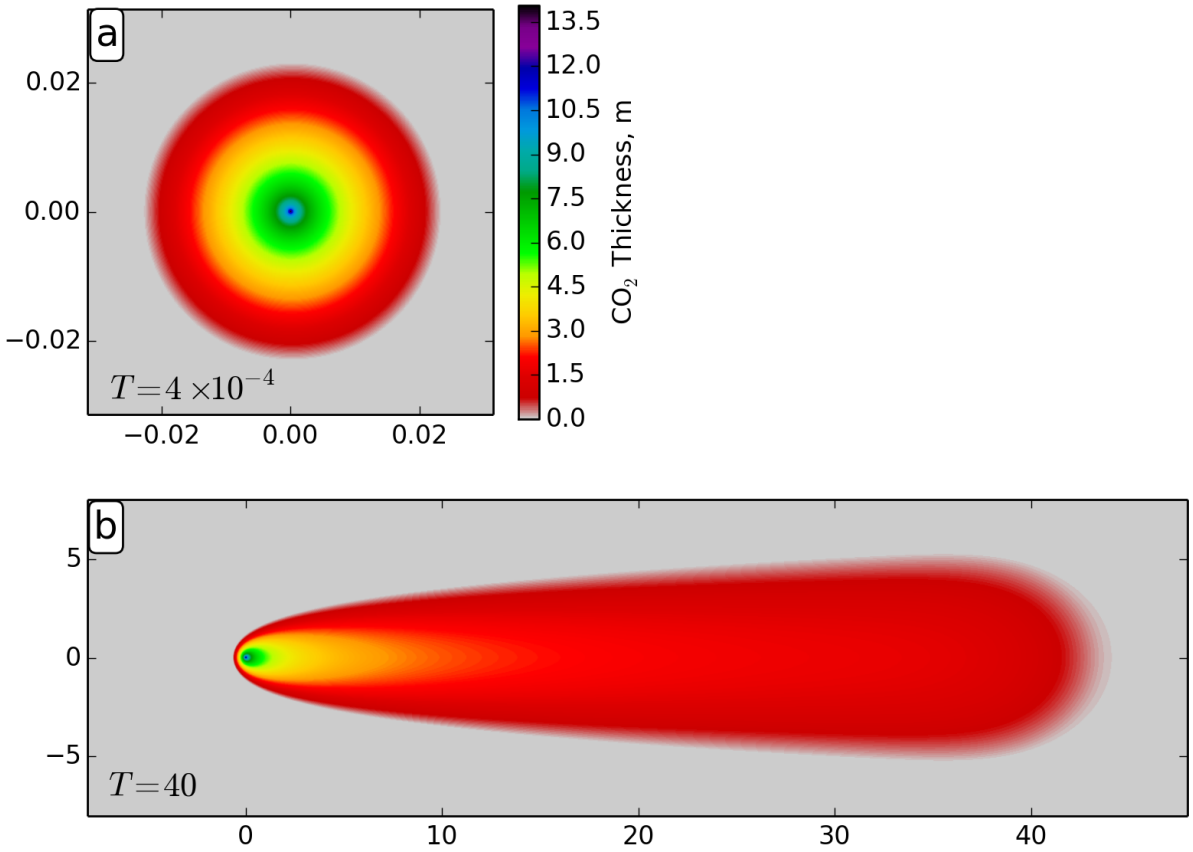

Figure 4.7: Thickness of gravity current on a constant slope. **(a)** Dimensionless time, $T = 4 \times 10^{-4}$, **(b)** dimensionless time, $T = 40$. Axes are given in dimensionless distance.

transitions to being proportional to time, while the cross-slope flow follows the analytical solution found by Vella & Huppert (2006). The maximum cross-slope extent occurs far from the injection point, near the maximum up-slope extent. It can be seen that the natural time scale, t_c, gives the transition time for both cross-slope and up-slope flow.

4.4 Forward Modelling of CO_2

Having benchmarked the numerical code against analytical solutions for a gravity current on a slope in three dimensions, this flow simulator can now be applied to modelling the flow of CO_2 in Layer 9. The governing equation for the flow of CO_2 in this simulation is given by

$$\frac{\partial h}{\partial t} = \nabla_H \cdot (u_{b\phi} h \nabla_H h - u_{b\phi} h \nabla_H d)\,, \tag{4.33}$$

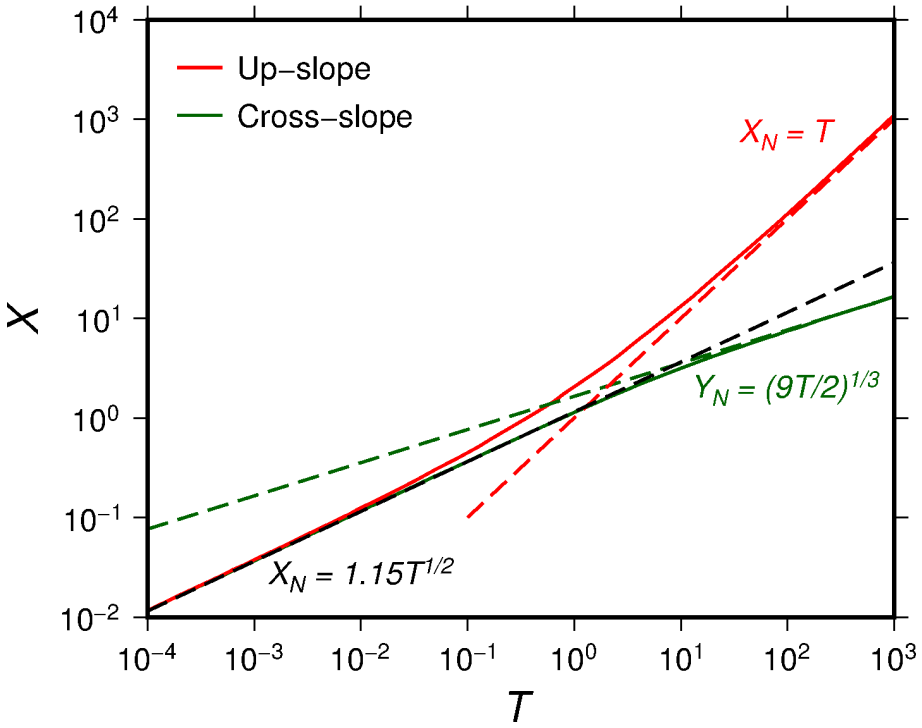

Figure 4.8: Up-slope and cross-slope extent of a porous gravity current on a constant slope. Solid lines show numerical solution. Dashed lines show asymptotic solutions at early and long time scales. Red = up-slope extent of nose of the current. Green = cross-slope extent of nose of the current. Black = early time asymptote in up and cross-slope directions.

which is equivalent to (4.25) divided by the porosity, and hence the buoyancy velocity, $u_{b\phi}$ is redefined as

$$u_{b\phi} = \frac{\Delta\rho g k}{\phi\mu}. \tag{4.34}$$

Dividing by the porosity means that $u_{b\phi}$ represents the fluid and reservoir properties in a single term. In this formulation, h is directly comparable to the observed thicknesses of CO_2 saturated sandstone calculated in Chapter 3. For application to an actual reservoir setting, the model requires four main inputs: an estimate of the geometry of the impermeable boundary that the carbon dioxide is spreading along, $d(x, y)$; the reservoir and fluid properties (i.e. permeability, porosity, fluid density and viscosity) that are used to calculate the buoyancy velocity, $u_{b\phi}$; the volume flux of CO_2 into the reservoir divided by the porosity, $V(t)/\phi$; and the location at which CO_2 is input into the layer. A summary of these variables and their attendant uncertainties is discussed below.

4.4.1 Reservoir Geometry

The reservoir geometry is extracted from the seismic survey by picking the top Utsira Formation reflection on the 1994 baseline survey. For the numerical simulations presented here, the 2008 processing of the baseline survey is chosen as it covers the largest region, thus providing the greatest scope for investigating flow in this layer. During processing, the seismic data is binned into 12.5 m $\times$ 12.5 m blocks, limiting the smallest scale topographic features visible using this data. The inability to resolve very small scale topographic features may cause discrepancies between observed and simulated CO_2 plumes. However, simulations run using 12.5 m $\times$ 12.5 m and 25 m $\times$ 25 m grid squares show only minor differences, indicating that increasing horizontal resolution does not significantly improve the simulation results. Differencing two-way travel time maps of the top Utsira Formation reflection picked from different seismic surveys shows that noise in this topography estimate is of order $\pm$ 1 m. A median filter is applied to the data in 50 m blocks to remove some of the smallest wavelength noise and the surface is then interpolated using a continuous curvature spline in tension with a low tension factor to create a smoothed estimate topography (Smith & Wessel, 1990). Smoothing also has the benefit of removing unphysical sharp gradients introduced by the noise that could cause the numerical flow simulation to become unstable. Conversion between two-way travel time and depth is discussed in Section 2.4.

4.4.2 Estimating Buoyancy Velocity

The buoyancy velocity given by (4.34) represents the velocity at which a fluid would rise under buoyancy through a porous medium. This term controls the velocity at which the CO_2 diffuses and advects through porous media, yet there is some uncertainty involved with estimating each of the parameters included in this term. These uncertainties are discussed below.

Reservoir Properties

Permeability and porosity of the Utsira Formation have been measured in well core from a well ∼1000 m from the injection point. This formation is composed of unconsolidated sand grains with a bimodal grain size distribution, with peaks at 3 μm and 0.2 mm (Zweigel *et al.*, 2004). The porosity of the sand has been measured to be $\phi = 0.37 \pm 0.03$ in core samples, in agreement with estimates from wireline logs. Despite burial at depths of $\sim$ 800 m, this rock is unconsolidated and the sand grains only exhibit minor indications of compaction.

The permeability of the Utsira Formation was measured to be $k = 2$–5 D (Lindeberg *et al.*, 2001; Zweigel *et al.*, 2004). Well tests from the nearby Grane and Oseberg areas found the permeability to be 1–8 D (Zweigel *et al.*, 2004). These authors suggest that the relatively low permeability for unconsolidated sand can be explained by the bimodal grain distribution, with smaller grains blocking the pore throats thereby reducing permeability. Core measurements of the Utsira Formation in the Sleipner area were taken from the main part of the Formation, rather than from the Sand Wedge containing Layer 9. Interpretation of gamma ray logs through the formation suggest that the Sand Wedge has a lower gamma ray signal to the rest of the reservoir and is therefore likely to have a lower mud content (Williams & Chadwick, 2017). Removing some of the smaller grains would have the effect of increasing the permeability. Experimental data on unconsolidated sand suggests that only a small increase in either the sorting of the grains or grain size can have a significant effect on the permeability of the porous medium (Beard & Weyl, 1973). Figure 4.9 shows that an increase in mean grain size of a few tenths of a millimetre can cause an order of magnitude change in permeability. It is therefore possible that this estimate for the permeability of the Sand Wedge is a lower bound.

Fluid Properties

Due to the proximity of CO_2 to its critical point in Layer 9, estimates of the density and viscosity of CO_2 in Layer 9 are very sensitive to estimates of the temperature within the aquifer. The density of CO_2 at the top of the reservoir has been estimated to be 675 ± 20 kg m^{-3}

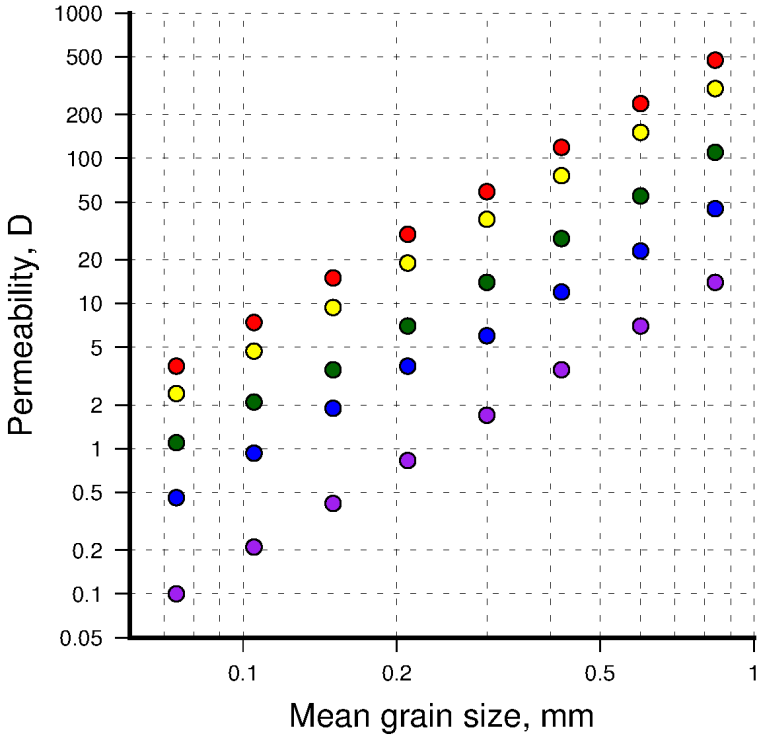

Figure 4.9: Permeability of unconsolidated sand against grain size for various degrees of sorting. Data from Beard & Weyl (1973). Red: very well sorted sand; Yellow: well sorted; Green: moderately well sorted; Blue: poorly sorted; Purple: very poorly sorted. See Beard & Weyl (1973) for definitions of sorting.

by modelling time-lapse micro-gravity measurements (Alnes *et al.*, 2011). Recent modelling of the entire reservoir using PFLOTRAN is in agreement with this estimate (Williams & Chadwick, 2017). At the pressures and temperatures thought to be present in the aquifer, the viscosity of CO_2 is $\mu_c = 5 \pm 1 \times 10^{-5}$ Pa s (Bickle *et al.*, 2007; Williams & Chadwick, 2017). Viscosity of the ambient brine is estimated to be $\mu_w = 7 \times 10^{-4}$ Pa s (Boait *et al.*, 2012). However, the viscosity of the ambient brine does not affect this calculation because the aquifer is considered to be unconfined, and therefore the forces required to displace the ambient brine are negligible.

Using these values, the buoyancy velocity is estimated to be $u_{b\phi} = 0.2 - 1.5 \times 10^{-3}$ ms^{-1} for permeability range of 1-8 D. Note that these estimates are for bulk reservoir properties.

4.4.3 Injection Point

The seismic chimneys described in Section 3.6.2 provide evidence of the vertical migration of CO_2 through the reservoir. The chimney identified in Figure 3.19 (SC1) is thought to be the major conduit for vertical CO_2 movement into both Layer 8 and Layer 9. This chimney is correlated with the first observed accumulation of CO_2 in these layers. The location of this chimney is therefore inferred to be the injection point for the CO_2 into the simulation. However, as can be seen on Figure 3.16, a small disconnected patch of CO_2 appears to the south of the major CO_2 layer in 2008. This outlying patch connects with the rest of the CO_2 layer by the time of the 2010 survey, but its presence indicates that there must be at least one other, considerably smaller, point of entry for CO_2 into Layer 9. However, due to its very small size, for the purposes of this simulation all CO_2 is considered to enter Layer 9 via the major central chimney.

4.4.4 Injection Rate

The volumetric flux into Layer 9 used in this simulation is taken from the volume calculations in Section 3.6.1. The data suggests that the volumetric injection rate is increasing with time, given by

$$q = \frac{d}{dx}\left(\frac{V(t)}{\phi}\right) = nC\left(t - t_0\right)^{n-1}, \tag{4.35}$$

where $C = 9500 \pm 5700$ m^3 yr^{-n}, $t_0 = 1998.1 \pm 0.5$ and $n = 2.1 \pm 0.2$. The error estimates on this injection rate come from the uncertainty in the thickness measurements and estimates in the velocity of seismic waves through CO_2 saturated sandstone (Section 3.5).

4.4.5 Modelling Results

Simulated CO_2 flow through Layer 9 is shown in Figure 4.10 and compared with the CO_2 distribution estimated in Section 3.5. In this simulation the permeability is uniform across the flow region, at a value of $k = 2$ D ($u_{b\phi} = 3.7 \times 10^{-4}$ ms^{-1}), as measured from nearby well cores (Zweigel *et al.*, 2004). While the shape of the plume agrees reasonably well with

the observed planform for the early time steps, clear discrepancies arise for later time steps. The southward extent of the plume is matched as well as can be expected in terms of both CO_2 thickness and area, without incorporating the extra input flux point to the south of the main plume. Encouragingly, the CO_2 layer has a relatively complex planform that is controlled by the topography of the caprock rather than by an increase in pressure caused by the input of CO_2 into this layer. However, the north running extension of the plume along the north-south striking topographic ridge does not flow quickly enough to reach the northern topographic dome in the time observed in the seismic images. This slow spreading rate has the added effect of causing the CO_2 to thicken up to over 12 m by 2010 close to the injection point, much thicker than the observed thickness.

These results suggest that this combination of input parameter estimates are not able to match the seismically observed distribution of CO_2. In the following sections, uncertainties in the caprock topography and the permeability are explored in order to improve the fit between the observed and modelled plume.

4.5 Topographic Uncertainty

Uncertainties in the stacking velocities reported by Chadwick *et al.* (2016) might be responsible for local discrepancies between observed and calculated CO_2 thickness. However, for the topography to be solely responsible for the observed misfit, a systematic steepening of the gradients in the caprock is required. Discrepancies of around ± 20 ms^{-1} have been measured in the average velocity to the top of the Utsira Formation in wells spaced several kilometres apart (Chadwick & Noy, 2010). These discrepancies could lead to differences in the depth to the top of the Utsira Formation of ≈ 10 m between wells that are unaccounted for by assuming a constant overburden velocity to calculate topography. The results of the base case, uniform permeability model suggest that one way to match the observed plume would be to increase the gradient of the caprock from north to south, increasing the size of the advective flux in that direction (Figure 4.10). To test this theory, a series of flow models were conducted with increased gradients towards the north of the modelled regions

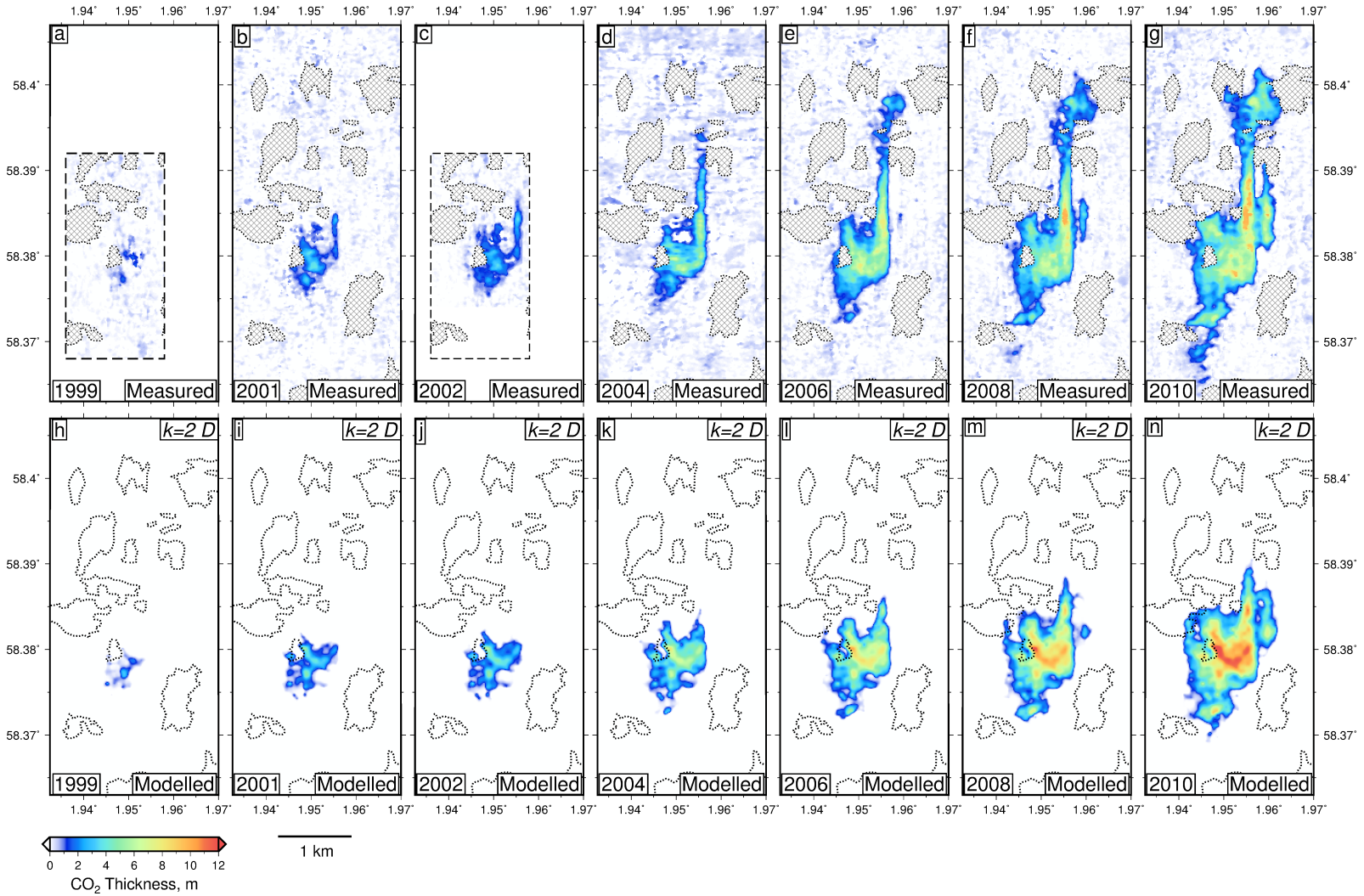

Figure 4.10: Measured and modelled CO_2 distribution in Layer 9 with $k = 2$ D. (a)-(g) Measured CO_2 thickness from Chapter 3. **(h)-(n)** Modelled distribution of CO_2 with $k = 2$ D. Hatched polygons = regions where reflections are incoherent due to natural gas pockets in the overburden.

and $k = 5$ D ($u_{b\phi} = 9 \times 10^{-4}$ ms^{-1}). A reasonable match to the northward migration rate of the CO_2 was obtained when an artificial gradient of 50 m across the modelled region was included (Figure 4.11). This value is considerably greater than thought likely given the relatively small uncertainties in the seismic wave velocity of the overburden. A side effect of this increased gradient is that the model no longer matches the southward migration of the plume. These tests suggest that changing the topography alone cannot be responsible for the poor match between observed and modelled CO_2 migration.

4.6 Inversion for Permeability Structure

Mismatches between observed and simulated CO_2 distributions suggests that the base-case uniform permeability reservoir model is not representative of the reservoir and fluid properties found in the Sand Wedge. To test this proposal, the reservoir simulation is inverted to find the permeability structure that produces the best match to the observed CO_2 distribution. Initially, a parameter sweep is performed to find the best-fitting global permeability. Due to the possibility that estimates of viscosity and density of the CO_2 will change as estimates of the temperature and pressure in Layer 9 are updated, the results of these inversions are also given for $u_{b\phi}$.

4.6.1 Inversion for homogeneous reservoir permeability

A parameter sweep is performed to find the best-fitting permeability for the region. The simulated distribution of CO_2 is compared to the observed distribution using a misfit function

$$M = \frac{1}{N_s} \sum_{j=1999}^{N_s} \left[\frac{1}{N} \sum_{i=1}^{N} \left(\frac{h_{ij}^s - h_{ij}^o}{\sigma_{ij}^o} \right)^2 \right]^{1/2}, \tag{4.36}$$

where i refers to a particular data point, N is the number of data points in each survey over 0.5 m thick, j refers to a particular seismic reflection survey in order from 1999 to 2010, N_s is the number of seismic reflection surveys, h^s is the simulated thickness of the CO_2 layer, h^o is the observed distribution of CO_2 from the seismic images, and σ^o is the uncertainty in

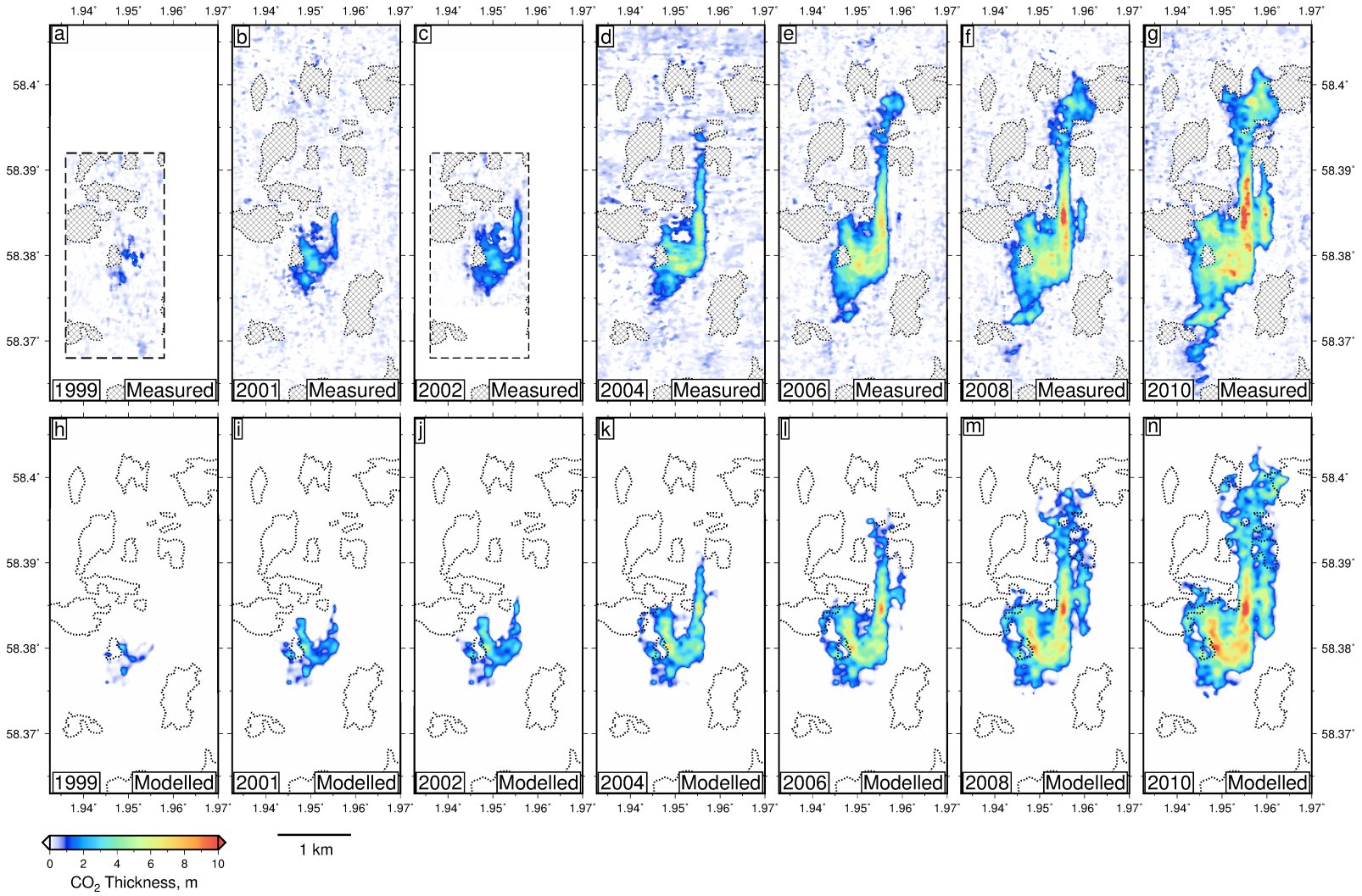

Figure 4.11: Measured and modelled CO_2 distribution in Layer 9 with tilted caprock. **(a)-(g)** Measured CO_2 thickness from Chapter 3. **(h)-(n)** Modelled distribution of CO_2 using $k = 5$ D and a tilt of 50 m across the modelled region. Hatched polygons = regions where reflections are incoherent due to natural gas pockets in the overburden.

the observed thickness (see Section 3.5.1). The threshold of 0.5 m is chosen based on the uncertainty in measuring the thickness of thin layers using the method described in Chapter 3 (Figure 3.8c).

The best-fitting uniform permeability was found to be $k = 5$ D ($u_{b\phi} = 9 \times 10^{-4}$ ms^{-1}; black arrow, Figure 4.12). The results of this simulation are similar to the 2 D simulation, suggesting that the permeability required to match the northward migration must be greater than that estimated from the well cores (Figure 4.10 & 4.13a-g). The southward migration rate is still matched reasonably well with this permeability estimate.

Figure 4.12 suggests that a low misfit can also be found for models in a range between 3–14 D. To investigate whether a higher uniform permeability can reproduce the rapid migration rate along the north striking ridge, a model with a uniform permeability of 12 D is tested ($u_{b\phi} = 2.2 \times 10^{-3}$ ms^{-1}; dashed arrow, Figure 4.12). As suggested in Section 4.4.2, this increase in the permeability of the reservoir rock is possible if the mean grain size is slightly larger than estimated from the well core (Figure 4.9). Given that the permeability was estimated from a sample taken from lower in the reservoir than the Sand Wedge, and that the Sand Wedge is thought to contain less small particulates, this increase in permeability estimate is reasonable.

The results of this simulation are shown in Figure 4.13h-n. This simulation matches the rate of northwards CO_2 migration observed in the seismic images. Minor differences between the shape of the modelled and observed CO_2 plume at the northern extent are probably due to local uncertainties in caprock topography. Around the northern dome of the reservoir, the gradients in topography are very shallow and so small uncertainties could cause discrepancies between the observed and calculated CO_2 distribution. However, at the southern limit of the plume there is significant misfit between the observed and modelled results. This discrepancy is interpreted to be a result of the high permeability permitting all CO_2 entering the reservoir to flow up-slope away from the migration point. This model shows that, while a homogeneous, high permeability can permit the desired spreading rate to the north, the

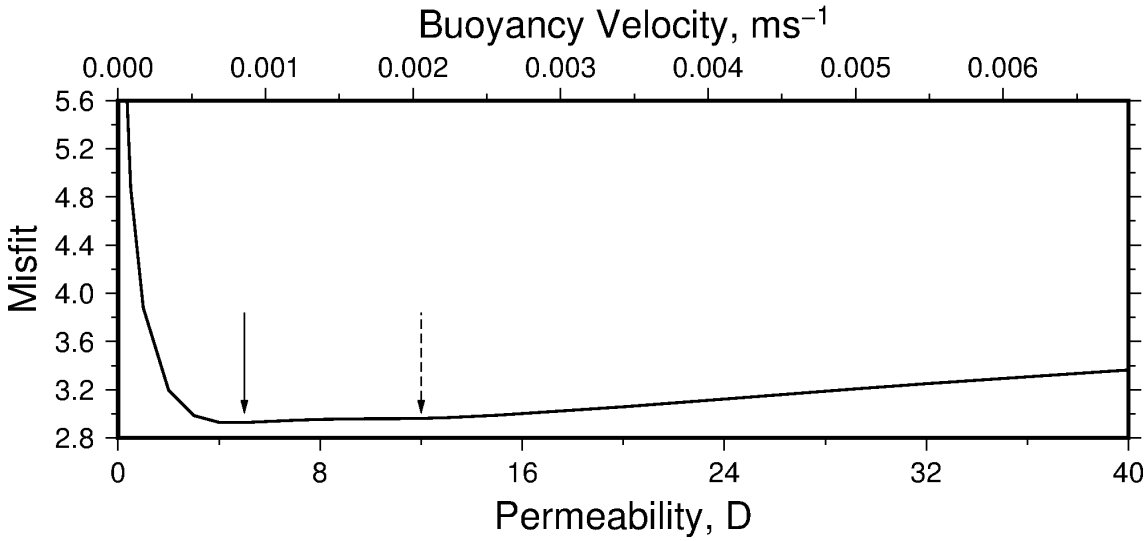

Figure 4.12: Misfit for uniform permeability simulations. Black arrow shows minimum misfit permeability. Dashed arrow shows secondary misfit low for higher permeability.

southward extent requires a lower permeability to pond some of the CO_2 around the input point.

These discrepancies between observed and calculated CO_2 distribution suggest that a homogeneous permeability may not be adequate to capture the observed CO_2 distribution and that a more complex permeability structure is required. The next section explores evidence for the existence of reservoir heterogeneity.

4.6.2 Large-scale Reservoir Heterogeneity

To investigate possible permeability heterogeneity in the Sand Wedge, spectral decomposition was performed on the top Utsira Formation reflection on the 1994 baseline survey. Spectral decomposition separates the reflected signal into its constituent frequencies, permitting the amplitude of the reflection at specific wavelengths to be analysed (Partyka *et al.*, 1999). Changes in amplitude are indicative of either constructive or destructive interference of the reflected wavelets. Constructive interference will occur at different bed thicknesses for different frequencies. By looking at the changing spectral response for three different

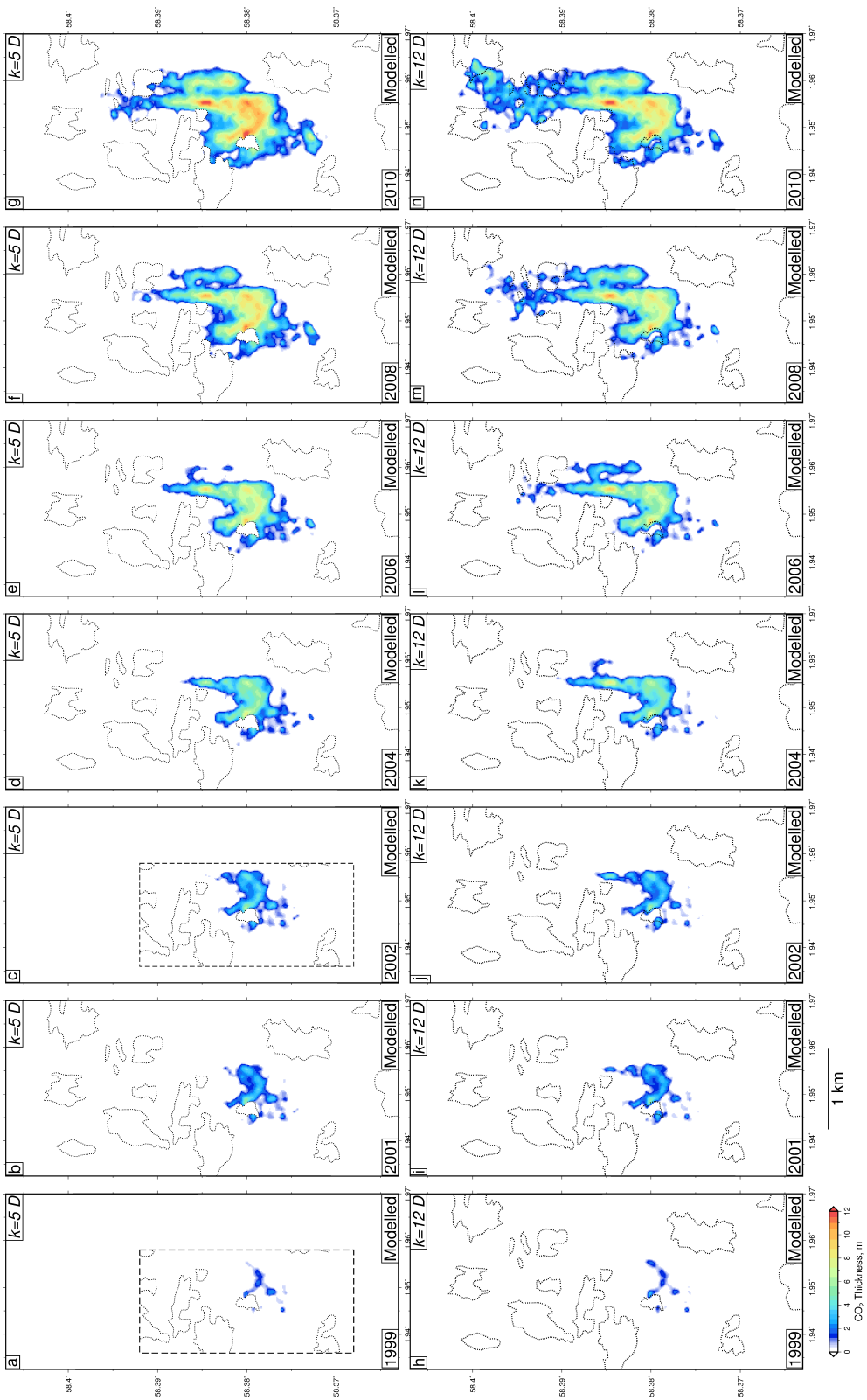

Figure 4.13: Modelled CO_2 distribution in Layer 9 for $k = 5$ D and $k = 12$ D. (a)-(g) Best-fitting modelled distribution of CO_2 using single buoyancy velocity model found by parameter sweep, with $k = 5$ D. **(h)-(n)** Modelled distribution of CO_2 with $k = 12$ D. Hatched polygons = regions where reflections are incoherent due to natural gas pockets in the overburden. Polygons = regions where reflections are incoherent due to natural gas pockets in the overburden for comparison with Figure 4.10a-g

frequency bands and overlaying the results, subtle changes in bed thickness, and therefore depositional environment, may be identified. Spectral decomposition is often used to identify channel structures and interpret other sub-resolution features.

Spectral decomposition was performed using OpendTect's wavelet coefficient attribute calculator. To calculate the wavelet coefficient, a continuous wavelet transform is performed on the top Utsira Formation reflection. A Mexican Hat wavelet is translated along the signal, and the correlation of the wavelet with the signal is calculated at each point. The correlation coefficient is termed the wavelet coefficient. The wavelet coefficient is calculated for three different central frequencies of the wavelet and can then be plotted as a blended red-green-blue image to highlight different frequency responses across the reservoir. The top Utsira Formation reflection was picked on the pre-injection survey so that changes in spectral response are not masked by the presence of CO_2.

Figure 4.14a,c show the topography of the top Utsira Formation and the blended rgb image showing the wavelet coefficient for 16 Hz (red), 28 Hz (green) and 56 Hz (blue). Panel b shows the thickness of the Sand Wedge. A linear north-south running feature that curves towards the east in the south of the region is evident on all three images. This feature has been previously interpreted as a submarine channel that cuts through the region. Channels have been observed throughout the Utsira Formation (Gregersen, 1998; Zweigel *et al.*, 2004). This feature is of a similar size, scale and sinuosity to observations of other low sinuosity submarine channels studied in the literature (Clark & Pickering, 1996). Sediments deposited in channel environments may be comprise coarser grained, higher porosity material than sediments deposited on the levees. Changes in grain size and sorting can have a significant effect on the permeability of these channel sands (Figure 4.9). Whether the channel observed in Layer 9 could have different reservoir properties is examined in the next section.

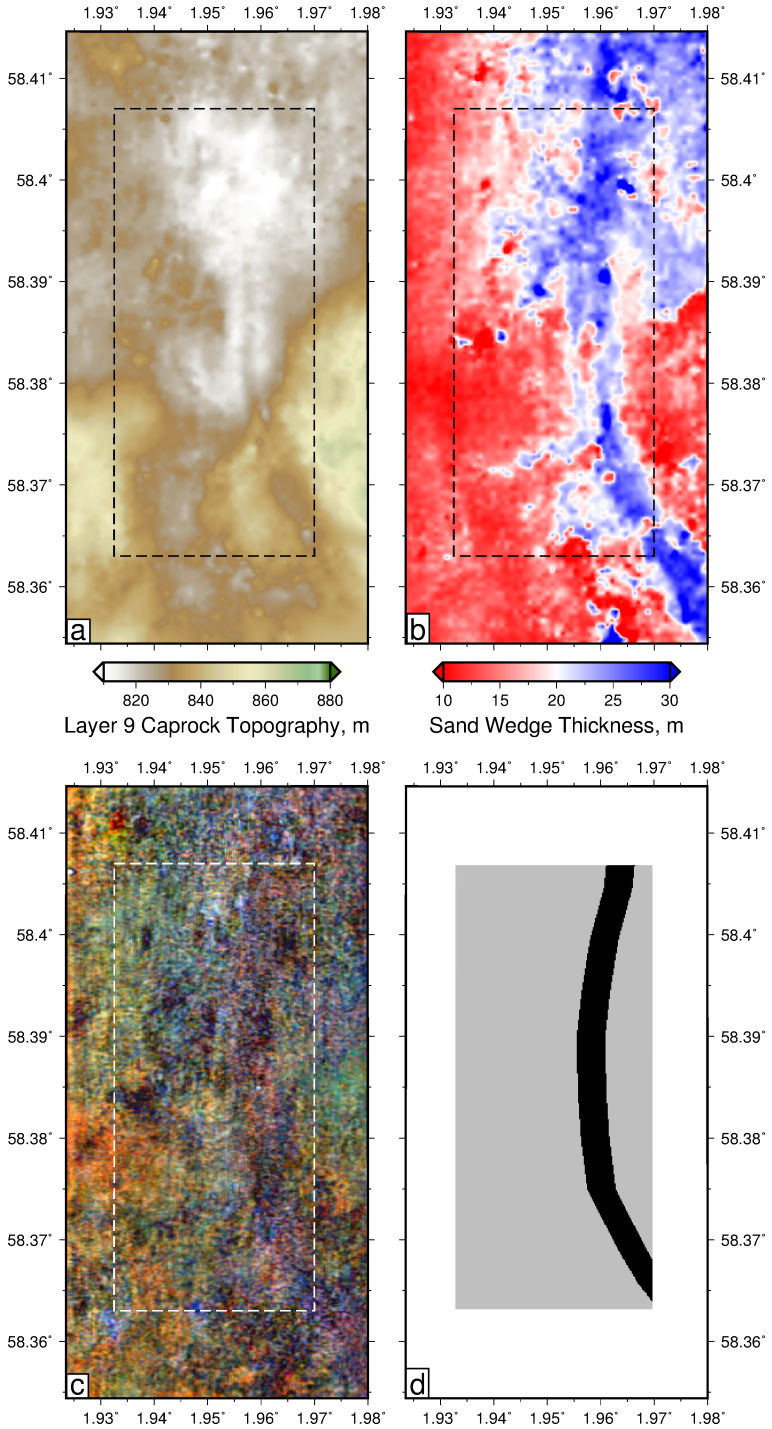

Figure 4.14: Evidence for channel in Sand Wedge. **(a)** Topography of top Utsira Formation in m. **(b)** Sand Wedge thickness in metres. **(c)** Blended rgb image showing wavelet coefficient for three different frequencies: 16 Hz (red), 28 Hz (green) and 56 Hz (blue). **(d))** Example model showing parameters k_1 (light grey), k_2 (black) and width, w (width of k_2 in x-direction).

4.6.3 Inversion for Reservoir Permeability Structure

If the linear feature identified in the previous section is indeed a submarine channel deposit that cuts through the area, it is plausible that different depositional environments will have led to different reservoir properties. To investigate this possibility, two inversion schemes that can recover the permeability of the region are proposed. First, a simple model that divides the region into two parts (the channel and the bulk reservoir) and allows the width of the channel and the permeability in the channel and bulk reservoir to vary independently. Secondly, due to the low computational expense of the forward model, it is feasible to invert for the permeability at a relatively significant number of nodes spread across the flow region. Synthetic flow modelling is used to determine the appropriate inversion procedure.

Synthetic Inversion

To ascertain whether a complex permeability structure can be recovered from inverse modelling schemes of CO_2 flow, a synthetic region is designed with a meandering high permeability channel in a topographic high (Figure 4.15 a-b). A baseline simulation with a constant input flux is performed as a forward model and the thickness of the resultant current is captured at six time steps (the final time step is shown in Figure 4.15c). Two inversion schemes are then tested. The first is a simple three parameter grid search finding a best-fitting bulk reservoir permeability, k_1, channel permeability, u_2, and the width of a simple straight channel, w (Figure 4.15d). The second inversion scheme involves inverting the permeability at a number of nodes spread across the region using Powell's minimisation algorithm, and interpolating between them (Figure 4.16d; Press, 2007). In these inversions it is assumed that the topography of the caprock is known.

Figure 4.15d shows the model set-up for the first inversion, and a grid search is used to test each combination of parameters. Misfit between the synthetic baseline and the test flow simulations is calculated using a similar expression to (4.36). Figure 4.17 shows that k_1 is very well constrained in this synthetic inversion. The width of the high permeability region is recovered reasonably well given the different geometries being matched. The recovered

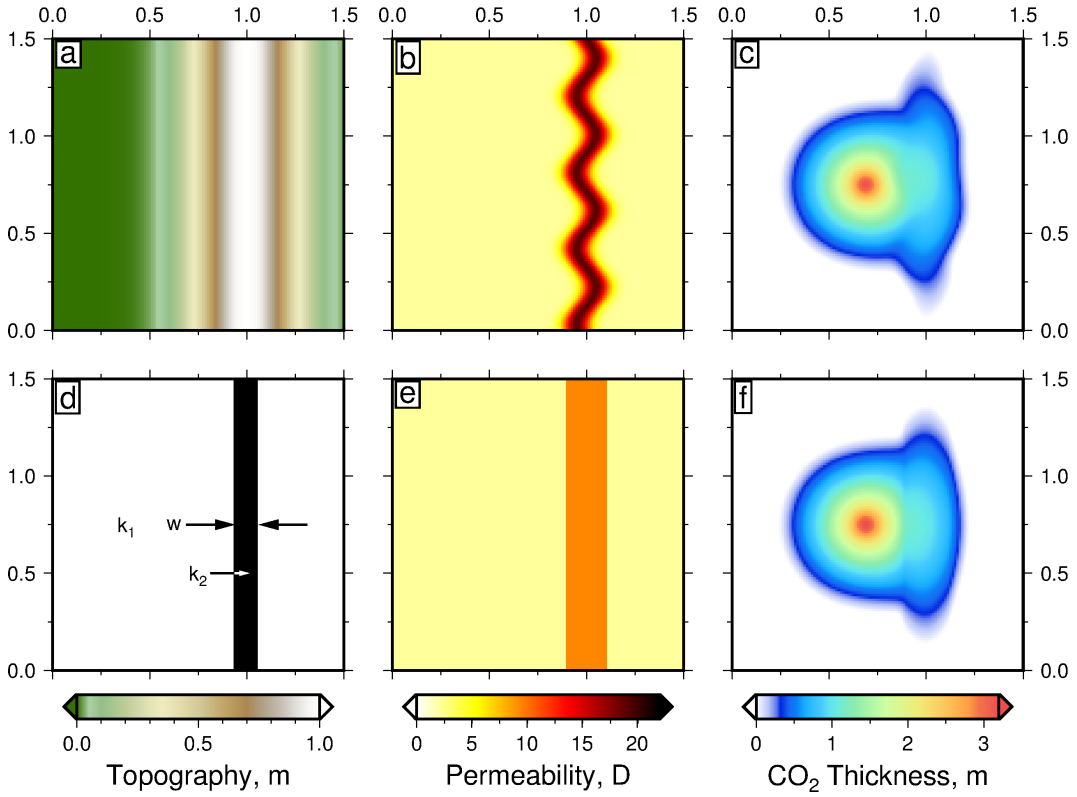

Figure 4.15: Synthetic flow model and best fit from inversion for permeability in a simple channel. **(a)** Topography of synthetic environment. **(b)** Synthetic permeability model. **(c)** Fluid thickness in synthetic model. **(d)** Parameters used in grid search. **(e)** Minimum misfit permeability model. **(f)** Fluid thickness from inversion.

value of k_2 is significantly lower than the maximum value in the channel, but approximates the median permeability of the channel. The shallower misfit wells for k_2 and w suggest that these values are less well constrained and that there is some trade off between k_2 and w (Figure 4.17e-f). The best-fitting reservoir model is shown in Figure 4.15e and the final time step for this model is shown in Figure 4.15f. The differences between Figure 4.15c and f are relatively minor, suggesting that this simplified model can replicate the CO_2 distribution of the baseline case well.

Figure 4.18 shows how these different permeability models can still result in flows with similar planforms. Streamlines were calculated from the two dimensional flux vector field using the streamplot function in Matplotlib. Figure 4.18a show the CO_2 flowing down the meanders of the high permeability channel, and therefore flowing further but at a higher velocity than for the straight channel model.

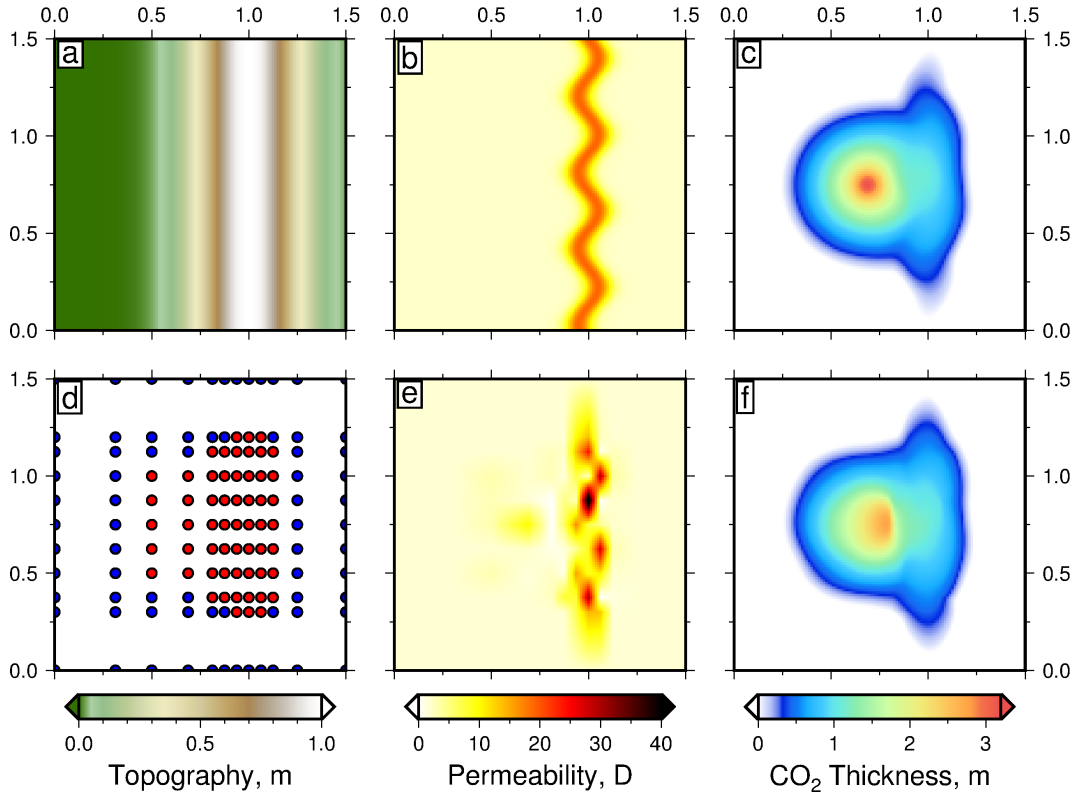

Figure 4.16: Synthetic flow model and best fit from inversion for permeability using 58 nodes spread across flow region. **(a)** Topography of synthetic environment. **(b)** Synthetic permeability model. **(c)** Thickness of fluid in synthetic model. **(d)** Location of nodes used in inversion. Red nodes can vary, blue nodes are fixed at a set value. **(e)** Minimum misfit permeability model. **(f)** Fluid thickness from inversion.

For the second inversion, the same baseline synthetic model was used (Figure 4.16a-b). 58 nodes were distributed across the flow region (red nodes, Figure 4.16d). These nodes were initiated with a uniform value for the permeability close to background permeability from the synthetic model. The permeability between the nodes was linearly interpolated. The permeability at each of these nodes was then inverted for using Powell's minimisation algorithm (Powell, 1964; Press, 2007). This minimisation scheme is suitable for this inversion as it does not require gradients in misfit space to be calculated. It is also superior to other minimisation algorithms because it can adjust the vectors it minimises along in parameter space, reducing the number of iterations required for convergence.

The optimal reservoir model found by this routine is shown in Figure 4.16e. This inversion

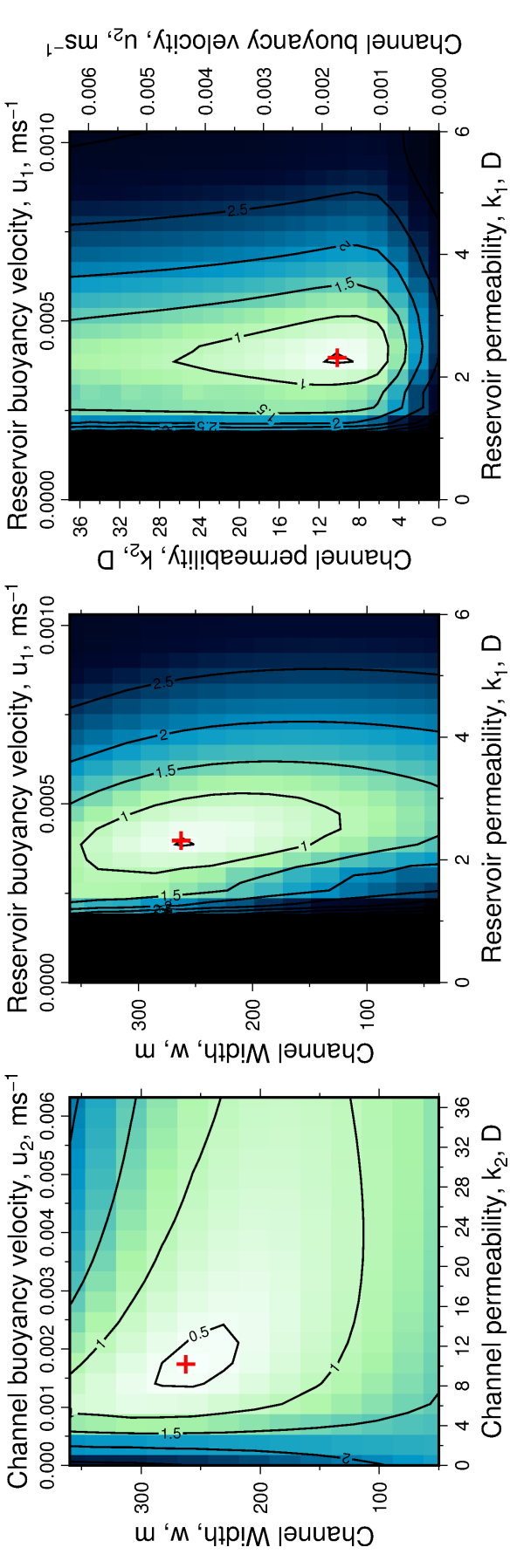

Figure 4.17: Parameter sweep for synthetic reservoir permeability. k_1 = permeability of the surrounding region, k_2 = permeability within a channel, w = width of channel, for a synthetic flow model. **(a)-(c)** Slices through misfit space showing the global minimum (red cross) and the trade-offs between k_1, k_2, and w.

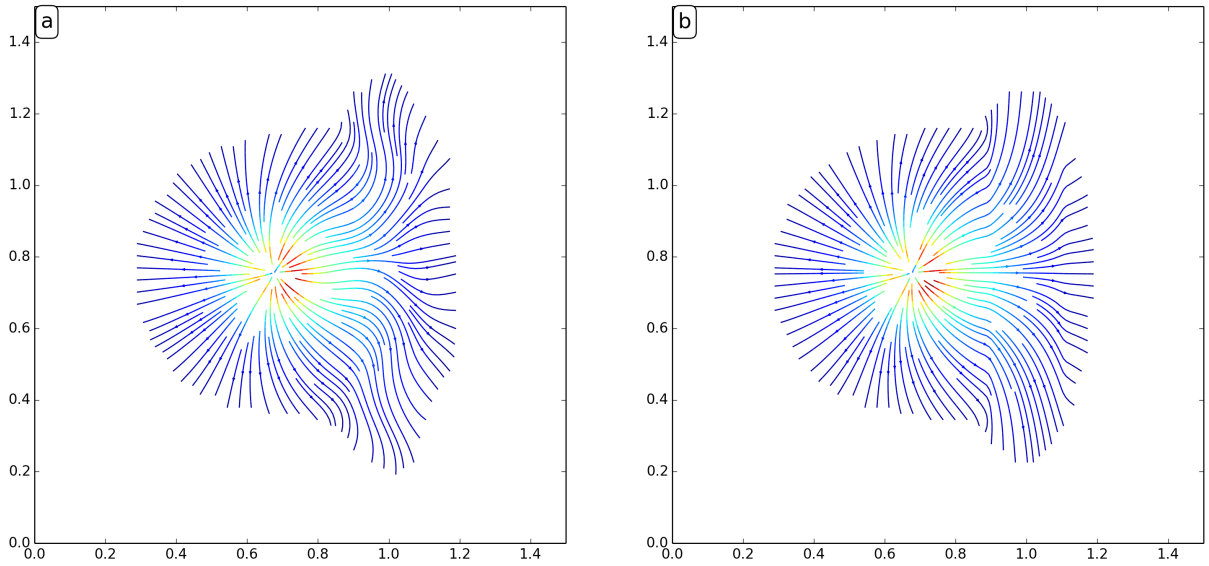

Figure 4.18: Streamlines showing flux direction and relative magnitude of flow. Streams lines for **(a)** synthetic meandering channel and **(b)** best-fitting straight channel model. Colour indicates relative magnitude of flux through the region.

shows that it is possible to capture some of the features of the meandering channel, such as the general shape of the meanders and the width of the high permeability region. However, the values for permeability found using the inversion are spread over many orders of magnitude, with the permeability at neighbouring nodes trading off against each other. While this inversion is potentially more informative than the grid search, it also has the potential to be misleading due its susceptibility to spatial aliasing. Without knowledge of the synthetic model, it would be easy to over-interpret the results. Figure 4.16f shows the final time step of the best-fitting model. The planform of the CO_2 layer is improved over the simple three parameter grid search, but the match around the injection point is poor.

Following this analysis, and taking into account the additional computational expense involved with running such a detailed inversion, the grid search was chosen to invert for the permeability of the reservoir, and the permeability and width of a simple channel in the aquifer of Layer 9.

Inversion for Dual Permeability

A grid search involving several thousand flow simulations was performed to find the best-fitting parameters for the reservoir model described by Figure 4.14d. Figure 4.19 shows the misfit space for a reservoir model where the channel is centred in the middle of the anomaly identified by spectral decomposition. A global minimum is found with $k_1 = 3 \pm 1$ D ($u_1 = 5.6 \pm 1.9 \times 10^{-4}$ ms^{-1}), $k_2 = 26 \pm 8$ D ($u_2 = 4.8 \pm 1.5 \times 10^{-3}$ ms^{-1}) and $w = 675 \pm 125$ m. The nature of the misfit function makes calculating formal uncertainties challenging. The quoted uncertainties here are estimated from the contour through misfit-space that shows a 1 % increase above the minimum misfit. These uncertainties clearly show that the reservoir permeability is tightly constrained, and there is no trade-off with the other parameters in this model. The value of k_1 constrained by this inversion is very similar to that estimated from the core material (Zweigel *et al.*, 2004). The values for channel permeability and channel width are less tightly constrained and exhibit a small trade-off. The value for k_2 is much higher than the maximum value that most previous models have tested for, and may explain why previous models have not been able to match the observed CO_2 planform.

A permeability contrast of one order of magnitude is reasonable in this channel environment if the channel deposits are coarser grained than the surrounding sediments (Figure 4.9; Beard & Weyl, 1973; Clark & Pickering, 1996). Estimates of grain size taken from nearby well cores suggest that the sand in the Utsira Formation has peaks at 3 μm and 0.2 mm (Zweigel *et al.*, 2004). These authors suggest that the relatively low permeability measured in the Utsira Formation of 2 D is due to the presence of this fine grained material. Faster fluid flow speeds within the channel will allow these fluids to carry larger sand grains. If the channel sands are dominated by the coarser material, then it is entirely plausible that the permeability is an order of magnitude higher.

The results of this best-fitting model are shown in Figure 4.20. The combination of low permeability near the injection region with a high permeability channel also provides the required reservoir properties to produce a good match to both southward and northward migration of the plume.

The region in which the fit to the observed data is poorest is in the east, where migration of CO_2 into the eastern side of the north running ridge occurs much earlier than observed on the seismic reflection surveys. One possible explanation is that a low permeability region exists between two distinct, parallel channels, which would reduce the flux into the eastern channel. An alternative and more likely suggestion for this early eastward migration is that the smoothing applied to the topography to remove noise has reduced the spill-point depth in this region.

The results of the flow simulation show that vertical equilibrium models can be used in combination with seismic analysis to create reservoir models that enable a low misfit between the observed and calculated CO_2 in Layer 9. The success of this application indicates that the flow of CO_2 within Layer 9 can be adequately described without the need to model pressure gradients in the ambient fluid. In this model, the flow is dominated by a combination of buoyancy-driven slumping and advection up slopes. However, further work is required before the influence of pressure gradients in the ambient fluid can be fully ascertained. Inverse modelling has also shed light on the properties of the reservoir Layer 9 resides in, and can be used alongside traditional reservoir characterisation techniques to forecast the flow of CO_2 at future CCS sites. This work has also shown that a good match to the observed data can be found with a simple inversion that does not require significant changes to the topography of the caprock.

4.7 CO_2 Flux Through Layer 9

The flux of CO_2 through the reservoir can also be calculated from the reservoir simulator. Figure 4.22 shows stream lines indicating the path taken by the CO_2 as it flows away from the input point. Streamlines were calculated from the two-dimensional flux vector field using Matplotlib's streamplot function. It can be seen that the regions of highest flux are along the northward running channel. Nearly all of the streamlines are focussed into the channel, indicating that the majority of the CO_2 entering Layer 9 will eventually migrate towards the northern topographic dome. The high permeability within the channel suggests that,

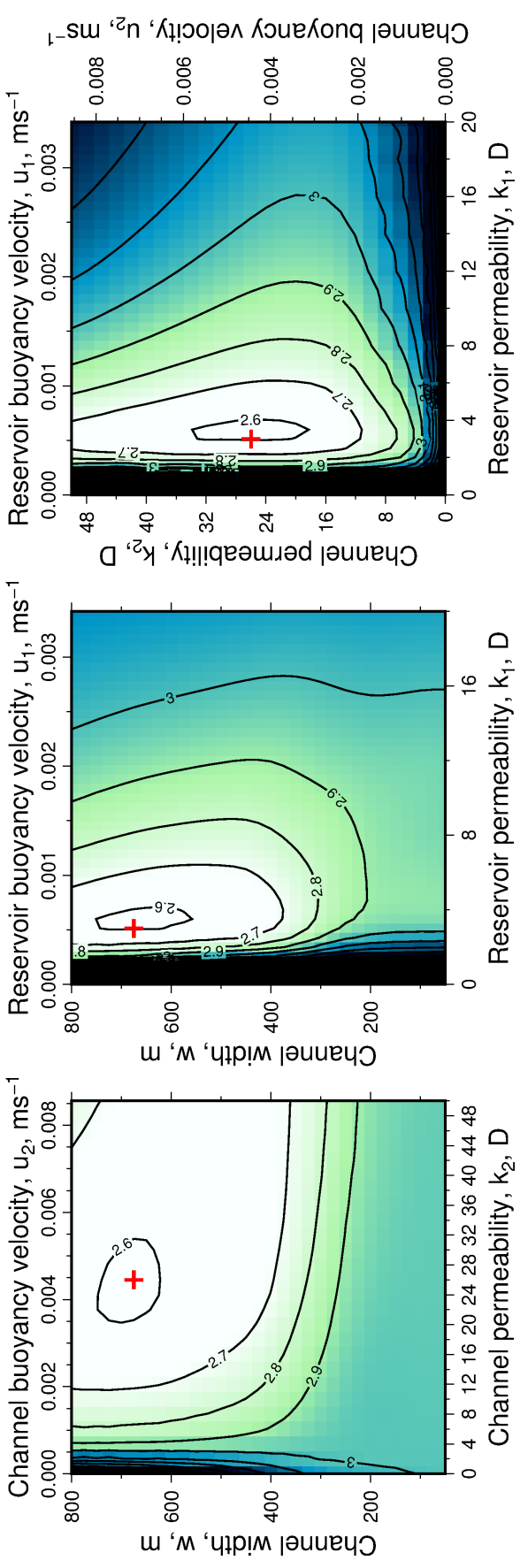

Figure 4.19: Parameter sweep for channel permeability model. Parameters are channel permeability, k_2, width of the channel, w, and permeability of the surrounding region, k_1, with the channel centred in the middle of the anomaly picked out by spectral decomposition. **(a)-(c)** Slices through misfit space showing the global minimum (red cross) and the trade-offs between k_1, k_2, and w. Minimum at $k_1 = 3$ D, $k_2 = 26$ D and $w = 675$ m ($u_1 = 5.6 \times 10^{-4}$ ms^{-1}, $u_2 = 4.8 \times 10^{-3}$ ms^{-1}).

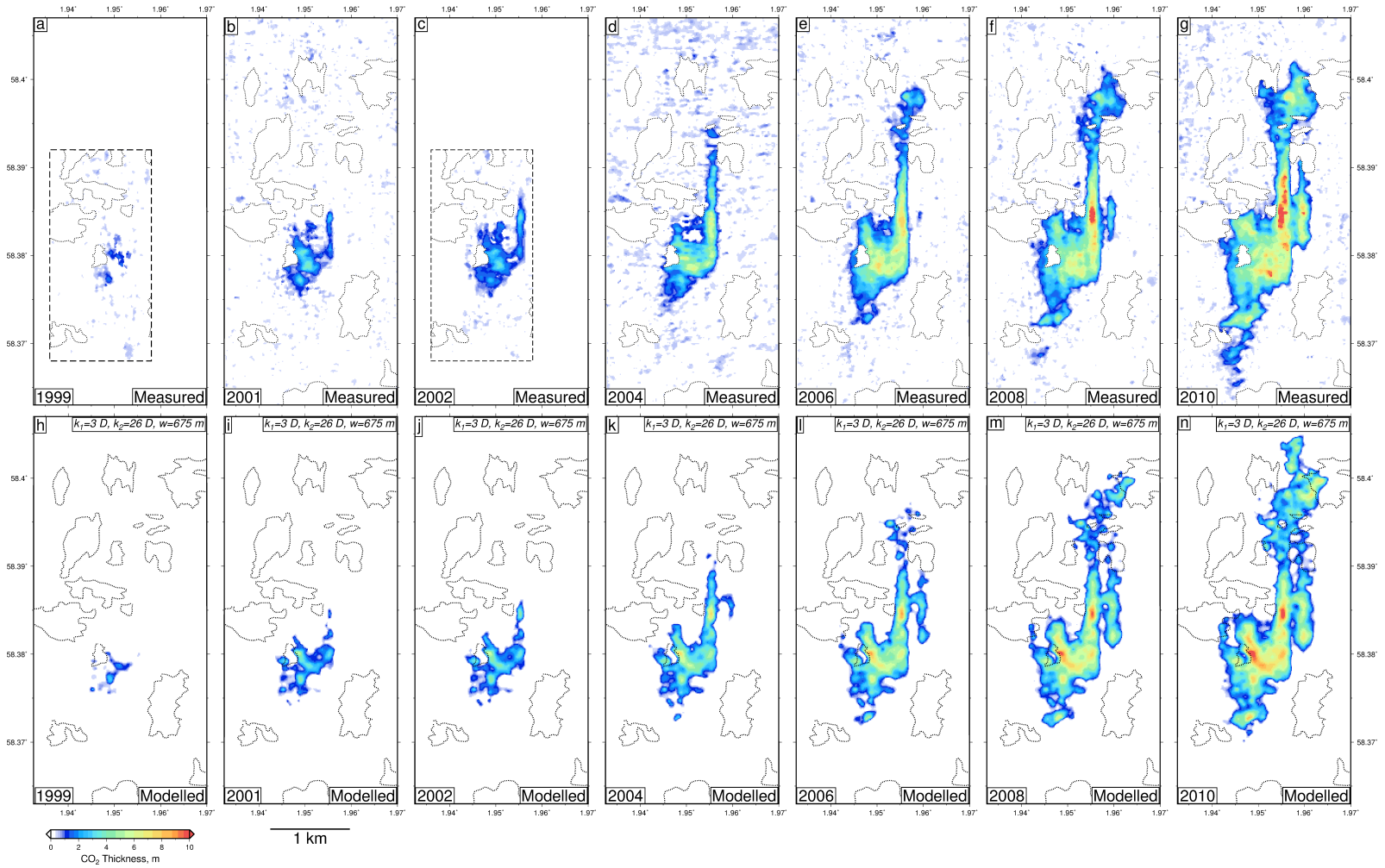

Figure 4.20: Measured and modelled CO_2 distribution in Layer 9 for channel centred in the middle of the spectral decomposition anomaly. **(a)-(g)** Measured CO_2 thickness from Chapter 3. **(h)-(n)** Best-fitting modelled distribution of CO_2 using channel permeability model found by inversion, where $k_1 = 3 \pm 1$ D, $k_2 = 26 \pm 8$ D and $w = 675 \pm 125$ m ($u_1 = 5.6 \pm 1.9 \times 10^{-4}$ ms^{-1}, $u_2 = 4.8 \pm 1.5 \times 10^{-3}$ ms^{-1}). Hatched polygons = regions where reflections are incoherent due to natural gas pockets in the overburden.

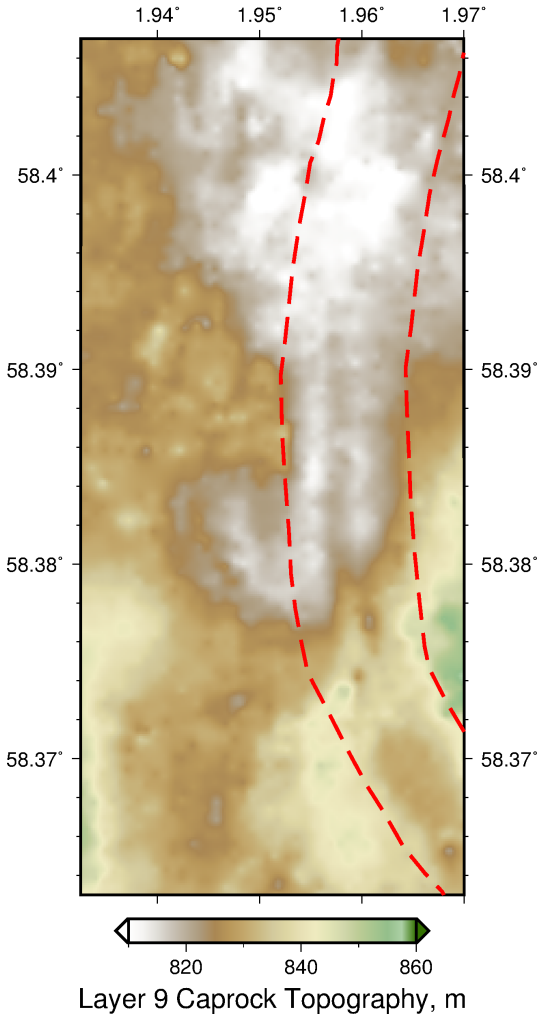

Figure 4.21: Topography of Layer 9 caprock with location of edges of best-fitting channels. Red dashed line shows best-fitting channel.

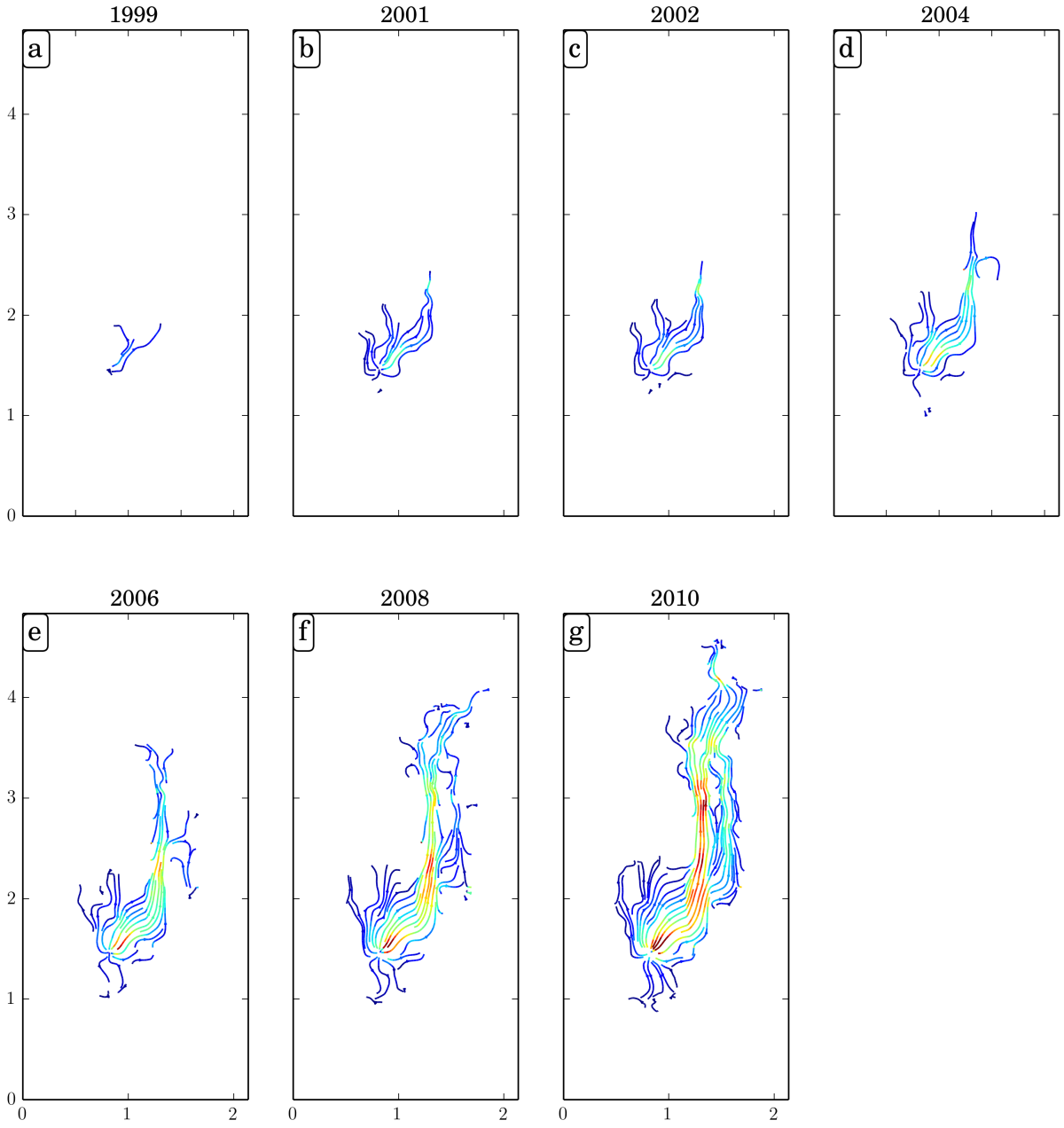

Figure 4.22: Streamlines showing flux through Layer 9 for high permeability channel model. Colours show relative magnitude of flux. Warmer colours show higher flux.

despite its relatively narrow width, it will not impede this migration. Hence, the volume of CO_2 in the southern topographic dome will not increase significantly in the near future.

Table 4.1: Forecasting CO_2 flow in Layer 9. Best-fitting parameters for flow model found by grid search for training set. Misfit for each seismic reflection survey for each set of trained parameters are shown in black. Misfits for test data shown in red.

Training Set	Model Parameters			Misfit						
	w, m	k_1, D	k_2, D	1999	2001	2002	2004	2006	2008	2010
1999-2010	675	3	26	2.61	2.08	2.33	2.41	2.63	3.10	3.00
1999-2008	600	4	37	2.62	2.05	2.31	2.35	2.67	3.04	3.26
1999-2006	650	4	33	2.60	2.06	2.30	2.34	2.67	3.07	3.21
1999-2004	650	4	37	2.60	2.06	2.29	2.35	2.70	3.07	3.29
1999-2002	675	3	50	2.60	2.04	2.27	2.47	2.78	3.06	3.45

4.8 Forecasting Flow within Layer 9

A requirement of a good reservoir simulator and the input reservoir model is the ability to forecast the future flow of CO_2. To test the ability of the simulator developed in this chapter to forecast CO_2 flow, the surveys are split into multiple training and test sets, divided in chronological order (Table 4.1). The best-fitting parameters are found for a training set, and the misfit is calculated between the simulation using these parameters and the observed CO_2 distribution for each seismic reflection survey. Subsequent surveys are then forecast by the simulator. If the misfit for a forecasted survey does not increase considerably relative to a baseline, then confidence in the model's ability to forecast future flow is high. In this case, the baseline misfit is calculated using all of the surveys to train the model.

The small number of data points in time makes this kind of analysis difficult for this time-lapse data set. Ideally, both the training and test sets would have many times more data points to both fit and test a model on. However, due to the expense of obtaining even a single data point using seismic reflection surveying, predictions of the flow of CO_2 in future carbon storage reservoirs will only ever be based on a small number of data points.

Table 4.1 shows that the model does a good job of predicting the flow of CO_2 through Layer 9 up to 2008 for all training sets. These misfit values indicate that a reasonable prediction of CO_2 flow up to 2008 could have been made using this model in 2002. However,

the misfit for 2010 in the test sets compared to the baseline training set shows a marked increase. This increase suggests that the simple permeability model cannot capture the true dynamics of the flow of CO_2 in 2010 in this layer. This observation is backed up by the lower value of permeability found in the baseline training set, indicating that the permeability of the channel decreases to the north. This variation in permeability suggests that the assumption of a single permeability for the channel is too simplistic and that this simple model is underfitting the data. It is therefore likely that there are variations in permeability along the length of the channel that are not accounted for in this model. This inference is in accordance with observations made by Clark & Pickering (1996), who suggested that deposition of channel sands can be variable along the length of channels, particularly near to channel bends, and so permeability may also vary. An alternative suggestion is that uncertainty in topography in this region is creating discrepancies between the observed and modelled CO_2 distribution.

The ability of a model to forecast new data can be described in terms of bias and variance (Figure 4.23; Geman *et al.*, 1992). Bias describes how strict the model assumptions are. Variance describes how sensitive a model is to uncertainties and noise in the training set. Models such as the one implemented here are high bias, low variance models. The model is high bias because only two different permeability regions are permitted to exist in the model, and the shape of these regions is well defined prior to training the parameters. The model is low variance because small changes in the training data would not have a significant effect on the model parameters and the misfit is weighted by the uncertainties in the data. High bias, low variance models underfit the data and can mean that a model is not complex enough to capture the full behaviour of a system.

At the other end of the scale are low bias, high variance models. These models put either no or limited bounds on the structure of the model or the number of parameters used to fit the model. These models fit the training data set very well, but can struggle to predict new data. This problem is known as overfitting. It could be argued that the model suggested by Nilsen *et al.* (2017) fits into this category, where the model parameters, such as caprock topography, permeability, CO_2 density, porosity and injection rates, were fitted to match

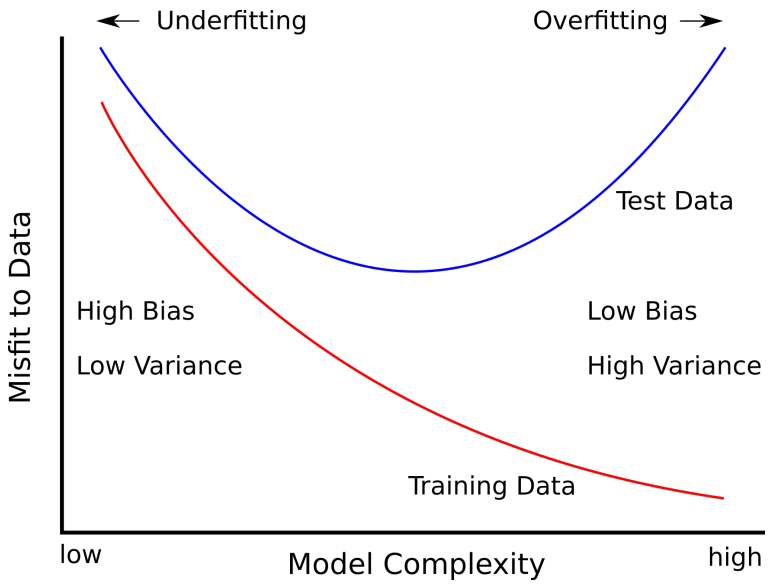

Figure 4.23: Model complexity against prediction error. Blue line - test data, red line = training data. Ideal model complexity fits the training set well without overfitting, and therefore losing predictive ability.

the available data as well as possible. An interesting test of this suggestion would be to see how well this model can forecast a previously unseen data set.

To find a better fit to the data, a model of intermediate complexity is required. The model presented here could be made more complex by the addition of a variable permeability within the channel. However, the seismic reflection surveys do not provide evidence for changes in permeability other than for the existence of a channel, and so a forecasting model that would provide a significant improvement on that presented here is difficult to create.

4.8.1 Future CO_2 Flow in Layer 9

Injection of CO_2 into the Utsira Formation is still ongoing in 2017. Given the high flux of CO_2 into Layer 9 in 2010, it seems likely that CO_2 is still migrating into Layer 9 at a significant rate, and will continue to do so for the foreseeable future. Using the reservoir model developed from the inversion of the flow model using data up to 2010, the future flow of CO_2 in Layer 9 can be forecast. The best-fitting permeability for the channel found by grid search in Section 4.6.3, $k_2 = 26$ D, and a channel width of $w = 675$ m are ex-

trapolated through the rest of the reservoir, informed by the spectral decomposition image and the thickness of the reservoir. A background reservoir permeability $k_1 = 3$ D is also used. While there are infinite possible models for the future volumetric flux into Layer 9, here I assume that the flux continues to follow the relationship given by (4.35) for the near future.

Figure 4.24 shows the predicted flow of CO_2 in Layer 9 until 2022. The volume of CO_2 trapped under the southern dome does not increase significantly over this time period, with the maximum thickness increasing by only ~ 3 m. The majority of the CO_2 that enters Layer 9 over this time period is accounted for by the increase in volume trapped underneath the northern dome. As noted in the previous section, the high permeability channel acts as a conduit for CO_2 to migrate to this northern dome unimpeded. This northern dome has a significantly larger potential CO_2 capacity than the southern dome, meaning that CO_2 can safely migrate into this layer for many years to come. However, as the CO_2 layer gets thicker, it is likely that reservoir confinement will start to become a factor in the flow dynamics. At this point, this current reservoir simulator will not be able to accurately describe the flow of CO_2 in this layer as the confinement of the current, and hence the flow of the ambient fluid, become important contributors to the evolution of the plume.

4.9 Summary

In this chapter, I have presented a numerical reservoir simulator to model the flow of CO_2 through an unconfined porous reservoir. This numerical model takes a different approach to existing three dimensional Darcy flow simulators, and provides an interesting test of vertically-integrated, sharp-interface models that have been previously explored – primarily theoretically – in the literature.

The model is based on buoyancy-driven gravity currents, and the numerical simulations have been benchmarked against analytical solutions for two- and three-dimensional flow on a slope, first given by Huppert & Woods (1995) and Vella & Huppert (2006). The numerical

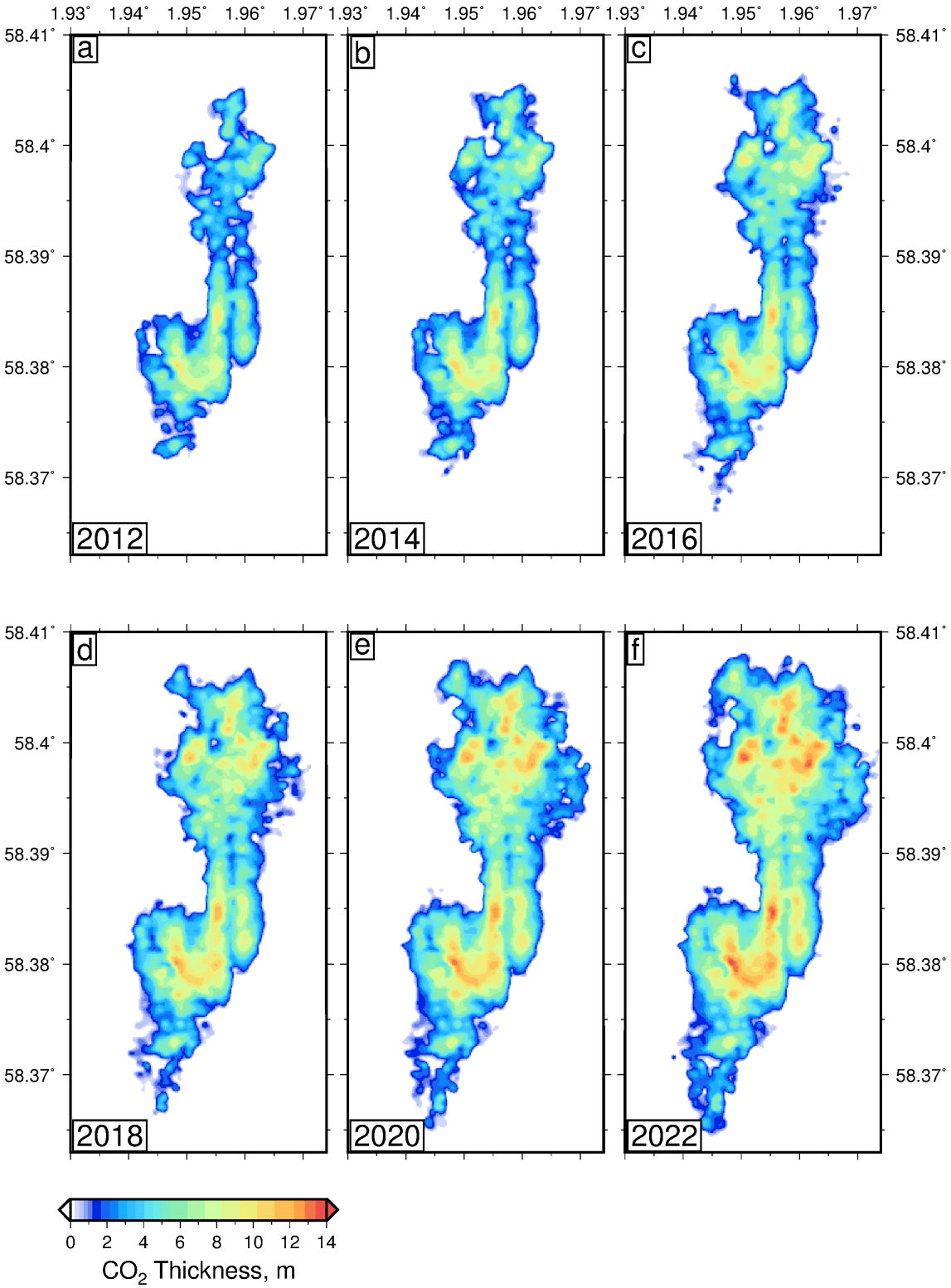

Figure 4.24: Future prediction of CO_2 thickness in Layer 9 for 2012 to 2022. Forecast simulated using 26 D channel.

model is computationally efficient and implements a three point differencing scheme to increase stability (Il'in, 1969). The numerical model is also straightforward to implement and only requires four input parameters: caprock topography, the buoyancy velocity of the CO_2 in the reservoir, the volumetric flux of CO_2 into the reservoir and the location that the CO_2 enters the reservoir.

The numerical model is used to gain insight into the dominant forces that control the flow of CO_2 in Layer 9 and the reservoir properties that are required to reproduce the seismically-derived distribution of CO_2 in three dimensions. Flow simulations using values of reservoir and fluid properties from the literature that include a homogeneous permeability did not provide a good match to the observed CO_2 distribution. Further testing found that simply increasing the permeability or gradients in the caprock topography could not improve the fit adequately.

Seismic analysis of the caprock-reservoir reflection suggested the existence of a submarine channel within the reservoir. A simple reservoir model of a channel of width w with a different permeability (k_2) to that of the surrounding aquifer (k_1) was developed. A grid search over the parameters found a good match to the seismically observed three-dimensional CO_2 distribution, suggesting that this model accurately represents the flow dynamics of the reservoir and that the match is not simply due to picking parameters that enable rapid migration of CO_2 through the reservoir. For the best-fitting model, the permeability of the reservoir was found to be in agreement with measurements from cores. The permeability of the channel was found to be approximately an order of magnitude higher than the surrounding reservoir. This increase in permeability is plausible based on evidence from other submarine channels documented in the literature.

Using this best-fitting reservoir model, the future flow of CO_2 within Layer 9 was explored assuming the volumetric flux into Layer 9 continues to follow the same relationship. The thickness of the CO_2 accumulation trapped under the southern dome is predicted to only increase by ~ 3 m in the next 12 years, which is accounted for by the significant increase in

the volume of CO_2 trapped under the northern dome. The high permeability channel allows the CO_2 to migrate northwards unimpeded.

The success of this reservoir simulation, alongside work by Nilsen *et al.* (2017), has shown that vertical equilibrium models are an accurate and computationally efficient alternative to conventional Darcy flow simulators when modelling the flow of CO_2 through porous media. The large body of literature that has already provided analytical solutions for gravity currents in a variety of situations means that this simulator can be adapted quickly and easily to solve these problems in geologically realistic environments.

However, this flow simulation assumes that the aquifer in which Layer 9 resides is unconfined. If this flow simulation is to be applicable in other settings, it is essential to account for the confinement of the aquifer, and therefore pressure in the ambient fluid. In the next chapter, the effect of confinement on the flow of CO_2 through an aquifer with topography is explored in detail.

Chapter 5

Confined Gravity Currents with Diverging Boundaries

5.1 Introduction

In fluid dynamical studies, geological CO_2 storage reservoirs are often assumed to be massive, unconfined sandstone formations with uniform permeability and porosity (e.g. Huppert & Woods, 1995; Lyle *et al.*, 2005; Pegler *et al.*, 2013). These assumptions are undoubtedly gross simplifications. Outcrops of formations similar to potential storage reservoir rocks, such as the Bridport Sands on the Jurassic Coast, Dorset, UK, provide useful insight into the possible problems that may be faced when modelling the flow of injected CO_2 (Figure 5.1a). Reservoir rocks such as these indicate that the assumption of massive sandstone beds are likely to be an oversimplification. At Bridport, the obvious, metre-scale, sub-parallel layering caused by variable calcareous cement content creates vertical permeability contrasts (Morris & Shepperd, 1982). These horizons of less permeable material may act as

baffles, confining the flow to regions of high permeability. This confinement has important consequences when considering the flow of injected fluid through formations such as these.

Inter-bedding of thin, laterally extensive mudstone layers with thicker, high permeability sandstones in the Utsira Formation suggests a turbiditic depositional environment (Chadwick *et al.*, 2004b; Zweigel *et al.*, 2004). Figures 5.1b shows an example of a turbidite sequence from the Mynydd Bach Formation, Aberystwyth Grits Group, with thick, near-parallel bedded sandstones and thin shale layers (Wilson *et al.*, 1992). However, sandstone beds in turbidite deposits can pinch out over large length scales, forming stratigraphic traps (McCaffrey & Kneller, 2001). The associated change in confinement is expected to have important consequences for the flow of fluid through such rocks.

CO_2 within Layer 9 at the Sleipner field is located in the uppermost part of the Utsira Formation, known as the Sand Wedge. In this part of the reservoir, the high permeability Utsira sandstone is bounded on top by a reservoir caprock, the Nordland Shale, and beneath by the '5 m Shale', an intra-reservoir shale layer that acts as the caprock for CO_2 Layer 8. These impermeable horizons are not parallel, and the thickness of the Layer 9 reservoir can vary by a factor of two (Figure 4.14b). On a larger scale, the Sand Wedge pinches out to the west, $\sim$5 km from the injection region. For reservoir parameters similar to those found in Layer 9 at Sleipner (e.g. a less viscous injected fluid, aquifer depth $\sim$20 m), Pegler *et al.* (2014) suggested that the effect of confinement is not anticipated to be significant for approximately 30 years. However, as the thickness CO_2 in Layer 9 increases, confinement could potentially play a significant role in controlling the flow of CO_2.

To assess the significance of aquifer geometry on fluid flow, this chapter focuses on analytical and numerical solutions for the propagation of a two-dimensional gravity current through an aquifer of variable thickness. In this formulation, I will consider the situation where the injected fluid is of equal viscosity to the ambient fluid. While this regime does not directly apply to the case of CO_2 flow in saline aquifers, the mathematical analysis is considerably simplified. Accounting for viscosity variations remains a potential area for future work. The

Figure 5.1: **(a)** Bridport Sands on the Jurassic Coast near Burton-Bradstock, Dorset, UK. People for scale. Grid reference: SY 467902 **(b)** Mynydd Bach Formation, Aberarth, UK. Rucksack for scale. Photographs courtesy of N. Woodcock.

model developed in this chapter will provide the necessary tools to incorporate confinement into the numerical reservoir simulator developed in Chapter 4.

5.2 Previous Work

Gravity currents in confined porous media have received significant attention. A range of analytical, numerical and experimental studies have investigated different flow regimes. Huppert & Woods (1995) proposed one of the first analytical models to describe exchange flows between two reservoirs connected by a permeable channel. They found that the flow is initially dominated by gravitational slumping, which transitions to a predominantly pressure-driven flow as the gradient of the interface between currents becomes shallower. For the pressure-driven regime of two fluids of equal viscosity, their analytical solution suggests that, to leading order, the current translates linearly in time as a direct consequence of conservation of mass. These authors also found that separation of contact points of the injected fluid front with the upper and lower boundaries of the reservoir increases at a rate proportional to the square root of time. Pegler *et al.* (2014) and Zheng *et al.* (2015) studied the flow of a buoyant gravity current through a two dimensional, horizontally confined aquifer with a constant injection rate. These authors focussed on the effect of differing ambient and injected fluid viscosities and again observed a transition from gravity-driven slumping to pressure-driven flow. This transition is linked to the contact of the front of the current with the upper and lower boundaries of the confining aquifer. The shape of the interface between the fluids in this regime is strongly controlled by the viscosity ratio of the two fluids (Zheng *et al.*, 2015). An analytical solution for a horizontally confined gravity current with fluids of different viscosities in radial coordinates has also been found (Nordbotten & Celia, 2006).

Further analytical developments of the basic confined gravity current model include incorporation of the effects of sloping confining boundaries, convective dissolution, capillary trapping, reactive transport, background flow and fault bounded aquifers (Hesse *et al.*, 2007; Verdon & Woods, 2007; Gunn & Woods, 2011, 2012; MacMinn *et al.*, 2012; MacMinn & Juanes, 2013). All of these models build on the basic confined gravity current equation,

and show the potential scope for application to situations that can be modelled numerically. However, these models all assume that the impermeable boundaries on the top and base of the aquifer are parallel to each other.

The effect of confinement has also been incorporated into numerical vertically integrated numerical flow simulators. In a study investigating leakage from a well, Gasda *et al.* (2009) included the thickness of the aquifer with parallel top and base. This model was then updated to investigate how topographic roughness on different length scales could be accounted for in reservoir simulations with fixed grid sizes (Gasda *et al.*, 2012, 2013). These schemes incorporate caprock topography and variable aquifer thickness that varies on short length scales with a zero-mean trend. However, during the up-scaling of topography to grid resolution in these models, the variable aquifer thickness is replaced by an average aquifer thickness, and so the results of these studies do not provide insight into how fluid flow is affected by variable aquifer thickness. A numerical model that accounts for changes in aquifer thickness is provided by Nilsen *et al.* (2016b). This model is incorporated into a larger numerical scheme that accounts for compressibility and solubility of the fluid, capillarity and relative permeability. While such models can account for variation in aquifer thickness, the effect of a changing aquifer thickness alone on the flow of a buoyant fluid has not previously been considered. In this chapter, I develop analytical and numerical solutions for a gravity current in an aquifer with divergent confining boundaries. These solutions are used to investigate the role of variable confinement on the migration rate of fluid through the aquifer.

5.3 Two-dimensional Theoretical Model

Consider a fluid of density, ρ_c, injected at a constant rate into a two dimensional aquifer of permeability, k, and porosity, ϕ, saturated with an ambient fluid of density, ρ_a. I consider the case for a buoyant injected fluid, where $\rho_c < \rho_a$. This analysis is appropriate for the case of CO_2 injection, but the model presented here is equally valid for a dense injected fluid. Additionally, the formulation only accounts for the situations in which viscosities of both fluids are equal. The case of unequal viscosities is a non-trivial extension and so is left for

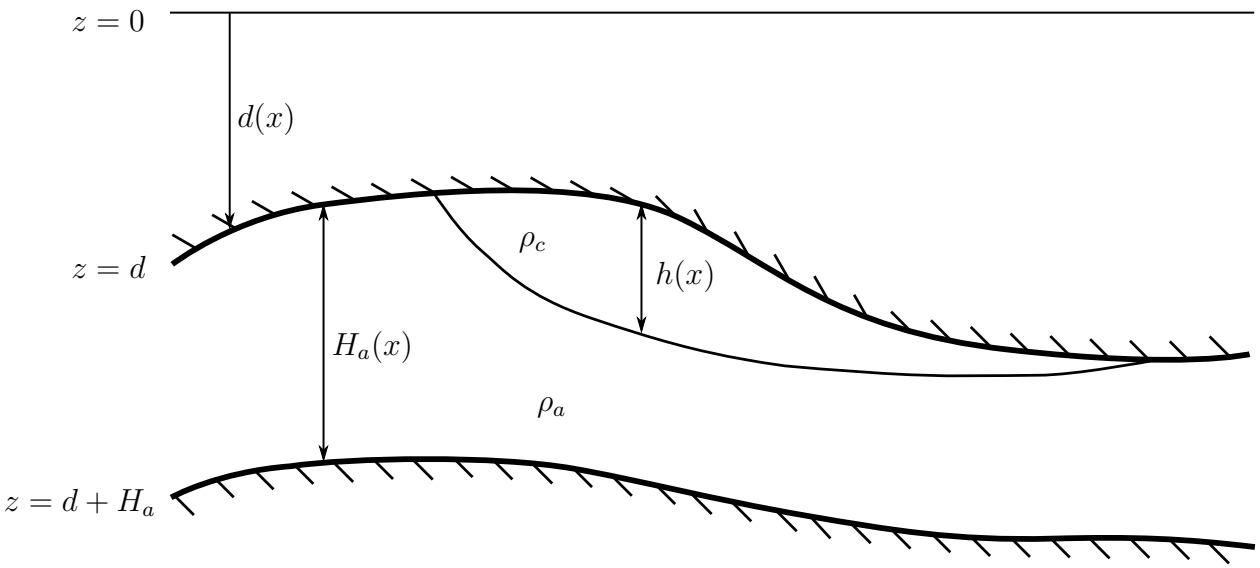

Figure 5.2: Generalised gravity current in two dimensions in aquifer of variable confinement. Bold lines = impermeable top and base of aquifer.

future research.

The aquifer is confined on both its upper and lower margins by impermeable boundaries. The depth to the upper boundary is given by $z = d(x)$, aquifer thickness is given by $H_a(x)$ and so the depth to the base of the aquifer is $z = d + H_a$ (Figure 5.2). A sharp interface between injected and ambient fluids at a depth $z = d(x) + h(x, t)$ is assumed. For simplicity, mixing between the two fluids and the effect of surface tension at the interface is neglected.

Flow within the aquifer is driven by lateral pressure gradients caused by the injection of fluid and the buoyancy of the injected fluid. The horizontal and vertical velocities of the injected fluid, u and w respectively, are described by Darcy's law and mass conservation, so that

$$\mathbf{u} = -\frac{k}{\mu}\left(\nabla p + \rho g \hat{\mathbf{z}}\right), \tag{5.1a}$$

$$\nabla \cdot \mathbf{u} = 0, \tag{5.1b}$$

where k is the permeability of the porous medium, μ is the viscosity of the fluid, p is the pore fluid pressure, and $\mathbf{u} = (u, w)$. When the aspect ratio of the aquifer is large, as is common

for reservoir rocks, the flow of the injected fluid is predominantly horizontal, $u \gg w$, and so to leading order the pressures are hydrostatic,

$$p_c = P_0 + \rho_a g d + \rho_c g(z-d) \qquad d < z < d+h, \tag{5.2a}$$

$$p_a = P_0 + \rho_a g d + \rho_c g h + \rho_a g(z-h-d) \qquad d+h < z < d+H_a, \tag{5.2b}$$

where p_c is the pressure in the injected fluid, p_a is the pressure in the ambient fluid, P_0 is the background pressure at $z = 0$, and g is the acceleration due to gravity (Figure 5.2). The horizontal velocities, including the effect of buoyancy, can therefore be described as

$$u_c = -\frac{k}{\mu}\left(\frac{\partial P_0}{\partial x} + \Delta\rho g \frac{\partial d}{\partial x}\right) \qquad d < z < d+h, \tag{5.3a}$$

$$u_a = -\frac{k}{\mu}\left(\frac{\partial P_0}{\partial x} - \Delta\rho g \frac{\partial h}{\partial x}\right) \qquad d+h < z < d+H_a, \tag{5.3b}$$

where $\Delta\rho = \rho_a - \rho_c$. The flux through the aquifer is constant, so

$$q = h u_c + (H_a - h) u_a, \tag{5.4}$$

which can be expressed in full as

$$q = -\frac{k}{\mu}\left[H_a \frac{\partial P_0}{\partial x} + \Delta\rho g h \frac{\partial d}{\partial x} - \Delta\rho g (H_a - h)\frac{\partial h}{\partial x}\right]. \tag{5.5}$$

Conservation of mass in the current is given by

$$\phi \frac{\partial h}{\partial t} + \frac{\partial}{\partial x}\left(u_c h\right) = 0. \tag{5.6}$$

Rearranging (5.5) for $\partial P/\partial x$ and substituting into (5.6) yields the governing equation for a buoyant fluid flowing through a confined aquifer of variable thickness,

$$\phi \frac{\partial h}{\partial t} + \frac{\partial}{\partial x}\left(\frac{q}{H_a} h\right) = \frac{k\Delta\rho g}{\mu}\frac{\partial}{\partial x}\left[\frac{(H_a - h)}{H_a} h \frac{\partial h}{\partial x} + \frac{(H_a - h)}{H_a} h \frac{\partial d}{\partial x}\right]. \tag{5.7}$$

Conservation of mass of the injected fluid is described by

$$V(t) = qt = \phi \int_0^{x_N} h \, dx, \tag{5.8}$$

where the total fluid volume, $V(t)$, is assumed to increase linearly with time and $x = x_N$ is the horizontal position of the nose of the current. At $x = x_N$, the thickness of the current must be zero,

$$h(x_N, t) = 0. \tag{5.9}$$

Integrating (5.7) between $x = 0$ and $x = x_N$ and substituting (5.8) and (5.9) provides the boundary condition at $x = 0$ for a constant input flux, q,

$$\left[\frac{\partial}{\partial x}\left(\frac{q}{H_a}h\right) - \frac{k\Delta\rho g}{\mu}\frac{\partial}{\partial x}\left\{\frac{(H_a - h)}{H_a}h\frac{\partial h}{\partial x} + \frac{(H_a - h)}{H_a}h\frac{\partial d}{\partial x}\right\}\right]_{x=0} = q. \tag{5.10}$$

Equation (5.7) is also subject to

$$h\frac{\partial h}{\partial x}\bigg|_{x=x_N} = 0, \tag{5.11}$$

which states that the flux at the nose of the current must be equal to zero. Equations (5.7)–(5.11) describe the flow of a buoyant fluid through an aquifer of variable confinement for the case of a constant injection flux. The change in thickness of the current with time is controlled by terms that determine the strength of pressure-driven flow, gravitational slumping and the advection of the fluid due to topographic gradients.

These equations can also be used to describe the flow of a dense current along the base of a confined aquifer. In this case, d refers to depth to the boundary that the fluid is flowing along and $\Delta\rho$ is of opposite sign.

5.4 Uniformly Increasing Aquifer Thickness

To investigate the effect of changing aquifer thickness on the flow of fluid in a simple case, thickness of the aquifer is defined as $H_a = H_0 + \alpha x$, where H_0 is the thickness of the aquifer at the origin and α is the gradient of the boundary. Two situations are then analysed in detail:

flow of a buoyant current beneath a horizontal boundary where d is a constant; and flow of a current beneath a sloping boundary where $d = d_0 - \alpha x$ (Figure 5.3). These situations are analogous to a dense current flowing along the base of the aquifer that is either horizontal or uniformly sloped, respectively.

The analytical solutions described in this section are compared with numerical solutions for a range of values of α for either the upper or lower boundary. These numerical simulations are carried out using a Crank-Nicholson finite difference scheme described in Section 4.3.4. This scheme exploits an adaptive time step and grid spacing to ensure that there is sufficient resolution at both short and long times and extents. The Il'in scheme is also implemented to ensure the stability of the simulation (Il'in, 1969, Appendix B).

5.4.1 Horizontal Upper Boundary

For the case where $H_a = H_0 + \alpha x$ and d is a constant (Figure 5.3a), (5.7) may be written as

$$\phi \frac{\partial h}{\partial t} + \frac{q}{H_0 + \alpha x} h = \frac{\partial}{\partial x} \left[\frac{k \Delta \rho g}{\mu} \frac{(H_0 + \alpha x - h)}{H_0 + \alpha x} h \frac{\partial h}{\partial x} \right], \tag{5.12}$$

with the boundary conditions

$$qt = \phi \int_0^{x_N} h \, dx, \tag{5.13a}$$

$$h(x_N) = 0, \tag{5.13b}$$

$$h \frac{\partial h}{\partial x} = 0. \tag{5.13c}$$

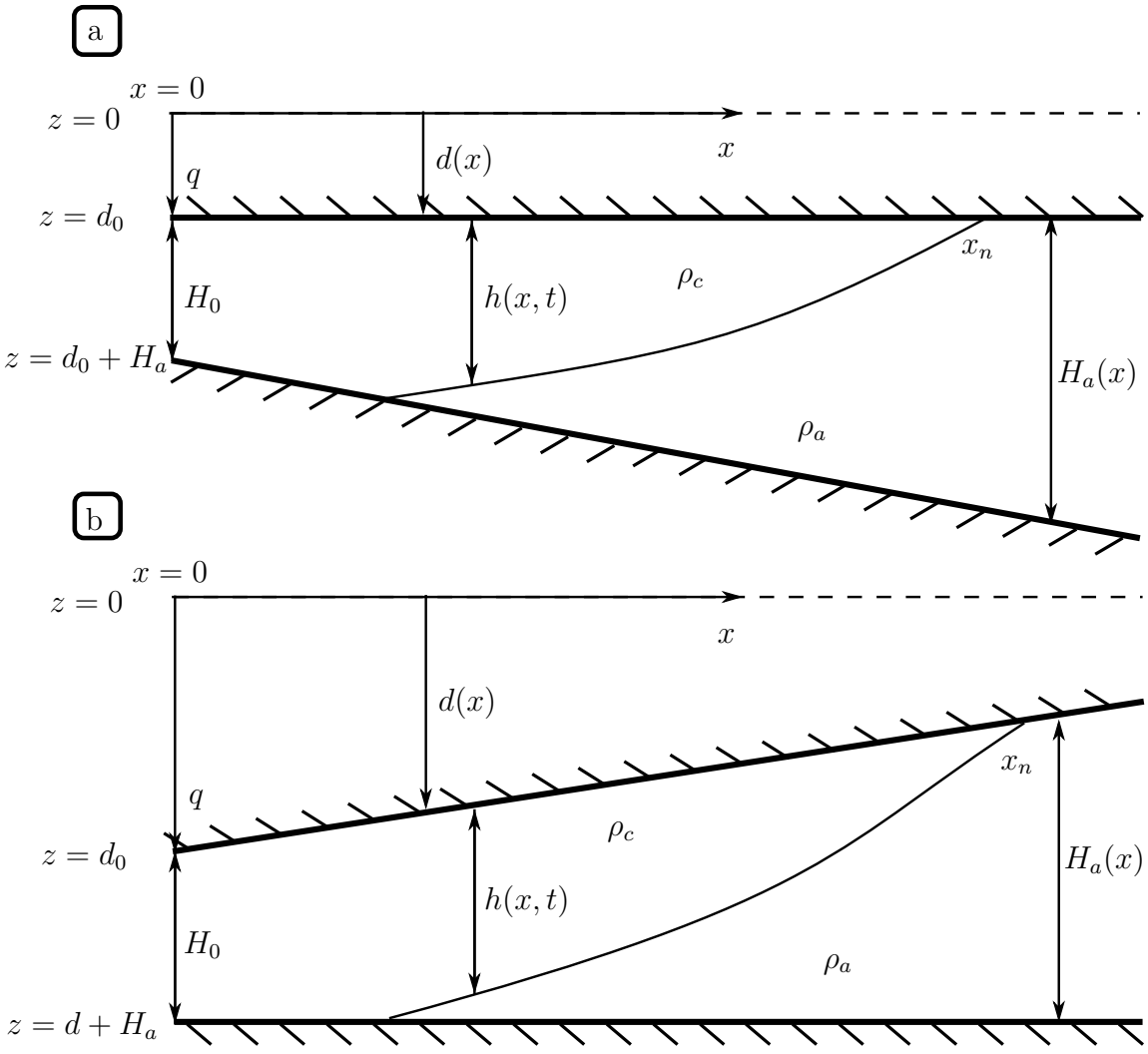

Figure 5.3: Gravity current in aquifer of uniformly diverging aquifer. (a) Aquifer with flat roof, where d is a constant and $H_a = H_0 + \alpha x$, where α is a constant. **(b)** Aquifer with sloped roof and flat base, where $d = d_0 - \alpha x$ and $H_a = H_0 + \alpha x$.

Scaling analysis of (5.12) and (5.13a) suggests characteristic thickness, length, slope and time scales

$$h_c = H_0, \tag{5.14a}$$

$$x_c = \frac{u_b H_0^2}{q}, \tag{5.14b}$$

$$\alpha_c = \frac{q}{u_b H_0}, \tag{5.14c}$$

$$t_c = \frac{\phi u_b H_0^3}{q^2}, \tag{5.14d}$$

where $u_b = (k\Delta\rho g)/\mu$ is the buoyancy velocity. These scalings indicate transitions between different flow regimes. Defining $H = h/h_c$, $X = x/x_c$, $A = \alpha/\alpha_c$ and $T = t/t_c$, (5.12) can be written in dimensionless form as

$$\frac{\partial H}{\partial T} + \frac{\partial}{\partial X}\left(\frac{H}{1+AX}\right) = \frac{\partial}{\partial X}\left[\frac{(1+AX-H)}{1+AX} H \frac{\partial H}{\partial X}\right], \tag{5.15}$$

subject to the boundary conditions

$$T = \int_0^{X_N} H dX, \tag{5.16a}$$

$$H(X_N) = 0, \tag{5.16b}$$

$$H\frac{\partial H}{\partial X}\Big|_{X_N} = 0. \tag{5.16c}$$

Figure 5.4 shows four snapshots of the numerical solution of (5.15) at four distinct stages of the current's evolution. Note the change in vertical exaggeration between the early and late time plots. At early times, the current only makes contact with the upper boundary. At early intermediate times, the current makes contact with the base of the aquifer, the front of the current propagates with a straight interface between the upper and lower contact points. At late intermediate times, the current is still attached to the base of the aquifer, but the distance between the upper and lower contact points has increased. Finally, at late times the majority of the front between the two fluids is distant from the confining base of the aquifer and the interface between the two fluids becomes convex. In the following sections, these four flow regimes are analysed and the migration rate and the change in thickness with

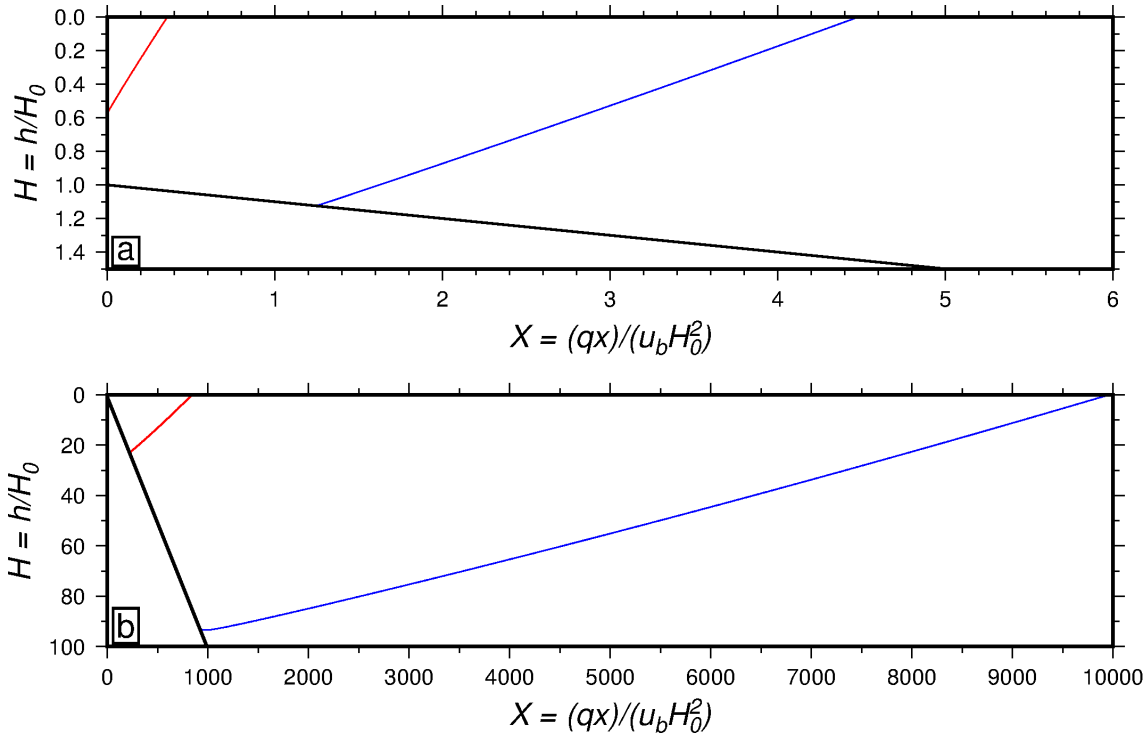

Figure 5.4: Snapshots of current on flat roof with $A = 0.1$**.** Black line shows base of aquifer $= H_a/H_0$. **(a)** Early to early intermediate times. Red: $T = 10^{-1}$, Blue: $T = 10^{0.5}$. Vertical exaggeration $= 1$. **(b)** Late intermediate to late times. Red: $T = 10^{4}$, Blue: $T = 10^{5.7}$. Vertical exaggeration $= 0.01$. Note different horizontal scales in (a) and (b).

time is discussed.

Regime 1: Early unconfined flow, $T \ll 1$

At early times, $T \ll 1$, the thickness of the current is small compared to the thickness of the aquifer, $H \ll 1$, flow is primarily driven by the buoyancy of the current rather than pressure gradients in the ambient fluid associated with confinement. In this regime, (5.15) can be approximated as

$$\frac{\partial H}{\partial T} = \frac{\partial}{\partial X}\left(H\frac{\partial H}{\partial X}\right), \tag{5.17}$$

and hence the current spreads as an unconfined gravity current as described in Section 4.3.2, with $X \sim T^{2/3}$ and $H \sim T^{1/3}$. Following the analysis in Section 4.3.2, similarity solutions can be found to describe the extent of the nose and the thickness of the current as a function

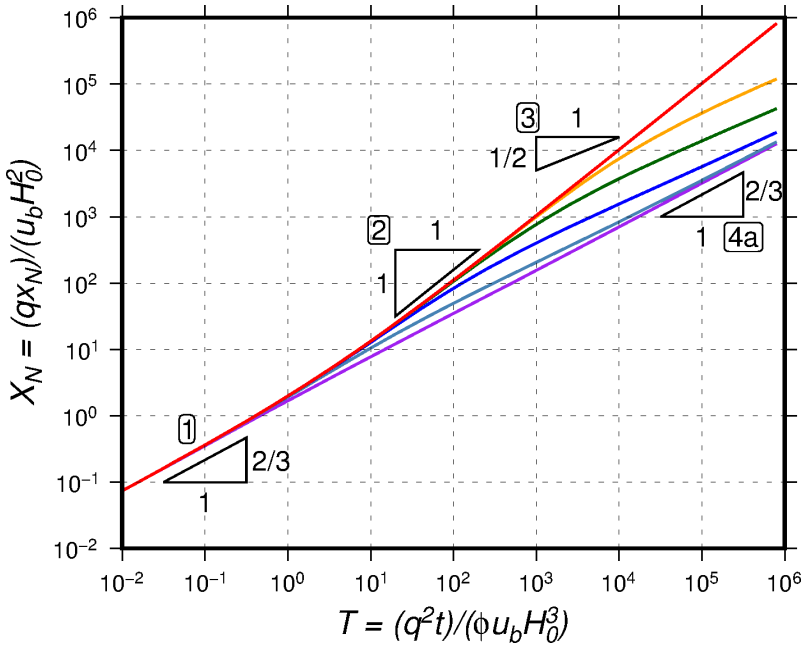

Figure 5.5: Extent of the nose of the injected fluid on the upper boundary against time for flow on flat roof with sloped base. Lines are coloured according to the slope of the base; Purple: $A = 1$, light blue: $A = 0.1$, blue: $A = 0.01$, green: $A = 0.001$, orange: $A = 0.0001$, red: $A = 0$. Flow regime asymptotes labelled on figure. Numbered labels refer to relevant flow regime.

of time, given by

$$X_N = 1.48T^{2/3}, \tag{5.18a}$$

$$H = 1.3T^{1/3}. \tag{5.18b}$$

These equations give the early time asymptotes for an unconfined gravity current, and are shown in Figures 5.5 & 5.6. These solutions are in agreement with Huppert & Woods (1995) for the early time regime.

Figure 5.7a shows the analytical solution and several time steps of the numerical solution collapsed by scaling of the axes. To be comparable with the numerical result, the analytical solution has been scaled to the range (0,1) on the vertical axis. The analytical and numerical solutions are in good agreement for this early time regime.

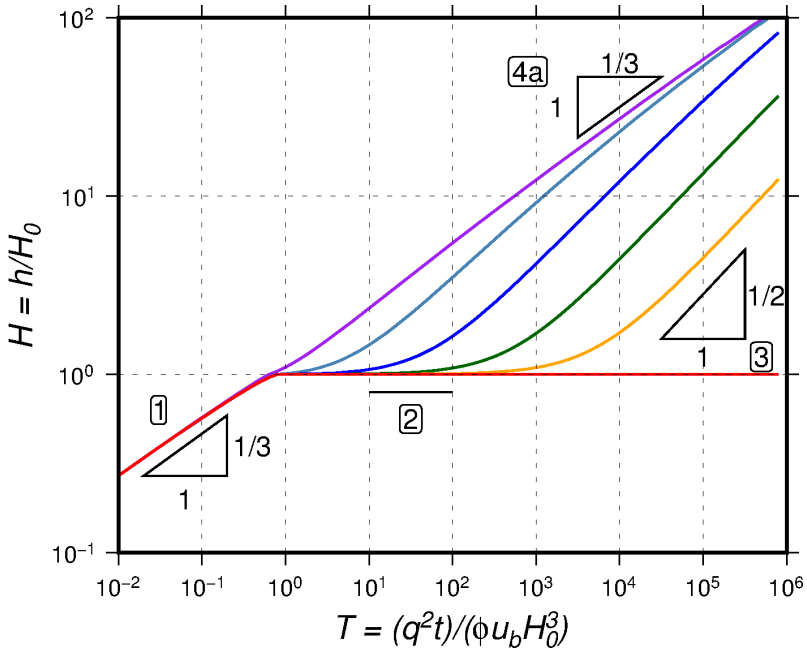

Figure 5.6: Maximum thickness of the injected fluid against time for flow on flat roof with sloped base. Lines are coloured according to the slope of the base; Purple: $A = 1$, light blue: $A = 0.1$, blue: $A = 0.01$, green: $A = 0.001$, orange: $A = 0.0001$, red: $A = 0$. Flow regime asymptotes labelled on figure.

Regime 2: Constant confinement, $T \sim 1$

At early intermediate times the slope of the aquifer is negligible, and the current propagates as a uniformly confined current. In this limit, $AX_N \ll 1$, and (5.15) may be approximated as

$$\frac{\partial H}{\partial T} + \frac{\partial H}{\partial X} = \frac{\partial}{\partial X}\left[(1-H)\,H\frac{\partial H}{\partial X}\right]. \tag{5.19}$$

In this regime, the current spans the width of the aquifer, $H \sim 1$, and so the flow of the bulk current can be described by considering the pressure-driven flow terms in (5.19),

$$\frac{\partial H}{\partial T} + \frac{\partial H}{\partial X} = 0. \tag{5.20}$$

Conservation of mass in this regime can be expressed as

$$T = \int_0^{X_N} dX, \tag{5.21}$$

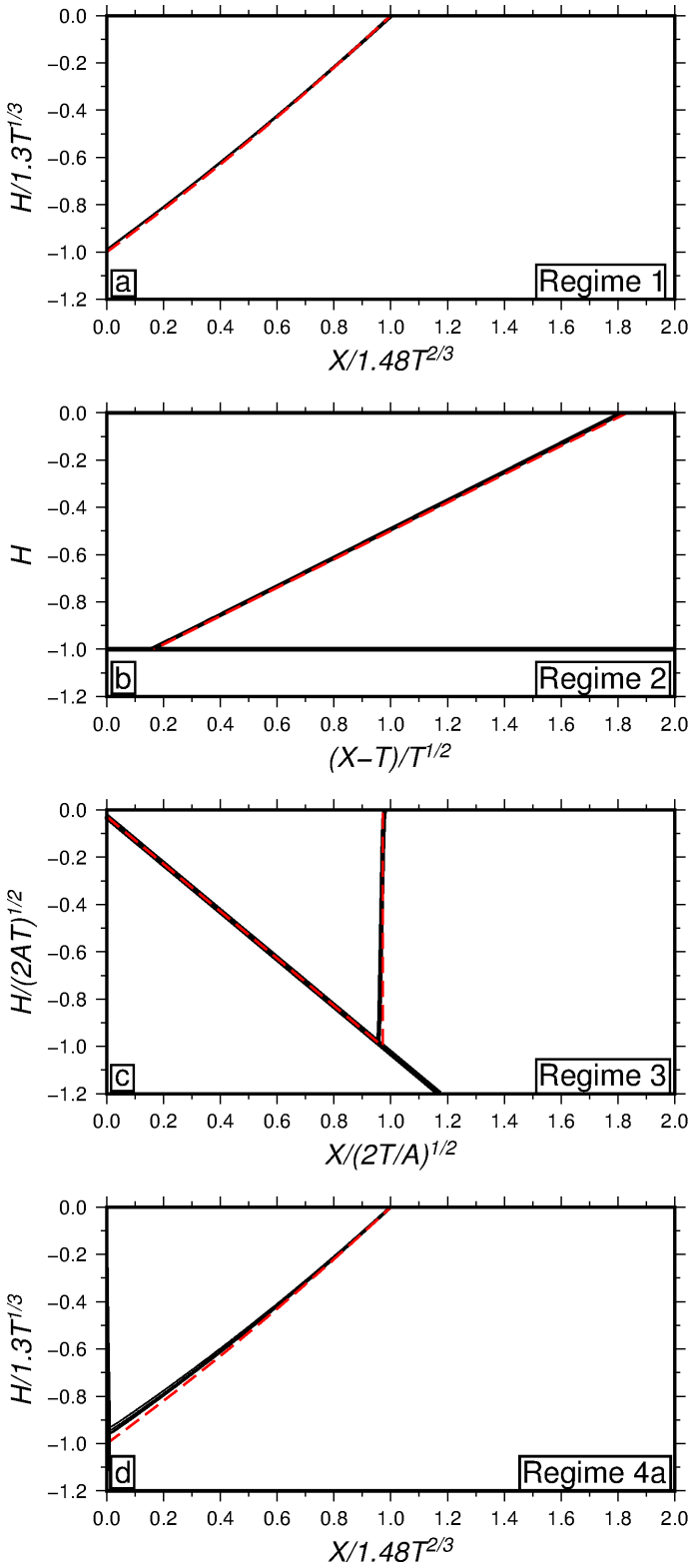

Figure 5.7: Gravity current in an aquifer with flat roof and diverging confinement. Analytical (red dash line) and numerical solutions (black line) shown for different regimes. **(a)** Regime 1, early times, $T \ll 1$. **(b)** Regime 2, early intermediate times, $T \sim 1$. **(c)** Regime 3, late intermediate times, $T \gg 1$, $AX \gg 1$. **(d)** Regime 4a, late times, $T \gg 1$, $AX \gg H$.

which leads to

$$X_N = T, \tag{5.22a}$$

$$H = 1. \tag{5.22b}$$

Equation (5.22) suggests that the bulk of the current is moving linearly with time and that the maximum thickness of the current is limited by the confinement of the aquifer.

Equation (5.19) can therefore be expressed in a moving reference frame $Y = X - T$,

$$\frac{\partial H}{\partial T} = \frac{\partial}{\partial Y}\left[(1-H)\,H\frac{\partial H}{\partial Y}\right], \tag{5.23}$$

with the boundary conditions

$$T = \int_0^{Y_N} H dY, \tag{5.24a}$$

$$H(Y_N) = 0. \tag{5.24b}$$

Using these expressions, similarity variables are given by

$$\eta = \frac{Y}{T^{1/2}}, \tag{5.25a}$$

$$H = f(\eta), \tag{5.25b}$$

which are valid for the region $-\lambda < \eta < \lambda$, with the boundary conditions $f(-\lambda) = 0$ and $f(\lambda) = 1$. Equation (5.23) can then be expressed in terms of η and $f(\eta)$ as

$$-\frac{1}{2}\eta\frac{\partial f}{\partial \eta} = \frac{\partial}{\partial \eta}\left[(1-f)f\frac{\partial f}{\partial \eta}\right], \tag{5.26}$$

which has a solution

$$f(\eta) = \frac{1}{2}(1+\eta), \tag{5.27}$$

where $\lambda = 1$. The thickness of the current front therefore decreases linearly with X once it detaches from the base of the aquifer until $H = 0$ at $X = X_N$. Combining (5.27) with (5.22)

provides the full analytical solution to flow in this regime. The bulk of the current flows at a rate proportional to T, while the gradient of the front of the current becomes shallower as the contact points on the upper and lower boundaries move apart at a rate proportional to $T^{1/2}$. Figure 5.7b shows this analytical solution with the translated and scaled numerical solution for comparison. Again, there is excellent agreement between the analytical and numerical solutions. These findings are identical to those of Huppert & Woods (1995), Pegler *et al.* (2014) and Zheng *et al.* (2015) for the case of horizontal confining boundaries and equal viscosity fluids.

Regime 3: Diverging boundaries, $T \gg 1$ & $AX_N \gg 1$

At late intermediate times, $T \gg 1$, the slope of the confining boundary means that the aquifer can no longer be considered to have uniform confinement, $AX_N \gg 1$, and so the slope of the aquifer must be accounted for. However, current is still confined by the aquifer, and so the flow is still predominantly pressure driven. In this regime, (5.15) can be approximated as

$$\frac{\partial H}{\partial T} + \frac{\partial}{\partial X}\left(\frac{H}{1+AX}\right) = 0. \tag{5.28}$$

When $AX_N \gg 1$, (5.28) can be expressed as

$$\frac{\partial H}{\partial T} + \frac{\partial}{\partial X}\left(\frac{H}{AX}\right) = 0, \tag{5.29}$$

which describes the advection of the current through an aquifer with diverging boundaries. The boundary conditions for this equation are

$$T = \int_0^{X_N} H dX, \tag{5.30}$$

$$H(X_N) = 0. \tag{5.31}$$

Scaling (5.29) and (5.30) suggests the similarity variables,

$$\eta = \frac{XA^{1/2}}{T^{1/2}}, \tag{5.32a}$$

$$H = (AT)^{1/2} f(\eta), \tag{5.32b}$$

which show that both the thickness of the current and its extent are proportional to $T^{1/2}$. These scalings also show that the gradient of the lower boundary plays an important role in controlling the speed and thickness of the current, even when $AX_N \gg 1$.

Using these newly defined variables, (5.29) becomes

$$(\eta^2 - 2)\left(\frac{\partial f}{\partial \eta} - \frac{1}{\eta} f\right) = 0. \tag{5.33}$$

Considering the right-hand bracket, f must be of the form $f = c\eta$, where c is a constant. The boundary conditions in this new frame are given by

$$1 = \int_0^{\eta_N} f \; d\eta, \tag{5.34a}$$

$$f(\eta_N) = 0, \tag{5.34b}$$

which can be integrated to give $\eta_N = \sqrt{2/c}$. The similarity solutions are therefore

$$X_N \sim \left(\frac{2T}{A}\right)^{1/2}, \tag{5.35a}$$

$$H \sim (2AT)^{1/2}. \tag{5.35b}$$

These calculations suggest that in this regime, the extent of the current increases proportional to $(T/A)^{1/2}$, and so the speed of propagation of the nose of the current depends on the slope of the confining gradient. Maximum thickness of the current is still dictated by the depth of the aquifer, increasing in proportion to $(AT)^{1/2}$. These solutions are determined by gradients in the background pressure due to the geometry of the diverging layer. The slope of the lower confining boundary is therefore important in controlling the speed and thickness of the current in this regime, despite the current being predominantly buoyancy-driven along

the upper boundary. Figures 5.5 and 5.6 shows that this regime is only fully observed for very small values of A. Figure 5.7c shows that the scalings suggested by (5.35) collapse of the numerical solution appropriately. In this figure, the analytical solution has been translated to account for the assumed non-zero thickness of the aquifer at the origin. This solution also does not provide information about the relationship between the upper and lower contact points of the front with the top and base of the aquifer.

Regime 4a: Late unconfined flow, $AX_N \gg H$ and $AX_N \gg 1$

At late times, extent of the current is large enough that the thickness of the aquifer is much greater than the thickness of the gravity current over most of its length, $AX_N \gg H$ and $AX_N \gg 1$. In this limit the current is predominantly driven by gravitational slumping of the front and the confining pressure is negligible. The similarity solution for this regime is therefore the same as given in Section 5.4.1. This solution indicates that for very long time scales the pressure in the ambient fluid is again negligible and hence the base of the aquifer is effectively infinitely distant from the top. Figures 5.5 and 5.6 show that the transition to this regime occurs for $A \sim 1$. The shape of the front of the current in this regime is well described by the unconfined similarity solution (Figure 5.7d).

5.4.2 Sloped Upper Boundary

For the situation of a sloped upper boundary, where $d = d_0 - \alpha x$, (5.7) can be scaled in a similar manner to (5.12) using (5.14) to give

$$\frac{\partial H}{\partial T} + \frac{\partial}{\partial X}\left(\frac{H}{1+AX}\right) = \frac{\partial}{\partial X}\left[\frac{(1+AX-H)}{1+AX}H\frac{\partial H}{\partial X}\right] - \frac{\partial}{\partial X}\left[\frac{(1+AX-H)}{1+AX}AH\right], \quad (5.36)$$

subject to the boundary conditions described by (5.16).

Snapshots of the current at four different stages of its evolution are shown in Figure 5.8. In a similar fashion to a current spreading on a flat roof, at early times, the current has not yet made contact with the base of the aquifer, and so spreading is effectively unconfined.

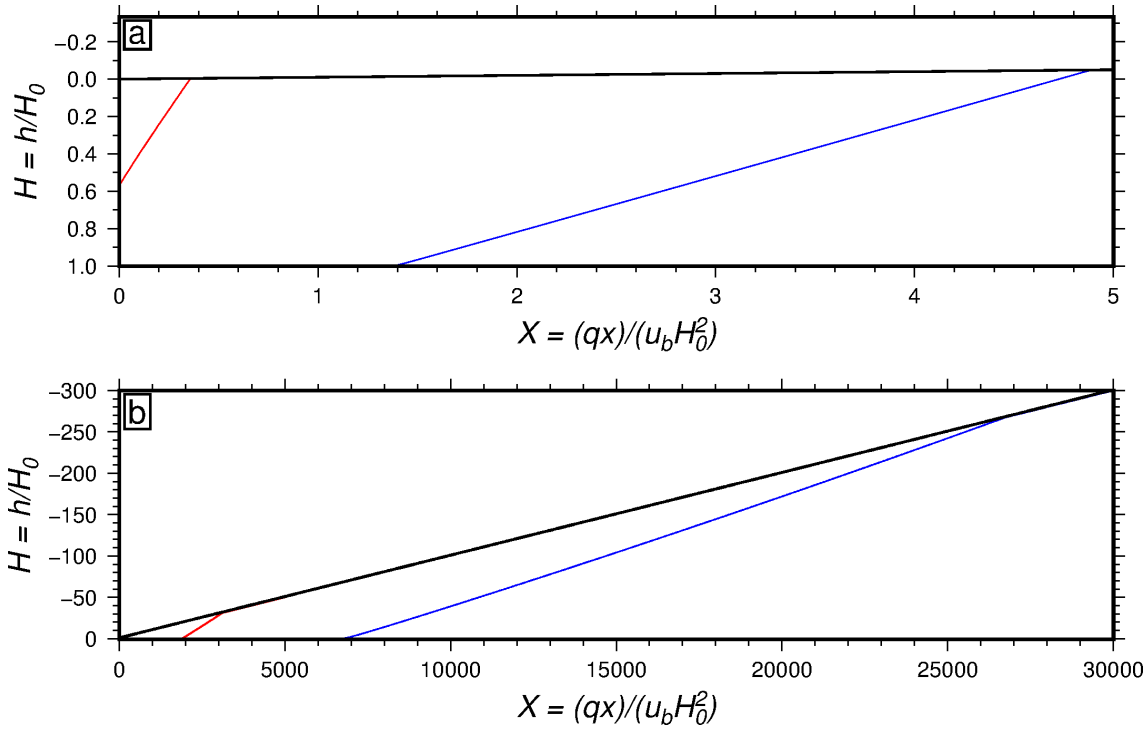

Figure 5.8: Snapshots of current on sloped roof with $A = 0.01$. (a) Early to early intermediate times. Red: $T = 10^{-1}$, Blue: $T = 10^{0.5}$. Vertical exaggeration = 1. **(b)** Late intermediate to late times. Red: $T = 10^{4.5}$, Blue: $T = 10^{6}$. Vertical exaggeration = 0.01. Black lines = aquifer boundary.

At early intermediate times, contact is made with the base. The current again experiences constant confinement and hence spreads with a straight interface between the roof and base contact points. At late intermediate times, the current still spreads along both the roof and base of the aquifer, but the contact points with these surfaces move further apart as gradients in the confinement become important. Finally, at late times the contact with the lower boundary ceases to advance, and the current propagates up the roof of the aquifer. In this late time regime, the interface between the two fluids parallels the upper surface beyond the contact point with the base of the aquifer, and only becomes thin near the nose of the current, consistent with flow up a sloping unconfined surface.

The first three terms of (5.36) are identical to (5.12), and hence the first three flow regimes encountered by a gravity current flowing up a slope with a horizontal confining base are the same as regimes 1–3, described above (Figures 5.9 & 5.10). Despite the current now flowing up the sloped boundary, the times at which transitions between these regimes occur

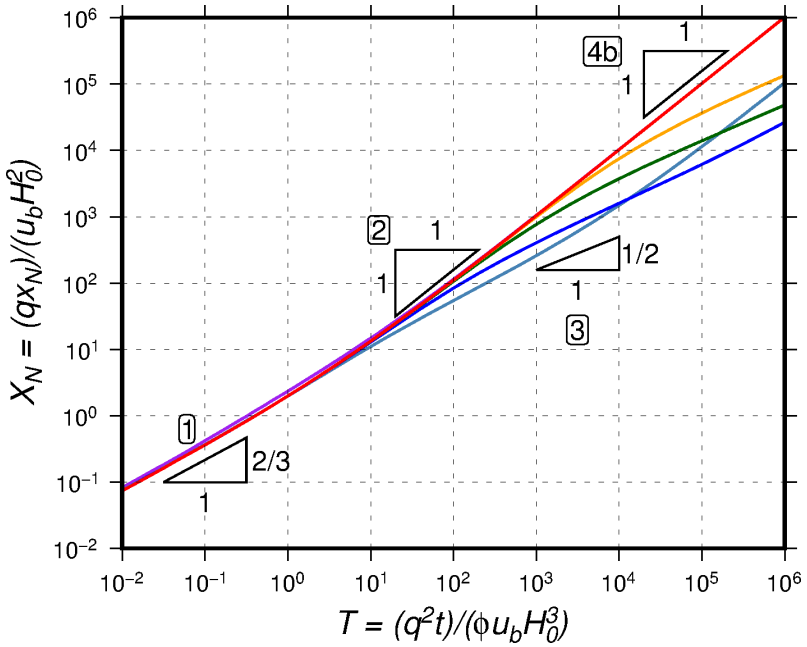

Figure 5.9: Nose contact position of the injected fluid against time for flow on sloped roof with flat base. Purple: $A = 1$, light blue: $A = 0.1$, blue: $A = 0.01$, green: $A = 0.001$, orange: $A = 0.0001$, red: $A = 0$. Flow regime asymptotes labelled on figure.

are comparable. Once again, the similarity solutions for regime 3 indicate that the base of the aquifer can control the flow of the current along the top surface. Figure 5.11 shows good agreement between the analytical and numerical solutions. The analytical solution for regime 3 has been translated to account for the non-zero aquifer thickness at the origin. However, (5.36) has an extra term that governs the up-slope advection of the current due to buoyancy and which controls the flow of the current at long time scales.

Regime 4b: Late buoyant flow up a slope, $T \gg 1$, $AX_N \gg H$ & $AX_N \gg 1$

At late times, $T \gg 1$, the confining base of the aquifer is distant compared to the thickness of the current, $AX \gg H$. In this regime, the pressure due to confinement is no longer the dominant driving force for the current. Instead, the fluid flows buoyantly beneath the sloped roof of the aquifer under gravity. In this regime, (5.36) can be expressed, in the limit that $AX \gg H$ and $AX \gg 1$, as

$$\frac{\partial H}{\partial T} + A\frac{\partial H}{\partial X} = 0. \tag{5.37}$$

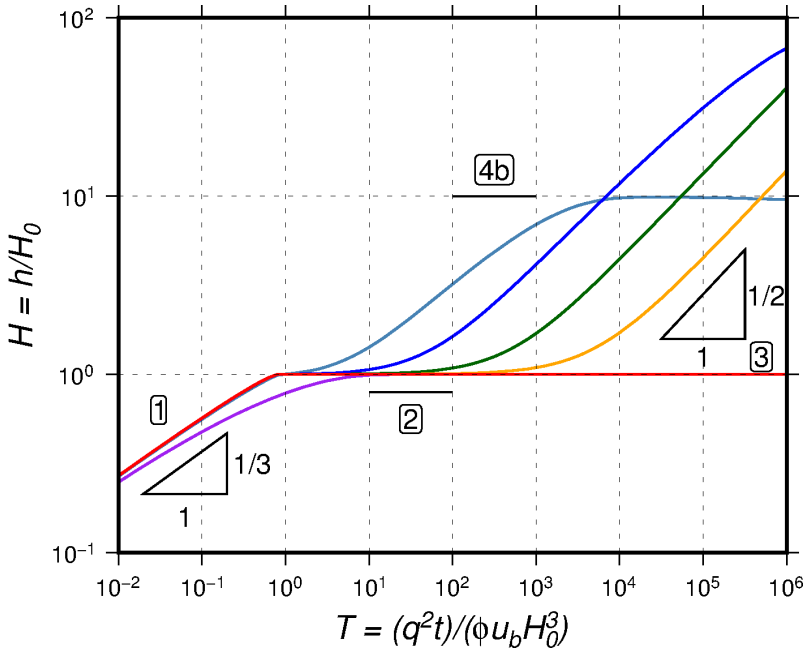

Figure 5.10: Maximum thickness of the injected fluid against time for flow on sloped roof with flat base. Purple: $A = 1$, light blue: $A = 0.1$, blue: $A = 0.01$, green: $A = 0.001$, orange: $A = 0.0001$, red: $A = 0$. Flow regime asymptotes labelled on figure.

This equation describes the advection of the current up-slope, and is independent of the thickness of the aquifer. Scaling (5.37) leads to the definition of the following similarity variables

$$\eta = \frac{X}{AT}, \tag{5.38a}$$

$$H = \frac{1}{A} f(\eta). \tag{5.38b}$$

These scalings indicate that the extent of the current is proportional to T, and moderated by the gradient of the upper boundary, A. The maximum thickness of the current is determined by the gradient of the upper boundary. These terms are independent of the thickness of the aquifer. Using the scalings given in (5.38), (5.37) becomes

$$(1 - \eta)\frac{\partial f}{\partial \eta} = 0, \tag{5.39}$$

which suggests that $f = c$, where c is a constant. Rescaling f and η, using $\xi = \eta/\eta_N$ and $f(\eta) = \eta_N^\beta F(\xi)$, leads to

$$(\eta_N^{\beta-1} - \xi\eta_N^\beta)F' = 0. \tag{5.40}$$

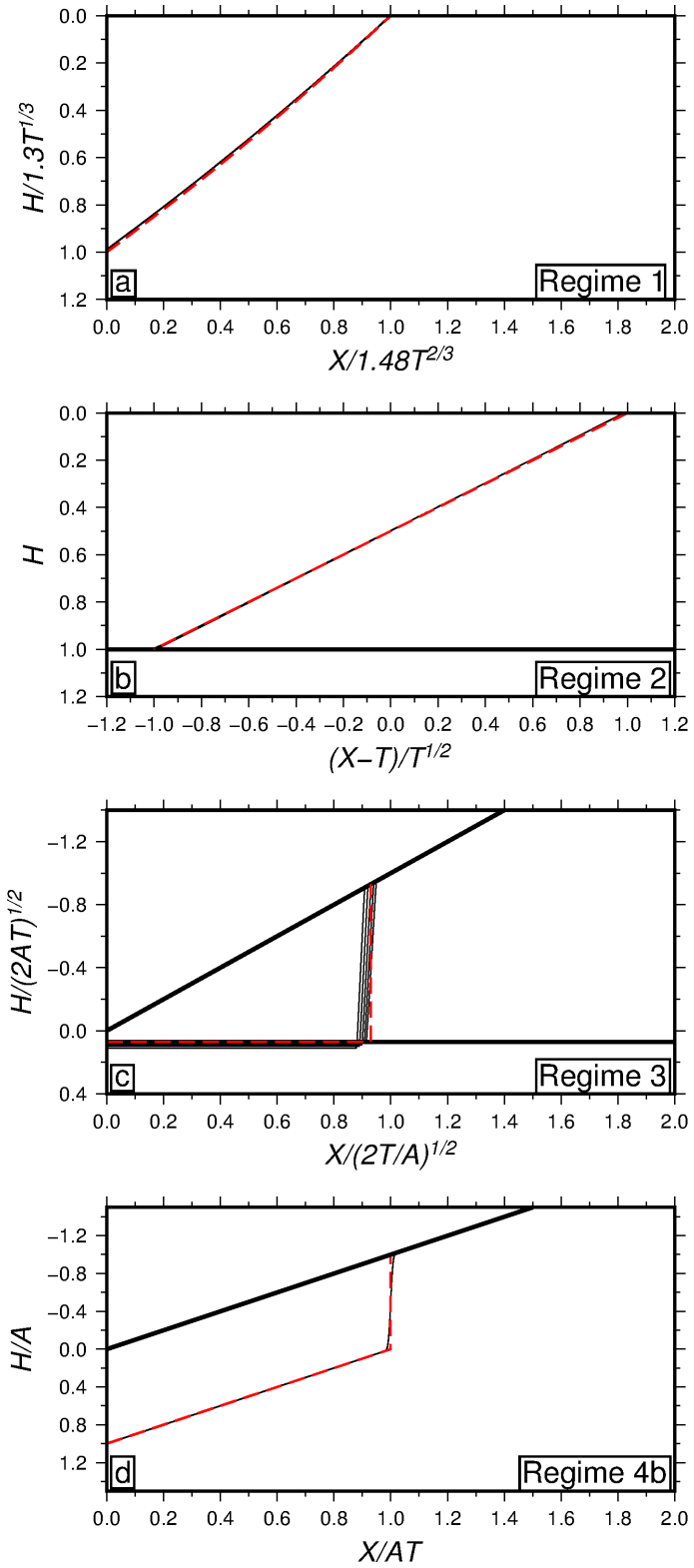

Figure 5.11: Gravity current in an aquifer with sloping roof and diverging confinement. Analytical (red dash line) and numerical solutions (black line) shown for different regimes. **(a)** Regime 1, early times, $T \ll 1$. **(b)** Regime 2, early intermediate times, $T \sim 1$. **(c)** Regime 3, late intermediate times, $T \gg 1$, $AX \gg 1$. **(d)** Regime 4b, late times, $T \gg 1$, $AX \gg H$. Note that the slope of the roof of the aquifer has been imposed on these analytical solutions for clarity.

Equating terms suggests that $\eta_N = 1$, and hence

$$(1 - \xi)F' = 0. \tag{5.41}$$

Again, to satisfy this equation, F is a constant, and so conservation of mass can be written as

$$1 = F \int_0^1 d\xi, \tag{5.42}$$

which gives $F = 1$ for $\xi = (0, 1)$. The similarity solutions are therefore

$$X_N = AT \tag{5.43a}$$

$$H = \frac{1}{A}. \tag{5.43b}$$

These solutions show that the extent of the nose of the current is controlled by the gradient of the slope of the aquifer, while the thickness of the current is a constant and determined by the inverse of the slope of the roof of the aquifer, in keeping with the solution found by Huppert & Woods (1995). Figures 5.9 and 5.10 show that for $A = 1$, this regime is entered immediately following the unconfined regime. Figure 5.11d shows that this analytical solution provides a good match to the numerical solution. The small differences between the numerical and analytical solutions are due to approximations made when neglecting the diffusive terms in the analytical solution.

5.5 Discussion

The flow regimes derived analytically above describe the extent of the nose of the current and the thickness of the current as a function of time. These regimes show good agreement with the numerical solutions in all regimes (Figures 5.7 and 5.11). These analytical and numerical solutions show that in the case of a buoyant fluid flowing in a confined aquifer with uniformly diverging boundaries, the base of the aquifer plays an important role in controlling the thickness and the extent of the current. The good agreement between the analytical and numerical solutions suggests that this numerical scheme is capable of modelling the flow of

fluids in variable confined aquifers. This numerical scheme is shown to be stable on a range of time scales, length scales and gradients in aquifer geometry.

The extent of the current in early times is controlled initially by buoyant slumping of the current under gravity. Once the current has made contact with the opposite confining boundary, pressure driven flow becomes dominant, and the current extends linearly with time. At late times, the extent is either controlled by unconfined spreading (horizontal top) or by advection up a slope (sloped top). These limits have been studied previously by Huppert & Woods (1995), Pegler *et al.* (2014) and Zheng *et al.* (2015). However, in between these end-members is a regime in which the extent of the current increases as $T^{1/2}$, which is moderated by the gradient of the aquifer thickness. This regime is observed regardless of whether the current is flowing along the horizontal or sloped boundary, and has not previously been studied.

Similarly, the thickness of the current at early times is limited by the thickness of the aquifer at the origin, H_0. At very long times, the thickness of the aquifer has no effect on the maximum thickness of the current. In between these end-member regimes, the thickness of the current is controlled by the gradient of the confining boundary. Again, this regime occurs regardless of which boundary the current is flowing along. It is worth noting again that, while these numerical experiments were calculated for a buoyant current, these calculations are also valid for a dense current in the equivalent confined aquifer with diverging boundaries.

Figures 5.5, 5.6, 5.9 and 5.10 show clearly that transition times between regimes are a function of the boundary gradient, A. Gravity currents flowing in aquifers with steeper boundary gradients do not appear to observe regimes 2 and 3. To understand how the boundary gradient affects the transition times between flow regimes, a regime diagram is constructed by equating the asymptotes for each regime in turn (Figure 5.12). Transitions between regimes 1, 2 and 3 are independent of which boundary is sloped. Transition between regimes 3 and 4 occurs at a slightly later time if the current is flowing along the sloped boundary (dashed line, Figure 5.12). Transition times between regimes are found by equating the analytical solutions for adjacent regimes. The transition time between early and early intermediate regimes is found to be $T_{12} \sim 1.48$[3]. The time of this transition does not depend

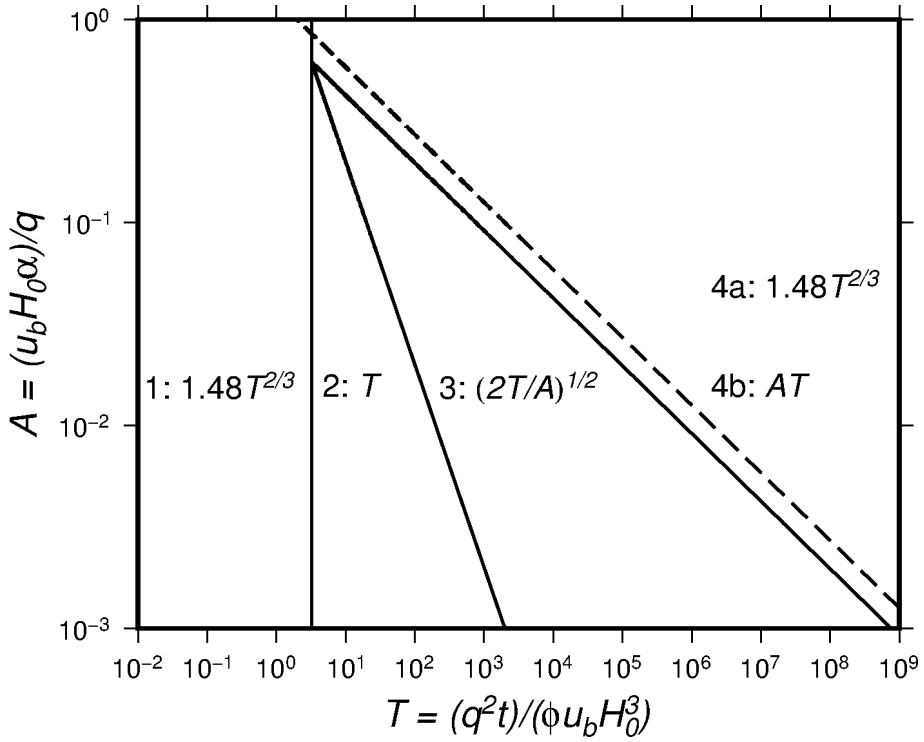

Figure 5.12: Regime diagram for extent of current showing time against slope angle. Dashed line shows transition from 3 to 4b.

on the gradient in aquifer thickness. The transition between early intermediate and late intermediate regimes occurs at $T_{23} \sim (2/A)$, meaning that this regime is entered later for shallower gradients in aquifer thickness. The transition between late intermediate and late regimes depends on whether the upper or lower boundary is sloped. For a buoyant fluid flowing beneath a flat roof, this transition occurs at $T_{34a} \sim [2/(1.48^2 A)]^3$. If instead the upper boundary is sloped, this transition occurs slightly later, when $T_{34b} \sim 2/A^3$. Once this transition has been crossed the the lower boundary no longer affects the maximum extent of the current. If A is small, the transition time for this final regime is very large. For large A, regimes 2 and 3 can effectively be bypassed, and the flow can transition directly from unconfined flow to either advection up slope or continue to flow in the unconfined regime. In the limit of $A = 0$, only regimes 1 and 2 are observed. Converging boundaries, $A < 0$, were not investigated in this study.

Figure 5.13 shows the relationships between the regimes controlling the thickness of the current and the gradient of the confining boundary. Again, the time of the transition be-

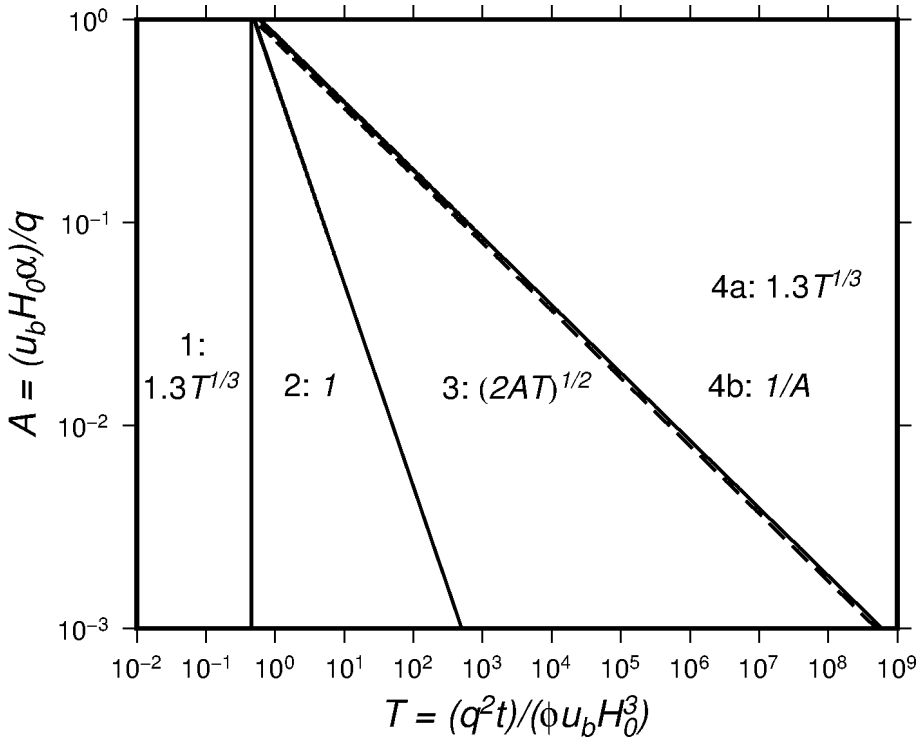

Figure 5.13: Regime diagram for thickness of current showing time against slope angle. Dashed line shows transition from 3 to 4b.

tween regimes can be found by equating the analytical solutions for flow in each regime. The transition time between the two early regimes is given by $T_{12} \sim 1.3^{-3}$, and is again independent of the gradient in aquifer thickness. Between early intermediate and late intermediate times, the transition time is found to be $T_{23} \sim 1/(2A)$. For a buoyant current flowing underneath a horizontal upper boundary, the transition to the late time regime occurs at $T_{34a} \sim [1.3^2/(2A)]^3$, while if the fluid is flowing underneath a sloped boundary $T_{34b} \sim 1/(2A^3)$. As for the extent of the current, once this transition has been crossed the the lower boundary no longer affects the maximum thickness of the current. The transition times between the late intermediate and late flow regimes are very similar, and are controlled by the gradient in aquifer thickness rather than whether the upper boundary is sloped or flat. These transitions occur slightly earlier time scales than the transitions for the current extent.

5.6 Summary

This study shows that variable confinement of an aquifer can play a significant role in controlling the shape and speed of a gravity current flowing within it. A previously unstudied flow regime for diverging aquifer boundaries has been described analytically and numerically. This regime occupies the transition between the effectively parallel confined regime and the unconfined end-members. The transition times between the different regimes have been estimated and verified analytically and numerically. The numerical scheme used to model the flow of fluid in a variably confined aquifer has been shown to be accurate and stable in two dimensions. Further work is now required to expand these equations to describe fluid flow in a three dimensional case in a Cartesian coordinate system.

Since this study focussed on a two dimensional aquifer with equal viscosity fluids, it is difficult to draw direct comparison between the results presented here and CO_2 flowing through a saline aquifer such as that found at Sleipner. However, this work shows that for an aquifer in which the confining boundaries are not parallel, the current may propagate at different rates based on the proximity of the base of the aquifer. For example, as the CO_2 in Layer 9 at Sleipner becomes thicker, the change in thickness of the aquifer around the north-striking ridge might promote flow through the thicker region of the aquifer. To test this idea further, this study needs to be expanded to three dimensions. This expansion, as well as considering fluids of different viscosities, remains a topic of future work.

Chapter 6

CO_2 flow within Layer 8

6.1 Introduction

Previous attempts to constrain the volume of CO_2 within individual layers at Sleipner have been confined almost exclusively to Layer 9. However, because $\sim$90 % of the total CO_2 injected into the Utsira Formation is thought to reside in layers below Layer 9, the lower part of the reservoir should not be neglected. Measurements of areal extent of the lowermost layers suggests that the growth rate of these layers is declining (Figure 2.16). Since the flux of CO_2 injected into the base of the reservoir is approximately constant, this observation suggests that the flux to the upper layers is increasing. In Chapter 3 the flux into Layer 9 was found to be increasing with time. Measuring the volume of CO_2 stored in Layer 8 as a function of time would provide further information on the vertical flux of CO_2 through the reservoir.

Estimating the volume of CO_2 below Layer 9 is complicated by multiple factors. Attenua-

tion and scattering of the seismic waves causes a reduction in the strength of the returned signal. Due to the low velocity of seismic waves passing through CO_2 in Layer 9, reflections below are pushed down, causing neighbouring traces to appear uncorrelated. Uncertainty in the distribution of CO_2 within the reservoir makes all of these factors difficult to account and correct for. Attempting to model the reflections from CO_2 layers using amplitudes and changes in travel-time are consequently subject to such large uncertainties that the results would not be meaningful. Previous attempts to estimate the volume of CO_2 stored in individual layers below Layer 9 using seismic reflections have therefore been limited to analytical models that match the seismically observed areal extent, or full reservoir simulations (e.g. Arts *et al.*, 2008; Bickle *et al.*, 2007; Boait *et al.*, 2012).

For the majority of these layers, the topography of the caprock that CO_2 is trapped beneath cannot be imaged in the baseline seismic reflection survey. It is only for the CO_2 in Layer 8, which is trapped by the 5 m Shale, that the topography of the caprock can be measured. In this chapter, I constrain the volume of CO_2 in Layer 8 using four methods that exploit this knowledge of the caprock topography. Potential future flow of CO_2 in this layer is also discussed.

6.2 Previous Work

Due to the difficulty in studying the layers below Layer 9, Layer 8 has received relatively little attention. Bickle *et al.* (2007) used reflection amplitudes to infer the thickness of Layer 8 up to 2002, under the assumption that the attenuation of the seismic signal caused by CO_2 in Layer 9 will not be significant due to its small size. These authors calibrated the amplitude-thickness relationship by assuming that the maximum amplitude reflection observed in the layer was equal to the tuning thickness. The maximum thickness in 2002 was estimated to be $\sim$6 m in the centre of the plume, gradually thinning towards the edge. However, as the authors point out, these measurements are subject to unquantified uncertainties in the calibration of the amplitude thickness relationship, the velocity of seismic waves through CO_2-saturated sandstone and the magnitude and lateral variation of attenuation caused by

CO_2 in Layer 9. Bickle *et al.* (2007) modelled the change in thickness and radial extent of the layer with time as a gravity current flowing across a flat plane in order to constrain the input flux of CO_2. The CO_2 flux into the layer was modelled as $q = nC(t - t_0)^{n-1}$, where C ($m^3 yr^{1/n}$) and n are constants, t is time in years and t_0 refers to the initiation time of the layer relative to the start of injection. The authors found that the fit improved for $n > 1$, indicating that the flux of CO_2 into Layer 8 is increasing with time. However, they also note that for $n > 2.5$, the initiation time is less than zero, implying that CO_2 had reached Layer 8 before it was injected at the base of the reservoir. While t_0 clearly cannot be negative, these results suggest that the flux into this layer is growing at an increasing rate in the early years.

Boait *et al.* (2012) used the areal extent of the layers measured on seismic reflection surveys up to 2008 to estimate the volume of CO_2 within all layers in the plume. Since caprock topography is unconstrained for most layers, two simple layer-spreading models were tested. First, the radial extent of the layer was modelled as a gravity current flowing on a flat plane with a constant input flux (i.e. $n = 1$). In this case, the radial extent of the CO_2 layer should be proportional to the square root of time. This approach produced a good fit to the data up to 2008 for Layer 8, and yielded an estimate of the flux of CO_2 into this layer of $q = 6.3 \times 10^4$ m^3 yr^{-1}. However, this model neglects the influence of caprock topography on the flow of fluid in the layer (Figure 6.1). Numerical modelling of the gravity current in Chapter 4 has shown that even shallow topographic gradients can have a significant effect on the planform of a layer from the early stages of its development. The assumption of flow across a flat surface may therefore not adequately capture the full dynamics of flow in this layer. The second model estimated the volume of fluid required to fill a hemi-ellipsoidal cap in order to match the basal area of the fluid with its seismically observed areal extent. Boait *et al.* (2012) determined the eccentricity of the ellipsoid using the CO_2 layer extent. The vertical axis was estimated to be 20 m for all layers. Due to the poor fit to the observed areal extent with time that this model produces for some layers, the authors preferred the gravity current model. However, the general trend of growth in areal extent for Layer 8 suggests that this model might be applicable with some modifications.

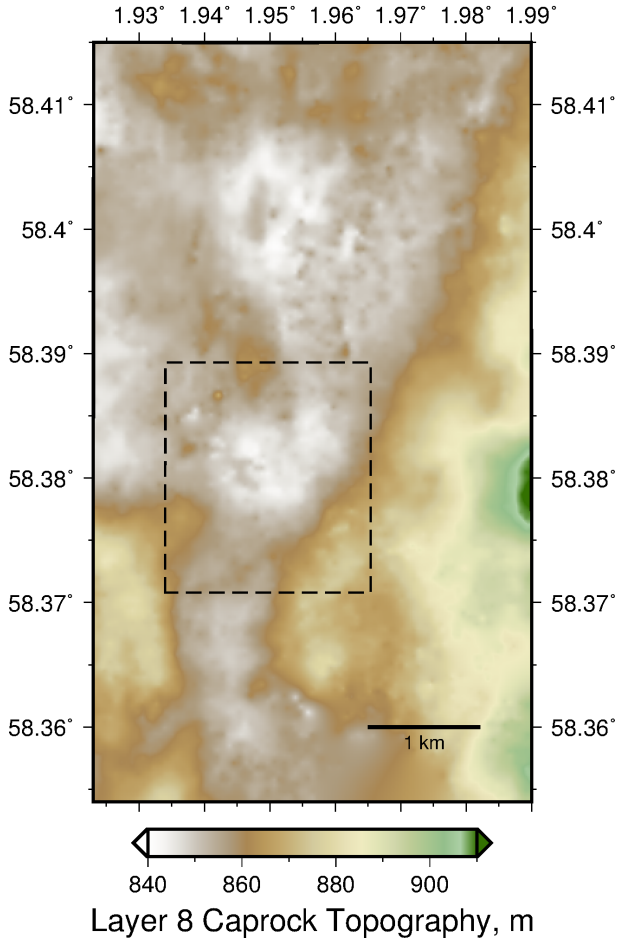

Figure 6.1: Topography of Layer 8 extracted from baseline seismic reflection survey. Dashed box shows extent of Figure 6.2.

Several authors have attempted to model the whole plume using simple reservoir simulations (e.g. Lindeberg *et al.*, 2001; Arts *et al.*, 2008; Chadwick & Noy, 2010). However, the focus of these studies was the flow of CO_2 through the reservoir as a whole, meaning that there is little discussion on the flow of CO_2 through individual layers. Boait *et al.* (2011) used the numerical Darcy flow simulator TOUGH2 to model the CO_2 flow through the entire reservoir. In this simulation, the properties of low permeability mudstones layers were adjusted so that the arrival time of CO_2 in each layer matched estimates made using the areal growth rate for each layer. The radial extent of Layer 8 in the simulation was found to be much greater than observed on the seismic reflection surveys. A possible cause of this discrepancy is the assumption of a flat caprock, which permits the area of the layer to increase uninhibited by topographic gradients.

6.3 Measuring the Thickness of Layer 8

The paucity of studies on the lower layers highlights the difficulty of making accurate measurements of the thickness of CO_2 below the shallowest layer from the seismic reflection surveys. The methods tested in this chapter rely either on measurements made on the pre-injection survey or on measurements that should not be significantly affected by overlying CO_2. Three of the methods used here rely on measurements of the areal extent of the layer. Due to the presence of low seismic velocity CO_2 above much of Layer 8, accurately measuring the edge of the plume using amplitude or travel-time anomaly measurements is more difficult. Measurements of the edge of the layer are therefore less tightly constrained than for Layer 9. For this reason, a higher threshold thickness of 0.75 m is chosen as the minimum thickness of CO_2 observable at the layer's edge, with upper and lower bounds of 1 m and 0.5 m chosen to give representative uncertainties on this measurement.

6.3.1 Separation of Reflections

As discussed in Chapter 3, a simple way to constrain the thickness of a CO_2 layer is to use the separation of the peak and trough of reflections from its top and base. The vertical resolution of the broadband seismic reflection survey enables the thickness of CO_2 layers as thin as $\sim$6.5 m to be measured (Section 3.4). Figure 6.2 shows the thickness of the central region of Layer 8 that can be determined using this method. In this central region, it can be seen that the layer is up to approximately 12 m thick. The thickest region of the layer corresponds to the centre of the topographic dome beneath which Layer 8 is trapped.

The measured CO_2 distribution suggests that the thickness of the layer's outer region can be approximated by extrapolating from the central region to the observed plume's edge while accounting for caprock topography. At the edge of the plume the CO_2 thickness is assumed to be 0.75 m (Figure 6.2b-c). The thickness of the layer is then determined to be the distance from the interpolated base to the caprock. This interpolation assumes that the base of the CO_2 layer is flat and therefore that the layer is in buoyant equilibrium. The increase in planform area between seismic reflection surveys suggests that CO_2 is still migrating into

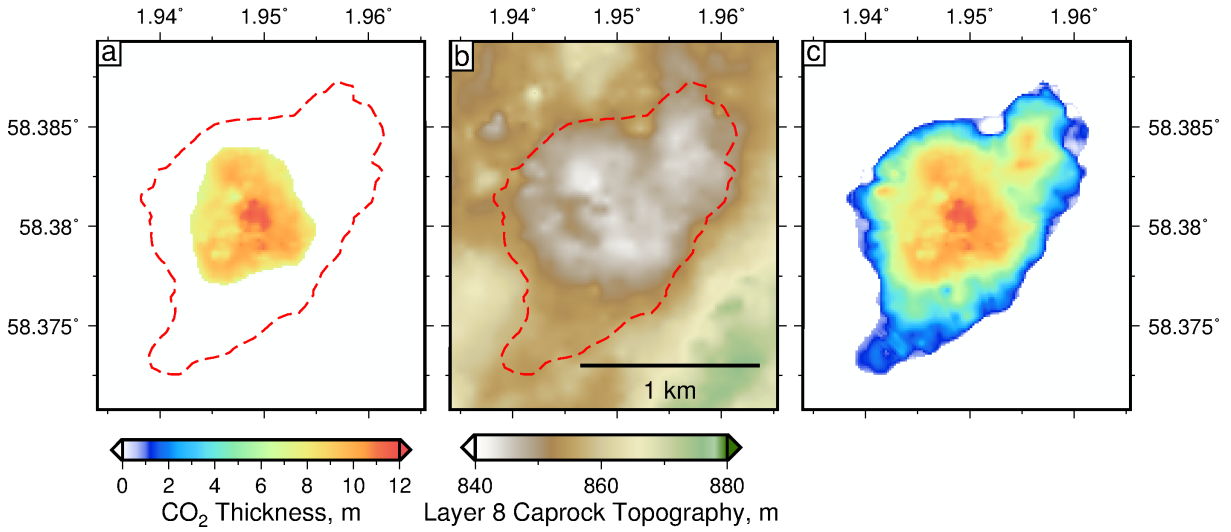

Figure 6.2: **(a)** Thickness of Layer 8 from 2010 broadband survey, measured using separation of reflections. Red dashed line = outline of CO_2 layer measured on seismic reflection surveys. **(b)** Topography of Layer 8 caprock. Red dashed line = outline of CO_2 layer measured on seismic reflection surveys. **(c)** Interpolated layer thickness using (a) and assuming edge of plume is 0.75 m thick.

Layer 8. Flow into and laterally through the layer means that its base is unlikely to be flat. However, due to the correlation between the edge of the layer and the structural trap, this assumption is likely to be reasonable (Figure 6.2b). Upper and lower bounds on this estimate are calculated using threshold thicknesses at the edge of the layer of 1 m and 0.5 m. Assuming a porosity of 0.37 and a uniform CO_2 saturation of 0.8, this method suggests that the CO_2volume in Layer 8 by 2010 is $\sim 2.1 \pm 0.05 \times 10^6$ m^3.

A small central region of this layer is thick enough to be measured using separation of reflections on the 2008 and 2010 time-lapse surveys. In 2008, the plume's central region was ~11 m at its thickest point, while in 2010 it was ~12 m. The fact that any of the layer is resolvable on these surveys shows that Layer 8 is thicker than Layer 9 on comparable surveys. However, the small size of resolvable regions on these surveys limits the conclusions that can be drawn. Due to the vertical resolution of the time-lapse seismic reflection survey, the CO_2 layer thickness cannot be constrained through time using this method.

6.3.2 Hemi-Ellipsoidal Trap Filling

The domed shape of the topographic trap for Layer 8 suggests that it can be approximated as the cap of a hemi-ellipsoid (Figure 6.3). The benefit of approximating the trap as a three-dimensional geometric shape is that a simple mathematical relationship can be found between the volume of fluid filling the cap and the planform area of the fluid layer's base.

Boait *et al.* (2012) used this relationship to estimate the volume of CO_2 in all layers at the Sleipner field. In their study, this model generally produced a poor fit to the planform area with time. However, the change in planform area with time has been reassessed in this study, and also includes information from the 2010 survey. The new measurements for Layer 8 suggests that this model might be able to provide insight into the filling of this layer.

Boait *et al.* (2012) used the planform area of Layer 8 to estimate the eccentricity of the ellipse. The height of the dome was assumed to be 20 m based on approximate thicknesses of the sand layer for each CO_2 horizon (10–40 m). In this study, the topography of the Layer 8 caprock is used to find the best-fitting hemi-ellipsoidal trap. Using this simplified geometry, the volume of fluid required to match the observed areal extent can be constrained.

The equation for a hemi-ellipsoidal trap is given by

$$\frac{[(x-x_0)\cos\theta+(y-y_0)\sin\theta]^2}{a^2}+\frac{[(x-x_0)\cos\theta-(y-y_0)\sin\theta]^2}{b^2}+\frac{(z-z_0)^2}{c^2}=1, \quad (6.1)$$

for positive x, y and z, where x_0, y_0 and z_0 refer to the location of the ellipsoid's centre in space, a, b and c are the size of the principal axes and θ refers to the rotation of the ellipsoid about the z axis. By fitting a, b, c, x_0, y_0, z_0 and θ to four cross sections through the topography extracted from the seismic images, a hemi-ellipsoid that approximates the topography of the Layer 8 trap can be constructed (Figure 6.3b). Example cross-sections through the topography and best-fit hemi-ellipsoidal trap are shown in Figure 6.3c-d. For Layer 8, the best-fitting principal axes are $a = 775 \pm 15$ m, $b = 1000 \pm 15$ m and $c = 22 \pm 1$ m.

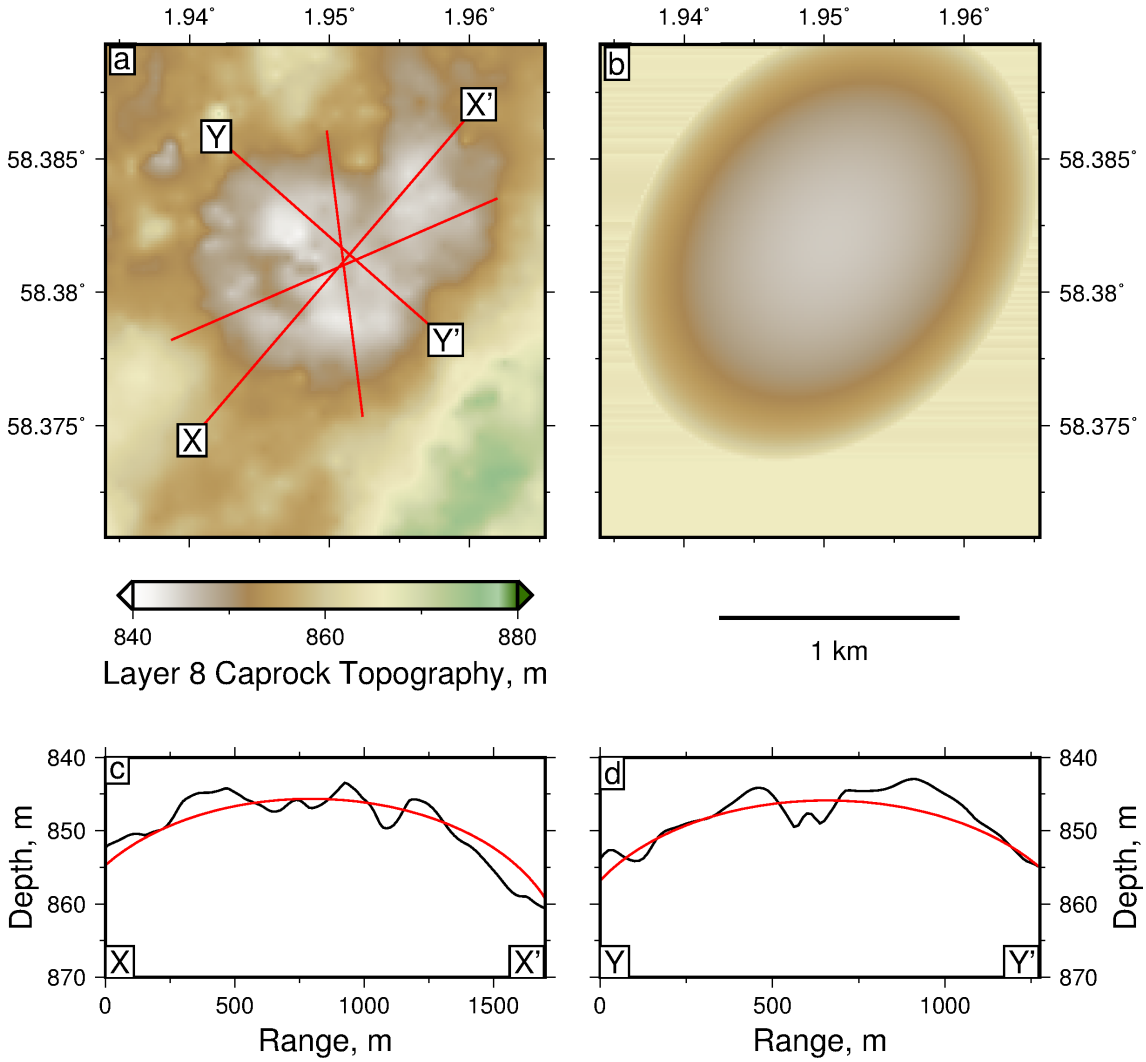

Figure 6.3: Topography of Layer 8 caprock. **(a)** Topography of caprock extracted from seismic reflection images. Red lines = transects used to fit hemi-ellipsoid. **(b)** Hemi-ellipsoid used to approximate topography of Layer 8 caprock. **(c)** Cross section through trap from X to X′. **(d)** Cross section through trap from Y to Y′. Black line = caprock topography. Red line = hemi-ellipsoidal trap.

Following the analysis of Boait *et al.* (2012), if the cap of this ellipsoid is filled with fluid to a depth h from the top, where $h = c - z$, the horizontal area of the base of the fluid, $A(h)$ can be calculated using

$$A(h) = \pi ab \left[\frac{2h}{c} - \left(\frac{h^2}{c^2} \right) \right]. \tag{6.2}$$

The volume of fluid, V, trapped in the cap of this ellipsoid is given by integrating (6.2) in the vertical direction between 0 and h,

$$V(h) = \pi \phi S_{CO_2} abc \left[\frac{h^2}{c^2} - \left(\frac{h^3}{3c^3} \right) \right], \tag{6.3}$$

where ϕ is the porosity and S_{CO_2} is the CO_2 saturation within the reservoir. If volume is approximated as $V = C(t - t_0)^n$, where t_0 is the initiation time of layer filling and C and n are constants, then the relationship between the layer's basal area and time is given by

$$t = t_0 + \left[\frac{\pi \phi S_{CO_2} abc}{q} \left(B^2 - \frac{B^3}{3} \right) \right]^{1/n}, \tag{6.4}$$

where

$$B = 1 - \sqrt{1 - \frac{A}{\pi ab}}. \tag{6.5}$$

Figure 6.4 shows planform area against time for Layer 8. Fitting (6.4) to the data with two free parameters, initiation time, t_0, and flux, C, with $n = 1$ (i.e. constant input flux) yields a reasonable fit to the data, with $t_0 = 1999.3 \pm 0.1$ and $C = 1.2 \pm 0.1 \times 10^5$ m^3 yr^{-1} (Figure 6.4). This fit to the area at early and late times is inhibited by the constant input flux constraint. However, this model fits the planform area within its estimated uncertainty. The fit exhibited by this model suggests an improvement could be made by allowing the flux to vary through time.

Allowing the flux to vary as a function of time produces an excellent fit to the change in area with time, where $t_0 = 1998.7 \pm 0.3$, $C = 5 \pm 1.7 \times 10^4$ m^3 yr^{-n} and $n = 1.4 \pm 0.1$ (Figure 6.4). Permitting a small flux at early times allows the initial area growth to be slower, while at late times the area growth can increase faster than for the constant flux case.

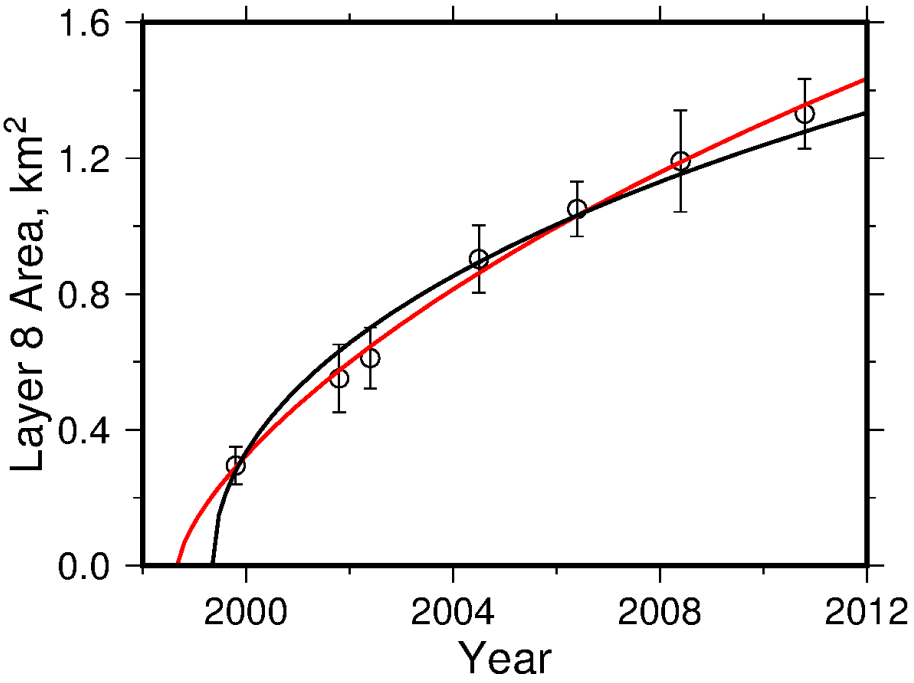

Figure 6.4: Layer 8 area against time. Black line = constant flux model. Red line = increasing flux model.

Due to the resolution of the seismic reflection surveys, the observed plume edge occurs when the CO_2 layer is ∼0.75 m thick (Bickle *et al.*, 2007). The assumption of a flat base on these layers means that the volume estimated using these areal measurements is likely to be an underestimate. To address the issue of resolution at the plume edge, a layer of CO_2 0.75 m thick is added to the estimated base of Layer 8 at each time step. This correction adds a volume of CO_2 equal to $0.75\phi S_{CO_2}A$ to the total volume estimate for each year. While this correction does not account for the extreme edges of the plume, these regions are not expected to contribute significantly to the overall volume. The volume of CO_2 in Layer 8 calculated from these two models with the added correction is shown in Figure 6.5. Both of these methods show approximately similar trends, and suggest that by 2010 the volume of CO_2 in Layer 8 is $\sim 1.8 \times 10^6$ m^3.

This method exploits a simple geometric relationship between volume and area for an ellipsoid. The assumptions involved in the method, such as the shape of the trap being approximately hemi-ellipsoidal and the CO_2 having a flat base, mean that this model is only appropriate for very specific cases. For example, these assumptions would clearly be invalid

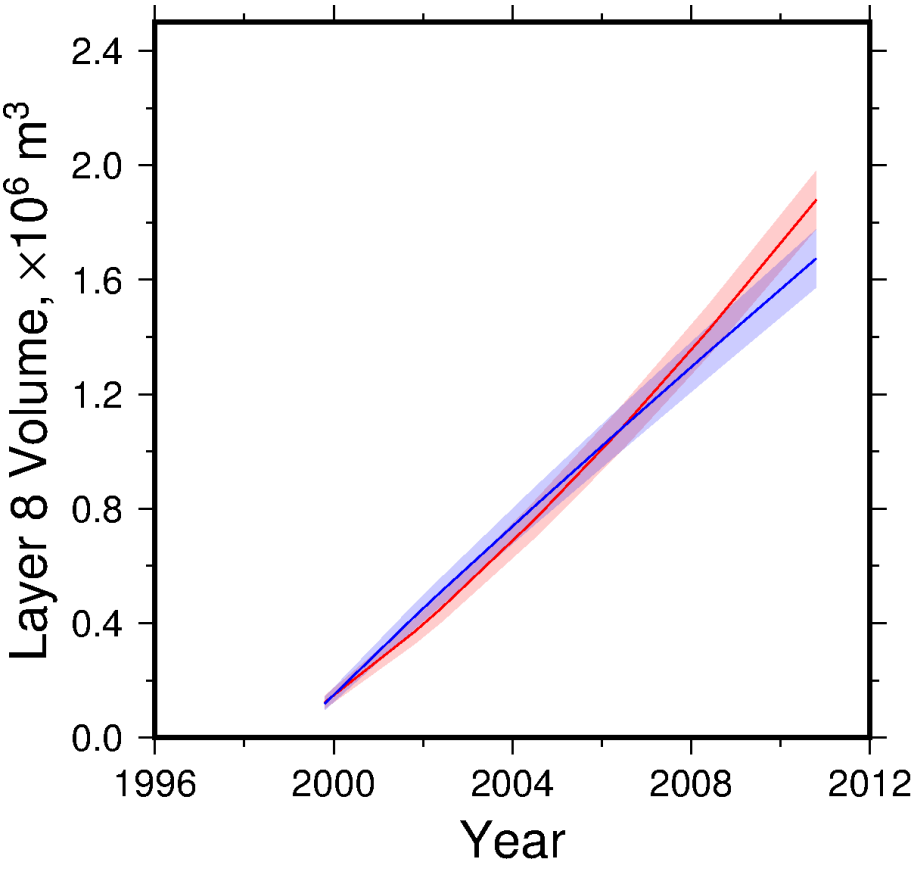

Figure 6.5: Layer 8 volume against time for hemi-ellipsoidal model. Blue line = constant flux model. Red line = increasing flux. Shaded areas = estimated uncertainty from ±0.25 m resolution of the edge of the layer.

for Layer 9 based on the results of Chapters 3 and 4, where CO_2 does not appear to fill a simple trap. The uncertainties involved in this method are significant, the largest of which come from the estimate of trap shape. First, conversion of the topography extracted from the seismic images from two-way travel time into depth is difficult due to uncertainties in the velocity of seismic waves through the overlying lithologies. Secondly, the topography's complex shape extracted from the seismic images cannot exactly be described as a hemi-ellipsoid. A third complication is that the input location of CO_2 into this layer is not at the centre of the hemi-ellipsoid. The off-centre location of the migration point means that in the early years, the CO_2 in Layer 8 will not simply be ponding beneath a structural trap. However, as the layer grows, the uncertainty introduced by this approximation decreases as the CO_2 layer edge encompasses the input location.

Despite these uncertainties, hemi-ellipsoidal trap filling provides a straightforward and simple way to calculate the volume of CO_2 within the layer without the need for complicated numerical modelling. While uncertainties in this method may be large, this approximation is likely to be an underestimate due to the assumption that the CO_2 layer has a flat base.

6.3.3 Structural Analysis

A third method to estimate the thickness of CO_2 in Layer 8 is structural analysis (Figure 6.6). This method assumes that the CO_2 in the layer is ponding beneath a topographic structure. If this layer is in buoyant equilibrium, the base of the CO_2 will be flat. By measuring the edge of the amplitude anomaly observed on the seismic reflection surveys and interpolating a flat base across the topography of the caprock, the thickness of the CO_2 layer can be estimated with time. This method removes the uncertainty associated with converting the topography of the structural trap into a hemi-ellipsoid.

Structural analysis has been used previously to constrain the thickness of Layer 9 with reasonable success (Chadwick & Noy, 2010). The correlation between the topography of Layer 8 and the extent of the amplitude anomaly observed on the seismic reflection surveys suggests that this technique may be appropriate for Layer 8 (Figures 6.3a and 6.7a-g). The CO_2 in Layer 8 appears to be filling a topographic dome, since the edge of the CO_2 layer approximately follows the topographic contours. The thickness of the CO_2 layer estimated using this technique is shown in Figure 6.7h-n. As for hemi-ellipsoidal trap filling, the thickness of CO_2 estimated using this method has been corrected to account for the 0.75 m resolution of the seismic reflection images at the edge of the plume (Figure 6.6). These results suggest that the plume approaches 11 m thick on the 2010 survey. The distribution of CO_2 in the central region in 2010 is similar to that observed using the separation of reflections method (Figure 6.2). The estimated change in volume with time using structural analysis is similar to that obtained using hemi-ellipsoidal trap filling (Figure 6.8).

One region in which structural analysis does not match the observed outline of the plume is

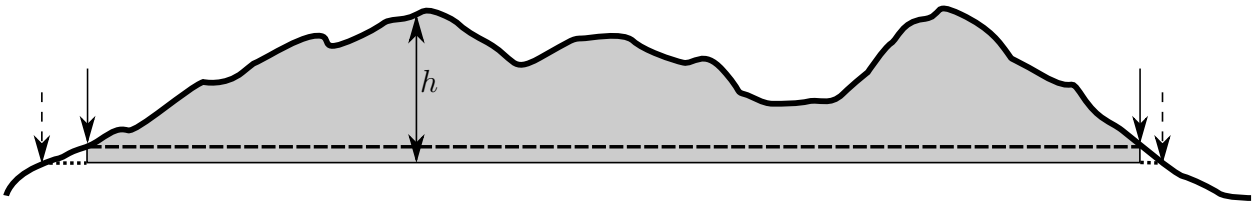

Figure 6.6: Cartoon of measuring CO_2 thickness, h, using structural analysis. Solid line = caprock topography; solid arrows = observed CO_2-water contact; dashed line = interpolated base of CO_2 layer; grey region = calculated volume of CO_2 corrected for resolution at edge of plume. Dashed arrows show how uncertainty is introduced if observed CO_2-water contact does not represent full extent of CO_2 layer.

at the north-eastern edge of the topographic dome (Figure 6.6). This region is estimated to be topographically lower than its surroundings from the seismic reflection surveys. However, this depressed topography produces a distribution of CO_2 that differs from the observed pattern. Analysis of the overburden suggests that this depression lies directly below a pocket of natural gas, and is therefore likely to be an artefact caused by pushdown of the seismic reflections. The magnitude of this pushdown is difficult to quantify, but will reduce the estimated volume of CO_2 in this layer.

6.3.4 Flow Model Inversion

Further insight into the distribution of CO_2 in Layer 8 can be gained by modelling the flow of CO_2 beneath the observed caprock topography using the reservoir simulator developed in Chapter 4. The small spatial extent of the layer means that each flow simulation takes approximately one minute on a single core. The speed of this simulation means that the volume of CO_2 in Layer 8 can be found by minimising the difference between the modelled and observed CO_2 distribution.

The implemented minimisation scheme is primarily based on the difference between the modelled and observed areal extent of the layer. All grid squares inside the measured areal extent on seismic reflection images are assigned a value of 1. If the modelled CO_2 layer in a particular grid square is thicker than a given threshold, that grid square is also assigned a value of 1. The sum of the difference between the modelled and measured area is then

Figure 6.7: Structural analysis of Layer 8. (a-g) Outlines of extent of CO_2 observed on seismic reflection images. **(h-n)** Estimated thickness of CO_2 using structural analysis for all seismic reflection surveys.

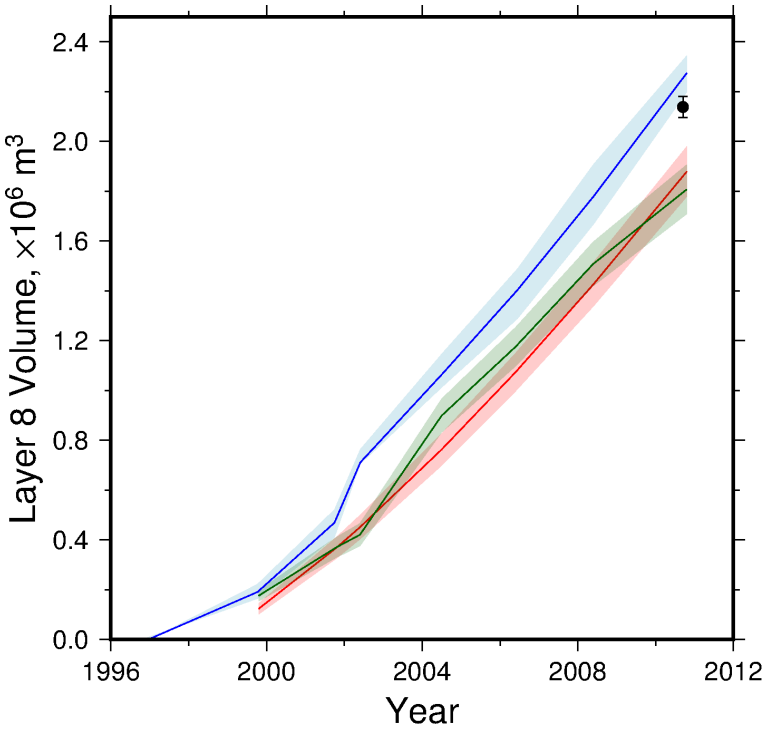

Figure 6.8: Volume estimates for Layer 8. Green line = volume from structural analysis. Red line = volume from hemi-ellipsoid trap filling. Black circle = volume in 2010 from separation of reflections from broadband survey interpolated to edge of amplitude anomaly. Blue line = averaged volume from flow model inversion using threshold of 0.75 m. Shaded areas = upper and lower bounds using threshold values of 1 m and 0.5 m for each method.

calculated and normalised by the measured areal extent. The thickness of the CO_2 layer measured using the 2010 broadband survey is also used to further constrain the parameters for this inversion. The difference between the observed thickness, h^o, and the simulated thickness in 2010, h^s, is found, and weighted by the uncertainty in the measurement of thickness, σ^o (Figure 3.4). The calculated misfit for the thickness measurement is weighted by W such that it is of similar magnitude to the misfit from the area matching calculation. The misfit equation is therefore expressed as

$$M = \sum_{j=1999}^{N_s} \left[\sqrt{\frac{1}{N_a} \sum_{i=1}^{N_a} \left(a_{ij}^s - a_{ij}^o\right)^2} \right] + \frac{1}{W} \sqrt{\frac{1}{N_h} \sum_{i=1}^{N_h} \left(\frac{h_i^s - h_i^o}{\sigma_i^o} \right)^2} \tag{6.6}$$

where i refers to a particular data point, j refers to a particular seismic reflection survey in order from 1999 to 2010, N_s is the number of seismic reflection surveys, a^s is an array of 1's and 0's that refer to all grid squares thicker than a given threshold in the simulation results,

a^o is the same array referring to the observed extent of the CO_2 layer, N_a is the number of grid squares observed to be occupied by CO_2, N_a is the number of grid squares in which the thickness of CO_2 is measurable on the 2010 survey. The misfit equation is minimised using Powell's multidimensional minimisation method (Powell, 1964; Press, 2007). This minimisation scheme is suited to this problem because it does not require gradients in the misfit to be calculated.

To test the validity of this method, the inversion is first performed on Layer 9 and compared to the volume and reservoir parameters estimates from Chapters 3 and 4. Once validated, the model is run on Layer 8.

Inversion for Layer 9

The free parameters in this inversion are the volume of CO_2 in the reservoir at the time of each seismic reflection survey, the initiation time of CO_2 entering the layer, the permeability of the reservoir, and the width and permeability of the channel identified in Chapter 4. The success of this inversion to constrain these parameters is judged against CO_2 volume estimated from the seismic reflection surveys in Chapter 3, and the reservoir parameters found by inversion in Chapter 4. The areal extent of Layer 9 is found using both amplitude and travel-time anomaly measurements to constrain the edge of the plume as tightly as possible (Figure 6.9a-g). Thickness of the central region of the CO_2 layer is constrained using the 2010 broadband survey (Figure 6.9g). Parameters such as the input location for CO_2 and the location of the channel are the same as used in Chapter 4. Due the higher run time for simulations of flow within Layer 9 ($\sim$10 minutes), these inversions take approximately one week to run on a single core.

Three threshold values for the minimum thickness of CO_2 that can be resolved on the seismic images are chosen for the inversion to give a range of possible volume curves. A mid-value of 0.75 m is chosen based on picking the edge of the CO_2 layer using both amplitude and travel-time anomaly measurements. Upper and lower bounds on this threshold are chosen as 1 m

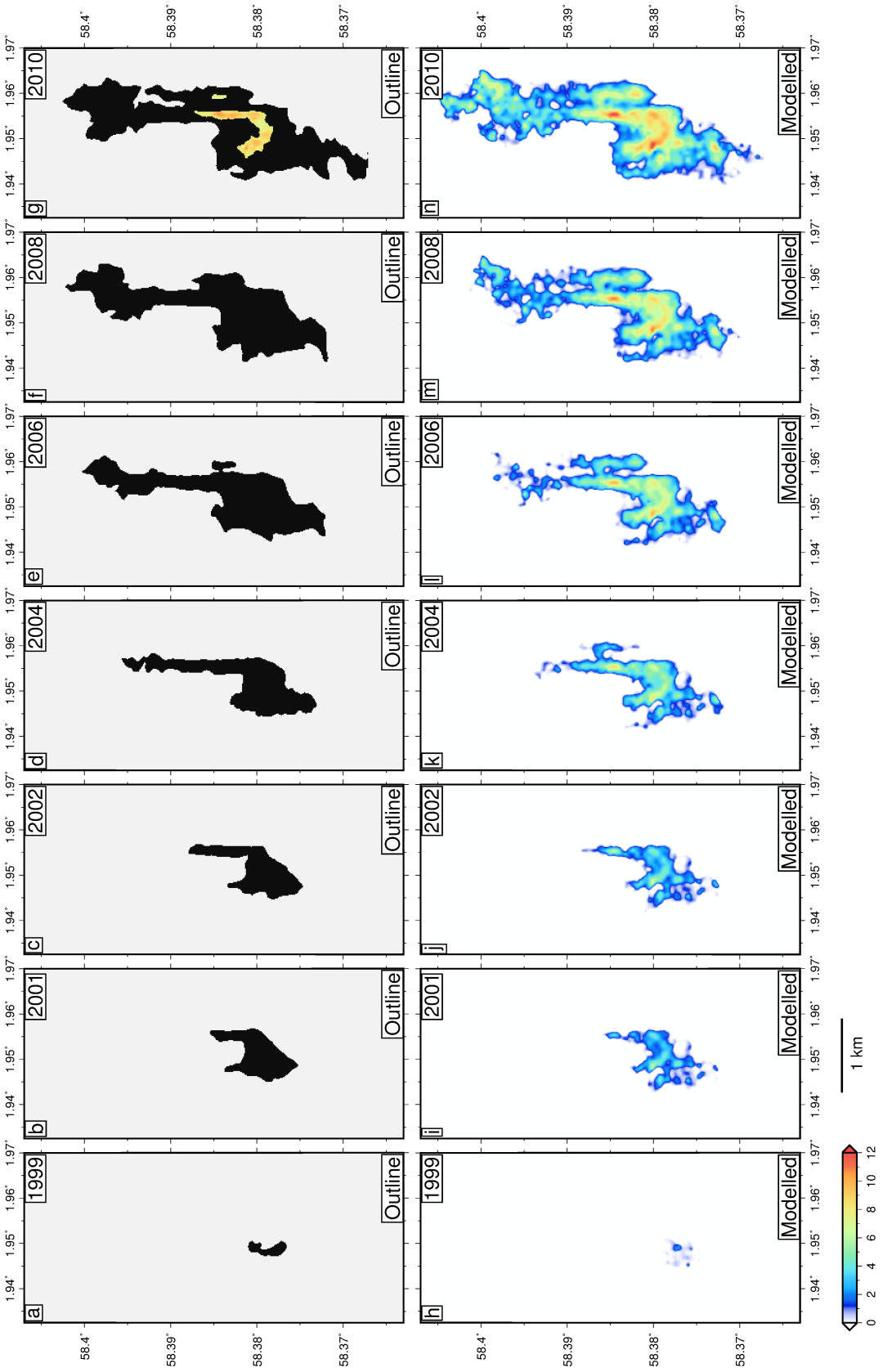

Figure 6.9: Flow model inversion for volume of Layer 9. (a-g) Outlines of extent of CO_2 observed on seismic reflection images. Thickness of central region extracted from broadband survey shown for 2010. **(h-n)** Estimated thickness of CO_2 from flow model inversion using 0.75 m thickness threshold.

and 0.5 m respectively to estimate the sensitivity of this method to this parameter. For each threshold value, five starting models are tested. Figure 6.10 shows the initial and final parameters found during this inversion for a threshold thickness of 0.75 m. The change in misfit per iteration shows that these models converge in relatively few iterations (Figure 6.10a). Despite the different starting models tested, final parameters found by the inversion for each model show good agreement with each other (Figure 6.10b-e). The reservoir permeability found by inversion is approximately 3.5 D, which agrees well with a permeability of 3 ± 1 D found by grid search in Chapter 4 (Figure 4.19). Figure 4.19 shows that a trade off between channel width and channel permeability exists. As a result, in this inversion these parameters are less tightly constrained than the reservoir permeability, producing values 16–22 D for the five starting models (Figure 6.10b). These estimates are almost all within the range of permeabilities found by grid search in Chapter 4 of 26 $\pm$ 8 D. The channel width found in this inversion, in the range of 700–800 m, also agrees well with the previously estimated value of 675 $\pm$ 125 m from Chapter 4 (Figure 6.10c).

Recovered CO_2 volume with time estimates for the five starting models are consistent with each other, and the initiation time for CO_2 entering the layer is well constrained (Figure 6.10c-e). The volume of CO_2 with time estimated from all three threshold thickness compares favourably to the estimated thickness from seismic images, particularly for early years (Figure 6.11). The discrepancy in volume estimates for later years is possibly due to central region being measured as thicker using the broadband seismic reflection survey than using the method described in Chapter 3. Uncertainty in the caprock topography and the simplicity of the permeability structure will also lead to discrepancies between modelled and observed CO_2 distributions. Figure 6.9 shows that the CO_2 distribution found by inversion produces a good match to the areal planform of Layer 9. This map of CO_2 distribution also compares favourably with measured CO_2 thickness in this layer from the seismic reflection surveys, despite limited information about plume thickness used in the inversion.

These results show that inversion of flow simulations is an appropriate method to constrain CO_2 volume in Layer 9. Figure 6.11 suggests that this estimate should be treated as an

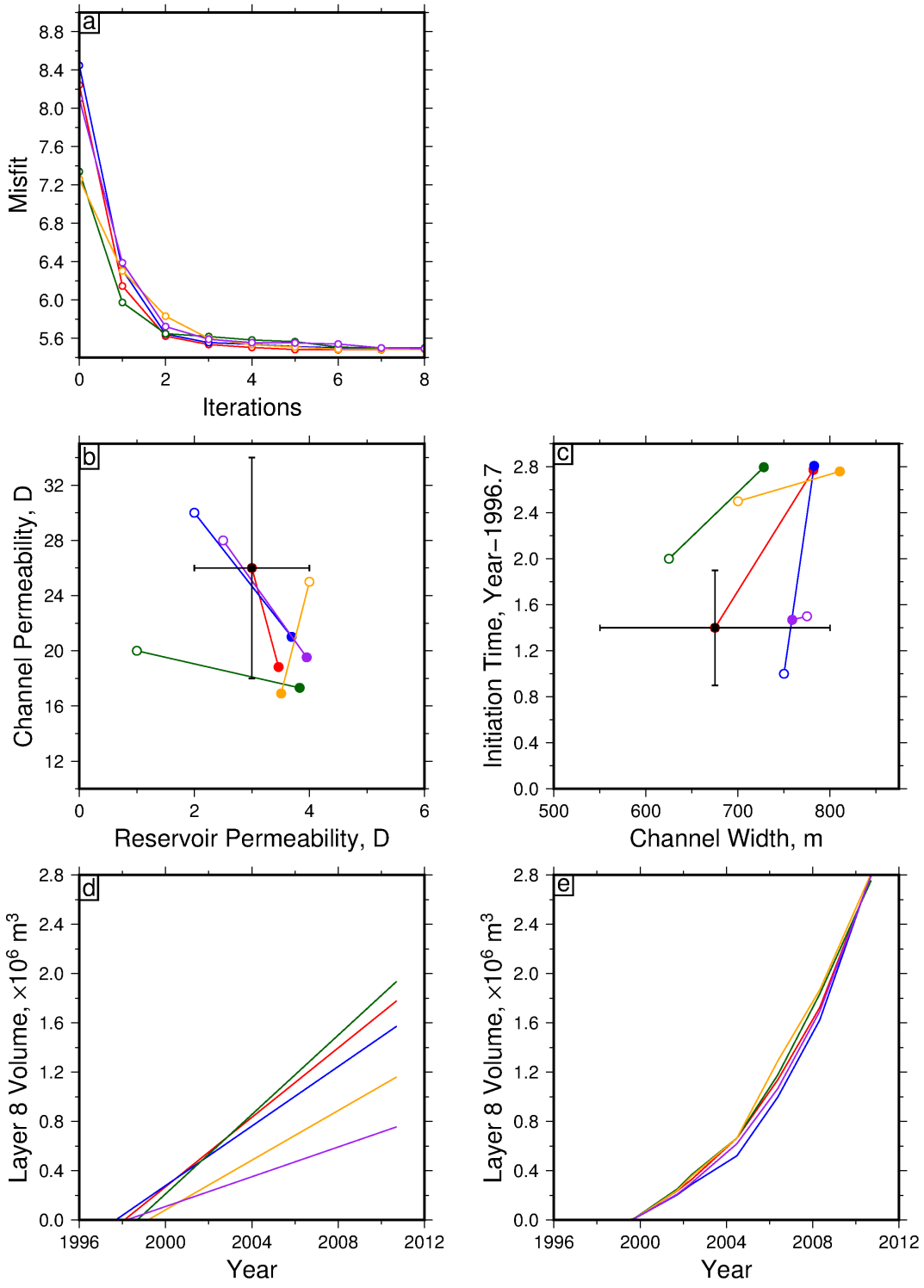

Figure 6.10: Inversion for Layer 9 area using threshold thickness of 0.75 m.(a) Misfit against number of iterations for each starting model.**(b)** Starting (open circle) and final (solid circle) parameter values for channel permeability and reservoir permeability. Black circle = estimates and uncertainties constrained by grid search in Chapter 4. **(c)** Starting (open circle) and final (solid circle) parameter values for initiation time (i.e. time after injection started at the base of reservoir) and channel width. Black circle = estimates and uncertainties constrained by grid search in Chapter 4 . **(d)** Initial models for volume of CO_2 input into reservoir. **(e)** Final CO_2 volume estimates found by inversion.

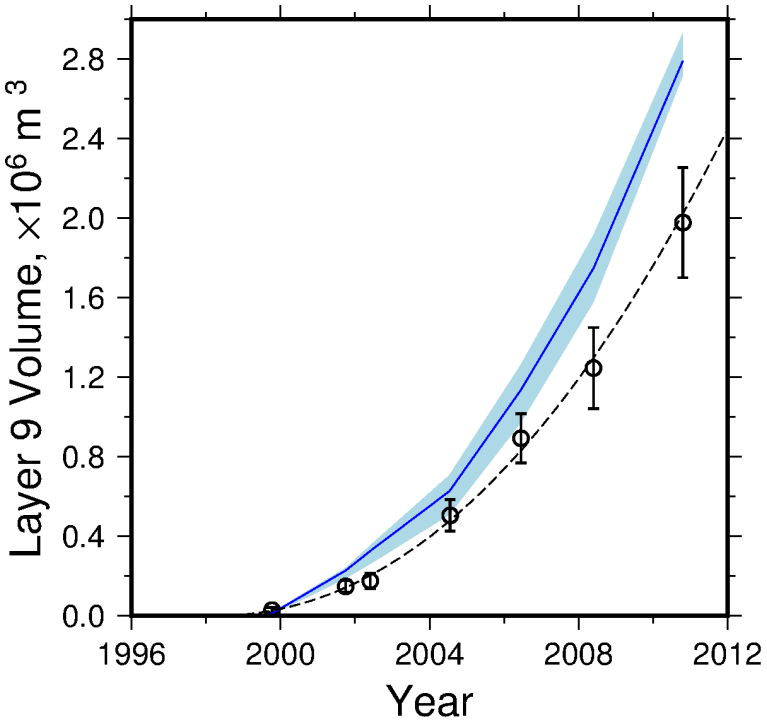

Figure 6.11: Layer 9 Volume. Points = volume of Layer 9 constrained from seismic observations. Dashed line = best fit to observed volume. Solid line = volume from flow model inversion for area for 0.75 m threshold thickness. Blue area = bounds on flow model inversion for threshold thicknesses of 0.5 m and 1 m. Volume calculated assuming uniform porosity of 0.37 and CO_2 saturation of 0.8.

upper bound of the CO_2 volume.

Inversion for Layer 8

A simplified inversion scheme is used to constrain the volume of CO_2 in Layer 8. However, to use the forward flow simulator in this layer, fluid properties, caprock topography and CO_2 input location must first be identified. The input point for the CO_2 in this reservoir model is informed by seismic images. The major seismic chimney identified in Chapter 3 is again used as the single input location for CO_2. Further evidence of the existence of this chimney as a conduit for CO_2 is provided by the existence of a 'pockmark' on the Layer 8 caprock reflection (Figure 6.12). Pockmarks are thought to be formed due to the escape of fluid or gas (Heggland, 1998). Since this pockmark is apparent on the pre-injection survey, it cannot have been formed by the injection of CO_2 into the reservoir. Analysis of CO_2 spreading on seismic reflection surveys suggests that this pockmark is the only location at

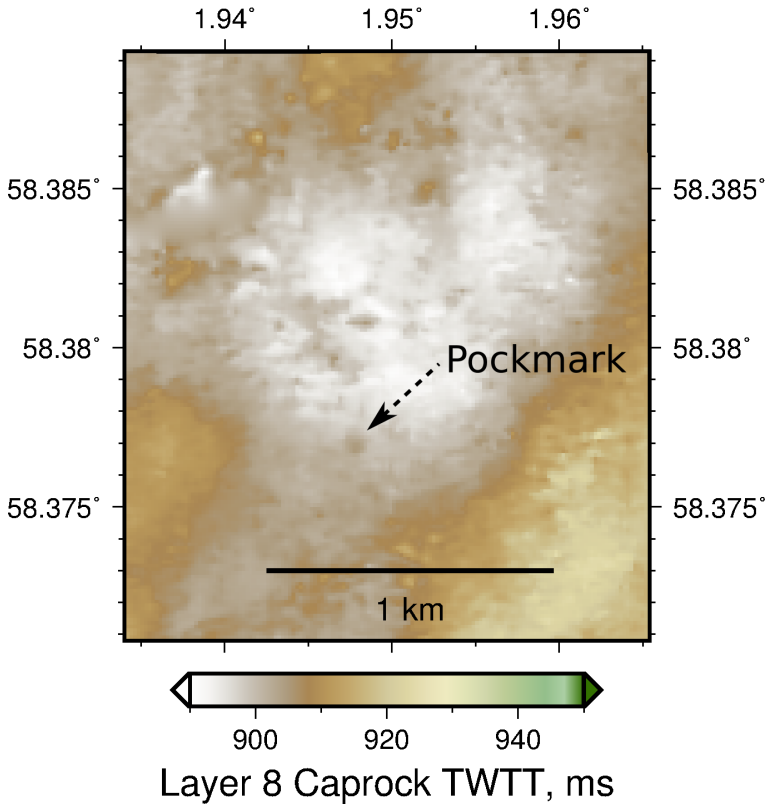

Figure 6.12: Pockmark on pre-injection survey. Background shows unfiltered Layer 8 caprock reflection topography in two-way travel time.

which CO_2 is entering this layer. However, the seismic images provide little information about the confinement of the layer. The intra-reservoir mudstone layers are too thin to be imaged on the seismic reflection surveys. However, for the majority of the area covered by Layer 8, no CO_2 is observed to pond immediately below it. At the southern edge of Layer 8, the proximity of Layer 7 is difficult to measure due to the resolution of the seismic images. However, Layer 8 is expected to be thin in this region, and so the layer in this analysis is considered to be unconfined.

The topography of Layer 8 is strongly correlated with that of the layer above. The topographic gradients appear to have been formed as a result of mud diapirism at the base of the formation that caused mass movement and compaction of sediment above. One important difference is that the prominent north-striking ridge evident in Layer 9 is not present in Layer 8. Instead, the topography to the north-east of the central dome transitions into a broad topographic high that contains no obvious structure (Figure 6.15). Permeability in

this inversion is therefore assumed to be uniform for the entire reservoir for simplicity.

The fluid parameters used in this inversion are slightly different to those used for Layer 9 due to the change in temperature and pressure caused by being situated deeper in the subsurface. The density of CO_2 is estimated to be 680 kg m^{-3} and the viscosity 5.4 $\times$ 10^{-5} Pa s. These estimates are based on numerical modelling of the plume using PFLOTRAN, which gives values of 8.2 MPa and 31.5 °C for the pressure and temperature in this layer (G. Williams, pers. comm., 2017; Williams & Chadwick, 2017).

As for the inversion for Layer 9 described above, threshold thicknesses of 0.5 m, 0.75 m and 1 m are chosen as the minimum resolvable thickness at the edge of the CO_2 layer. The edge is picked using amplitude measurements and, where the layer is not overlain by CO_2 in Layer 9, travel-time anomaly measurements. The inversion is then initiated using a randomly assigned starting permeability of 1 to 5 D, and a uniform input flux (Figure 6.13b-c). Six starting models are inverted for each of the three threshold thickness values, with a minimum found for each of the models within a few iterations (Figure 6.13a). The minimum misfit model found by the inversions produces a clear consensus on the permeability of the region, finding a value of $\sim$2 D for each of the starting models (Figure 6.13b). This permeability estimate is in good agreement with measurements taken from cores from adjacent wells (Zweigel *et al.*, 2004). The initiation time of CO_2 entering the layer is less well constrained, but all models suggest that it occurs within 0.5 years of injection starting at the base of the reservoir. The volume flux of CO_2 in Layer 8 appears to be approximately constant following a transient period of increasing flux (Figure 6.13d).

Figure 6.14 shows the thickness of CO_2 in Layer 8 based on the flow model inversion with threshold thickness of 0.75 m compared to the layer's observed areal extent in all years and thickness in 2010. It can be seen that, especially for later years, the area of the plume is well matched. The good match between modelled and observed area suggests that this layer is predominantly controlled by topographic gradients. However, there is some discrepancy in early years between observed and modelled plumes. The discrepancy is again centred on

the topographic dome's depressed north-western edge that was discussed previously (Section 6.3.3). If the reflection from this region has been anomalously pushed down due to natural gas in the overburden, then it is likely to affect the modelled CO_2 distribution more when the layer is thin. In later years, when the modelled plume is thick enough to flow across this depressed region, the areal match is much improved. As a result, the volume of CO_2 found by inversion for early years is likely to be underestimated. Bounds on this estimate are provided by the higher and lower thickness thresholds tested (Figure 6.8). The inversion results for each threshold thickness tested are mutually consistent. However, the uncertainties in these volume estimates do not account for uncertainties in the topography of the caprock. As discussed for the inversion for Layer 9, this estimate should be treated as an upper bound.

6.4 Volume of Layer 8

The volumes of CO_2 in Layer 8 estimated using four methods discussed in this chapter are shown in Figure 6.8. The two structural trapping methods (i.e. hemi-ellipsoidal trapping and structural analysis) are based on the assumption that CO_2 fills topographic dome with a flat base. These two methods produce very similar estimates for the change in volume with time (Figure 6.8). Flow models inverted with three threshold thicknesses and varied starting parameters are mutually consistent. The uncertainty introduced by using different threshold thicknesses is observed to be small (Figure 6.8). The volume of CO_2 in 2010 estimated using this inversion is found to be higher than for the reflection separation method and interpolated into the surrounding region (Figure 6.8). The differences between the two thickness estimates mostly occur in the central region.

The three methods that can constrain the volume of CO_2 with time suggest that initial flux into Layer 8 was low. After a period of $\sim$4 years, the flux into this layer is approximately constant. Assuming porosity of 0.37 and CO_2 saturation of 0.8, the volume flux is estimated to be $\sim 2.2 \times 10^5$ m^3 yr^{-1}. By 2010, all four methods suggest that there is approximately $1.8 \pm 0.4 \times 10^6$ m^3 of CO_2 in Layer 8. Comparison with the total injected mass at the

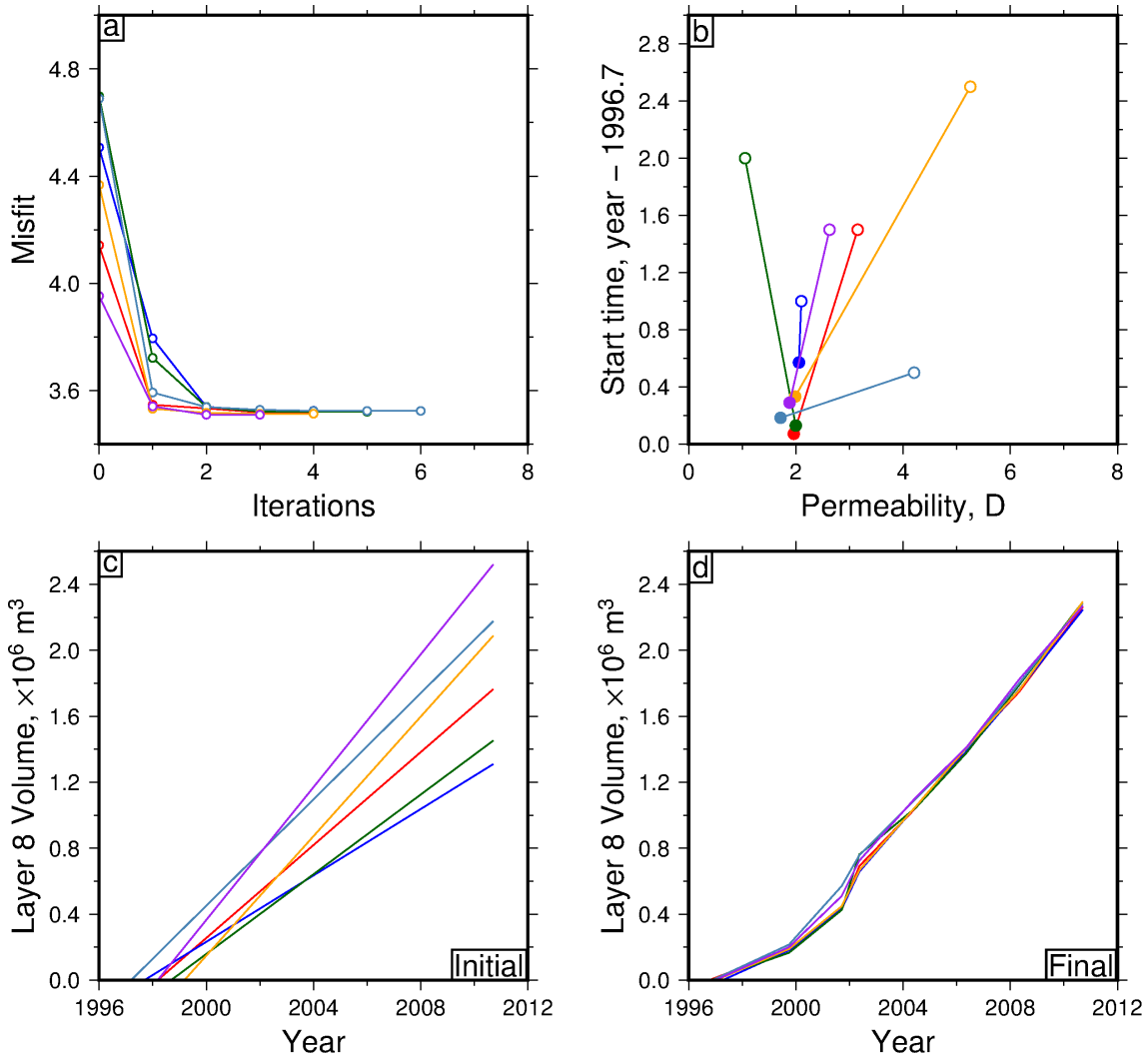

Figure 6.13: Inversion for Layer 8 area using threshold thickness of 0.75 m. (a) Misfit against number of iterations for each starting model. **(b)** Starting (open circle) and final (solid circle) parameter values for reservoir permeability and initiation time (i.e. time after injection started at the base of reservoir). **(c)** Initial models for volume of CO_2 input into reservoir. **(d)** Final CO_2 volume estimates found by inversion.

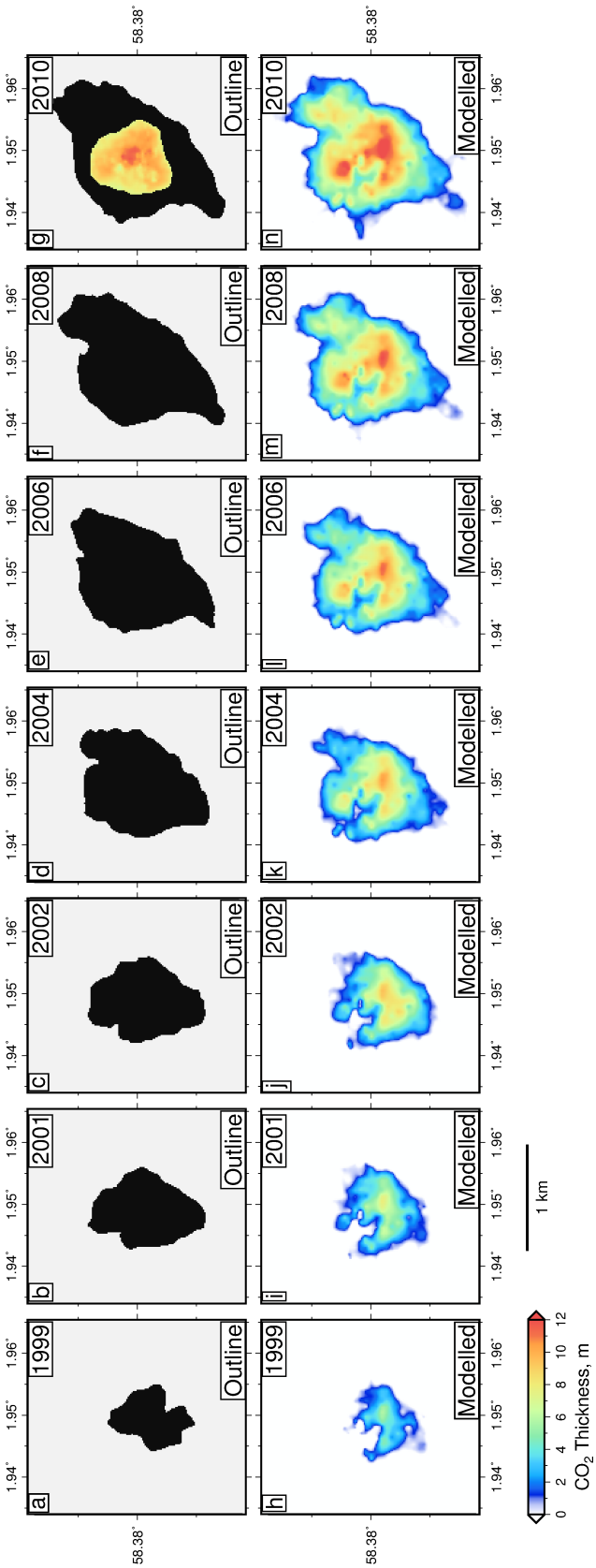

Figure 6.14: Flow model inversion for volume of Layer 8. (a-g) Outlines of CO_2 extent observed on seismic reflection images. Thickness of central region extracted from 2010 broadband survey in (g). **(h-n)** Estimated thickness of CO_2 from flow model inversion using 0.75 m thickness threshold.

base of the reservoir suggests that Layer 8 contains approximately 11 % of the total injected CO_2. Between 2008 and 2010, the flux of CO_2 into Layer 8 was ∼15 % of the CO_2 injected in this period.

Discrepancies between estimates produced by these methods are likely to be caused by uncertainties in caprock topography and the assumption of a flat base. For example, if the gradients in the caprock are overestimated (i.e. if velocity of seismic waves through these formations is overestimated), then the thickness of the central region will increase in order to match the outer edge of the plume. As discussed previously, the assumption of a flat base in the structural trapping methods mean that these results are likely to be a lower bound on the volume of CO_2 in the layer.

6.5 Future flow within Layer 8

The margin of the CO_2 plume in 2010 is now at the limit of the dome-shaped structural trap present in the caprock topography (Figure 6.15). CO_2 in Layer 8 is therefore likely to spill out of this dome in the near future. The most likely directions for this over-spill are to the north and west (Figure 6.15). Due to uncertainty in the exact depths of spill points to the west and north it is difficult to predict which of these will be the dominant migration pathway. Without a high permeability channel to act as a conduit to remove CO_2 from the central region, the CO_2 accumulating below the domal trap is also likely to increase in thickness at a higher rate than for Layer 9. The seismic cube available in this study is not large enough for a detailed prediction of the long-term flow of CO_2 in this layer. However, Zweigel *et al.* (2004) suggest that the predicted long-term CO_2 migration pathways away from this trap are initially to the north, and then to the west to fill a larger topographic dome.

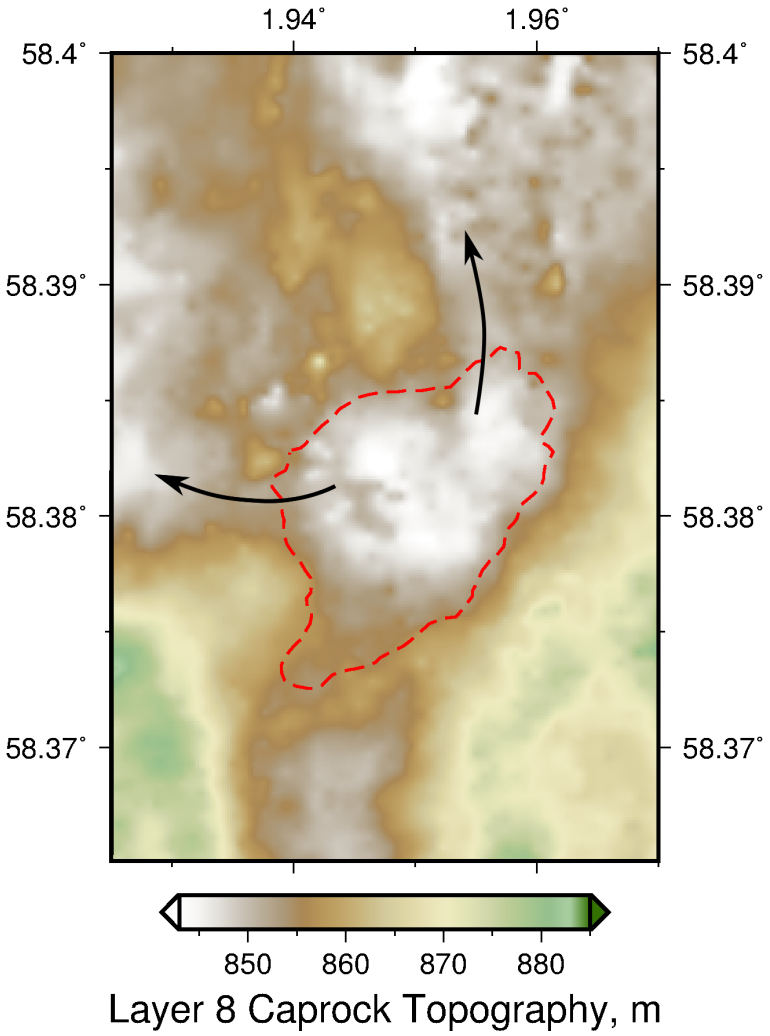

Figure 6.15: Likely future flow paths for CO_2 in Layer 8. Dashed red line = outline of Layer 8 in 2010 picked from amplitude and travel-time anomaly measurements. Solid arrows = likely future migration pathways.

6.6 Summary

Due to the attenuation of seismic waves by CO_2 in Layer 9, CO_2 volume within Layer 8 cannot be measured reliably using amplitude measurements alone. In this chapter, estimates of the volume of CO_2 with time have been made using four methods that do not rely on direct measurements of amplitude and two-way travel time. The methods discussed are reflection separation, trap filling, structural analysis and inverse flow modelling (Figure 6.8). While uncertainties in these CO_2 volume estimates are high, the results provide some insight into general trends of CO_2 migration into this layer. Testing of the area-matching flow model inversion on Layer 9 produced volume estimates comparable to those estimated from the seismic reflections. The success of this inversion shows that it is possible to find a good estimate of the volume of CO_2 in Layer 8 using only limited information about the thickness of the plume.

The volume of CO_2 trapped in Layer 8 accounts for a significant proportion of the total injected CO_2. However, the flux of CO_2 into Layer 8 is $\sim$17 % of the injected CO_2, meaning that a significant proportion of injected CO_2 is migrating to the top of the reservoir. Due to the thick and laterally extensive nature of the caprock for Layer 8, this layer is likely to become a significant store of CO_2 in the future.

By 2010, the CO_2 in Layer 8 appears to have filled the structural trap that it is ponding beneath. The likely spill points from this dome are to the north and west. In the long term, the CO_2 has been predicted to flow to the west to occupy larger structural traps (Zweigel *et al.*, 2004). The large length scales of this predicted migration suggest that the storage capacity of this layer will contribute significantly to the total reservoir capacity.

Chapter 7

Conclusions and Future Work

7.1 Summary

CO_2 injected into the Utsira Formation has been studied in detail using a variety of geophysical observations and fluid dynamical models. The main findings from this dissertation are based on two questions asked in Chapter 1. Can the flux of CO_2 into the seismically observed layers be constrained? What are the dominant controls on the lateral flow of CO_2 through the reservoir?

A detailed analysis of the 1994 pre-injection survey permitted estimates of the caprock topography for Layers 8 and 9 to be made. Due to the limited resolution of the seismic reflection surveys, interpretation of other intra-reservoir shale layers was not possible, but their existence is inferred from wire-line logs acquired from nearby wells. Detailed mapping of the seven available post-injection surveys (1999 to 2010) reaffirmed the existence of nine consistently bright reflections within the reservoir, that are interpreted as thin layers

of CO_2 trapped by intra-reservoir mudstones. In contrast to Boait *et al.* (2012), the lower layers do not appear to shrink in later surveys. The discrepancy between these results can be attributed to the more conservative approach taken to mapping the lower layers in this study. The 2010 survey was acquired with a dual-sensor streamer, which enabled the receiver ghost to be removed during processing, increasing the bandwidth of frequency content of the recorded signal. The improved resolution allows the edge of each layer to be more accurately picked. However, reflections towards the base of the plume cannot be identified with any certainty due to attenuation and scattering of the seismic signal by the overlying CO_2-filled layers. Based on regular mapping of seismic reflection amplitudes over the fourteen year period, the lateral extent of the upper layers continues to increase with time.

An inverse method is developed for measuring the thickness of thin layers of fluid using time-lapse seismic reflections to gain insight into the thickness of the shallowest CO_2-filled layer, Layer 9. This method uses the reflection amplitude and changes in two-way travel time of the reflection between pre- and post-injection surveys (i.e. travel-time anomalies) to constrain parameters in a reflection model. Parameters that are inverted for are the peak frequency of the seismic wavelet, the amplitude of the upper reflection, and the ratio of amplitudes between the top and base of the CO_2 layer. These parameters are used to calibrate the relationship between reflection amplitude, travel-time anomaly and layer thickness. This relationship can be used to measure the thickness of a fluid layer between 1–6 m thick with good accuracy. Uncertainty of these measurements is estimated using synthetic models. The distribution of CO_2 within Layer 9 was measured on all post-injection seismic reflection surveys using this method. Comparison between this measurement of the thickness of the central region of Layer 9 and the thickness measured on the broadband survey from 2010 suggests that these methods produce adequately similar results within the range of uncertainties for each technique. Flux of CO_2 into Layer 9 is observed to increase with time.

A computationally efficient reservoir simulator was developed to model the flow of CO_2 within Layer 9. The numerical model is based on the equation for a gravity current on a slope. The model was benchmarked against analytical solutions in two and three dimensions.

A poor fit to the measured distribution of CO_2 in Layer 9 was found using a uniform reservoir permeability. Spectral decomposition images suggest the presence of a linear channel within this part of the reservoir. Permeability of the reservoir was recovered using an inversion to match flow simulations to the observed distribution of CO_2 on all time-lapse seismic reflections surveys. The bulk permeability for the reservoir was found to be 3 Darcys, in agreement with measured values from cores taken from the reservoir. Permeability of the channel was found to be 26 Darcys. The width of the channel found by the inversion agrees well with observations on the seismic reflection survey. An inversion of this scale carried out by grid search is only possible due to the short run time of each simulation.

Motivated by variations in the thickness of the aquifer that Layer 9 resides in, the effect of variable aquifer thickness on gravity currents was investigated in two dimensions using analytical and numerical models. Two possibilities were considered: first, a buoyant current flowing underneath a flat roof with a uniformly increasing aquifer thickness, and second, a buoyant current flowing underneath a uniformly sloping roof, while the base of the aquifer is kept flat. In the case of a buoyant injected fluid, of equal viscosity to the ambient fluid, the current was found to experience four regimes. Initially, the fluid flows without feeling the effect of the lower boundary and so is effectively unconfined. Once contact is made with the base, the fluid transitions to a pressure-driven regime and flows at a constant rate that is proportional to time. At later times, the rate of advance of the nose of the current is controlled by the gradient of the sloped boundary, regardless of whether it is the roof or base that is sloping. Finally, at late times, for the case of flow underneath a flat roof, the base of the aquifer is effectively distant, and so the current again flows in the unconfined regime. For the case of a sloped roof, the current flows buoyantly up the slope, again unaffected by the base of the aquifer. These models suggest that the thickness of the aquifer can play an important role in determining the flow rate of the injected fluid, if the current is of comparable thickness to the reservoir.

Finally, a variety of different techniques was used to constrain the volume of CO_2 in Layer 8. Thickness of the central region of Layer 8 was measured using the separation of reflections

from the top and base of the CO_2 layer on the 2010 broadband survey. The volume of CO_2 within the layer can also be constrained by approximating the topography of the caprock as a hemi-ellipsoid. Using a simple relationship between the volume of fluid filling a cap and the area of the base of the fluid, the observed area of the layer measured from the seismic reflection surveys can be related to the volume of CO_2 within the layer. Structural analysis was also used to determine the base of the CO_2 layer by interpolating a flat base between the observed CO_2-water-contact at the edge of the plume. The difference between the flat base and the caprock topography provides an estimate of the volume of CO_2 in the layer. Finally, the flow model developed in Chapter 4 was used to invert for the change in CO_2 volume with time by finding the optimal match to the observed area of the plume. All four methods suggest that the volume of CO_2 in Layer 8 in 2010 was $\sim 2 \pm 0.2 \times 10^6$ m^3. The flux of CO_2 into Layer 8 has increased with time. Layer 8 is estimated to have reached the spill point of the domal structure within which it is currently trapped.

7.2 Conclusions

The volume of CO_2 stored within the top two layers has been determined using a combination of detailed seismic analysis and fluid dynamical modelling. In 2010, the volume of CO_2 in both Layer 8 and 9 was approximately equal. It is estimated that the top two layers account for 23% of the total CO_2 injected at the base of the reservoir. However, flux of CO_2 into these layers has increased with time and by 2010 it is estimated to be approximately 40% of the total injected at the base of reservoir. While the flux of CO_2 into Layer 8 appears to be approaching a constant, the flux into Layer 9 continues to grow (Figure 7.1).

Increasing flux to the uppermost layers suggests that the capacity of vertical migration pathways within the reservoir is growing. The primary entry point for both Layer 8 and 9 is thought to be the major seismic chimney (Chapter 3). Flux into Layers 8 and 9 is currently less than the total injected flux into the reservoir. Combined with the observation that the lower layers do not appear to be shrinking, flux into the upper reservoir provides no evidence that CO_2 trapped within the lower layers has remobilised. If CO_2 within the lower layers is

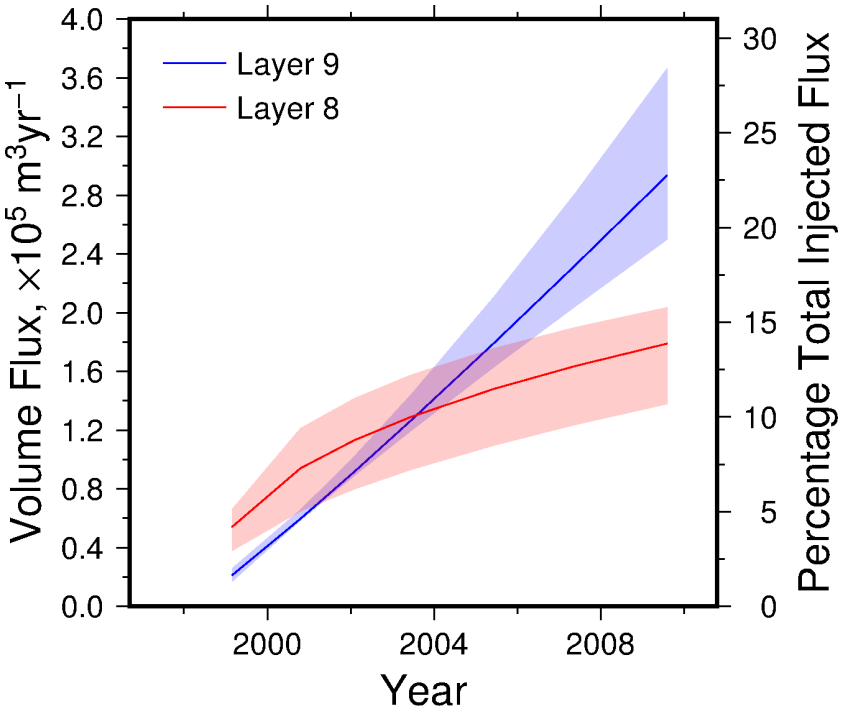

Figure 7.1: CO_2 flux into Layers 8 and 9. Blue line = estimated flux into Layer 9 from best fit to measured volume (see Chapter 3). Red line = estimated flux into Layer 8 from best fit to volume estimated from area fitting (see Chapter 6). Shaded areas show uncertainty estimates. Black line = 1/9th flux of CO_2 injected at base of the reservoir.

trapped permanently, the potential storage capacity of the reservoir will be increased.

Success of the reservoir simulator developed in Chapter 4 suggests that the dominant control on the flow of CO_2 in Layers 8 and 9 is caprock topography. The relative simplicity of this model increases its stability and means that run time is short. The computational efficiency of the model is also due to the vertically integrated nature of the governing equations, reducing the grid over which the flow is simulated from three dimensions to two and implicitly improving the numerical resolution of the model. The short run time of the model means that parameters such as the permeability or the input flux can be found by inversion. The results of the flow simulations for Layer 9 suggest that the confinement of the reservoir is not significantly influencing CO_2 flow within the aquifer. However, the results of analytical and numerical models in Chapter 5 suggest that confinement could play an important role in flow in Layer 9, if the CO_2 layer becomes comparable to the Layer 9 reservoir thickness.

The ability of the reservoir simulator to predict the CO_2 distribution observed on post-2006 surveys, using only information from 2004 and earlier, suggests that the predictive power of this model is high. This analysis gives confidence in the predicted future flow of CO_2 through the reservoir. The ability to recover an accurate estimate of the volume of CO_2 in a layer by primarily matching the observed planform area indicates that this model can provide insight into the flow of CO_2 in situations where geophysical observations have limited resolution.

7.3 Future Work

Two additional seismic reflection surveys have been acquired over the CO_2 plume in 2013 and 2016. Mapping of reflections from the CO_2 plume on these surveys would provide further information on the flux of CO_2 into the upper layers. The observed extent of CO_2 in Layer 9 would provide a significant test of the flow model predictions made in Chapter 4 (Figure 4.24).

Expanding the confined gravity current model explored in Chapter 5 to three dimensions, and accounting for viscosity variations between the injected and ambient fluid, are important next steps. Incorporating confinement of the reservoir into the reservoir simulator will enable the influence of the observed changes in aquifer thickness on the flow of CO_2 in Layer 9 to be investigated as the layer thickens.

As well as accounting for aquifer confinement, adaptations can be made to the gravity current model to account for the effect of capillarity and dissolution of CO_2 into the ambient brine. However, despite the importance of CO_2 dissolution into ambient brine for storage security, the rate at which CO_2 dissolution occurs has not been accurately measured in field experiments. Fluid samples taken from field sites would provide valuable information on this important parameter. Small-scale pilot projects that have finished injecting CO_2 (e.g. Otway in Australia, Ketzin in Germany) would be ideal locations to take these fluid samples.

Gravity currents have been shown by experiment to adequately describe the flow of fluids through homogeneous porous media. However, in sedimentary rocks, small-scale heterogeneities exist in the distribution of grain sizes within and across beds. These heterogeneities can exist on different length scales, and can have a large effect on the permeability of the rock. Anderson *et al.* (2003) numerically and analytically explored the effect of sinusoidally varying permeability in both horizontal and vertical directions. This work could be expanded to look at larger permeability changes over a range of scales. Gravity currents in porous media with discontinuous changes in grain size in the vertical direction, analogous to sedimentary bedding, could also be explored. Investigating these possibilities experimentally would provide insight into the validity of assuming a homogeneous medium when modelling large-scale fluid flow.

Several pilot projects have now demonstrated that CO_2 can be safely stored in subsurface reservoirs (e.g. Sleipner, Snøhvit). However, in many of these pilot studies the volume of CO_2 injected has been relatively low (e.g. Otway, Ketzin). In order to store CO_2 on the scale required to meaningfully reduce CO_2 emissions, it will be necessary to inject CO_2 on the scale of millions of tonnes per year, possibly using several injection sites within the same reservoir. The effect on reservoir pressure caused by multiple injection sites has recently been explored theoretically, but field scale studies would improve understanding in this area (Agada *et al.*, 2017).

As of January 2017, an estimated 16.5 Mt of CO_2 has been injected. Due to limited reserves of natural gas remaining in the Sleipner Vest field, and a lower CO_2 content of this gas, it is now anticipated that a further 1 Mt CO_2 will be injected into the reservoir by 2020. These figures represent a sharp drop in the CO_2 injection rate at the base of the reservoir. When injection does cease, continued monitoring of the reservoir is of considerable importance for understanding CO_2 flow within the reservoir. The pattern of reflections after cessation of injection would provide valuable information on the long-term storage of the CO_2 in each of the layers. Given that the injection period is likely to be of short duration compared with the total life of the reservoir, understanding the post-injection behaviour of CO_2 will provide

a useful indication of the long-term evolution of the CO_2 plume.

7.4 Designing an ideal carbon storage project

While the Sleipner carbon capture and storage project has provided unparalleled insight into the dynamics of CO_2 flow through a porous reservoir on the field scale, the project was not optimised for scientific purposes. For example, the main objective of the baseline seismic reflection survey was to image the deeper natural gas field, reducing the vertical resolution of this seismic reflection survey, and therefore subsequent surveys too (Eiken *et al.*, 2000; Furre & Eiken, 2014). The lack of a down-hole temperature and pressure measurements from the base of the injection well has also created uncertainty in estimates of CO_2 density and viscosity within the reservoir.

In an ideal experiment, a broadband seismic reflection survey would be acquired over the target reservoir prior to injection of CO_2. The reservoir would be approximately the same depth as the Sleipner reservoir – deep enough that the CO_2 is in the super-critical phase, but shallow enough to optimise imaging from seismic reflection surveys. Several boreholes would penetrate the reservoir in the region that the CO_2 is anticipated to spread into. From these wells, core samples could be analysed to determine the permeability of the reservoir and how this may vary laterally and vertically. These wells could also be used as observation wells to sample fluids within the reservoir at different times, which can be then compared to baseline fluid samples. These measurements could be used to estimate the fine-scale distribution of CO_2 within the reservoir – is CO_2 distributed in uniformly high saturation layers or in a more patchy manner. These fluid samples could also be used to estimate the dissolution rate of CO_2 within the ambient reservoir pore fluid.

Injection of CO_2 would occur at a high rate (i.e. $\sim$ Mt yr^{-1}) at several injection sites within the reservoir. Pressure sensors at the injection point and within the monitoring wells could be used to investigate the evolution of pressure within the reservoir and assess whether this scale of injection is feasible. Subsequent seismic reflection surveys would ideally be acquired

using the same source and receiver parameters as the baseline survey and the processing would be carried out by the same contractor. This continuity would minimise differences between seismic reflection surveys and increase confidence in measuring differences between surveys.

References

Agada, S., Jackson, S., Kolster, C., Mac Dowell, N., Williams, G., Vosper, H., Williams, J., & Krevor, S., 2017. The impact of energy systems demands on pressure limited CO_2 storage in the Bunter Sandstone of the UK Southern North Sea, *Int. J. Greenh. Gas Cont.*, **65**, 128–136.

Alnes, H., Eiken, O., Nooner, S., Sasagawa, G., Stenvold, T., & Zumberge, M., 2011. Results from Sleipner gravity monitoring: Updated density and temperature distribution of the CO_2 plume, *Energy Procedia*, **4**, 5504–5511.

Anderson, D. M., McLaughlin, R. M., & Miller, C. T., 2003. The averaging of gravity currents in porous media, *Phys. Fluids*, **15**(10), 2810–2829.

APGTF, 2014. *Cleaner Fossil Power Generation in the 21st Century Moving Forward*, UK Advanced Power Generation Technology Forum.

Arts, R., Brevik, I., Eiken, O., Sollie, R., Causse, E., & Van Der Meer, B., 2000. Geophysical methods for monitoring marine aquifer CO_2 storage–Sleipner experiences, in *5th Int. Conf. on Greenh. Gas Cont. Tech.*.

Arts, R., Eiken, O., Chadwick, A., Zweigel, P., van der Meer, L., & Zinszner, B., 2004. Monitoring of CO_2 injected at Sleipner using time-lapse seismic data, *Energy*, **29**(9-10), 1383–1392.

Arts, R., Chadwick, A., Eiken, O., Thibeau, S., & Nooner, S., 2008. Ten years' experience of monitoring CO_2 injection in the Utsira Sand at Sleipner, offshore Norway, *First Break*, **26**(1).

Baklid, A., Korbol, R., Owren, G.,*et al.*, 1996. Sleipner Vest CO_2 disposal, CO_2 injection into a shallow underground aquifer, in *SPE Annual Technical Conference and Exhibition*, Society of Petroleum Engineers.

Bandilla, K. W., Celia, M. A., & Leister, E., 2014. Impact of Model Complexity on CO_2 plume modeling at Sleipner, *Energy Procedia*, **63**, 3405–3415.

Bear, J., 1972. *Dynamics of fluids in porous media*, Dover.

Beard, D. & Weyl, P., 1973. Influence of texture on porosity and permeability of unconsolidated sand, *Am. Assoc. Pet. Geol. Bull.*, **57**(2), 349–369.

Benson, S. M. & Cole, D. R., 2008. CO_2 Sequestration in Deep Sedimentary Formations, *Elements*, **4**(5), 325–331.

Bickle, M., Chadwick, A., Huppert, H. E., Hallworth, M., & Lyle, S., 2007. Modelling carbon dioxide accumulation at Sleipner: Implications for underground carbon storage, *Earth Planet. Sci. Lett.*, **255**(1-2), 164–176.

Boait, F., 2012. *Seismic Imaging of Sequestered Carbon Dioxide*, Ph.D. thesis, University of Cambridge.

Boait, F., White, N., Chadwick, A., Noy, D., & Bickle, M., 2011. Layer spreading and dimming within the CO_2 plume at the sleipner field in the north sea, *Energy Procedia*, **4**, 3254–3261.

Boait, F. C., White, N. J., Bickle, M. J., Chadwick, R. A., Neufeld, J. A., & Huppert, H. E., 2012. Spatial and temporal evolution of injected CO_2 at the Sleipner Field, North Sea, *J. Geophys. Res. Solid Earth*, **117**(B3).

Cantillo, J., 2012. Throwing a new light on time-lapse technology, metrics and 4D repeatability with SDR, *Lead. Edge*, **31**(4), 405–413.

Carcione, J. M., Picotti, S., Gei, D., & Rossi, G., 2006. Physics and Seismic Modeling for Monitoring CO_2 Storage, *Pure Appl. Geophys.*, **163**(1), 175–207.

Cavanagh, A., 2013. Benchmark Calibration and Prediction of the Sleipner CO_2 Plume from 2006 to 2012, *Energy Procedia*, **37**, 3529–3545.

Cavanagh, A. & Nazarian, B., 2014. A new and extended Sleipner Benchmark model for CO_2 storage simulations in the Utsira Formation, *Energy Procedia*, **63**, 2831–2835.

Chadwick, R. & Noy, D., 2010. History-matching flow simulations and time-lapse seismic data from the Sleipner CO_2 plume, *Geol. Soc., London, Pet. Geol. Conf.*, **7**(1), 1171–1182.

Chadwick, R., Arts, R., Eiken, O., Kirby, G., Lindeberg, E., & Zweigel, P., 2004. 4D seismic imaging of an injected $C0_2$ plume at the Sleipner Field, central North Sea, *Geol. Soc. London, Mem.*, **29**(1), 311–320.

Chadwick, R., Zweigel, P., Gregersen, U., Kirby, G., Holloway, S., & Johannessen, P., 2004. Geological reservoir characterization of a CO_2 storage site: The Utsira Sand, Sleipner, northern North Sea, *Energy*, **29**(9-10), 1371–1381.

Chadwick, R., Williams, G., & White, J., 2016. High-resolution imaging and characterization of a CO_2 layer at the Sleipner CO_2 storage operation, North Sea using time-lapse seismics, *First Break*, **34**(February), 79–88.

Chadwick, R. A. & Noy, D. J., 2015. Underground CO_2 storage: demonstrating regulatory conformance by convergence of history-matched modeled and observed CO_2 plume behavior using Sleipner time-lapse seismics, *Greenh. Gases Sci. Technol.*, **5**(3), 305–322.

Chadwick, R. A., Arts, R., & Eiken, O., 2005. 4D seismic quantification of a growing CO_2 plume at Sleipner, North Sea, *Geol. Soc. London, Pet. Geol. Conf. Ser.*, **6**(0), 1385–1399.

Clark, J. & Pickering, K., 1996. Architectural elements and growth patterns of submarine channels: application to hydrocarbon exploration, *Am. Assoc. Pet. Geol. Bull.*, **80**(2), 194–220.

Clauser, C. & Kiesner, S., 1987. A conservative, unconditionally stable, second-order three-point differencing scheme for the diffusion–convection equation, *Geophys. J. Int.*, **91**(3), 557–568.

Eiken, O., Brevik, I., Arts, R., Lindeberg, E., & Fagervik, K., 2000. Seismic monitoring of CO_2 injected into a marine aquifer, *SEG Int. Conf. 70th Annu. Meet. Calgary*.

Eiken, O., Ringrose, P., Hermanrud, C., Nazarian, B., Torp, T. A., & Høier, L., 2011. Lessons learned from 14 years of CCS operations: Sleipner, In Salah and Snøhvit, *Energy Procedia*, **4**, 5541–5548.

Furre, A. & Eiken, O., 2014. Repeated time-lapse seismic data quantify amplitude tuning at the Sleipner CO_2 injection site, in *76th EAGE Conf. & Exhib. 2014*.

Furre, A.-k., Kiær, A., & Eiken, O., 2015. Special section : Thin beds CO_2 -induced seismic time shifts at Sleipner, *Interpretation*, **3**(3), 23–35.

Gasda, S. E., Nordbotten, J. M., & Celia, M. A., 2009. Vertical equilibrium with sub-scale analytical methods for geological CO_2 sequestration, *Comput. Geosci.*, **13**(4), 469–481.

Gasda, S. E., Nilsen, H. M., Dahle, H. K., & Gray, W. G., 2012. Effective models for CO_2 migration in geological systems with varying topography, *Water Resour. Res.*, **48**(10).

Gasda, S. E., Nilsen, H. M., & Dahle, H. K., 2013. Impact of structural heterogeneity on upscaled models for large-scale CO_2 migration and trapping in saline aquifers, *Adv. Water Resour.*, **62**, 520–532.

Geman, S., Bienenstock, E., & Doursat, R., 1992. Neural networks and the bias/variance dilemma, *Neural computation*, **4**(1), 1–58.

Ghaderi, A. & Landro, M., 2009. Estimation of thickness and velocity changes of injected carbon dioxide layers from prestack time-lapse seismic data, *Geophysics*, **74**(2), O17.

Golding, M., Neufeld, J., Hesse, M., & Huppert, H., 2011. Two-phase gravity currents in porous media, *J. Fluid Mech.*, **678**, 248–270.

Gregersen, U., 1998. Upper Cenozoic channels and fans on 3D seismic data in the northern Norwegian North Sea, *Pet. Geosci.*, **4**(1).

Gregersen, U., Michelsen, O., & Sørensen, J. C., 1997. Stratigraphy and facies distribution of the Utsira formation and the Pliocene sequences in the northern North Sea, *Mar. Pet. Geol.*, **14**(7), 893–914.

Gunn, I. & Woods, A., 2011. On the flow of buoyant fluid injected into a confined, inclined aquifer, *J. Fluid Mech.*, **672**, 109–129.

Gunn, I. & Woods, A., 2012. On the flow of buoyant fluid injected into an aquifer with a background flow, *J. Fluid Mech.*, **706**, 274.

Hall, M., 2007. Smooth operator: Smoothing seismic interpretations and attributes, *Lead. Edge*, **26**(1), 16–20.

Halland, E. K., Gjeldvik, I., Johansen, W., Magnus, C., Meling, I., Pedersen, S., Riis, F., Solbakk, T., & Tappel, I., 2011. CO_2 Storage Atlas Norwegian North Sea, *Norwegian Petroleum Directorate*.

Heggland, R., 1998. Gas seepage as an indicator of deeper prospective reservoirs. A study based on exploration 3D seismic data, *Mar. Pet. Geol.*, **15**(1), 1–9.

Hesse, M., Tchelepi, H., & Cantwel, B., 2007. Gravity currents in horizontal porous layers: transition from early to late self-similarity, *J. Fluid Mech.*, **577**, 363–383.

Huppert, H. E. & Woods, A. W., 1995. Gravity-driven flows in porous layers, *J. Fluid Mech.*, **292**, 55–69.

Il'in, A., 1969. Differencing scheme for a differential equation with a small parameter affecting the highest derivative, *Math. Notes Acad. Sci.*, **6**(2), 596–602.

IPCC, 2005. *IPCC Special Report on Carbon Dioxide Capture and Storage. Prepared by Working Group III of the Intergovernmental Panel on Climate Change*, Cambridge University Press.

IPCC, 2014. *Climate Change 2014: Mitigation of Climate Change. Contribution of Working Group III to the Fith Assessment Report of the Intergovernmental Panel on Climate Change*, Cambridge University Press.

Kallweit, R. S. & Wood, L. C., 1982. The limits of resolution of zero-phase wavelets, *Geophys.*, **47**(7), 1035.

Kiær, A. F., 2015. Fitting top seal topography and CO_2 layer thickness to time-lapse seismic amplitude maps at Sleipner, *Interpretation*, **3**(2), 47–55.

Korbøl, R. & Kaddour, A., 1995. Sleipner Vest CO_2 disposal - injection of removed CO_2 into the Utsira formation, *Energy Convers. Manag.*, **36**(6-9), 509–512.

Kragh, E. & Christie, P., 2002. Seismic repeatability, normalized rms, and predictability, *Lead. Edge*, **21**(7), 640–647.

Kragh, E., Muyzert, E., Curtis, T., Svendsen, M., & Kapadia, D., 2010. Efficient broadband marine acquisition and processing for improved resolution and deep imaging, *Lead. Edge*, **29**(4), 464–469.

Lichtner, P., Karra, S., Hammond, G., Lu, C., Bisht, G., Kumar, J., Mills, R., & Andre, B., 2015. PFLOTRAN user manual: A massively parallel reactive flow and transport model for describing surface and subsurface processes, Tech. rep., Los Alamos National Laboratory (LANL).

Lindeberg, E., Zweigel, P., Bergmo, P., Ghaderi, A., & Lothe, A., 2001. Prediction of CO_2 distribution pattern improved by geology and reservoir simulation and verified by time lapse seismic, in *Conf. Greenh. Gas Contr. Tech.*, pp. 299–304.

Liu, Y., Wang, L., & Yu, B., 2010. Sharp Front Capturing Method for Carbon Dioxide Plume Propagation during Injection into a Deep Confined Aquifer, *Energy & Fuels*, **24**(2), 1431–1440.

Loseth, H., Wensaas, L., Arntsen, B., & Hovland, M., 2003. Gas and fluid injection triggering shallow mud mobilization in the Hordaland Group, North Sea, *Geol. Soc. London, Spec. Publ.*, **216**(1), 139–157.

Lyle, S., Huppert, H., Hallworth, M., Bickle, M., & Chadwick, A., 2005. Axisymmetric gravity currents in a porous medium, *J. Fluid Mech.*, **543**(-1), 293.

MacMinn, C., Neufeld, J., & Hesse, M., 2012. Spreading and convective dissolution of carbon dioxide in vertically confined, horizontal aquifers, *Water Resour. Res.*, **48**(11).

MacMinn, C. W. & Juanes, R., 2013. Buoyant currents arrested by convective dissolution, *Geophys. Res. Lett.*, **40**(10), 2017–2022.

Martens, S., Kempka, T., Liebscher, A., Lüth, S., Möller, F., Myrttinen, A., Norden, B., Schmidt-Hattenberger, C., Zimmer, M., Kühn, M., & Group, T. K., 2012. Europe's longest-operating on-shore CO_2 storage site at Ketzin, Germany: a progress report after three years of injection, *Environ. Earth Sci.*, **67**(2), 323–334.

Mavko, G. & Mukerji, T., 1998. Bounds on lowfrequency seismic velocities in partially saturated rocks, *Geophys.*, **63**(3), 918–924.

Mavko, G., Mukerji, T., & Dvorkin, J., 2009. *The rock physics handbook: Tools for seismic analysis of porous media*.

McCaffrey, W. & Kneller, B., 2001. Process controls on the development of stratigraphic trap potential on the margins of confined turbidite systems and aids to reservoir evaluation, *Am. Assoc. Pet. Geol. Bull.*, **85**(6).

Morris, K. A. & Shepperd, C. M., 1982. The role of clay minerals in influencing porosity and permeability characteristics in the Bridport Sands of Wytch Farm, Dorset, *Clay Miner.*, **7**, 41–54.

Neufeld, J. A. & Huppert, H. E., 2009. Modelling carbon dioxide sequestration in layered strata, *J. Fluid Mech.*, **625**, 353.

Nilsen, H., Herrera, P., Ashraf, M., Ligaarden, I., & Iding, M., 2011. Field-case simulation of CO_2-plume migration using vertical-equilibrium models, *Energy Procedia*, **4**, 3801–3808.

Nilsen, H. M., Lie, K.-A., & Andersen, O., 2016. Robust simulation of sharp-interface models for fast estimation of CO_2 trapping capacity in large-scale aquifer systems, *Comput. Geosci.*, **20**(1), 93–113.

Nilsen, H. M., Lie, K.-A., & Andersen, O., 2016. Fully-implicit simulation of vertical-equilibrium models with hysteresis and capillary fringe, *Comput. Geosci.*, **20**(1), 49–67.

Nilsen, H. M., Krogstad, S., Andersen, O., Allen, R., & Lie, K.-A., 2017. Using sensitivities and vertical-equilibrium models for parameter estimation of CO_2 injection models with application to Sleipner data, *Energy Procedia*, **114**, 3476–3495.

Nooner, S. L., Eiken, O., Hermanrud, C., Sasagawa, G. S., Stenvold, T., & Zumberge, M. A., 2007. Constraints on the in situ density of CO_2 within the Utsira formation from time-lapse seafloor gravity measurements, *Int. J. Greenh. Gas Control*, **1**(2), 198–214.

Nordbotten, J. & Celia, M., 2006. Similarity solutions for fluid injection into confined aquifers, *J. Fluid Mech.*, **561**, 307–327.

Oldenburg, C. M., Mukhopadhyay, S., & Cihan, A., 2016. On the use of Darcy's law and invasion-percolation approaches for modeling large-scale geologic carbon sequestration, *Greenh. Gases Sci. Technol.*, **6**(1), 19–33.

Partyka, G., Gridley, J., & Lopez, J., 1999. Interpretational applications of spectral decomposition in reservoir characterization, *Lead. Edge*, **18**(3), 353.

Peaceman, D. W. & Rachford, H. H., 1955. The Numerical Solution of Parabolic and Elliptic Differential Equations, *J. Soc. Indust. Appl. Math.*, **3**(1), 28–41.

Pegler, S. S., Huppert, H. E., & Neufeld, J. A., 2013. Topographic controls on gravity currents in porous media, *J. Fluid Mech.*, **734**, 317–337.

Pegler, S. S., Huppert, H. E., & Neufeld, J. A., 2014. Fluid injection into a confined porous layer, *J. Fluid Mech.*, **745**, 592–620.

Powell, M., 1964. An efficient method for finding the minimum of a function of several variables without calculating derivatives, *Computer J.*, **7**(2), 155–162.

Press, W. H., 2007. *Numerical recipes 3rd edition: The art of scientific computing*, Cambridge university press.

Pruess, K., 1991. *TOUGH2: A general-purpose numerical simulator for multiphase fluid and heat flow*, Lawrence Berkeley Lab. Berekeley, California.

Rubino, J. G., Velis, D. R., & Sacchi, M. D., 2011. Numerical analysis of wave induced flow effects on seismic data: Application to monitoring of CO_2 storage at the Sleipner field, *J. Geophys. Res.*, **116**(B3), 1–16.

Ryan, H., 1994. Ricker, Ormsby, Klauder, Butterworth a choice of wavelets, *Can. Soc. Explor. Geophys. Record*, **19**(7), 8–9.

Sengupta, M. & Mavko, G., 2003. Impact of flowsimulation parameters on saturation scales and seismic velocity, *Geophys.*, **68**(4), 1267–1280.

Smith, W. H. F. & Wessel, P., 1990. Gridding with continuous curvature splines in tension, *Geophysics*, **55**(3), 293–305.

Soubaras, R. & Dowle, R., 2010. Variable-depth streamer–a broadband marine solution, *First Break*, **28**(12).

Tenghamn, R., Vaage, S., & Borresen, C., 2007. A dualsensor towed marine streamer: Its viable implementation and initial results, in *SEG Tech. Progr. Expand. Abstr. 2007*, pp. 989–993, Society of Exploration Geophysicists.

Toms, J., Müller, T. M., & Gurevich, B., 2007. Seismic attenuation in porous rocks with random patchy saturation, *Geophysical Prospecting*, **55**(5), 671–678.

Vella, D. & Huppert, H. E., 2006. Gravity currents in a porous medium at an inclined plane, *J. Fluid Mech.*, **555**, 353.

Verdon, J. & Woods, A. W., 2007. Gravity-driven reacting flows in a confined porous aquifer, *J. Fluid Mech*, **588**.

Verdon, J. P., Kendall, J.-M., White, D. J., Angus, D. A., Fisher, Q. J., & Urbancic, T., 2010. Passive seismic monitoring of carbon dioxide storage at Weyburn, *Lead. Edge*, **29**(2), 200–206.

White, J., 1975. Computed seismic speeds and attenuation in rocks with partial gas saturation, *Geophysics*, **40**(2), 224–232.

Widess, M., 1973. How thin is a thin bed?, *Geophysics*, **38**(6), 1176–1180.

Williams, G. & Chadwick, A., 2012. Quantitative seismic analysis of a thin layer of CO_2 in the Sleipner injection plume, *Geophysics*, **77**(6), 245–256.

Williams, G. A. & Chadwick, R. A., 2017. An improved history-match for layer spreading within the Sleipner plume including thermal propagation effects, *Energy Procedia*, **114**(Supplement C), 2856–2870.

Wilson, D., Davies, J. R., Waters, R. A., & Zalasiewiczt, J. A., 1992. A fault-controlled depositional model for the Aberystwyth Grits turbidite system, *Geol. Mag.*, **129**(05), 595.

Yilmaz, Ö., 2001. *Seismic data analysis: Processing, inversion, and interpretation of seismic data*, Soc. Explor. Geophys.

Zheng, Z., Guo, B., Christov, I. C., Celia, M. A., & Stone, H. A., 2015. Flow regimes for fluid injection into a confined porous medium, *J. Fluid Mech.*, **767**(6), 881–909.

Zhu, C., Zhang, G., Lu, P., Meng, L., & Ji, X., 2015. Benchmark modeling of the Sleipner CO_2 plume: Calibration to seismic data for the uppermost layer and model sensitivity analysis, *Int. J. Greenh. Gas Control*, **43**, 233–246.

Zweigel, P., Arts, R., Lothe, A. E., & Lindeberg, E. B. G., 2004. Reservoir geology of the Utsira Formation at the first industrial-scale underground CO_2 storage site (Sleipner area, North Sea), *Geol. Soc. London, Spec. Publ.*, **233**(1), 165–180.

Appendix A

Estimating Acoustic Velocity through CO_2-Saturated Sandstone

A.1 Introduction

The Gassmann model is used to calculate the acoustic velocity of seismic waves through a CO_2-saturated sandstone (Mavko & Mukerji, 1998). The effective fluid bulk modulus depends on the distribution of CO_2 within the porous medium (see Section 2.5.1). The Reuss model is used to describe the uniform saturation case, while the Brie and Voigt models provide estimates for the patchy saturation case. Here, the differences between the models are discussed. Uncertainties in the estimates of input parameters are then used to determine upper and lower bounds for the uniform saturation case (Table A.1).

A.2 The Gassmann Model

Body wave velocities through a homogeneous, elastic, isotropic medium are given by

$$v_P = \left(\frac{K + \frac{4}{3}\mu}{\rho} \right)^{\frac{1}{2}} \tag{A.1}$$

$$v_S = \left(\frac{\mu}{\rho} \right)^{\frac{1}{2}} \tag{A.2}$$

where v_P and v_S are the P-wave and S-wave velocities, respectively. K is the effective bulk modulus of the rock, μ is the shear modulus, and ρ is the density of the medium.

If velocities are known, then the bulk and shear moduli of the medium can be estimated using

$$\mu = \rho {v_S}^2 \tag{A.3}$$

$$K = \rho({v_P}^2 - \tfrac{4}{3}{v_S}^2). \tag{A.4}$$

The change in bulk modulus of a fluid saturated rock caused by substitution of the ambient brine for some saturation of CO_2 is calculated using the following equation

$$\frac{K_{sat}}{K_{min} - K_{sat}} - \frac{K_{br}}{\phi(K_{min} - K_{br})} = \frac{K_{sat}(S_{CO_2})}{K_{min} - K_{sat}(S_{CO_2})} - \frac{K_{fl}(S_{CO_2})}{\phi[K_{min} - K_{fl}(S_{CO_2})]}, \tag{A.5}$$

where ϕ is the porosity of the rock, K_{sat} is the bulk modulus of the brine-saturated rock, S_{CO_2} is the saturation of CO_2 in the rock, $K_{sat}(S_{CO_2})$ is the bulk modulus of the rock with some saturation of CO_2, K_{br} is the bulk modulus of the brine and $K_{fl}(S_{CO_2})$ is the bulk modulus of the fluid mixture of CO_2 and brine. The effective fluid bulk modulus depends on the mixing of the fluids within the pore space (Mavko *et al.*, 2009). For uniformly mixed saturation of CO_2, the bulk modulus of the fluid mixture is calculated using Reuss averaging and is given by

$$K_{fl}(S_{CO_2}) = \left(\frac{S_{CO_2}}{K_{CO_2}} + \frac{(1 - S_{CO_2})}{K_{br}} \right)^{-1}. \tag{A.6}$$

Alternatively, the Voigt average can be used to calculate an upper bound for K_{fl} for the

patchy saturation case

$$K_{fl}(S_{CO_2}) = S_{CO_2}K_{CO_2} + (1 - S_{CO_2})K_{br}. \tag{A.7}$$

A more useful estimate for K_{fl} is given by an empirical model known as Brie's model

$$K_{fl}(S_{CO_2}) = (K_{CO_2} + K_{br})(1 - S_{CO_2})^e + K_{CO_2}, \tag{A.8}$$

where e is an empirical constant (Mavko *et al.*, 2009). For this analysis $e = 5$, as used by Carcione *et al.* (2006) based on a comparison with White's model of patchy saturation (White, 1975).

The shear modulus is unchanged by pore fluid (i.e. $\mu_{dry} = \mu_{sat}$). The density of the partially CO_2 saturated rock is given by

$$\rho(S_{CO_2}) = (1 - \phi)\rho_{min} + \phi S_{CO_2}\rho_{CO_2} + \phi(1 - S_{CO_2})\rho_{br}. \tag{A.9}$$

These values are used to find $v_P(S_{CO_2})$ for $0 \leq S_{CO_2} \leq 1$ using

$$v_P(S_{CO_2}) = \left(\frac{K_{sat}(S_{CO_2}) + \frac{4}{3}\mu}{\rho(S_{CO_2})}\right)^{\frac{1}{2}}. \tag{A.10}$$

The parameter values used to estimate $v_P(S_{CO_2})$ are given in Table A.1. P- and S-wave velocities were measured at a nearby well and their values are generally agreed upon. For the bulk modulus and density of the mineral phase of the sandstone, there is also broad agreement, although some uncertainty is introduced by the possible variation in mineralogy within the Utsira Formation. Porosity was also measured at nearby wells and does vary throughout the Utsira Formation. However, there is a broad consensus that the average value is 0.37 (Chadwick *et al.*, 2005). The bulk modulus of the brine is well known (E. Lindeberg, written communication, 2000). Due to the uncertainties of pressure and temperature estimates for Layer 9, values of the bulk modulus and the density for dense-phase CO_2 can vary. I use values favoured by the Institut Français du Petrole based on a temperature of 29°C with a methane content of 1 %. Uncertainties for all input parameters were chosen to

Table A.1: Parameter values and their uncertainties used to calculate v_{CO_2}.

Parameter	Symbol	Value	Uncertainty	Units
P-wave velocity	v_P	2050	±30	m s^{-1}
S-wave velocity	v_S	693	±25	m s^{-1}
Mineral bulk modulus	K_{min}	36.9	±0.1	GPa
Mineral density	ρ_{min}	2650	±25	kg m^{-3}
Porosity	ϕ	0.37	±0.3	
Brine bulk modulus	K_{br}	2.31	±0.1	GPa
Brine density	ρ_{br}	1040	±20	kg m^{-3}
CO_2 bulk modulus	K_{CO_2}	88	±30	MPa
CO_2 density	ρ_{CO_2}	692	±30	kg m^{-3}

reflect the range of estimates found in the literature. Using these values, v_{CO_2} was calculated to be 1428 ± 95 m s^{-1}.

To understand how sensitive v_{CO_2} is to each of the input parameters, each parameter is varied in turn. In Figure A.1, v_{CO_2} is plotted as a function of S_{CO_2} and each input parameter is varied by ± 10 %. These results show that changes in the bulk modulus and in the density of CO_2 have little impact upon the value of v_{CO_2}. The parameters that have the greatest effect on acoustic velocity are v_P, ρ_{min}, ϕ and K_{br}. Since v_P and ρ_{min} are well constrained, the largest uncertainties stem from K_{br} and from the porosity distribution within the Utsira Formation.

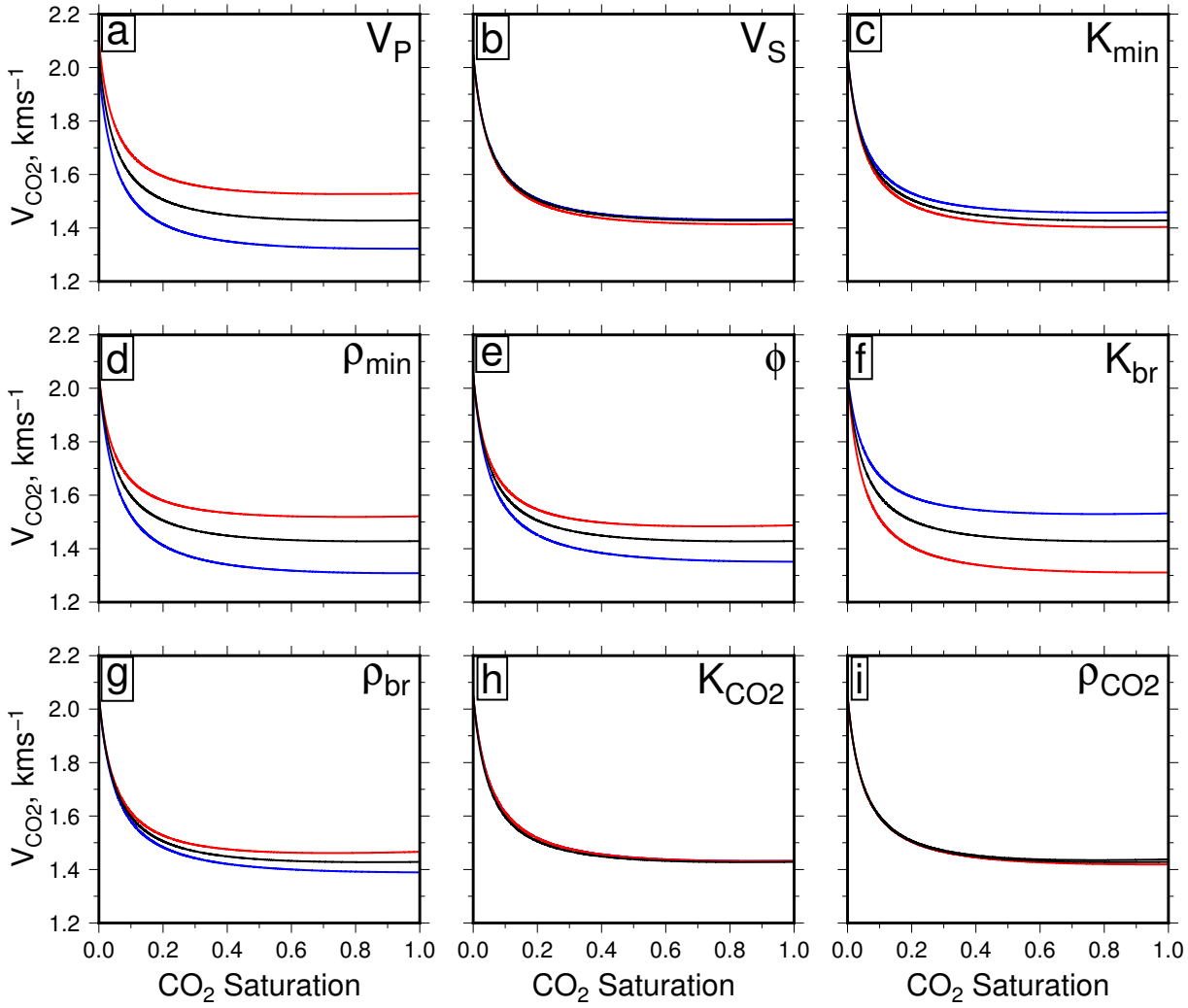

Figure A.1: P-wave velocity calculations showing sensitivity to input parameters. **(a)** Black line = P-wave velocity as function of CO_2 saturation through water-saturated sandstone; red/blue lines = uncertainty range for input $v_P \pm 10$ %. **(b)** S-wave velocity. **(c)** Bulk modulus of mineral material. **(d)** Density of mineral material. **(e)** Porosity. **(f)** Bulk modulus of ambient brine. **(g)** Density of ambient brine. **(h)** Bulk modulus of CO_2. **(i)** Density of CO_2.

Appendix B

Numerical Methods

B.1 Numerical Forward Modelling of Gravity Currents

The numerical models in this dissertation (e.g. Equation 4.7) are solved using a Crank-Nicholson finite-difference scheme. The non-linear diffusive buoyancy is accounted for using a predictor corrector step. This scheme permits the thickness of the fluid at the next time-step to be calculated using information about the thickness of the fluid at the current time-step. Mass is conserved throughout the region, and therefore the change in the thickness of the fluid, h, in each grid cell, i, between time-steps, n, must be equal to the flux of fluid in to the cell, $F_{i-1/2}$, minus the flux out, $F_{1+1/2}$,

$$\phi \frac{h_i^{n+1} - h_i^n}{\Delta t} = \frac{F_{i-1/2} - F_{i+1/2}}{\Delta x}, \tag{B.1}$$

where h_i^n refers to the thickness of the current at grid cell i at time-step n, Δx is the distance between neighbouring grid cells, Δt is the time between adjacent time-steps and ϕ is the porosity of the porous medium.

The Crank-Nicholson scheme is centred in space between grid cells and in time between time-steps. To calculate the flux, the right hand side of (4.7) is discretised such that it is centred at the midpoint between time-steps and grid cells. The flux out of the cell, centred at the $n + 1/2$th time-step is therefore given by

$$F_{i+1/2}^{n+1/2} = u_{i+1/2} h_{i+1/2}^{m} \left(\frac{h_{i+1}^{n+1/2} - h_{i}^{n+1/2}}{\Delta x} \right) + u_{i+1/2} \left(\frac{d_{i+1} - d_i}{\Delta x} \right) h_{i+1/2}^{n+1/2}. \tag{B.2}$$

where, for example,

$$h_{i+1/2}^{n+1/2} = \frac{1}{2} \left(\frac{h_{i+1}^{n+1} + h_{i+1}^{n}}{2} + \frac{h_{i}^{n+1} + h_{i}^{n}}{2} \right). \tag{B.3}$$

The superscript m denotes either the nth or the $n + 1/2$th time-step, depending on which step of the predictor corrector scheme is being calculated. Since the scheme is centred in space, information about the thickness of the current at the $n + 1/2$th time-step is required to solve the equation accurately. To estimate this thickness, the thickness of the flow at the current time-step is used to advance the scheme to the half time-step. This information can then be used to calculate the thickness of the current at the next time-step.

Substitution of (B.2) and its equivalent at the $i - 1/2$th grid cell (i.e. the flux into the grid cell) into (B.1) produces the fully discretised version of (4.7). After some algebra, we find that it can be reduced to the following tridiagonal system

$$A_{l,i} h_{i-1}^{n+1} + A_{d,i} h_{i}^{n+1} + A_{u,i} h_{i+1}^{n+1} = b, \tag{B.4}$$

where $A_{l,i}$ contains information on the advective and diffusive terms associated with h_{i-1}^{n+1}, and similarly for $A_{d,i}$ and $A_{u,i}$. b is a vector containing information on the grid cells $i - 1$, i and $i + 1$ at the nth time-step. Equation B.4 can be written in a general form for all grid cells as

$$A\mathbf{x} = b \tag{B.5}$$

where A is a tridiagonal matrix and $\mathbf{x}$ is a vector containing the thickness of the fluid at the $n + 1$th time-step (i.e. the values being solved for). This tridiagonal system is fast and

efficient to solve, and advances the simulation by one time-step.

B.1.1 Il'in Scheme

While the numerical scheme above is adequate for gravity currents flowing along simple topography, the scheme becomes unstable for realistic caprock topography. Steeper topographic gradients cause unphysical numerical oscillations to develop due to the advective term's spatial derivative. Alternative methods of discretising equations such as (4.7), for example 'upwind' or 'downwind' schemes, are able to contend with sharp changes in parameters by preferentially taking more information either from in front of or behind the grid cell being caluclated. However, these methods can suffer from numerical diffusion that can smear the fronts of these simulations. To get around this problem, an unconditionally stable three point differencing scheme first proposed by Il'in (1969) and later by Clauser & Kiesner (1987) that permits the propogation of sharp fronts at high Peclet numbers is implemented. The full derivation of the scheme is given in Clauser & Kiesner (1987).

In this scheme, the flux between the ith and $i+1$th grid square is expressed as

$$F_{i+1/2} = \frac{D}{\Delta x}(h_{i+1} - h_i) - v\left[\frac{h_{i+1} + h_i}{2} + \alpha\frac{(h_i - h_{i+1})}{2}\right] \tag{B.6}$$

where v is the advective term, D is the diffusive term and α is calculated using

$$\alpha = \coth(q) - \frac{1}{q} \tag{B.7}$$

where

$$q = \frac{v\Delta x}{2D} \tag{B.8}$$

is the Peclet number for the grid divided by 2. α acts as a spatial weighting parameter that determines how much 'local upwinding' is required depending on the strength of the advective and diffusive parameters at each grid cell. The effect of this parameter is shown below in three examples.

In this formulation, if $0 < D \ll v$ (i.e. large Peclet numbers), then $\alpha \approx 1$ and so equation B.6 becomes

$$F_i = \frac{D}{\Delta x}(h_{i+1} - h_i) - v h_i, \tag{B.9}$$

meaning that the advective term is strongly influenced by information from the 'upwind' direction. For $0 < v \ll D$ (i.e. small Peclet numbers) then $\alpha \approx 0$ and so equation B.6 becomes

$$F_i = \frac{D}{\Delta x}(h_{i+1} - h_i) - v\frac{(h_{i+1} + h_i)}{2}, \tag{B.10}$$

which is equivalent to a normal Crank-Nicholson scheme. For $v \ll 0 < D$ then $\alpha \approx -1$ and so equation B.6 becomes

$$F_i = \frac{D}{\Delta x}(h_{i+1} - h_i) - v h_{i+1}, \tag{B.11}$$

meaning that the advective term is strongly influenced by information from the 'downwind' direction. These three examples show that depending on the size of v and whether it is positive or negative, α will determine how much upwinding is required to ensure that the scheme remains stable.

Using this finite difference scheme, the full discritisation of equation 4.7 is as follows:

$$\begin{aligned}\frac{h_i^{n+1} - h_i^n}{\Delta t} =& \frac{1}{\Delta x}\left(\frac{D}{\Delta x} - \frac{v}{2}(1-\alpha)\right)_{i+1/2}^{n+1/2} h_{i+1}^{n+1/2} \\ &- \frac{1}{\Delta x}\left[\left(\frac{D}{\Delta x} - \frac{v}{2}(1-\alpha)\right)_{i-1/2}^{n+1/2} + \left(\frac{D}{\Delta x} + \frac{v}{2}(1+\alpha)\right)_{i+1/2}^{n+1/2}\right] h_i^{n+1/2} \\ &+ \frac{1}{\Delta x}\left(\frac{D}{\Delta x} + \frac{v}{2}(1+\alpha)\right)_{i-1/2}^{n+1/2} h_{i-1}^{n+1/2}\end{aligned} \tag{B.12}$$

To simplify notation, define

$$c_{xa} = \frac{D}{\Delta x} - \frac{v}{2}(1-\alpha) \tag{B.13}$$

$$c_{xb} = \frac{D}{\Delta x} + \frac{v}{2}(1+\alpha) \tag{B.14}$$

Equation B.12 is then rearranged to collect terms relating to the known time-step and terms

relating to the time-step to be calculated,

$$\begin{aligned} -(c_{xa})^{n+1/2}_{i+1/2}h^{n+1}_{i+1} + \left[\frac{1}{\Delta t} + (c_{xb})^{n+1/2}_{i+1/2} + (c_{xa})^{n+1/2}_{i-1/2}\right] h^{n+1}_{i} - (c_{xb})^{n+1/2}_{i-1/2}h^{n+1}_{i-1} \\ = (c_{xa})^{n+1/2}_{i+1/2}h^{n}_{i+1} + \left[\frac{1}{\Delta t} - (c_{xb})^{n+1/2}_{i+1/2} - (c_{xa})^{n+1/2}_{i-1/2}\right] h^{n}_{i} + (c_{xb})^{n+1/2}_{i-1/2}h^{n}_{i-1}. \end{aligned} \tag{B.15}$$

This scheme can then be solved using a tridiagonal solver.

B.1.2 Alternating Direction Implicit Method

To model VO_2 flow in three dimensions I use an operator splitting method known as the Alternating Direction Implicit (ADI) method (Peaceman & Rachford, 1955). This method advances the numerical simulation by a half time-step in the x-direction, and then by a half time-step in the y-direction, thus advancing the flow of CO_2 by a whole time-step after one iteration.

In three dimensions, Equation 4.7 becomes

$$\phi\frac{\partial h}{\partial t} = \frac{\partial}{\partial x}\left(uh\frac{\partial h}{\partial x}\right) + \frac{\partial}{\partial x}\left(u\frac{\partial d}{\partial x}\right)h + \frac{\partial}{\partial y}\left(uh\frac{\partial h}{\partial y}\right) + \frac{\partial}{\partial y}\left(u\frac{\partial d}{\partial y}\right)h. \tag{B.16}$$

Using the ADI scheme, this equation is then solved in four stages. In the first stage, the thickness of the current in the y direction is held constant, and the predictor step calculates the thickness of the current in the x direction at the $n + 1/4$th time-step while holding the thickness of the current in the y direction constant. In the corrector step, the the x-terms are then advanced to the $n + 1/2$th time-step using coefficients centred at the $n + 1/4$th time-step, again while holding the terms in the y direction constant, as shown below

$$\begin{aligned} -(c_{xa})^{n+1/4}_{i+1/2,j}h^{n+1/2}_{i+1,j} + \left[\frac{1}{\Delta t} + (c_{xb})^{n+1/4}_{i+1/2,j} + (c_{xa})^{n+1/4}_{i-1/2,j}\right] h^{n+1/2}_{i,j} - (c_{xb})^{n+1/4}_{i-1/2,j}h^{n+1/2}_{i-1,j} \\ = (c_{ya})^{n+1/4}_{i,j+1/2}h^{n}_{i,j+1} + \left[\frac{1}{\Delta t} - (c_{yb})^{n+1/4}_{i,j+1/2} - (c_{ya})^{n+1/4}_{i,j-1/2}\right] h^{n}_{i,j} + (c_{yb})^{n+1/4}_{i,j-1/2}h^{n}_{i,j-1}, \end{aligned} \tag{B.17}$$

where c_{ya} and c_{yb} are the same as for c_{xa} and c_{xb}, but in the y-direction, and j refers to the grid cell index in the y-direction. To advance the current in the y-direction, the same

procedure is followed as before, but holding the x-direction constant,

$$\begin{aligned} -(c_{ya})^{n+3/4}_{i,j+1/2} h^{n+1/2}_{i,j+1} + \left[\frac{1}{\Delta t} + (c_{yb})^{n+3/4}_{i,j+1/2} + (c_{ya})^{n+3/4}_{i,j-1/2}\right] h^{n+1/2}_{i,j} - (c_{yb})^{n+3/4}_{i,j-1/2} h^{n+1/2}_{i,j-1} \\ = (c_{xa})^{n+3/4}_{i+1/2,j} h^{n}_{i+1,j} + \left[\frac{1}{\Delta t} - (c_{xb})^{n+3/4}_{i+1/2,j} - (c_{xa})^{n+3/4}_{i-1/2,j}\right] h^{n}_{i,j} + (c_{xb})^{n+3/4}_{i-1/2,j} h^{n}_{i-1,j}. \end{aligned} \tag{B.18}$$

This method can still be solved using a tridiagonal matrix solver, and is therefore a fast and efficient calculation.